Master of Science Thesis

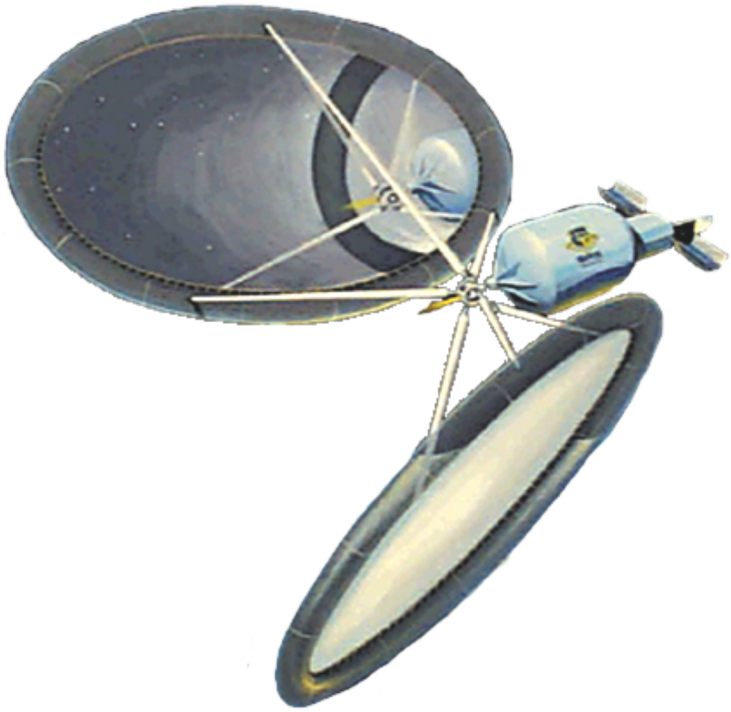

Design of a Solar Thermal Power-Propulsion System for a Small Satellite

A feasibility study of a solar thermal hybrid system

J.J. Preijde

29th of January 2015

Faculty of Aerospace Engineering · Delft University of Technology

TU Delft Delft University of Technology

Challenge the future

Design of a Solar Thermal Power-Propulsion System for a Small Satellite

A feasibility study of a solar thermal hybrid system

Master of Science Thesis

For obtaining the degree of Master of Science in Aerospace Engineering at Delft University of Technology

J.J. Preijde

29th of January 2015

Faculty of Aerospace Engineering · Delft University of Technology

Copyright © J.J. Preijde
All rights reserved.

Delft University Of Technology
Department Of
Space Systems Engineering

The undersigned hereby certify that they have read and recommend to the Faculty of Aerospace Engineering for acceptance a thesis entitled **"Design of a Solar Thermal Power-Propulsion System for a Small Satellite"** by **J.J. Preijde** in partial fulfillment of the requirements for the degree of **Master of Science**.

Dated: 29th of January 2015

Head of department: _____
Prof.dr. E.K.A Gill

Supervisor: _____
A. Cervone

Reader: _____
C.M. De Servi

Summary

Besides chemical, cold gas and electric propulsion, solar thermal propulsion (STP) provides an alternative approach to spacecraft propulsion.
This technology can also be adapted to provide power to the spacecraft by converting a part of the totally available thermal energy into electrical energy. If combined, one can build a solar thermal power-propulsion hybrid system. This thesis focuses on a system for a small satellite with a dry mass of 200 kg and a bus volume of 1 m^3.

The propulsion subsystem concerns a primary and secondary solar concentrator, a receiver/absorber cavity (RAC), a heat exchange mechanism between absorber and propellant, a propellant storage and feed system, a thruster chamber and a thruster nozzle.

The power subsystem consists of an interface between the absorber and a heat exchanger, the heat exchanger which heats up the working fluid in the Organic Rankine Cycle (ORC) power subsystem, a turbine which provides the power and a condenser which dissipates a part of the heat in the working fluid. Finally, a small pump is used to force the cold fluid to the heat exchanger and increase the pressure of the fluid.

A Design, Analysis and Optimization (DAO) tool has been built to model the hybrid system. Results from the tool have yielded performances of particular designs and have provided answers whether such a system is feasible and offers advantages over conventional power and propulsion subsystems.
The DAO model consists of a solar flux and orbit model to calculate the orbit characteristics and available solar flux. The thermal and thruster models subsequently calculate the temperature of the thermal nodes of the system as well as the propulsive performance.
Nine thermal nodes have been used to calculate the temperatures from solar concentrators to the interface between absorber and ORC heat exchanger. These nodes have been divided in a total of 17 sub-nodes.
After model integration a long iterative cycle has been performed where different design variables have been changed to evaluate design-performance relations. These variables include the type of propellant, material choices for the thermal nodes, shape of the absorber, shape of the thruster nozzle as well as the width and length of the different nodes. A maximum of three orbits is simulated to limit computing time. Thrust is assumed to be generated during that entire time to achieve a worst-case scenario. Within those three orbits eclipse is taken into account. During those eclipse periods propellant flow is interrupted whereas power generation continues.

Application of the DAO tool yielded that a conical nozzle produces less thrust than a bell-shaped nozzle. In terms of non-cryogenic propellants water and hydrogen respectively achieved too low temperatures and a too high storage volume to be practical. This left liquid ammonia and liquid hydrogen as propellant candidates. Due to the larger length of propellant tubing in a spiral configuration of one feed line in comparison to a linear configuration of multiple feed lines, the former was selected for the conceptual designs.
The conceptual design phase yielded six designs, each set of two with a conical, cylindrical or spherical absorber. Each concept either had ammonia or hydrogen as propellant to allow comparison of the performance of different propellants.
Analyzing the scalability of the system in terms of its performance resulted in limited scalability for output power with a doubling of the power requiring a too large heat dissipation out of the condenser. Also for specific impulse the scalability was limited. A good scalability however was achieved in terms of the thrust from 1 N originally to at least 5 N. The assumption here was that no large design changes have to occur to achieve higher performance.

After running the DAO tool for the concepts and making a trade-off, the third concept was selected. It has a cylindrical RAC and uses liquid ammonia. The liquid hydrogen option for the same RAC configuration was deemed infeasible due to the 20-K storage temperature requirement which is very difficult to achieve in a small satellite.
The third concept has a relatively low system complexity, a high thrust and an advantageously low system volume estimate. Its main disadvantage however is the low system-specific impulse meaning it will require more system mass to generate a certain amount of impulse.

The detailed design phase led to a more detailed design and accurate characterization of the concept.
The decision was made to include an on-axis primary concentrator as this device is easier to model than an off-axis concentrator. A comparison between the two types is beyond the scope of this thesis. The secondary concentrator is a refractive one made of a single-crystal sapphire material. The secondary concentrator casing and the other components are made of molybdenum since this material has a high thermal conductivity and can cope with temperatures up to 2800 K.

The casing has a white-paint coating to limit its emissivity and temperature increase due to external radiation. The pre-cavity chamber connecting the casing and the RAC lid is insulated with multi-layer insulation (MLI) and fastened and grounded with hook-and-pile fasteners and conductive tape. The RAC lid has a 14 mm molybdenum core and on both sides a 43-mm thick MLI blanket to insulate the cavity from the rest of the system in front of it.
The cylindrical RAC has an outer diameter of 14 cm and a wall thickness of 10.8 mm. It has a length of 30 cm. The interior has a high-performance black-paint coating giving it an absorptance of 0.96 and an emissivity of 0.88.
Three mounting options for the RAC were traded-off: mounting by aluminium struts, passive orbit disconnect struts (PODS) or encapsulation by MLI. Although the MLI option preserved the RAC temperature the best it also had the largest mass. Aluminium struts caused a large dissipation of RAC heat. PODS were therefore selected. They

maintain the RAC relatively well and the eight struts have a combined mass of only 64 g.

While discussing the propellant feed system, pump-driven and blow-down systems were briefly compared. Since a pump-fed system would increase the mass ans size of the entire system considerably, a blow-down scheme was selected.

For the thruster nozzle a bell-shape was selected due to the smaller loss of thrust compared to a conical nozzle. After comparing 12 nozzle shapes, a nozzle with an expansion ratio of 300 and a length of 9 cm was designed. The nozzle throat convergence half angle is 25 degrees, the throat divergence half angle is 30 degrees and the nozzle exhaust divergence half angle is 13.8 degrees. This yielded a specific impulse of 185 s and thrust of 1.31 N. The thruster mass estimate is 0.064 kg. The required propellant mass is 29.3 kg.

The tubing was compartmentalized in three parts, the tubing from propellant tank to the RAC, the RAC tubing and the tubing from RAC to the thruster. Summing the three tubing lengths up, resulted in a total tubing length of 9.14 m and an accompanying tubing mass of 0.914 kg. The pressure loss in the gaseous flow, the liquid flow and due to acceleration pressure and two-phase flow was summed up to a loss of 128 kPa. If the thruster chamber pressure is 1 bar, the pressure at the tank exit must therefore be at least 2.28 bar.

A cylindrical propellant tank was designed, since a spherical tank would be impractical within the spacecraft bus. The tank has a volume of 0.052 m^3. It has a total length of 65 cm and an inner radius of 17.6 cm. The tank wall has a thickness of 1.1 mm with a safety factor of 1.5. The pressurant gas helium must be at a pressure of 11.4 to guarantee this pressure during the entire blow-down process. The total tank mass is estimated at 2.10 kg. Together with the propellant and pressurant gas a total propellant tank mass of 31.4 kg was determined. Passive and active thermal control for the propellant tank was also discussed. Since active thermal control is troublesome to integrate and requires heavy components, only passive thermal control was used. Three options were analyzed and traded-off. First, an MLI option only was analyzed. Second and third, an MLI with a radiator and an MLI with optical solar reflectors (OSRs) option were looked at. The first and third option would increase the temperature of the propellant tank beyond the 243-K requirement. Only the second option maintained a constant temperature. In addition, the radiator could be integrated into the spacecraft bus, saving mass. Therefore, the MLI-radiator option was selected with an insulation mass of 1.4 kg.

Two check vales are used to fill the propellant tank with helium pressurant and ammonia propellant. A check valve in front of the thruster makes sure a minimum thrust is guaranteed. Two relief valves can evacuate over-pressurized propellant flow if necessary without leading to severe attitude disturbances. A solenoid valve and pressure regulator respectively control the activation of propellant flow and the pressure down-stream of the propellant tank. The total valve mass is 3.7 kg.
Together with the 25-kg mass for the RAC system this yields a total dry propulsion subsystem mass of 36 kg.

As stated previously, the power subsystem has four main components: the evaporator, turbine, condenser and pump. The working fluid in the ORC is toluene and the heating gas to the evaporator is air. The heat transfer between evaporator heating gas channel and the RAC occurs through radiative processes. This saves system volume and mass over a conductive heat channel.
The heating gas channel has an outer diameter of 3.5 cm and a tube thickness of 2.7 mm. This yields a channel mass of 0.940 kg. The air in the channel is fed into the evaporator heat exchanger at a pressure of 5 kPa. A plate fin heat exchanger with a mass of 14 kg was selected to provide the heat exchange between the air and the working fluid.

The micro-turbine was linearly scaled based on turbine literature. The turbine must deal with a turbine inlet temperature of the toluene of 565 K, an inlet pressure of 13.67 bar and a working fluid flow rate of 0.85 g/s. Its rotor diameter would be 1-3 cm and from linear scaling a mass of 0.413 kg was determined. The long-term performance and specific design of the turbine are matters which will need to be researched and analyzed. These issues are however beyond the scope of this thesis.

The condenser is a passive device as an active condenser would increase the mass substantially and add another fluid cycle to the spacecraft. The condenser needs to dissipate 573 W to ensure a working fluid temperature of 313 K. The heat can be dissipated to space and/or the spacecraft interior.
A box was simulated with a total external area of m^2, an emittance of 0.80 and a view factor to the surroundings of 0.9. It needed to be kept at a temperature of 15 degrees Celsius, assuming an environment temperature of 173.15 K. A heat of 223 W was required for heating purposes. The condenser therefore needed to dissipate 350 W to space.
A condenser conducting channel with a length of 10 cm and a diameter of 16 mm was calculated to transfer the heat from the condenser to the radiator plate. The condenser outer radius is 8.5 mm and the length over which the working fluid is cooled is 5 cm. A total mass of 0.209 kg was calculated for these two components. The radiator plate is incorporated into the bus structure and has an area of 0.4 m^2.

A micro-pump is used to increase the pressure of the working fluid to the evaporating pressure of 13.67 bar and force the fluid from condenser to evaporator. A representative device was procured. The device uses 100 mW and has a mass of 0.34 kg. This device is a magnetic drive pump with a maximum speed of 8000 rpm.

For the working fluid feed system, a total tubing length of 1.06 m including a 10% margin for bends was calculated. The outer tubing diameter is 1.7 cm and the wall has a thickness of 1.3 mm. The Al-6061 aluminium alloy was selected for the tubing material as the fluid temperature does not exceed 400 K. This yielded a tubing mass of 0.184 kg.
Including a 20% design margin to take into account unknowns and the unknown air and toluene mass, the total power subsystem mass became 19.3 kg.

The total wet system mass then became 84.8 kg. After running the model for a final

time, a thrust, specific impulse and power was generated of respectively 1.31 N, 185 s and 115 W. The system had a maximum daylight efficiency in the third orbit of 37% and a minimum efficiency in eclipse of 17%. The system-specific impulse was 65 s.
An estimate of 0.83 m^3 was given for the practical space left in the spacecraft bus after hybrid system integration.

Compared to a conventional system which generates the same kind of power, thrust and specific impulse, the hybrid system mass were way more than the 30.9 kg for the conventional system. Furthermore, the system-specific impulse was lower than the 123 s for the conventional system. The major operational advantage of the hybrid system however is that it can generate power during both daylight and eclipse, saving the need for batteries.
For larger satellites with a larger bus and mass this system will be more appropriate as it will need a relatively smaller fraction of the bus volume and mass due to non-linear scaling of the system.

After this design and feasibility study, the research questions posed at the beginning could be answered.
If one looks at the difference in thrust and specific impulse when the propellant is changed from ammonia to hydrogen, the thrust decreased only marginally. The specific impulse however increased by a factor of 3.2 to 4.0. Water increased the specific impulse by 9% and nitrogen was representative of the performance of ammonia. The latter however requires a large storage volume. Nitrogen can thus be used for testing purposes when no cryogenic equipment is available.
One could therefore conclude that using liquid hydrogen creates a lighter and smaller system with respect to the use of liquid ammonia. The concepts which use ammonia however require a smaller primary concentrator.

The concepts which use hydrogen and have a conical or spherical RAC provided the fastest and largest heat exchange between the RAC and the propellant.
A radiative interface between the RAC and evaporator heating gas conduit had a smaller mass as it required no physical connection between the RAC and the conduit. It was therefore the most appropriate for the design considered.
It was determined after a number of iterative simulations that appreciable scalability within the same system is only achieved for thrust; the power and specific impulse can barely be scaled up.

Equation 5.5 gives the efficiency equation for the hybrid system and includes the input solar power, thrust, thruster equivalent exhaust velocity and the output turbine power. To increase the measure of efficiency for the same ORC power output one should increase the exhaust velocity by increasing the propellant temperature. Furthermore, the nozzle shape can be changed to limit thrust loss.
The hydrogen concepts generated a daylight efficiency of 9% versus an efficiency of 29-42% for the ammonia concepts. The ammonia concepts offered greater efficiency in eclipse as well; they had an efficiency in the range of 13-19% whereas the hydrogen concepts offered only 4% efficiency.

Acknowledgements

I wish to thank the following individuals for the help they provided me during my thesis research:

Angelo Cervone, for the supervision and feedback on my thesis as well as the research process;

Adam Head and Sebastian Bahamonde, for the help in applying and integrating the *ORCHID-VPE* model into the thesis model;

and prof. Piero Colonna, for providing additional information on ORC processes.

J.J. Preijde

Delft, The Netherlands
29th of January 2015

Contents

Summary v

Acknowledgements xi

List of Figures xxii

List of Tables xxiv

Nomenclature xxv

Glossary xxxi

1 Introduction 1

2 Research framework 3
- 2.1 Research questions . . . 3
- 2.2 Objectives . . . 4
- 2.3 Operational scenarios . . . 5
- 2.4 System requirements . . . 6

3 Design, Analysis and Optimization Tool 9
- 3.1 Orbit and solar flux model . . . 10
  - 3.1.1 Orbit model . . . 10
  - 3.1.2 Solar flux model . . . 12
- 3.2 Thermal model . . . 13
  - 3.2.1 Introduction . . . 13
  - 3.2.2 Geometries and properties of nodes . . . 15
    - 3.2.2.1 Primary concentrator geometry and properties . . . 16
    - 3.2.2.2 Secondary concentrator geometry and properties . . . 17
    - 3.2.2.3 RAC geometry and properties . . . 17
  - 3.2.3 Tubing configurations . . . 19
    - 3.2.3.1 Spiral tubing configuration . . . 19
    - 3.2.3.2 Linear tubing configuration . . . 20
  - 3.2.4 Heat conducting channel and evaporator . . . 21
  - 3.2.5 View factors . . . 21

3.2.6 Gebhart factors and thermal couplings . . . 22
3.2.7 Convective heat flow . . . 23
3.2.7.1 Nusselt, Prandtl and Reynolds numbers . . . 23
3.2.8 Flow properties in tubing . . . 23
3.2.9 Temperature calculations . . . 24
3.2.10 Pressure losses . . . 26
3.2.10.1 Single-phase flow friction pressure loss . . . 27
3.2.10.2 Two-phase flow friction pressure loss . . . 28
3.2.10.3 Acceleration pressure loss . . . 29
3.3 Thruster Model . . . 29
3.3.1 Introduction . . . 29
3.3.2 Nozzle shape . . . 29
3.3.2.1 Conical nozzle . . . 30
3.3.2.2 Bell-shaped nozzle . . . 30
3.3.3 Nozzle critical flow conditions . . . 31
3.3.4 Chamber flow conditions . . . 32
3.3.5 Thruster and propulsion subsystem performance . . . 32
3.4 Verification and validation . . . 34
3.4.1 Thrust, specific impulse and mass flow validation . . . 35
3.4.2 Temperature validation . . . 36
3.5 Observations . . . 39
3.5.1 Increasing convection area . . . 39
3.5.2 Increasing cavity dimensions . . . 40
3.5.3 Too large primary concentrator . . . 41
3.5.4 Increasing power output . . . 42
3.5.5 Decreasing propellant mass flow . . . 42
3.5.6 Applying insulation around RAC . . . 42
3.5.7 Conclusions concerning observations . . . 44

4 Organic Rankine Cycles 47
4.1 Working principles . . . 47
4.2 Condenser performance . . . 50

5 Conceptual design 53
5.1 Conceptual system requirements and assumptions . . . 53
5.1.1 Requirements . . . 53
5.1.2 Assumptions . . . 54
5.1.2.1 Mass estimates . . . 54
5.1.2.2 RAC and interfaces . . . 55
5.1.2.3 Thermal nodes and tubing conditions . . . 55
5.1.2.4 External fluxes and temperatures . . . 56

5.2 General design considerations . . . 59
5.2.1 System efficiency . . . 59
5.2.2 Materials and constituent fluids and gases . . . 60
5.2.3 Nozzle shape . . . 61
5.2.4 Tubing configuration . . . 63
5.2.5 Power subsystem . . . 64
5.3 Concepts . . . 66
5.3.1 Thermal nodes and summary of the concepts . . . 66
5.3.2 Concept 1 . . . 67
5.3.2.1 Performance with water as non-cryogenic propellant . . . 70
5.3.2.2 Performance with nitrogen as non-cryogenic propellant . . . 71
5.3.3 Concept 2 . . . 72
5.3.4 Concept 3 . . . 75
5.3.5 Concept 4 . . . 77
5.3.6 Concept 5 . . . 80
5.3.7 Concept 6 . . . 83
5.4 Mass and size comparison of concepts . . . 85
5.4.1 Mass of the concepts . . . 85
5.4.2 Size of the concepts . . . 86
5.5 Performance comparison of concepts . . . 88
5.6 Scalability . . . 89
5.6.1 Power . . . 90
5.6.2 Thrust . . . 90
5.6.3 Specific impulse . . . 91
5.7 Thermal stresses . . . 92
5.8 Overall comparison of concepts . . . 94
5.8.1 Performance . . . 94
5.8.2 Thermal stresses and expansions . . . 94
5.9 Conceptual trade-off . . . 95
5.9.1 Trade-off criteria . . . 95
5.9.1.1 Weighting factors . . . 95
5.9.1.2 System volume criterion . . . 96
5.9.1.3 System complexity criterion . . . 97
5.9.2 Trade-off and selection of final concept . . . 98

6 Detailed design **101**
6.1 System architecture and design options . . . 101
6.2 Propulsion subsystem . . . 102
6.2.1 Functional and physical architecture . . . 102
6.2.2 Secondary concentrator . . . 104
6.2.2.1 Concentrator lens . . . 104
6.2.2.2 Concentrator casing . . . 105
6.2.3 Pre-cavity chamber . . . 106
6.2.4 RAC and RAC lid . . . 106
6.2.4.1 PODS . . . 108
6.2.4.2 Aluminium struts . . . 110
6.2.4.3 MLI and fasteners . . . 111
6.2.4.4 Comparison of mounting options . . . 111
6.2.4.5 Mass budget . . . 112
6.2.5 Propellant feed system . . . 113
6.2.5.1 Thruster . . . 114
6.2.5.2 Propellant tubing . . . 115
6.2.5.2.1 Pressure loss for liquid propellant . . . 117
6.2.5.2.2 Pressure loss for gaseous propellant . . . 117
6.2.5.2.3 Two-phase propellant and acceleration pressure losses . . . 118
6.2.5.2.4 Total pressure loss . . . 118
6.2.5.3 Propellant tank . . . 120
6.2.5.4 Propellant tank thermal control . . . 121
6.2.5.4.1 Propellant tank covered in MLI . . . 122
6.2.5.4.2 Propellant tank covered in MLI and interfacing with radiator panel . . . 123
6.2.5.4.3 Propellant tank covered in MLI and covered with OSRs . . . 125
6.2.5.4.4 Comparison of propellant tank thermal control options . . . 125
6.2.5.5 Valves . . . 126
6.2.5.5.1 Solenoid valves . . . 126
6.2.5.5.2 Pressure regulator valve . . . 126
6.2.5.5.3 Pressure relief valves . . . 127
6.2.5.5.4 Check valves . . . 127
6.2.6 Mass budget . . . 127
6.3 Power subsystem . . . 128
6.3.1 Functional and physical architecture . . . 128
6.3.2 Evaporator . . . 129
6.3.2.1 Heat transfer through conduction . . . 130
6.3.2.2 Heat transfer through radiation . . . 130

6.3.2.3 Comparison of heat transfer options . . . 131
6.3.2.4 Evaporator heating gas channel properties . . . 131
6.3.2.5 Evaporator heat exchanger . . . 132
6.3.3 Turbine . . . 132
6.3.4 Condenser . . . 133
6.3.5 Pump . . . 135
6.3.6 Working fluid feed system . . . 135
6.3.7 Mass budget . . . 135
6.4 System integration . . . 136
6.5 Comparison with conventional system . . . 138
6.5.1 Conventional power and propulsion system . . . 139
6.5.1.1 Power subsystem . . . 139
6.5.1.2 Propulsion subsystem . . . 140
6.5.2 Performance comparison . . . 140

7 Answering research questions 143

8 Conclusions and recommendations 147
8.1 Conclusions . . . 147
8.2 Recommendations . . . 148
8.2.1 Test recommendations . . . 148
8.2.2 Research recommendations . . . 149

References 151

A View factors 159
A.1 Node 1 to Node 5 . . . 159
A.2 Node 6 . . . 161
A.2.1 Conical RAC . . . 161
A.2.2 Cylindrical RAC . . . 162
A.2.3 Spherical RAC . . . 163
A.3 View factors to space . . . 164

B Design parameters for conceptual designs 165

List of Figures

2.1 Representative sequence diagram for propulsion subsystem 5
2.2 Representative sequence diagram for power subsystem 6

3.1 Process diagram for DAO tool 9
3.2 Orbit angles to determine solar flux Larson & Wertz (2005) 11
3.3 Plot for the available power and the eclipse time over one year for the reference mission 13
3.4 Schematic of the thermal model node network 15
3.5 Representation of the concentrator lens variables 16
3.6 Representation of the RAC variables 18
3.7 Representation of the spiral tubing variables 20
3.8 Process diagram for thermal model 27
3.9 Two-phase flow region identification (McKetta Jr. 1992) 28
3.10 Representation of nozzle shape 30
3.11 Process diagram for thruster model 34
3.12 Leenders & Zandbergen (2008) test results 35
3.13 Instability of the initial propellant temperature values 37
3.14 Temperatures for the DUT concept as modelled by the DAO tool 38
3.15 Final propellant temperature for different number of spiral tubing turns . 40
3.16 Final propellant temperature for different tubing diameters 40
3.17 Final propellant temperature for different RAC diameters 40
3.18 Final propellant temperature for different RAC configurations 40
3.19 RAC and final propellant temperatures for different primary concentrator and cavity sizes 41
3.20 Secondary concentrator temperature with and without thermal straps . . 42
3.21 Cavity, final propellant and ORC working fluid temperatures at 100 W and 150 W power output 43
3.22 Final propellant temperatures with different throat radii 44
3.23 RAC and final propellant temperatures with and without RAC insulation 45

4.1 Temperature versus entropy plot for simple ORC (Saleh et al. 2007) . . . 48
4.2 Schematic for a solar powered ORC system (Wang et al. 2014) 48

4.3 Schematic showing measurement points of enthalpy states (Kapooria et al. 2008) . . . 49

5.1 Schematic of the heating gas channel and RAC interface . . . 56
5.2 Thermal node temperatures for Concept 1 with continuous propellant flow after flow initialisation . . . 57
5.3 Thermal node temperatures for Concept 1 with tungsten components . . . 61
5.4 Conical nozzle design . . . 62
5.5 Bell-shaped nozzle design . . . 62
5.6 Propellant flow velocity in the conical nozzle for Concept 1 . . . 63
5.7 Propellant flow velocity in the bell-shaped nozzle for Concept 1 . . . 63
5.8 Temperature of thermal nodes for Concept 3 with a linear configuration with 20 propellant tubes . . . 64
5.9 ORC thermal efficiency versus evaporating pressure for Concept 1 . . . 65
5.10 Concept schematic with conical RAC configuration . . . 67
5.11 Temperature of thermal nodes for Concept 1 . . . 68
5.12 Thermal mesh rear view at 60 minutes after model initialisation for Concept 1 68
5.13 Thermal mesh front view at 60 minutes after model initialisation for Concept 1 . . . 68
5.14 Thrust and power generation for Concept 1 . . . 69
5.15 Specific impulse for Concept 1 . . . 69
5.16 System efficiency for Concept 1 . . . 69
5.17 Mean dissipated heat out of ORC condenser for Concept 1 . . . 70
5.18 Thermal node temperatures for Concept 1 with water as propellant . . . 71
5.19 Thermal node temperatures for Concept 1 with nitrogen as propellant . . . 72
5.20 Illustration of thermal straps interfaced with the secondary concentrator . 73
5.22 Thermal mesh rear view at 60 minutes after model initialisation for Concept 2 73
5.23 Thermal mesh front view at 60 minutes after model initialisation for Concept 2 . . . 73
5.21 Temperature of thermal nodes for Concept 2 . . . 74
5.24 Thrust and power generation for Concept 2 . . . 74
5.25 Specific impulse for Concept 2 . . . 74
5.26 System efficiency for Concept 2 . . . 75
5.27 Mean dissipated heat out of ORC condenser for Concept 2 . . . 75
5.28 Temperature of thermal nodes for Concept 3 . . . 76
5.29 Thermal mesh rear view at 60 minutes after model initialisation for Concept 3 76
5.30 Thermal mesh front view at 60 minutes after model initialisation for Concept 3 . . . 76
5.31 Thrust and power generation for Concept 3 . . . 77
5.32 Specific impulse for Concept 3 . . . 77
5.33 System efficiency for Concept 3 . . . 77
5.34 Mean dissipated heat out of ORC condenser for Concept 3 . . . 78

5.35 Temperature of thermal nodes for Concept 4 78
5.36 Thermal mesh rear view at 60 minutes after model initialisation for Concept 4 79
5.37 Thermal mesh front view at 60 minutes after model initialisation for Concept 4 79
5.38 Thrust and power generation for Concept 4 79
5.39 Specific impulse for Concept 4 79
5.40 System efficiency and effective exhaust velocity for Concept 4 80
5.41 Mean dissipated heat out of ORC condenser for Concept 4 80
5.42 Temperature of thermal nodes for Concept 5 81
5.43 Thermal mesh rear view at 60 minutes after model initialisation for Concept 5 81
5.44 Thermal mesh front view at 60 minutes after model initialisation for Concept 5 81
5.45 Thrust and power generation for Concept 5 82
5.46 Specific impulse for Concept 5 82
5.47 System efficiency for Concept 5 82
5.48 Mean dissipated heat out of ORC condenser for Concept 5 83
5.49 Temperature of thermal nodes for Concept 6 83
5.50 Thermal mesh rear view at 60 minutes after model initialisation for Concept 6 84
5.51 Thermal mesh front view at 60 minutes after model initialisation for Concept 6 84
5.52 Thrust and power generation for Concept 6 84
5.53 Specific impulse for Concept 6 84
5.54 System efficiency for Concept 6 85
5.55 Mean dissipated heat out of ORC condenser for Concept 6 85
5.56 Illustration of the system's footprint 86
5.57 Propellant tank temperature for Concept 2 98
5.58 Propellant tank temperature with passive radiator cooling 98

6.1 System architecture and design options 102
6.2 Hatley-Pirbhai diagram for propulsion subsystem 103
6.3 Propulsion subsystem physical architecture 103
6.4 Temperature profile for Concept 3 with 15 thermal straps attached to the secondary concentrator lens 105
6.5 Schematic for secondary concentrator assembly 106
6.6 Schematic for pre-cavity chamber assembly 107
6.7 Schematic for PODS (Plachta et al. 2006) 108
6.8 Cross-sectional schematic for RAC assembly 109
6.9 Rear-view schematic for RAC assembly 109
6.10 Temperature profile for Concept 3 with PODS 110
6.11 Temperature profile for Concept 3 with Al 6061-rods between mounting frame and RAC 111
6.12 Temperature profile for Concept 3 with 10-cm thick MLI around RAC . . 112

6.13 Nozzle length-exhaust diameter ratio versus thrust 115
6.14 Schematic for propellant tubing from propellant tank to RAC 116
6.15 Schematic for propellant tubing fasteners 119
6.16 Schematic for radiator-propellant tank interface 124
6.17 System architecture of the propellant feed system 128
6.18 Hatley-Pirbhai diagram for power subsystem 129
6.19 Propulsion subsystem physical architecture 129
6.20 Schematic for heat exchange options between RAC and heating gas channel 131
6.21 Temperature profile for detailed design 137
6.22 Thrust and power for detailed design 138
6.23 Specific impulse for detailed design 138
6.24 System efficiency for detailed design 138

List of Tables

2.1 System requirements . . . 7
2.2 Functional requirements coupled to operational scenarios . . . 8

3.1 Mission input parameters . . . 10
3.2 Model input variables for validation (Leenders & Zandbergen 2008) . . . 36
3.3 Comparison of model and test performance . . . 36
3.4 Comparison of model and test temperatures . . . 38

5.1 Maximum operating temperatures for thermal nodes . . . 54
5.2 Reference mass budgets for small satellites . . . 54
5.3 Performance comparison between a conical and bell-shape nozzle for the same hybrid system . . . 62
5.4 Summary of the conceptual designs . . . 67
5.5 Component thickness . . . 68
5.6 Mass comparison of the concepts . . . 86
5.7 Estimate of the footprint of the concepts . . . 87
5.8 Size comparison of the concepts . . . 88
5.9 Performance comparison of the concepts . . . 88
5.10 System-specific impulse and related variables for the concepts . . . 89
5.11 Scalability results in terms of power . . . 90
5.12 Scalability results in terms of thrust . . . 91
5.13 Maximum thermal stresses for each concept's thermal nodes in GPa . . . 92
5.14 Maximum thermal expansion in axial and radial direction for each concept's thermal nodes in mm . . . 93
5.15 Trade-off criteria comparison matrix . . . 96
5.16 System volume estimate of concepts . . . 97
5.17 Concepts trade-off . . . 99

6.1 Mass budget for RAC system . . . 113
6.2 Final comparison of nozzle shapes . . . 114
6.3 Pressure losses . . . 119
6.4 MLI performance . . . 124
6.5 Comparison of thermal control options . . . 126

6.6 Mass budget for propulsion subsystem 128
6.7 Mass budget for propulsion subsystem 131
6.8 Mass budget for power subsystem 136
6.9 Mass budget for total hybrid system 137
6.10 Hybrid and conventional systems comparison 140

7.1 Flow initialization times for concepts 145

A.1 View factors for detailed design 164

B.1 Design parameters for Concept 1 166
B.2 Design parameters for Concept 2 167
B.3 Design parameters for Concept 3 168
B.4 Design parameters for Concept 4 169
B.5 Design parameters for Concept 5 170
B.6 Design parameters for Concept 6 171

Nomenclature

Latin Symbols

a	Semi-major axis	$[km]$
A	Area	$[m^2]$
B	Gebhart factor	$[-]$
B_x	1st Baker parameter	$[-]$
B_y	2nd Baker parameter	$[-]$
$c_{specific}$	Specific heat	$[JK^{-1}]$
$c_{thrust-loss}$	Thrust loss fraction	$[-]$
C	Thermal conductive coupling	$[WK^{-1}]$
$C_{Sutherland}$	Sutherland constant	$[K]$
d	Maximum thickness of a lens	$[m]$
D	Diameter	$[m]$
$D_{Sun-Earth}$	Earth's instantaneous distance to the Sun	$[km]$
e	Orbit eccentricity	$[-]$
E	Young's modulus	$[Pa]$
f	Focal length of a lens	$[m]$
f_D	Darcy friction factor	$[-]$
f_{safety}	Safety factor	$[-]$
F_{axial}	Axial load	$[N]$
$F_{critical}$	Critical load	$[N]$
F_{ij}	View factor	$[-]$
F_{tank}	View factor from propellant tank to radiator	$[-]$
g_0	Standard gravitational acceleration	$[ms^{-2}]$
G	Thermal conductance	$[WK^{-1}]$
Gr	Grashof number	$[-]$
GM	Standard gravitational parameter	$[km^3s^{-2}]$
h	Enthalpy	$[Jkg^{-1}]$
h_a	Apogee altitude	$[km]$

$h_{aperture}$	Height of the aperture's spherical cap	$[m]$
h_c	Convective heat transfer coefficient	$[Wm^{-2}K^{-1}]$
h_p	Perigee altitude	$[km]$
H_{RAC}	RAC length	$[m]$
i	Inclination	$[deg]$
I_d	Inherent solar cell degradation	$[-]$
I_{sp}	Specific impulse	$[s]$
k	Thermal conductivity	$[Wm^{-1}K^{-1}]$
L_d	Lifetime solar cell degradation	$[-]$
L_i	Conductive path length	$[m]$
L_{tubing}	Total length of tubing	$[m]$
m	Mass flow	$[kgs^{-1}]$
Ma	Mach number	$[-]$
n	Mean motion	$[rads^{-1}]$
n_i	Material refraction index	$[-]$
n_{turns}	Total number of turns in spiral tubing	$[-]$
Nu	Nusselt number	$[-]$
p	Pressure	$[Pa]$
P	Orbit period	$[s]$
P_a	Available power	$[Whrm^{-2}]$
P_e	Eclipse period	$[hr]$
P_{EOL}	End-of-life solar array output power	$[W]$
P_{net}	Net generated power	$[W]$
$P_{required}$	Required solar array output power	$[W]$
P_{sun}	Solar power output	$[W]$
P_{tubing}	Spiral tubing pitch	$[m]$
Pr	Prandtl number	$[-]$
Q	Heat	$[W]$
q_{latent}	Latent heat	$[Jkg^{-1}]$
R	Radius	$[m]$
R_1	Curvature radius of convex part of a thin lens	$[m]$
R_2	Curvature radius of concave part of a thin lens	$[m]$
R_{gas}	Specific gas constant	$[Jkg^{-1}K^{-1}]$
R_{ij}	Radiative thermal coupling	$[m^2]$
Ra	Rayleigh number	$[-]$
Re	Reynolds number	$[-]$
S	Solar flux	$[Wm^{-2}]$
S_{Earth}	Earth albedo flux	$[Wm^{-2}]$

$S_{Earth_{IR}}$	Earth IR flux	$[Wm^{-2}]$
t	Wall thickness	$[m]$
t_{thrust}	Thrust time	$[s]$
T	Temperature	$[K]$
T_f	Propellant film temperature	$[K]$
$T_{loss_{bl}}$	Thrust loss due to nozzle flow boundary layer	$[N]$
T_{thrust}	Thrust	$[N]$
U	Velocity	$[ms^{-1}]$
W_p	ORC pump power	$[W]$
W_t	ORC turbine power	$[W]$

Greek Symbols

α	Solar absorptance	$[-]$
$\alpha_{aperture}$	Angular diameter of the RAC aperture	$[rad]$
α_{te}	Thermal expansion coefficient	$[m/mK]$
β_s	Angle of the Sun above the orbital plane	$[deg]$
γ_{prop}	Specific heats ratio of the propellant	$[-]$
δ	Sun's declination angle wrt Earth's equator	$[deg]$
δ_{bend}	Tubing bend angle	$[deg]$
δ_{cone}	Cone half angle	$[rad]$
δp	Pressure loss	$[Pa]$
ΔL	Thermal expansion	$[m]$
ΔQ	Net heat flux	$[W]$
Δt	Time step	$[s]$
ϵ	IR emissivity	$[-]$
ϵ^*	Effective emissivity	$[-]$
η	Efficiency	$[-]$
θ	True anomaly of Earth	$[deg]$
θ_1	Angular curvature of the lens	$[rad]$
$\theta_{convergence}$	Nozzle convergence half angle	$[-]$
$\theta_{divergence}$	Nozzle divergence half angle	$[rad]$
$\theta_{exhaust}$	Nozzle exhaust divergence half angle	$[rad]$
θ_{local}	Local true anomaly of the spiral tubing arc	$[rad]$
$\theta_{momentum}$	Momentum loss thickness	$[-]$
κ	Thermal conductivity	$[Wm^{-1}K^{-1}]$
λ	Pressure loss scaling factor	$[-]$
μ	Viscosity	$[Pas]$

μ_{prop_0}	Propellant viscosity at 273.15 K	$[Pas]$
ν	Poisson's ratio	$[-]$
ξ	Pressure loss coefficient	$[-]$
ρ	Density	$[kgm^{-3}]$
ρ_{Earth}	Angular radius of the visible Earth disk	$[deg]$
σ	Stefan-Boltzmann constant	$[Js^{-1}m^{-2}K^{-4}]$
σ_l	Liquid propellant flow surface tension	$[-]$
σ_{normal}	Normal stress	$[Pa]$
σ_{yield}	Yield strength	$[Pa]$
ϕ	Unit pressure loss	$[-]$
Φ	Vandenkerckhove function	$[-]$
Φ_{orbit}	Orbit rotation angle in eclipse	$[deg]$
ψ	Reflectivity factor	$[-]$
Ω	right ascension of the ascending node (RAAN)	$[deg]$
$\dot{\Omega}$	RAAN rate of change	$[deg/min]$

Subscripts

$bend$	Propellant tubing bend
$cell$	Solar cell
$chamber$	Thruster chamber
$cond$	Conductive
$condenser$	Condenser
$conductor$	Conductor
$conv$	Convective
$critical$	Critical conditions
cs	Cross-section
$curved$	Curved convergent section of nozzle
d	Dry system
$daylight$	Solar array in daylight
$diss$	Heat dissipation channel
$Earth$	Earth
$eclipse$	Solar array in eclipse
env	Local environment
eq	Equivalent exhaust
$exhaust$	Nozzle exhaust
ext	External
$final$	Final

$free-stream$	Free-stream conditions
$friction$	Frictional
i	Thermal node
in	Inlet
$initial$	Initial
$inner-tubing$	Inner tubing
ins	MLI
int	Interior
j	Facing thermal node
k	Surrounding thermal node in enclosure
l	Liquid
m	Mean
max	Maximum
new	New
$nominal$	Nominal
ORC	ORC
out	Outlet
$path$	Spiral propellant tubing path
$PODS$	PODS
$prim$	Primary concentrator
$prop$	Propellant
RAC	RAC
rad	Radiative
$radiator$	Radiator
sec	Secondary concentrator
$single-phase$	Single-phase propellant
$solar-array$	Solar array
$system$	Hybrid system
$tank$	Propellant tank
$throat$	Nozzle throat
$total$	Total
$tubing$	Propellant tubing
$turbine$	Turbine
$two-phase$	Two-phase propellant
v	Vapor
$wall$	Wall conditions
wet	Wet propulsion subsystem
wf	Working fluid

Glossary

ADCS attitude determination and control system

AHP Analytical Hierarchy Process

ASME American Society of Mechanical Engineers

DAO Design, Analysis and Optimization

DUT Delft University of Technology

EPS electric power system

ESA European Space Agency

IR infrared

KPP Key Performance Parameter

LEO low earth orbit

MEMS micro-electro-mechanical systems

MLI multi-layer insulation

NASA National Aeronautics and Space Administration

OBC on-board computer

ORC Organic Rankine Cycle

OSR optical solar reflector

PODS passive orbit disconnect struts

RAAN right ascension of the ascending node

RAC receiver/absorber cavity

RCI random consistency index

STP solar thermal propulsion

TRL technological readiness level

Chapter 1

Introduction

Besides chemical, cold gas and electric propulsion, solar thermal propulsion (STP) provides an alternative approach to spacecraft propulsion. It uses thermal energy generated by absorbing solar radiation to heat propellant which expands and provides thrust.
Over the past two decades there has been intermittent research into this technique. It offers superior specific impulse over conventional propulsion systems at a lower system mass and volume. Furthermore it can be relatively easily scaled to produce more thrust if a larger spacecraft is adopted. Also, this propulsion system can be adapted to provide power to the spacecraft by converting a part of the totally available thermal energy into electrical energy. This last hybrid capability will be researched in this thesis, thereby developing a solar thermal power-propulsion hybrid system.

A solar thermal power-propulsion hybrid system consists of both a propulsion and power subsystem which are connected and share the same energy source.
First, the propulsion subsystem concerns a solar concentrator, an absorber, a heat exchange mechanism between absorber and propellant, a propellant storage and feed system, a thruster chamber and a thruster nozzle (Calabro 2003).
Second, the power subsystem makes use of an Organic Rankine Cycle (ORC). This cycle uses an organic working fluid which is heated, evaporated and is thereafter expanded through a turbine which provides work. The evaporated fluid is finally condensed and fed back into the heat exchanger, beginning the cycle once more.
The power subsystem consists of a power converter, such as a turbine, a heat exchanger (otherwise known as evaporator), a heat dissipater (or condenser) and an interface between the absorber and the heat exchanger.
The absorber will absorb incident solar radiation thereby increasing its temperature. It will thereafter first transfer the thermal energy to the power subsystem.
Afterwards, the residual heat is transferred to the propellant in the propulsion subsystem.

The STP subsystem under consideration uses an inflatable solar concentrator which concentrates the incident solar radiation onto a focal area. The concentrator would be inflated after orbit insertion and rigidized. The absorber is also known as the receiver/absorber cavity (RAC). It receives the solar radiation from the concentrator and heats up subsequently. The heat from the RAC is transferred via conduction and/or radiation to the wall of the propellant vessel and to the evaporator. Convection processes transfer the heat from the propellant vessel inner wall to the propellant which expands and provides thrust.

All of the critical STP subsystems have reached a technological readiness level (TRL) of 5 to 6. Actual in-orbit testing of a full STP system has yet to occur. In 1996 an inflatable antenna concentrator was partly successfully deployed in low earth orbit (LEO) however (Freeland et al. 1996).

Possible cryogenic propellants for this system are for example liquid ammonia and liquid hydrogen (Stewart & Martin 1995). Respectively they have a boiling temperature of $-33.3°$ Celsius and $-252.8°$ Celsius (Çengel & Boles 2011). Therefore, they will have to be cryogenically stored to prevent boil-off and also to limit the propellant tank volume. Non-cryogenic propellants such as water and nitrogen can also be used, but may suffer from worse performance and a larger required storage volume.

At this point especially further development of the RAC, thruster and interface with the power subsystem and propellant is needed to see whether solar thermal power-propulsion hybrid systems are feasible. This should eventually culminate in the design and building of an integrated solar thermal power-propulsion system which can be deployed on board a small satellite.
These satellites have been selected as they are the most likely candidates for in-orbit demonstration missions and offer the minimum space to integrate such a system. Furthermore, Delft University of Technology (DUT) is focused on the development of small space (sub-)systems.
During the thesis the propulsion part of the system will be analyzed extensively, whereas the analysis of the power part will borrow from previous work concerning thermal power generation. The work in question concerns heat cycle modelling. The analysis tool is verified and quantitatively validated.
As recommended in last paragraph, the thesis work will draw-up a design of the propulsion and power subsystems. For completeness, the propellant storage system will also be designed. The concentrator is not analyzed but a certain concentrator design is assumed for designing and modelling the RAC.
The main goal is to produce substantiated estimates about the performance of the hybrid system in a small satellite context and confirm feasibility of the system. It is therefore principally an academic exercise, but has relevance for future follow-up research into this topic.

This thesis study is laid out as follows. First, in Chapter 2 the research framework of the thesis is laid out. Afterwards, in Chapter 3 the Design, Analysis and Optimization (DAO) tool is discussed. The thesis continues in Chapter 4 where the applicable theory concerning ORCs is summarized. Chapter 5 discusses the requirements and assumptions associated with the conceptual design phase. Afterwards the conceptual designs themselves are introduced and compared with each other. Furthermore, a trade-off is performed to select one concept for the detailed design. Chapter 6 elaborates on this detailed system design. Chapter 7 answers the research questions posed in Chapter 2. The study is concluded in Chapter 8.

Chapter 2

Research framework

This chapter details the research framework behind the thesis and makes an inventory of the research questions, thesis objectives and system requirements.
The research questions will be answered in Chapter 7.

2.1 Research questions

The main research question of this thesis research deals with the feasibility of solar thermal power-propulsion hybrid systems in small satellites. The specific question is as follows: *"Can solar thermal power-propulsion hybrid systems be miniaturized to fit and function in a 1m x 1m x 1m small satellite while delivering at least 100 W in power, at least 100 s in specific impulse and at least 1 N in thrust?"*

Sub-questions are defined within the main question. The sub-questions are given below:

1. What is the difference in performance when liquid ammonia, liquid hydrogen or gaseous nitrogen are used as propellant?
   (a) What is the difference in thrust and specific impulse when the propellant is changed?
   (b) What is the difference in system mass and system volume when the propellant is changed?
   (c) How representative is the performance of an STP thruster with gaseous nitrogen with respect to a thruster which uses a liquid propellant?
2. Which system designs have the best performance in terms of power, delivered thrust and delivered specific impulse given their size envelope and mass?
   (a) Which design keeps the primary concentrator size to a minimum?
   (b) Which combined propellant tubing and RAC configuration provides the fastest and largest heat exchange between the RAC and the propellant?
   (c) Which interface design with the power subsystem offers the required heat transfer whilst keeping its size and volume limited?
   (d) What is the degree of scalability of each system design?

3. How can one define the efficiency of the total hybrid system?

Sub-question 1.c addresses the fact that resources do not allow validation testing with liquid propellants due to the lack of cryogenic storage equipment. Luckily, DUT has access to gaseous nitrogen which can be stored at room temperature and is relatively cheap. Before one however can use gaseous nitrogen, one has to find out how representative the measured performance with nitrogen is with respect to the real-life case where liquid propellants would be used.
Sub-question 2 discusses the main purpose of this study; namely to evaluate the performance of a feasible hybrid system design.
The third sub-question concerns the definition of efficiency for the hybrid system as the system generates both thrust and power. Therefore a combined efficiency value needs to be calculated to compare designs.

2.2 Objectives

The research questions can be answered by satisfying the research's main objective which is the following:
Design and characterize a solar thermal power-propulsion hybrid system, assuming a certain primary solar concentrator configuration.

The main objective can be compartmentalized into several sub-objectives:

1. Developing a Design, Analysis and Optimization (DAO) tool
   (a) Modelling radiative heat exchange processes
   (b) Modelling conductive heat exchange processes
   (c) Modelling convective heat exchange processes
   (d) Modelling thermodynamic processes in the thruster
   (e) Integrating the existing power subsystem model
   (f) Estimating the size and mass of the total hybrid system
2. Verifying the tool by testing it with unit-inputs and validating the tool with respect to previous STP data sets
3. Executing the conceptual design process by setting up a number of conceptual designs, based on previous concepts.
4. Trading-off the conceptual designs and selecting one for further design and analysis.
5. Executing a more detailed design of the RAC, the propellant tubing and their shared interface area for the selected conceptual design.
6. Executing a more detailed design of the evaporator and the interface with the RAC for the selected conceptual design.
7. Analyzing the detailed design and provide thrust, power, size and mass budgets.

2.3 Operational scenarios

A one-year reference technology-demonstration mission has been selected of which the orbit characteristics can be seen in Table 3.1. Due to the high-drag environment and the large eclipse time associated with LEO, a number of operational scenarios can be synthesized. Only the scenarios which impact the power and propulsion subsystems have been included:

1. Orbit insertion *Spacecraft calibration and initial power generation*
2. Daylight operations *Generating and storing power*
3. Eclipse operations *Storing power and diverting power to subsystems*
4. Station-keeping *Providing small amounts of thrust to keep the spacecraft in the initial orbit*
5. Observations and in-flight technology validation *Using instrumentation and sending down telemetry which requires certain pointing of the spacecraft*

In Figure 2.1 and Figure 2.2 two sequences of events are shown which are representative for the functioning of the power and propulsion subsystems for all the scenarios. The three actors are the propulsion subsystem, the power subsystem and the on-board computer (OBC) which controls the spacecraft.

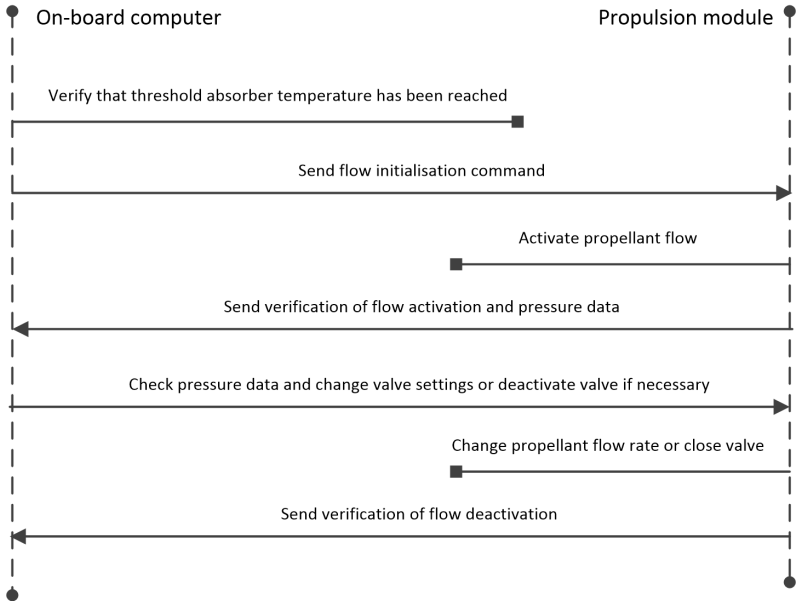

Figure 2.1: Representative sequence diagram for propulsion subsystem

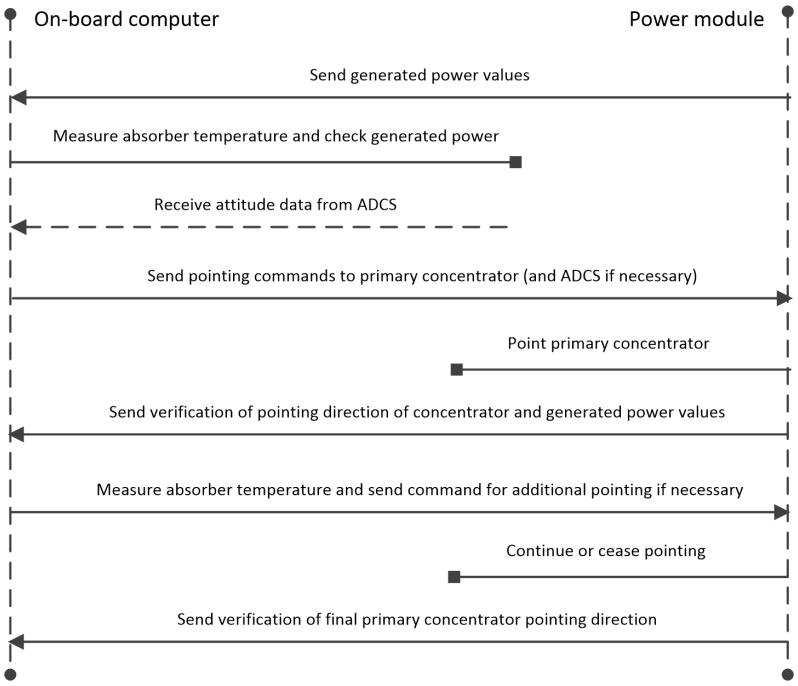

Figure 2.2: Representative sequence diagram for power subsystem

2.4 System requirements

To check for compliance at the end of the thesis study, system requirements must be stated for the system based on the research questions and operational scenarios for the reference mission.
Each requirement has an acceptance criterion as well as a rationale as given in Table 2.1. Requirements can be put in the functional or non-functional category.

Table 2.1: System requirements

	Requirement	Acceptance Criterion	Rationale
	Non-Functional		
1	Volume	The entire system shall fit in a 1x1x1 m spacecraft bus	This bus size is representative of small satellites
2	Wet system mass	The wet system mass shall take up a maximum of 65% of the total spacecraft mass budget	Literature and a number of assumptions dictate this threshold[†]
	Functional		
3	Thrust	The system shall produce at least 1 N in thrust when thrust is required	This is representative for small satellites and in the range of small thrusters
4	Specific impulse	The system shall produce at least 100 s in specific impulse when thrust is required	Limited specific impulse is required for station-keeping as the thruster will be fired only for short pulses
5	Power	The system shall generate at least 100 W in power during the entire orbit	This is representative of the power needs for small satellites and takes into account power needs in daylight and eclipse
6	ΔV	The system shall generate a total ΔV budget of 210 m/s	One assumes 175 m/s in maximum required ΔV per year for station-keeping at the 600 km altitude orbit (Larson & Wertz 2005, p 177). A 20% margin is added which results in a total ΔV budget of 210 m/s
7	Propellant flow control	The system must be capable of storing all the required propellant within the spacecraft and activate propellant flow when necessary	Without proper propellant control the propulsion subsystem cannot perform reliably (see Figure 2.1)
8	Pointing	The system must be able to point the primary concentrator such that constant power and thrust generation is guaranteed	Depending on the temperature of the absorber the primary concentrator must be pointed differently to minimize or maximize the amount of received sunlight (see Figure 2.2)

[†] Looking at Ekpo & George (2013), which details the design of small satellites, the spacecraft's subsystems, excluding power and propulsion, can amount to 40% of the dry mass with current technologies. Assuming 25% of the total spacecraft mass is propellant in the worst-case scenario, this remaining subsystem mass budget is 30% of the total mass. Since one is dealing with a demonstration mission, a 5% payload budget at the minimum should be sufficient. This yields the requirement that a maximum of 65% of the total mass budget should be used for the wet system

The first six requirements can be considered the Key Performance Parameters (KPPs) of the system as these define whether the hybrid system is feasible or not. The last two requirements merely deal with the operations of the system.
The functional requirements can be attached to the operational scenarios in the previous section (Table 2.2).

Table 2.2: Functional requirements coupled to operational scenarios

Operational scenario	**Functional requirements**
1	5,8
2	5,8
3	5,8
4	3,4,5,6,7,8
5	5,8

One notes that all operational scenarios involve Requirement 5 and 8 as without power the spacecraft cannot function. In the final scenario Requirement 8 is the driving requirement as the pointing of instruments and antennae may inhibit the optimal pointing of the primary concentrator and therefore limit power generation. The exact operations of the primary concentrator are beyond the scope of this thesis, but recommendations will be made on this topic in Chapter 8.

In terms of the spacecraft mass, a dry-mass of 200 kg is assumed. This value is taken to ensure that the system mass fraction will not become too high as candidate materials molybdenum and tungsten have a high density. This also means that this system is not feasible for micro-satellites. Furthermore, choosing this value puts the reference spacecraft in the middle of the small satellite category, allowing some scalability of the system if required.
Depending on the final design the feasibility question will be answered in the affirmative or not. In case of uncertainties and/or unknowns further recommendations will be made for future studies into this hybrid technology.

Chapter 3

Design, Analysis and Optimization Tool

The Design, Analysis and Optimization (DAO) tool is a collection of numerical models which approximate the performance of a solar thermal hybrid system given a number of assumptions. This chapter will detail these assumptions and the underlying theory behind the models as well as some intermediate results.
MATLAB has been used for creating and running the models.

In Figure 3.1 the process for the DAO tool has been detailed. One can see that the main iteration in the tool consists of the computation of the propellant flow rate and flow temperature. The flow rate is derived from among others the chamber temperature which in turn is derived from the mean propellant temperature. The flow rate is calculated in the thruster model whereas the mean flow temperature is calculated in the thermal model. The final propellant temperature is used for determining the thruster performance.

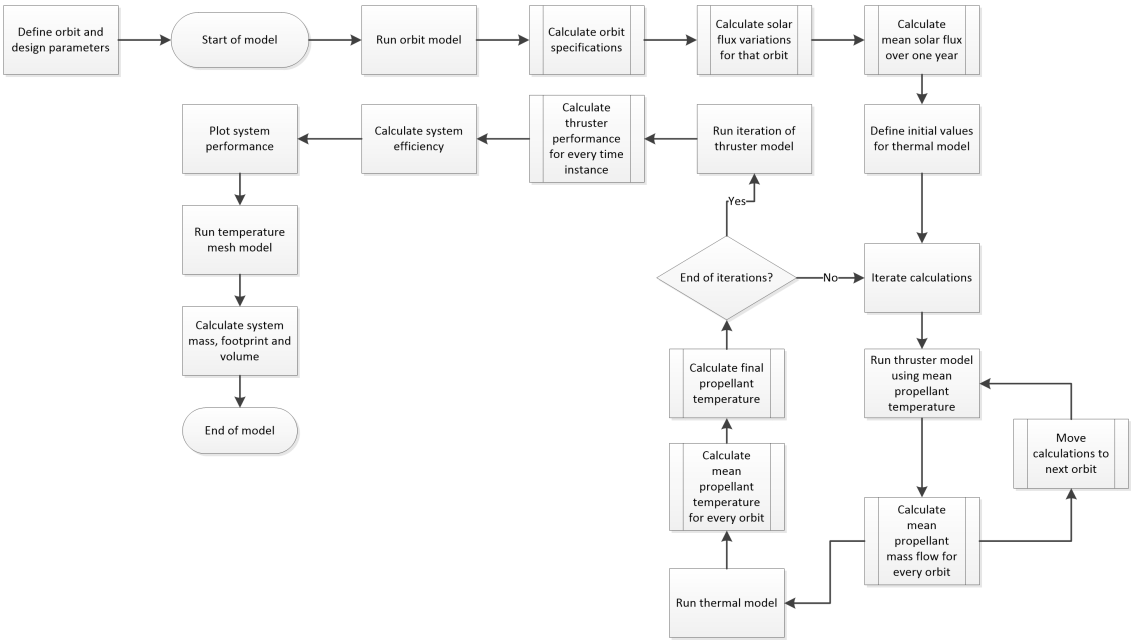

Figure 3.1: Process diagram for DAO tool

The DAO tool consists of:

- an orbit and solar flux model;
- a thermal model;
- and a thruster model

The individual models will also be detailed with a process diagram in subsequent sections. In Table 3.1 the mission input parameters are given.

Table 3.1: Mission input parameters

Mission parameter	Value
Perigee altitude	600 [km]
Orbital eccentricity	0 [-]
Orbital inclination	80 [deg]
Initial right ascension of the ascending node (RAAN)	50 [deg]
Thermal model time step	0.1 [s]

3.1 Orbit and solar flux model

This model will detail the orbit of the reference mission and provide an estimate of the expected solar flux. Finally, it will yield the power in Watts available to the spacecraft. The first section details the computation of orbit parameters. The second features some calculations concerning the received solar radiation.

3.1.1 Orbit model

First, the shape of the orbit needs to be determined by setting a value for the perigee and apogee altitude. The semi major axis a is calculated with Equation 3.1. The equations are derived from (Larson & Wertz 2005, p. 137 and 143).

$$a = \frac{h_p + h_a}{2} \tag{3.1}$$

Here, h_p is the perigee altitude and h_a is the apogee altitude.

The orbit's eccentricity e, orbital period P and mean motion n are calculated with respectively Equation 3.2, Equation 3.3 and Equation 3.4.

$$e = 1 - \frac{h_p}{a} \tag{3.2}$$

$$P = 2\pi\sqrt{\frac{a^3}{GM}} \tag{3.3}$$

$$n = \sqrt{\frac{\mu}{a^3}} \tag{3.4}$$

Here, GM is the standard gravitational parameter of the parent body around which a satellite orbits. For Earth it is 398600.4418 $\mathrm{km^3 s^{-2}}$, for the Sun it is $132712.44 \cdot 10^6$ $\mathrm{km^3 s^{-2}}$.

Besides perigee, apogee and eccentricity, an orbit is also defined by the RAAN Ω and the inclination i. Due to the oblate shape of the Earth the gravitational attraction of the Earth is not homogeneous which causes a number of perturbations which in turn cause the precession of the RAAN. In Equation 3.5 this precession is calculated; the largest term in the total perturbation is the J2-term and the computation therefore takes solely its effect into account.

$$\dot{\Omega} = -1.5 \cdot n \cdot J2 \cdot (R_{Earth}/a)^2 \cdot \cos(i) \cdot (1 - e^2)^{-2} \tag{3.5}$$

Here, R_{Earth} is the radius of the Earth. The rate of change in RAAN $\dot{\Omega}$ can be multiplied with the time step and added to the initial RAAN angle to calculate the instantaneous RAAN during the mission.

A number of angles are required to compute the eclipse time. The applicable equations have been taken from (Larson & Wertz 2005, p. 107). These include:

- δ, the sun's declination angle with respect to Earth's equator;
- β_s, the angle of the Sun above the orbital plane;
- and Φ_{orbit}, the orbit's rotation angle when the spacecraft is in eclipse.

The last two angles can be seen in Figure 3.2.

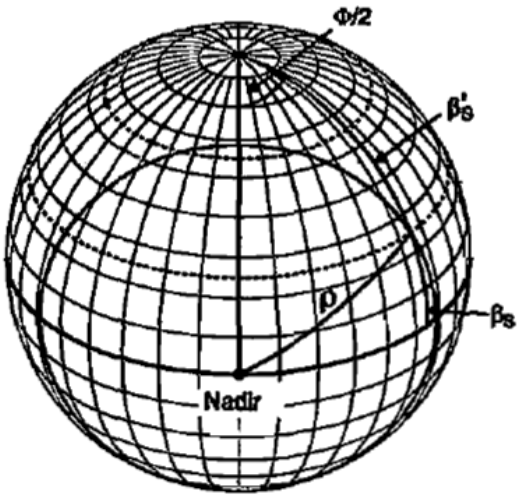

Figure 3.2: Orbit angles to determine solar flux Larson & Wertz (2005)

First, the δ-angle is computed with Equation 3.6. The d term in the equation indicates the number of days which have passed since the first of January in a particular day. The subtraction by 81 is to take into account the equinoxes when the declination angle is 0°.

$$\delta = \arcsin\left((\sin(23.45)\sin((360/365)(d-81))\right) \tag{3.6}$$

Second, the β_s-angle is calculated with Equation 3.7. Note that Ω does not have to be subtracted with the Sun's RAAN angle as both are determined based on the direction of the vernal equinox.

$$\beta_s = \arcsin(\cos(\delta)\sin(i)\sin(\Omega) + \sin(\delta)\cos(i)) \tag{3.7}$$

Third, Φ_{orbit} is calculated in Equation 3.8.

$$\Phi_{orbit} = 2\arccos\left(\frac{\cos(\rho_{Earth})}{\cos(\beta_s)}\right) \tag{3.8}$$

Here ρ_{Earth} is the angular radius of the visible Earth disk as seen by the spacecraft. Equation 3.9 gives values for this variable.

$$\rho_{Earth} = \arcsin(R_e/h_p) \tag{3.9}$$

Finally, the eclipse time P_e is calculated in Equation 3.10.

$$P_e = P \cdot \left(\frac{\Phi_{orbit}}{360}\right) \tag{3.10}$$

3.1.2 Solar flux model

With the orbit model concluded, the solar flux is modelled in a simplified way. The true anomaly θ indicates the angular position of Earth in its orbit with respect to the perihelion point on the 3rd of January. It is used to calculate an accurate estimate of Earth's instantaneous distance $D_{Sun-Earth}$ to the Sun (Equation 3.11).

$$D_{Sun-Earth} = \frac{a_{Earth}(1-e_{Earth}^2)}{(1+e_{Earth}\theta)} \tag{3.11}$$

Here, a_{Earth} and e_{Earth} are respectively the semi-major axis and eccentricity of Earth's orbit. The solar flux in W/m^2 is calculated with the equation below whilst using the inverse square law. P_{sun} is the solar power output which is nearly constant at $3.856{\cdot}10^{26}$ W.

$$S = \frac{P_{sun}}{4\pi(D_{Sun-Earth}\cdot 1000)^2} \tag{3.12}$$

The available power per hour P_a is calculated with Equation 3.13 where the orbital period P is in seconds and the eclipse time P_e is in hours.

$$P_a = S \cdot (P/3600 - P_e) \tag{3.13}$$

Looking at Figure 3.3 the available power indeed fluctuates slightly throughout the year. It indicates the radiation exposure over one year for a circular LEO orbit with an altitude of 600 km, an inclination of 80° and a RAAN of 50°. The power fluctuates over the year from 1325 Whr/m^2 to 1417 Whr/m^2 with a mean at 1371 Whr/m^2. In literature the mean solar flux or solar constant is indeed around 1371 Whr/m^2 for LEO (Larson & Wertz 2005).

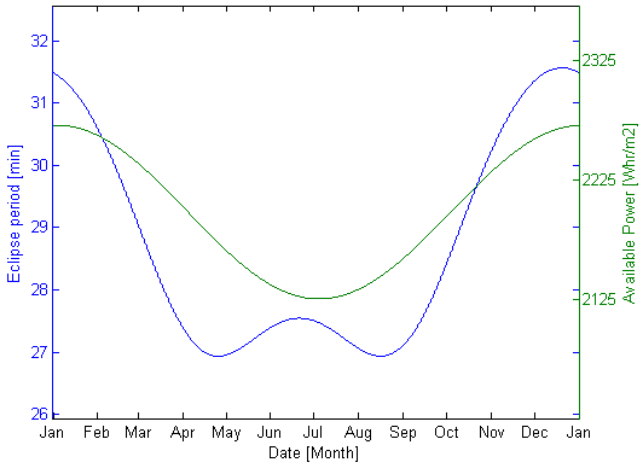

Figure 3.3: Plot for the available power and the eclipse time over one year for the reference mission

It is difficult to establish the fraction of incoming solar radiation or incoming solar power which is reflected by the concentrator to the RAC. Ideally a prototype testing campaign would be initiated and an average concentrator efficiency would be established. If one wants to determine an efficiency without tests, an average value has to be derived from literature. In Nakamura et al. (2004) a concentrator efficiency of 70% to 90% was established. Therefore a concentrator efficiency of 80% is assumed for the thermal model.

3.2 Thermal model

3.2.1 Introduction

The thermal model calculates the heat flow from the primary concentrator to the propellant and the power subsystem's evaporator. In the introduction this heat transfer process was already shortly explained. To reiterate the following happens:

1. The primary concentrator radiates thermal energy to space and to the secondary concentrator; furthermore, it focuses solar radiation into the secondary concentrator.

2. The secondary concentrator radiates energy to space and to the cavity behind it; it also further focuses the solar radiation and conducts thermal energy to its casing.

3. The RAC absorbs most of the incoming solar radiation and conducts and/or radiates heat away to the adjacent propellant tubing and a heat conducting channel, depending on the design. It furthermore conducts heat towards the surrounding insulation layers.
4. The propellant tubing absorbs the thermal energy which increases its wall temperature; thermal equilibrium is obtained by conducting heat away to its surroundings and by convection to the propellant.
5. The propellant moves inside the tubing and thereby transports the energy to the thruster where it exits the nozzle under increased temperature and pressure.
6. The heat conducting channel transfers RAC thermal energy to the evaporator heating fluid/gas channel.
7. The evaporator heating fluid/gas channel, as part of the evaporator, uses convection through a fluid or gas to transport energy to the working fluid of the ORC.

The following nodes apply for the transient model. In the parentheses one finds into how many sub-nodes each node has been compartmentalized.

1. On-axis primary concentrator (1)
2. Secondary concentrator (1)
3. Secondary concentrator casing (2)
4. Pre-cavity chamber (3)
5. RAC lid with aperture (2)
6. RAC (3)
7. Propellant tubing (3)
8. Heat conducting channel (1)
9. ORC evaporator heating fluid/gas channel (1)
10. ORC condenser channel (1)
11. ORC condenser heat conducting channel (1)
12. ORC condenser radiator (1)

It is assumed that the system is insulated from the rest of the spacecraft and its components. Therefore there is no heat dissipation or heat transfer to the external environment. Exceptions however are the heat dissipation to space for Node 1 up to Node 3 and the heat dissipation from the RAC through the surrounding multi-layer insulation (MLI) insulation to the interior of the spacecraft. Respectively these heat sinks are kept at 3 K and 293.15 K.

The last three nodes are only used to calculate the architecture needed to replace the power subsystem model's active fluid-cooled condenser with a condenser with a passive interface with deep space (see Section 6.3.4).
For Nodes 1 to 9 the thermal network is schematically depicted in Figure 3.4. The *Rad*, *Cond* and *Conv* depict respectively radiative, conductive and convective heat fluxes. Between Node 8 and Node 9 either a conductive or radiative interface can be realized. Both options are compared in terms of mass and size in Section 6.3.2.3.

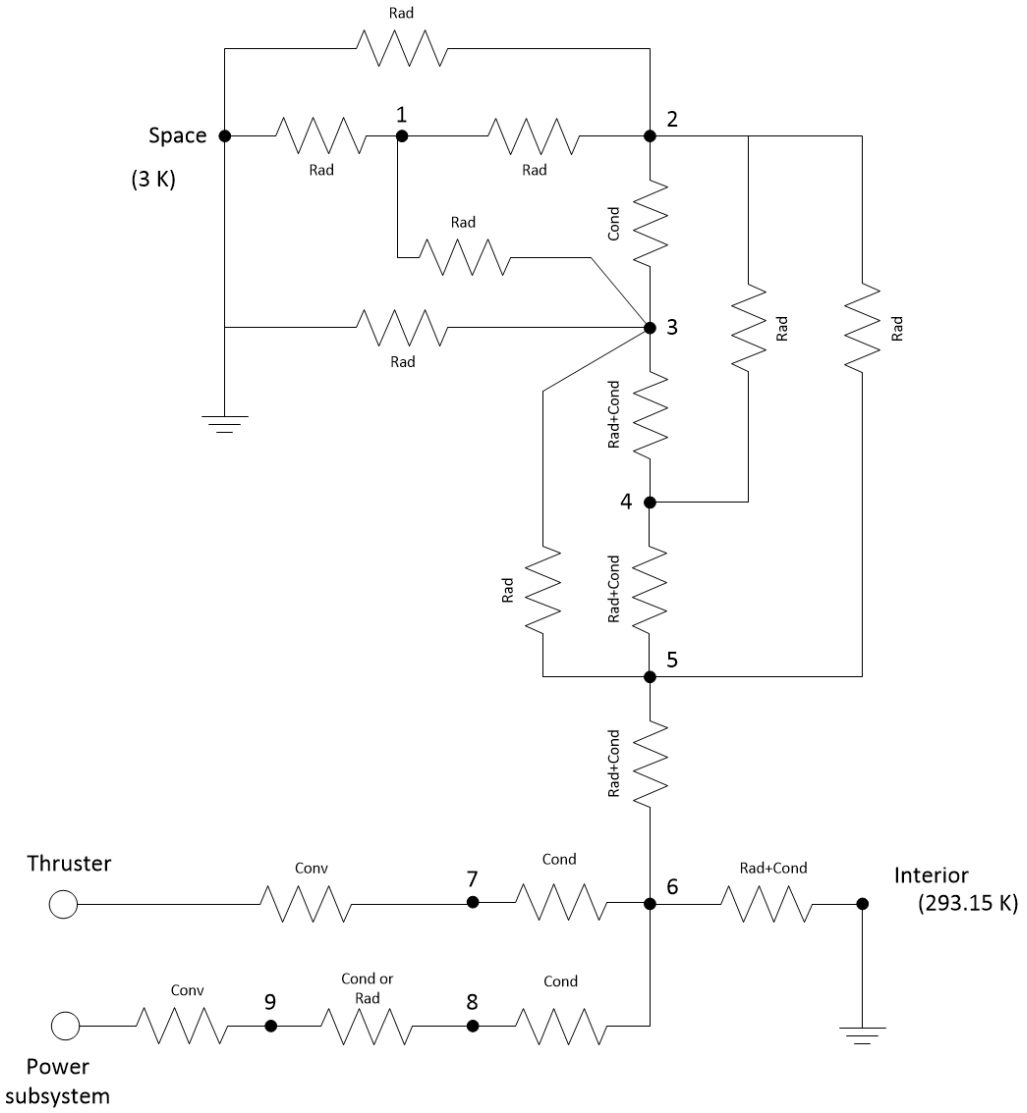

Figure 3.4: Schematic of the thermal model node network

3.2.2 Geometries and properties of nodes

After the nodes have been established, the necessary geometries and properties have to be determined.

3.2.2.1 Primary concentrator geometry and properties

First, the inflatable lens geometry for the primary concentrator is detailed. It consists of two polyimide-film membranes which form a lens and between which a pressure is applied to inflate them. To form an inflatable lens, both a convex and a concave membrane have to be fitted together. By assuming a value for the radius of curvature of the convex membrane and the lens' required focal length, the lens geometry can be calculated.
First, in Equation 3.14 the relation between the curvature of both membranes is given. This equation is also known as the lensmaker's equation Jenkins & White (1957).

$$f \cdot n_i = R_1 - R_2 + \frac{n_i \cdot R_1 \cdot R_2}{(n_i - 1) \cdot d} \tag{3.14}$$

Here f is the focal length, n_i is the refraction index of the polyimide film, R_1 is the radius of the convex membrane and R_2 is the radius of the concave membrane. Last, d is the maximum thickness of the lens.

The cross-sectional radius of the lens is also given. With the two radii of curvature and the lens height, the back and frontal areas of the lens are calculated as both sides of the lens are treated as spherical caps. See Equation 3.15, 3.16 and 3.17 for more details. This equation also holds for the concave membrane.

$$\theta_1 = \sin(R_{cs}/R_1) \tag{3.15}$$
$$h_1 = R_1(1 - \cos(\theta_1)) \tag{3.16}$$
$$A_1 = 2\pi R_1 h_1 \tag{3.17}$$

Figure 3.5 shows a graphical representation of the lens variables. Note that the lens area is

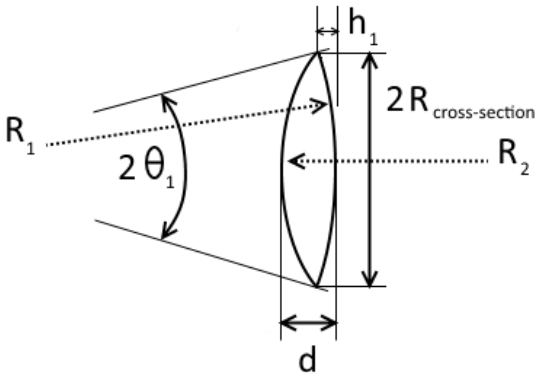

Figure 3.5: Representation of the concentrator lens variables

only important for calculating the radiating area to space. For receiving the solar energy only the area perpendicular to the solar vector is used. This is simply a circular area with a radius equal to the primary concentrator cross-sectional radius.

The refraction index of Kapton polyimide is 1.70 and its thermal conductivity is 0.12 W/mK (DuPont 2014). Its coating is a white paint with an emissivity of 0.9 and a solar

absorptance of 0.17 (AZ Technology 2008). Recall that in Section 3.1 a solar radiation throughput efficiency of 80% was determined for the concentrator.

The secondary concentrator is modelled as a small parabolic lens in front of the RAC. Since the secondary concentrator lens is a thin lens, its lensmaker's equation gets reduced from Equation 3.14 to Equation 3.18 (Jenkins & White 1957).

$$R_1 = \frac{1}{\frac{1}{R_1} + \frac{1}{f} \cdot (\frac{1}{n-1})} \tag{3.18}$$

3.2.2.2 Secondary concentrator geometry and properties

The refractive secondary concentrator is assumed to be made of a single-crystal sapphire material. For such lenses an efficiency of 87% has been determined in solar vacuum tests (Wong et al. 2000). The emissivity of the single-crystal material is 0.02 and its highest thermal conductivity at 20° Celsius is 42 W/mK (Kyocera 2013).

The secondary concentrator casing is modelled as a thick disk around the secondary concentrator. In addition the thickness of the disk itself is assumed to be as long as the sum of the height of the concave and convex part of the secondary concentrator. The width of the disk is the difference between the radius of the pre-cavity chamber and the cross-sectional radius of the secondary concentrator.
The other cylindrical or spherical components in the solar thermal system assembly have a thickness based on literature and procurement data. Barlow's equation is used to check whether the tubing thicknesses are sufficient for the tubing to cope with internal pressures (Equation 3.19).

$$t_{tubing} = \frac{p_{tubing} D_{outer-tubing}}{2\sigma_{yield}} \tag{3.19}$$

Here, p_{tubing} is the fluid or gas pressure inside the tubing, $D_{outer-tubing}$ is the tubing outer diameter, σ_{yield} is the tubing material's yield strength and t_{tubing} is the tubing wall thickness.

3.2.2.3 RAC geometry and properties

The RAC can have different shapes. Different high conductive materials are available, such as tungsten, molybdenum and copper.
The interior coating selection depends on its optical characteristics and the operating temperature range. It must have a high absorptance so that the RAC absorbs a lot of solar radiation. Gilmore (2002) has been used to select the coating for this part of the system. A carbon black paint coating is selected for the RAC. The coating's absorptance and emissivity are respectively 0.96 and 0.88.
To limit the temperature of the secondary concentrator casing, a barium sulphate white paint coating is applied with an absorptance of 0.06 and an emissivity of 0.88. This allows Node 3 to absorb as little direct sunlight as possible whilst emitting a large infrared (IR)

heat flux, cooling the node.

Three different RAC shapes have been determined in the research plan for this thesis, namely a conical, a cylindrical and a spherical shape. The first two have been found in previous literature on STP technology such as Leenders & Zandbergen (2008) and Shimizu et al. (2001). The spherical shape is included for completeness.

Equation 3.20, Equation 3.21 and Equation 3.22 calculate the total interior area for respectively the conical, cylindrical and spherical RAC. The H and R terms indicate the length and the outer radius of the RACs respectively.
Equation 3.24 gives the spherical cap height of the aperture part of the spherical RAC.
Equation 3.23 gives the angular diameter for the aperture in the cavity. These values are directly put into Equation 3.22.
All these equations have been derived geometrically.

$$A_{RAC_{cs}} = \pi(H_{RAC} - t_{RAC})\sqrt{(H_{RAC} - t_{RAC})^2 + (R_{RAC} - t_{RAC})^2} \tag{3.20}$$

$$A_{RAC_{cs}} = \pi(R_{RAC} - t_{RAC})^2 + 2\pi(R_{RAC} - t_{RAC}) \cdot H_{RAC} \tag{3.21}$$

$$A_{RAC_{cs}} = 4\pi(R_{RAC} - t_{RAC})^2 - 2\pi(R_{RAC} - t_{RAC}) \cdot h_{aperture} \tag{3.22}$$

$$\alpha_{aperture} = 2\sin(R_{aperture}/R_{RAC}) \tag{3.23}$$

$$h_{aperture} = R_{RAC} - R_{RAC}\cos(\alpha_{aperture}/2) \tag{3.24}$$

Figure 3.6 shows the RAC variables used in the equations above. Besides the area the volume of the cavity is also calculated.
Finally, the area of the propellant tubing around the RAC has to be computed as well as the interface area between the two. The RAC shape will naturally influence these two values.

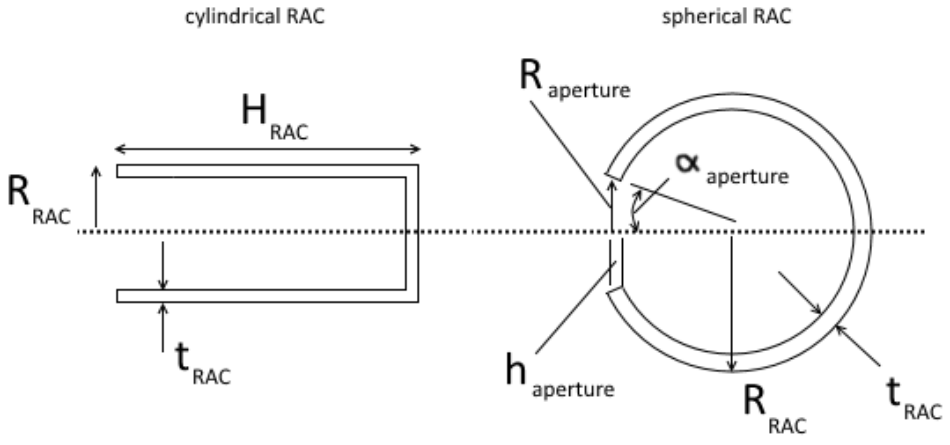

Figure 3.6: Representation of the RAC variables

3.2.3 Tubing configurations

Besides the absorber, the tubing configuration has to be detailed for the conical, cylindrical and spherical cavities respectively. First, the spiral configuration will be examined; afterwards the linear configuration will be discussed.

3.2.3.1 Spiral tubing configuration

The spiral arc length can be detailed with the help of three parametric equations. Per configuration respectively this set of three equations is given in Equation 3.25, Equation 3.26 and Equation 3.27. The parametric equations have been applied of respectively a conical spiral, a helix and a spherical spiral.

$$x = a\cos(\theta_{local}) \tag{3.25a}$$

$$y = a\sin(\theta_{local}) \tag{3.25b}$$

$$z = c \cdot \theta_{local} \tag{3.25c}$$

$$a = \frac{\tan(\delta_{cone}) \cdot P_{tubing}}{(2\pi \cdot \theta_{local})} \tag{3.25d}$$

$$c = \frac{P_{tubing}}{2\pi} \tag{3.25e}$$

$$x = a\cos(\theta_{local}) \tag{3.26a}$$

$$y = a\sin(\theta_{local}) \tag{3.26b}$$

$$z = c \cdot \theta_{local} \tag{3.26c}$$

$$a = R_{path} \tag{3.26d}$$

$$c = \frac{P_{tubing}}{2\pi} \tag{3.26e}$$

$$x = \frac{R_{path}\cos(\theta_{local})}{\left(\sqrt{c^2 \cdot \theta_{local}^2 + 1}\right)} \tag{3.27a}$$

$$y = \frac{R_{path}\sin(\theta_{local})}{\left(\sqrt{c^2 \cdot \theta_{local}^2 + 1}\right)} \tag{3.27b}$$

$$z = \frac{-c \cdot R_{path}\theta_{local}}{\left(\sqrt{c^2 \cdot \theta_{local}^2 + 1}\right)} \tag{3.27c}$$

$$c = \frac{P_{tubing}}{2\pi} \tag{3.27d}$$

In the equations above, R_{path} is the maximum radius of the spiral tubing's path and P_{tubing} is the pitch of the spiral tubing which is the distance between each turn of the spiral.
Figure 3.7 shows the variables for spiral tubing around a hypothetical cylindrical RAC.

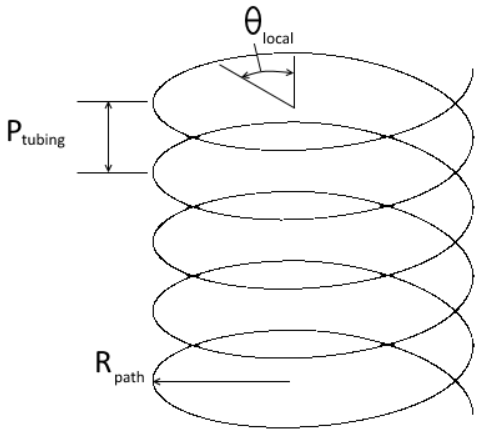

Figure 3.7: Representation of the spiral tubing variables

Finally, each parametric equation is differentiated with respect to θ_{local}, which yields x', y' and z'. These terms are squared, summed up and combined in a finite integral which is solved along the interval of $[0 : 2\pi \cdot n_{turns}]$ where n_{turns} are the total number of turns in the spiral (Equation 3.28).

$$L_{tubing} = 0.92 \cdot \int_0^{[2\pi \cdot n_{turns}]} \sqrt{x'^2 + y'^2 + z'^2} \tag{3.28}$$

The final interface area is calculated by multiplying L_{tubing} with the width of the interface area between the RAC and tubing. A 25% margin is taken from one third of the tubing length to account for a decrease of the practical length due to geometrical constraints at the rear side of the RAC. This translates to about an 8% decrease of the total length.

3.2.3.2 Linear tubing configuration

Now the linear tubing geometric characteristics are discussed. Equation 3.29 to 3.31 calculate all three RAC tubing lengths. As with the spiral tubing, a margin is taken off the tubing length of the third tubing part to take into account the loss of tubing due to geometrical constraints. Since straight tubing is less challenging in terms of integration,

only a margin of 10% is assumed. This translates to around a 3% decrease of the total length.

$$L_{tubing} = 0.97\sqrt{R_{path}^2 + H_{RAC}^2} \tag{3.29}$$

$$L_{tubing} = 0.97 H_{RAC} \tag{3.30}$$

$$L_{tubing} = 0.97 \pi R_{path} \tag{3.31}$$

The number of linear propellant feed lines is only taken into account when computing the final propellant temperature, as the convection area increases with more propellant tubing along the RAC.

3.2.4 Heat conducting channel and evaporator

The heat conducting channel interfaces with the RAC and the evaporator heating fluid/gas channel. It is modelled as a solid rod emanating radially from the RAC with a predetermined length.
The total contact surfaces between the RAC and the conduits and the conduits and the evaporator are a multiplication of the number of channels with their individual cross-sectional areas.

3.2.5 View factors

The view factors will partly determine the amount of thermal energy which is radiated between the nodes. Bergman et al. (2011) has been consulted for the necessary equations. Before one can start with calculating the view factors two relations must be put forward.

$$\Sigma F = 1 \tag{3.32a}$$

$$A_1 \cdot F_{12} = A_2 \cdot F_{21} \tag{3.32b}$$

Equation 3.32 states that the sum of all view factors from one node to the others must be 1. It also says that the product of the view factor of one node to another and the area of the first node must equal the product of the reciprocal terms concerning the second node.

Note that the secondary concentrator casing and the cavity lid are considered insulated at their sides. Therefore, the sides of these components are not taken into account when computing view factors. For the computation of the view factors one is referred to Appendix A.
One should also note that the assumption is made for all cavity configurations that there is no radiative heat exchange between node 2 and node 6, since re-radiation is limited due to the presence of the cavity lid.
Last, the spherical RAC's view factors are calculated with the assumption that the view factor between Node 5 and the interior of Node 6 is zero as calculating this view factor is considered too complex and time consuming without more advanced software.

3.2.6 Gebhart factors and thermal couplings

Gebhart factors indicate the ratio of absorbed radiation by a surface over the total radiation emitted by the principal surface. These factors are necessary to calculate radiative heat transfer. As with the view factors, the sum of all Gebhart factors from any surface must be 1. Since the view factors have been preliminarily calculated, the sum for each node might not amount to exactly 1. As this is a feasibility study, this is deemed acceptable.
In addition, Equation 3.33 applies. The Gebhart factors themselves can be computed with Equation 3.34 (Bergman et al. 2011).

$$\epsilon_i A_i B_{ij} = \epsilon_j A_j B_{ji} = R_{ij} = R_{ji} \tag{3.33}$$

$$B_{ij} = F_{ij}\epsilon_j \tag{3.34}$$

Here B_{ij} is the Gebhart factor. The variable ϵ is the emissivity of the surface and R_{ij} is the radiative coupling between thermal nodes.
The effect of reflections from other neighbouring surfaces needs to be taken into account in case of an enclosed surface. Equation 3.35 Bergman et al. (2011) shows this.

$$B_{ij} = B_{ij} + \psi \cdot F_{ik} B_{kj} \tag{3.35}$$

Here ψ is the reflectivity factor which is $(1 - \epsilon)$. The subscript k indicates adjacent or facing surfaces other than node i or node j. The equation is applied for Node 2 up to Node 5 as the pre-cavity chamber (Node 4) and its adjacent nodes can be considered a virtually closed section.

With the Gebhart factors known the radiative couplings can be calculated. Besides radiative couplings one can also discern conductive couplings which represent conduction processes between nodes. These can be calculated with Equation 3.36 (Bergman et al. 2011).

$$C_{ij} = \frac{k_i \cdot A_{i_{cs}}}{L_i} \tag{3.36}$$

Here, C_{ij} is the conductive coupling, k_i is the thermal conductivity of the node's material, $A_{i_{cs}}$ is the cross-sectional area of the node and L_i is the conductive path length between nodes.
Note that conductance between the primary concentrator and its struts or other components is assumed negligible.

The radiative and conductive heat fluxes are calculated with equations 3.37 and 3.38 (Bergman et al. 2011).

$$Q_{ij_{rad}} = R_{ij}\sigma(T_i^4 - T_j^4) \tag{3.37}$$

$$Q_{ij_{cond}} = C_{ij}(T_i - T_j) \tag{3.38}$$

3.2.7 Convective heat flow

Finally, the convective heat transfer from the propellant tubing inner wall to the propellant is discussed.
First, the convective heat transfer coefficient must be calculated. To this end Cornelisse et al. (1979) provides Equation 3.39.

$$h_c = \frac{Nu \cdot k}{D_{inner-tubing}} \tag{3.39}$$

The coefficient is h_c. The Nu parameter is the Nusselt number and $D_{inner-tubing}$ is the propellant tubing inner diameter.

3.2.7.1 Nusselt, Prandtl and Reynolds numbers

The Nusselt number is calculated with Equation 3.40. This Sieder-Tate correlation takes into account the viscosity variations in the propellant, assuming turbulent gaseous flow as detailed in Sieder & Tate (1936).

$$Nu = 1.86(Re \cdot Pr)^{(1/3)} \left(\frac{D_{outer-tubing}}{L_{tubing}}\right)^{(1/3)} \left(\frac{\mu_{prop_{free-stream}}}{\mu_{prop_{wall}}}\right)^{0.14} \tag{3.40}$$

Here, Pr is the Prandtl number, Re is the Reynolds number and μ_{prop} is the propellant flow viscosity, here in two different locations and computed through Equation 3.45. Equation 3.41 calculates the Prandtl number (Bergman et al. 2011).

$$Pr = \frac{c_{specific_{prop}} \mu_{prop}}{k} \tag{3.41}$$

The specific heat capacity of the propellant is denoted by $c_{specific_{prop}}$. The Reynolds number is calculated with Equation 3.42 (Bergman et al. 2011).

$$Re = \frac{\rho_{prop} U_{prop} D_{inner-tubing}}{\mu_{prop}} \tag{3.42}$$

The propellant flow density is denoted by ρ_{prop}; U_{prop} is the propellant flow velocity.

3.2.8 Flow properties in tubing

The flow velocity, viscosity and density in the tubing are calculated according to the equations below and fed into Equation 3.42.

$$\rho_{prop} = \frac{(p_{chamber} + \delta p)}{R_{gas} T_{prop_{initial}}} \tag{3.43}$$

Here, $p_{chamber}$ is the thruster chamber pressure, δp is the pressure loss in the tubing and R_{gas} is the specific gas constant. The equation is an expression of the ideal gas law (Bergman et al. 2011).

The flow velocity in the tubing is calculated with Equation 3.44 according to the law of conservation of mass (Bergman et al. 2011).

$$U_{prop} = \frac{m_{prop}}{\rho_{prop} A_{tubing_{cs}}} \tag{3.44}$$

In this equation m_{prop} is the mass flow through the tubing and $A_{tubing_{cs}}$ is the inner cross-sectional area of the RAC-adjacent propellant tubing.

The flow viscosity is calculated using Sutherland's equation (Equation 3.45) (Sutherland 1893).

$$\mu_{prop} = \mu_{prop_0} \cdot \frac{273.15 + C_{Sutherland}}{(T_f/273.15)^{(3/2)}} \tag{3.45}$$

Here, μ_{prop_0} is the propellant viscosity at 273.15 K, T_f is the average propellant film temperature and $C_{Sutherland}$ is the Sutherland constant which is unique for every propellant.

The film temperature is an average between the wall temperature and the propellant temperature. Since the propellant temperature varies along the length of the propellant tubing, the propellant temperature in question is itself an average of the final and initial temperature.

3.2.9 Temperature calculations

The energy flux associated with the convection processes in the propellant tubing (Node 7) and the evaporator heting fluid/gas channel (Node 9) is calculated in Equation 3.46. As previously, Bergman et al. (2011) has been consulted for the applicable equations.

$$Q_{conv} = m_{prop} c_{specific_{prop}} (T_{prop_{final}} - T_{prop_{initial}}) \tag{3.46}$$

As one can see the convective heat transfer is multiplied with the mass flow and the specific heat capacity of the propellant as well as with the difference between initial and final propellant temperature. The final propellant temperature is calculated in Equation 3.48.
The initial propellant temperature $T_{prop,initial}$ is already defined. The initial mean propellant temperature T_m can therefore be calculated.

$$T_{m_{initial}} = \frac{T_{prop_{initial}} + T_{inner-tubing_{wall}}}{2} \tag{3.47}$$

$$T_{prop_{final}} = T_{prop_{initial}} + h_c \frac{(T_{inner-tubing_{wall}} - T_m) A_{inner-tubing_{cs}}}{m_{prop} c_{specific_{prop}}} \tag{3.48}$$

$$T_{m_{new}} = \frac{T_{prop_{initial}} + T_{prop_{final}}}{2}$$

In the case that latent heat needs to be put into the propellant to change its phase Equation 3.48 becomes Equation 3.49.

$$T_{prop_{final}} = T_{prop_{initial}} + h_c \frac{(T_{inner-tubing_{wall}} - T_m) A_{inner-tubing_{cs}}}{m_{prop} c_{specific_{prop}}} - \frac{q_{latent}}{c_{specific_{prop}}} \tag{3.49}$$

Here, q_{latent} is the latent heat required to vaporize the selected propellant.

These equations are used in an iterative process where for each time instance the values are recalculated. Note that $T_{m_{initial}}$ is only valid up until the point that the propellant starts flowing. Afterwards $T_{m_{new}}$ takes its place since it is more accurate than the former variable. The final propellant temperature is subsequently calculated and plotted for each time instance. The maximum value in the array of final propellant temperatures is used in the same iterative scheme for performing calculations in the thruster model. At the start of the iterative cycle however an arbitrary value for the final propellant temperature will be put into the thruster calculations.

In addition these equations are used when calculating the heat flux from the ORC working fluid via the passive condenser to space.
The applicable heat flux equations for the passive condenser are as follows.

$$\Delta Q_{condenser} = Q_{conv} - C_{cond_1} - Q_{rad_{int}} \tag{3.50}$$
$$\Delta Q_{conductor} = C_{cond_1} - C_{cond_2} \tag{3.51}$$
$$\Delta Q_{radiator} = Q_{rad_{int}} + C_{cond_2} - Q_{rad_{ext}} \tag{3.52}$$
$$Q_{convection} = m_{wf} c_{specific} (T_{wf_{initial}} - T_{wf_{final}}) \tag{3.53}$$
$$Q_{rad_{ext}} = \epsilon \sigma A_{radiator} T^4_{radiator} \tag{3.54}$$

The *ext* and *int* subscripts indicate whether the flux comes from inside or outside the system. The *cond* subscripts indicate first the conduction between condenser and conductor channel and second between conductor channel and the radiator. The radiator has an area $A_{radiator}$ and a temperature $T_{radiator}$. The *rad* subscript indicates a radiative heat flux.
The internal radiative heat flux occurs between the condenser outer wall and the radiator panel interior. The external radiative heat flux occurs from the radiator exterior to space. If conductive heat exchange is selected for the heat transfer between condenser and radiator $Q_{rad_{int}}$ becomes zero. If radiative heat exchange is selected $\Delta Q_{conductor}$ and the C_{cond} terms become zero.

As the model is transient, the heat fluxes are dependent on time, as is seen in Equation 3.55. Here, the change in flux for each node has been computed (Equation 3.56).

$$T_i(t) = T_i(t-1) + \frac{\Delta Q_i(t)}{M_i c_{specific_i}} \Delta t \tag{3.55}$$

Here ΔQ_i is the net heat flux into node i. It is computed according to Equation 3.56.

$$\Delta Q_i(t) = Q_{i_{ext}} + \Sigma Q_{in_{int}} - \Sigma Q_{out_{int}} \tag{3.56}$$

Also the variable M_i indicates the mass of the thermal node. The mass for each node is calculated by multiplying the frontal surface areas by the representative thickness and multiplying this value by the material's density. Alternatively, the density is multiplied with the node's volume.

The time step is denoted by Δt. This calculation is made for every node at every time t which is incremented by time step Δt after every calculation. The temperature $T(t-1)$ at the previous time instance is taken from previous calculations with a pre-defined initial value at t = 0.

The external flux terms previously defined as $Q_{i_{ext}}$ are calculated with Equations 3.57 to 3.61.

$$Q_{1_{ext}} = \alpha_1 A_{prim_{cs}} S \tag{3.57}$$
$$Q_{2_{ext}} = \alpha_2 A_{prim_{cs}} S \eta_{prim} \tag{3.58}$$
$$Q_{6_{ext}} = \alpha_2 A_{prim_{cs}} S \eta_{prim} \eta_{sec} \tag{3.59}$$
$$Q_{albedo} = 0.3S \cdot A\alpha_{node} \tag{3.60}$$
$$Q_{IR} = 244 \cdot A\epsilon_{node} \tag{3.61}$$

Here, α is the solar absorptance of the node, ϵ is the IR emissivity of the node, $A_{prim_{cs}}$ is the cross-sectional area of the primary concentrator facing the Sun and S is the solar flux. The η-terms are the (throughput) efficiency of the primary and secondary concentrator. In Section 3.2.2 values for these efficiencies were respectively identified at 0.80 and at 0.87.

The last two equations are respectively the albedo radiation and the average IR radiation which are both emitted by the Earth and received by Node 1 to Node 3. Note that in eclipse there is no sunlight and therefore also no albedo.

Note that the propellant flow is only initialized after the cavity has reached a certain temperature. This 'propellant flow initialization cavity temperature' can be varied according to the necessary performance of the system. The model assumes that during propellant flow solar radiation will constantly be focused towards the cavity. In addition the initial propellant temperature is assumed to be the propellant storage temperature.

The thermal model process is illustrated by the process diagram in Figure 3.8. The main iterative cycle occurs when the thermal node temperatures and the accompanying mean heating gas temperature are calculated. This also involves iterations of the *ORCHID-VPE* model which details the thermodynamic processes in the power subsystem. Afterwards the final and mean propellant temperatures are calculated and put in the output data array. More details about the *ORCHID-VPE* model are given in Section 4.1.

3.2.10 Pressure losses

The pressure losses in the tubing need to be calculated to estimate the pressure in the propellant feed system. Equation 3.62 computes the single-phase friction pressure losses. Equation 3.66 deals with the pressure losses due to the phase change in the first part of the RAC tubing. Equation 3.67 calculates the acceleration pressure loss due to the vaporization of the propellant.

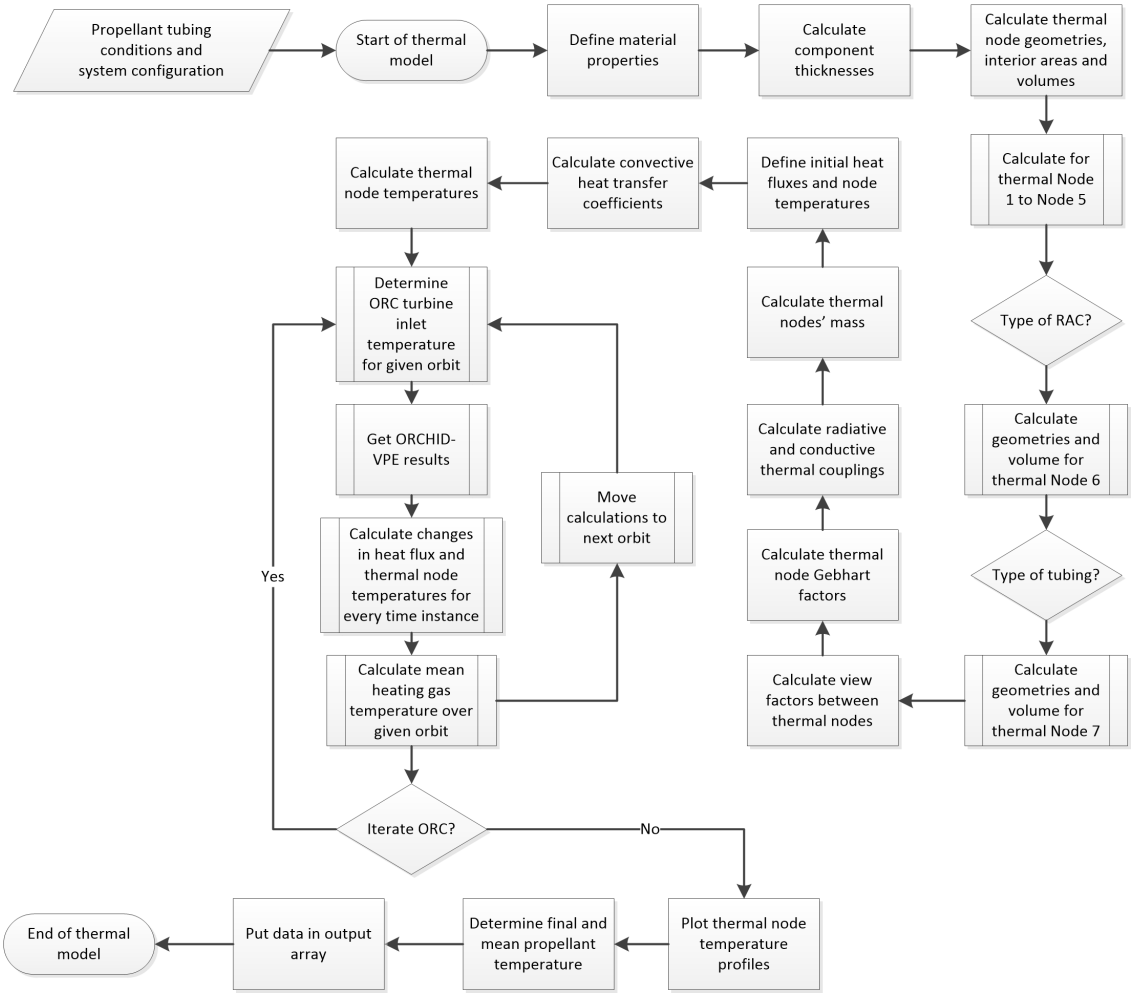

Figure 3.8: Process diagram for thermal model

3.2.10.1 Single-phase flow friction pressure loss

The Darcy-Weisbach equation is used to calculate the single-phase friction pressure loss.

$$\delta p_{friction_{single-phase}} = f_D \frac{L}{D} \frac{\rho V^2}{2} \tag{3.62}$$

The term f_D is the Darcy friction factor associated with the nature of the flow. It is calculated with the Blasius equation (Equation 3.63). This is assuming smooth propellant tubes. The L and D terms are respectively the length and inner diameter of the tubing in question. The ρ and V variables are the density and velocity of the propellant in the tubing.

$$f_D = \frac{0.316}{Re^{0.25}} \tag{3.63}$$

3.2.10.2 Two-phase flow friction pressure loss

McKetta Jr. (1992) offers a method to estimate pressure losses due to the existence of two phases within a pipe. The two-phase flow patterns within a pipe can be identified based on Baker parameters. These parameters are B_x and B_y. Equation 3.64 and 3.65 are used to compute them.

$$B_x = 2.1039 \frac{W_l}{W_v} \frac{\sqrt{\rho_l \rho_v}}{\rho_l^{(2/3)}} \frac{\mu_l^{(1/3)}}{\sigma_l} \tag{3.64}$$

$$B_y = \frac{25524.62 W_v}{\left(A\sqrt{\rho_l \rho_v}\right)} \tag{3.65}$$

Here, W is the flow rate and ρ is the density of the propellant. The liquid phase viscosity and the liquid phase surface tension are represented by μ_l and σ_l. The terms at the front of the equations are scaling factors to take into account metric units as the original equations use imperial units. The subscripts l and v indicate respectively that one is dealing with the liquid and gaseous properties of the propellant.
Looking at Figure 3.9 and taking the intersection of the calculated Baker parameters, a particular two-phase flow regime can be identified.

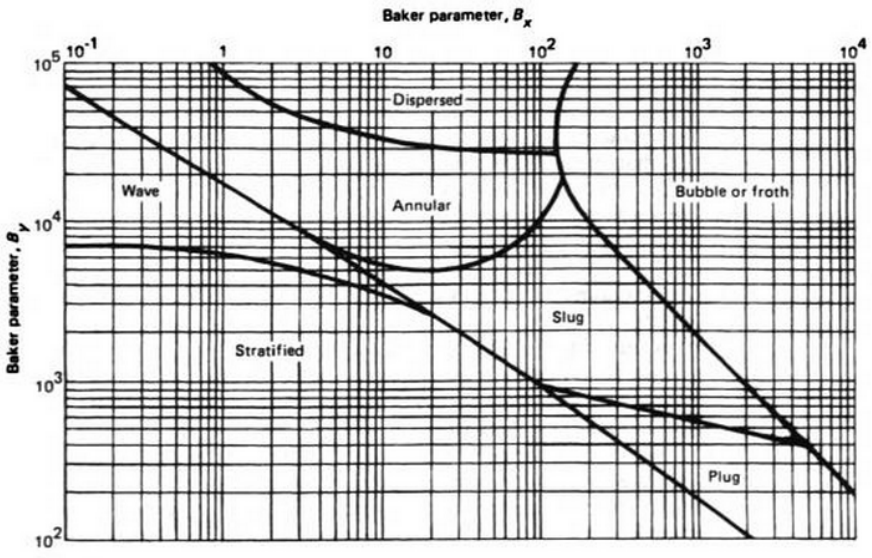

Figure 3.9: Two-phase flow region identification (McKetta Jr. 1992)

Depending on the region a different unit loss correlation is selected. The unit loss ϕ is used in Equation 3.66 to calculate the pressure loss. Here, the pressure loss of the gaseous state δp_v is calculated with Equation 3.62 along the length where the two-phase mixture exists.

$$\delta p_{friction_{two-phase}} = \delta p_v \cdot \phi^2 \tag{3.66}$$

3.2.10.3 Acceleration pressure loss

The acceleration pressure loss originates from the acceleration of the propellant flow due to vaporization of the liquid propellant. Fang et al. (2012) gives Equation 3.67 which is a derived equation for this pressure loss.

$$\delta p_{acceleration} = \left(\frac{m}{A}\right)^2 \left(\frac{1}{\rho_{out}} - \frac{1}{\rho_{in}}\right) \tag{3.67}$$

The *in* and *out* subscripts indicate the in- or outlet flow conditions. The total pressure loss is then determined by summing up the different pressure losses.

$$\delta p_{total} = \delta p_{friction_{total}} + \delta p_{acceleration} \tag{3.68}$$

In Chapter 6 these pressure losses will be calculated when designing the detailed propellant feed system.

3.3 Thruster Model

3.3.1 Introduction

The thruster model produces a first estimate of thruster performance in terms of specific impulse, thrust and propellant mass. The input variables are chamber conditions such as pressure, propellant density and temperature. Viscosity, specific heats ratio and specific gas constant are dependent on the propellant choice. Nozzle shape variables such as expansion ratio round up the input variables.

3.3.2 Nozzle shape

The nozzle shape depends on whether a conical or bell-shape nozzle is selected. The basic nozzle shape however is always the same (Figure 3.10):

- A convergent segment
- A curved convergent region towards the throat
- The throat with constant cross-sectional area
- A curved divergent region away from the throat
- A divergent segment with linearly or non-linearly increasing cross-sectional area

The assumption is made that the chamber radius equals the maximum radius of the convergent section. The throat radius is a set fraction of the maximum radius. The exhaust radius $R_{exhaust}$ determined by taking the squared root of the expansion ratio and multiplying this by the throat radius. In Equations 3.69 and 3.70 the x- and y-coordinate

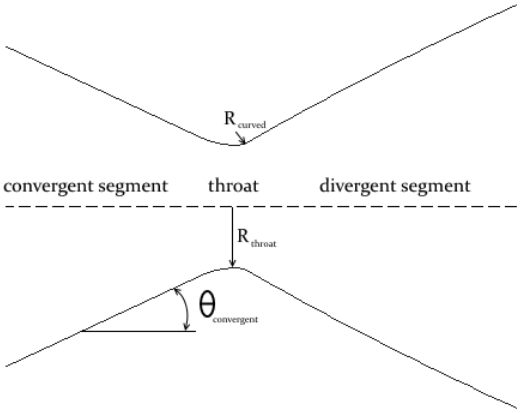

Figure 3.10: Representation of nozzle shape

of the start of the curved convergent region is calculated in order to plot the shape of the nozzle using basic geometrical relations.

$$x_{curved} = R_{curved} \sin(\theta_{convergence}) \tag{3.69}$$

$$y_{curved} = R_{throat} + R_{curved} \left(1 - \cos(\theta_{convergence})\right) \tag{3.70}$$

Here, R_{throat} is the throat radius, R_{curved} is the radius of the curved convergent section and $\theta_{convergence}$ is the nozzle convergent half angle. Figure 3.10 shows these variables.
The same procedure is used for the divergent curved section. The length from the start of the nozzle to the throat is added, after the x-coordinate has been calculated, to provide a consistent nozzle x-axis.

3.3.2.1 Conical nozzle

The conical nozzle shape is finished by using the nozzle exhaust radius to define the length of the divergent segment as the latter is dependent on the former and the nozzle divergence half angle. The nozzle divergence half angle $\theta_{divergence}$ denotes the slope of the divergent segment. The y-coordinate is therefore dependent on the x-coordinate as seen in Equation 3.71

$$y = y_{curved} + \tan(\theta_{divergence} \cdot (x - x_{curved}) \tag{3.71}$$

3.3.2.2 Bell-shaped nozzle

The bell-shaped nozzle requires a parametric expression for a parabola to estimate the bell shape of the nozzle. Three coefficients first need to be determined. They are dependent on $\theta_{exhaust}$ which is the nozzle exhaust divergence half angle or the angle which the nozzle has at the exhaust with respect to the horizontal. Equation 3.72 to 3.74 show the expressions for the coefficients.
Equation 3.75 gives the calculation for the x coordinate of the exhaust. By taking a number of values for x_{nozzle} and solving Equation 3.76 for y_{nozzle} the y-coordinates of the

divergent segment of the bell-shaped nozzle can be determined.

$$a = \frac{(\tan(\pi/2 - \theta_{exhaust}) - \tan(pi/2 - \theta_{exhaust}))}{2(R_{exhaust} - y_{curved})} \tag{3.72}$$

$$b = \tan(\pi/2 - \theta_{divergence}) - 2\frac{(\tan(\pi/2 - \theta_{exhaust}) - \tan(pi/2 - \theta_{exhaust}))}{2(R_{exhaust} - y_{curved})} \cdot y_{curved} \tag{3.73}$$

$$c = x_{curved} - a \cdot y_{curved}^2 - b \cdot y_{curved} \tag{3.74}$$

$$x_{exhaust} = a \cdot R_{exhaust}^2 + b \cdot R_{exhaust} + c \tag{3.75}$$

$$x_{nozzle} = a \cdot y_{nozzle}^2 + b \cdot y_{nozzle} + c \tag{3.76}$$

3.3.3 Nozzle critical flow conditions

In order to design an optimal nozzle the critical conditions need to be known in the throat so that the flow achieves sonic conditions exactly at the throat. This will prevent shocks and severe pressure drops in the nozzle. The subscript *critical* denotes the critical conditions in the throat. The subscript *chamber* specifies thruster chamber conditions. Equation 3.77 to Equation 3.81 calculate respectively the local pressure, local density, temperature, mass flow and flow velocity in the throat under sonic conditions (Anderson 2010).

$$p_{critical} = p_{chamber}\left(\frac{2}{\gamma_{prop}+1}\right)^{\left(\frac{\gamma_{prop}}{\gamma_{prop}-1}\right)} \tag{3.77}$$

$$\rho_{critical} = \rho_{chamber}\frac{p_{critical}}{p_{chamber}}^{(1/\gamma_{prop})} \tag{3.78}$$

$$T_{critical} = T_{chamber}\frac{2}{\gamma_{prop}+1} \tag{3.79}$$

$$m_{critical} = p_{chamber}\Phi\frac{\pi R_{throat}^2}{\sqrt{R_{gas}T_{chamber}}} \tag{3.80}$$

$$U_{critical} = \sqrt{\gamma_{prop}RT_{critical}} \tag{3.81}$$

$$\tag{3.82}$$

The variable γ_{prop} is the specific heats ratio of the selected propellant. $T_{critical}$ is the critical propellant flow temperature. $T_{chamber}$ is the propellant temperature in the thruster chamber. The assumption is made that between the end of the propellant tubing adjacent the RAC and the thruster chamber the propellant temperature decreases by 5% due to heat dissipation out of the tubing. The variable $m_{critical}$ is the critical mass flow in the throat. Φ is the Vandenkerckhove function and R_{gas} is the specific gas constant.
Finally, the throat flow velocity $U_{critical}$ can be calculated.

3.3.4 Chamber flow conditions

The ideal flow velocity in the chamber is calculated with the following equation (Anderson 2010). The resulting $U_{chamber}$ is usually significantly smaller than $U_{critical}$.

$$U_{chamber} = \frac{\rho_{critical} A_{throat} U_{critical}}{\rho_{chamber} A_{chamber}} \tag{3.83}$$

The corresponding Mach number is achieved through Equation 3.84 (Anderson 2010). These values can also be calculated all along the nozzle length.

$$Ma_{chamber} = \frac{U_{chamber}}{\sqrt{\gamma_{prop} R T_{chamber}}} \tag{3.84}$$

In this equation Ma is the Mach number. If the calculations of the flow velocity and Mach number are successfully executed, one will observe a Mach number of 1 at the throat.

3.3.5 Thruster and propulsion subsystem performance

Once the propellant flow in the nozzle has been determined, the equivalent or effective exhaust velocity U_{eq} can be calculated with Equation 3.85 (Sutton & Biblarz 2001). Note that the ambient pressure p_a outside of the nozzle in this case is 0 bar as one operates in a vacuum. The pressure at the exhaust is p_e.

$$U_{eq} = U_{exhaust} + \frac{(p_e - pa) A_{exhaust}}{m_{exhaust}} \tag{3.85}$$

The specific impulse I_{sp} is calculated through Equation 3.86 (Sutton & Biblarz 2001).

$$I_{sp} = \frac{U_{eq}}{g_0} \tag{3.86}$$

The parameter g_0 is the standard gravitational acceleration which is 9.81 m/s^2.

Before the resulting thrust is calculated, thrust losses due to flow divergence and the presence of a boundary layer need to be taken into account. The first component is computed with Equation 3.87 and 3.88 for respectively a conical and bell-shaped nozzle (Berton 1991), the second with Equation 3.91.

$$c_{thrust-loss} = \frac{1 + \cos(\theta_{divergence})}{2} \tag{3.87}$$

Note that $c_{thrust-loss}$ is a fraction of the total thrust.

For a bell-shaped nozzle correlation data is present, although an equation is unavailable. Therefore an equation is devised by subtracting the nozzle exhaust divergence half angle from the nozzle divergence half angle in Equation 3.87. An additional correction factor of 0.99 is put in to match actual correction factors for bell-shaped nozzles (Sutton & Biblarz 2001, p. 81). This yields Equation 3.88.

$$c_{thrust-loss} = 0.99 \frac{1 + \cos(\theta_{divergence} - \theta_{exhaust})}{2} \tag{3.88}$$

The boundary layer thrust loss is calculated as follows. Equation 3.89 calculates the momentum thickness due to the presence of a boundary layer (Schlichting & Gersten 2000, p. 161). Equation 3.90 uses this value to calculate the resulting thrust loss per unit span (Tennekes & Lumley 1972, p. 112). Multiplying by the nozzle edge length, which is $2\pi R_{exhaust}$, gives the thrust loss estimate as shown in Equation 3.91.

$$\theta_{momentum} = 0.664 \cdot \frac{\sqrt{\mu_{prop} x_{bl}}}{U_{exhaust}} \tag{3.89}$$

$$\frac{\delta T_{loss_{bl}}}{\delta x} = \theta_{momentum} \rho_{exhaust} U_{exhaust}^2 \tag{3.90}$$

$$T_{loss_{bl}} = \theta_{momentum} \rho_{exhaust} U_{exhaust}^2 \cdot 2\pi R_{exhaust} \tag{3.91}$$

Here, $\theta_{momentum}$ is the momentum thickness as a function of edge length and the thrust loss is an absolute value in Newton. The x_{bl} variable specifies the distance downstream from the throat where the boundary layer develops along the nozzle wall. In this case a distance of one third of the total divergent nozzle length is assumed.
The final thrust T_{thrust} is computed, using Equation 3.92 (Sutton & Biblarz 2001).

$$T_{thrust} = c_{thrust-loss} m_{exhaust} U_{exhaust} + (p_e - p_a) A_{exhaust} - T_{loss_{bl}} \tag{3.92}$$

Note that the thrust takes into account the thrust due to output mass flow as well as the thrust due to the pressure differential between the exhaust pressure and the space vacuum. The boundary layer thrust loss is calculated and can be considered negligible for these small nozzles.

The required propellant mass is calculated by solving Equation 3.93 which is Tsjolkovski's rocket equation.

$$\Delta V_{required} = U_{eq} \log \left(\frac{M_d + M_{prop}}{M_d} \right) \tag{3.93}$$

The M_d is the spacecraft dry mass and M_{prop} is the total propellant mass stored within the spacecraft. A 20% residual propellant margin is added on top of the required propellant mass to take into account inaccuracies and possible attitude determination and control system (ADCS) use of the propellant.
The thrust time, total impulse and system-specific impulse are respectively calculated with Equation 3.94, 3.95 and 3.96 (Sutton & Biblarz 2001). The variable M_{wet} is the wet propulsion subsystem mass.

$$t_{thrust} = \frac{M_p}{m_p} \tag{3.94}$$

$$I_{total} = T_{thrust} t_{thrust} \tag{3.95}$$

$$I_{ssp} = \frac{I_{total}}{g_0 M_{wet}} \tag{3.96}$$

Figure 3.11 details the process in the thruster model.

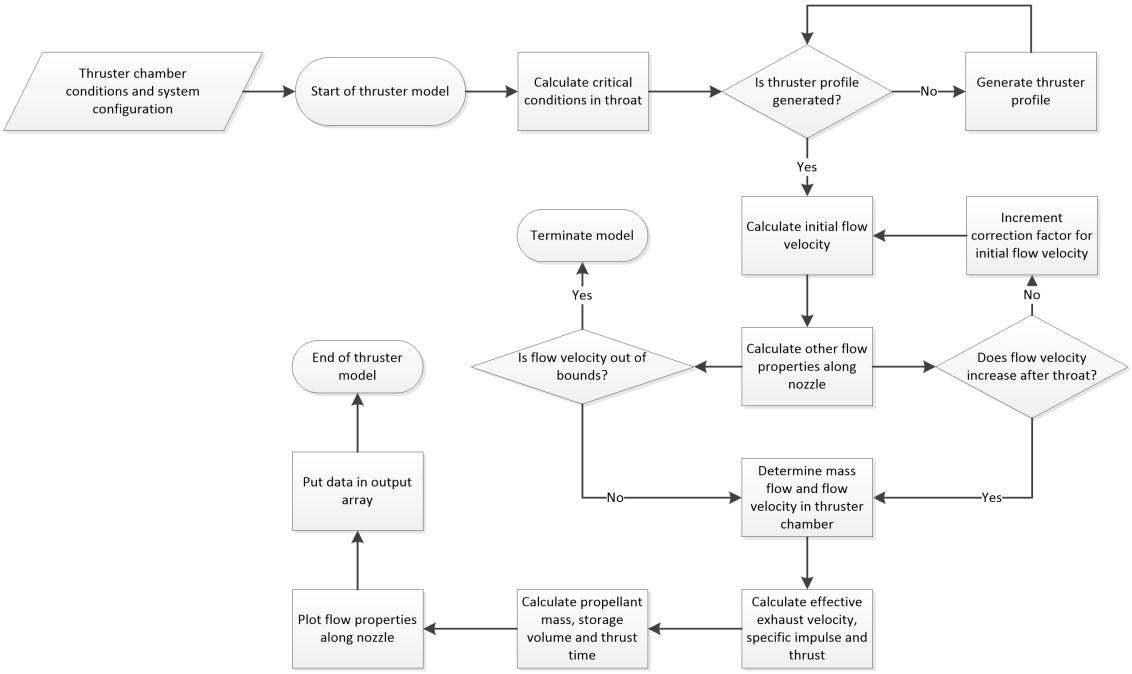

Figure 3.11: Process diagram for thruster model

3.4 Verification and validation

As one is dealing with mathematical models verification and validation need to be performed to detect faults.

Verification was first performed by varying design variables and seeing whether thrust, system mass and component temperatures increased or decreased as expected. Furthermore arbitrary design variables were selected to see whether performance values were in the order of magnitude as defined in Leenders & Zandbergen (2008), Shimizu et al. (2001), Nakamura et al. (2004), Sahara & Shimizu (2003) and Sahara et al. (2000). These include absorber temperatures in the range 1000-3000 K, thrust levels from 0.1-1 N and specific impulses of 700-900 s for hydrogen propellants. The absorber sizes which have been used during verification are in the range of 4 mm to 25 mm as derived from the previously identified literature.

After successful verification, the model was validated using test results from literature. First, the variables with regard to the thruster were validated as detailed in Subsection 3.4.1. Subsection 3.4.2 features the validation results in terms of final propellant and RAC temperatures. Because of the scarcity of test data only a qualitative validation could be pursued. A quantitative validation will have to be performed in the future once an actual system has been built.

3.4.1 Thrust, specific impulse and mass flow validation

First, the properties from the DUT solar thermal thruster as developed and reported by Leenders & Zandbergen (2008) are applied to the model.
The thruster is a conical copper thruster which is provided with gaseous nitrogen propellant to generate thrust. The propellant feed lines along the RAC are linear and integrated into the absorber wall. The nozzle itself is a micro nozzle.
Tests with and without propellant flow were performed with the former being the most interesting in this case. The highest stable propellant temperature achieved was 525 K at a mass flow of 50 mg/s. When increasing the mass flow, the thrust and pressure increased whereas the propellant and cavity temperature decreased. Thrust levels of 29 to 81 mN were measured.
Figure 3.12 provides a temperature profile for one of the tests.

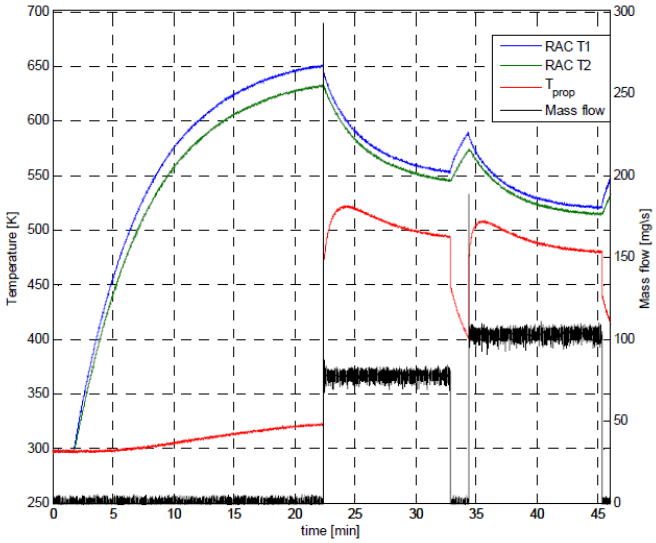

Figure 3.12: Leenders & Zandbergen (2008) test results

The input variables and their values for the validation have been given in Table 3.2. Note that the evaporator conducting channel and heating fluid/gas channel have not been included whilst running the model. Also the 10% margin decrease of part of the linear tubing length has been omitted. Furthermore the outside secondary concentrator casing is assumed made of molybdenum with a white paint coating. The cavity and propellant tubing are assumed made of copper. The pre-cavity and apertured cavity cover have MLI radiative properties.

The model is run. This yields the following results. First, a thrust of 100.6 mN is calculated. The specific impulse is 71.3 s. The mass flow at the exhaust is 104 mg/s.
For the 2-bar inlet pressure the test results give a mass flow of 77 mg/s and a thrust of 28.9 mN.

Although the results in Table 3.3 do not correspond exactly, they are within the same order of magnitude. This is considered acceptable, since the exact configuration of the DUT propulsion system is unknown, except for a small number of design variables. In addition ideal thruster performance has been assumed and thrust losses have been

Table 3.2: Model input variables for validation (Leenders & Zandbergen 2008)

Model variable	Value
Cross-sectional radius of primary concentrator	0.05 [m]
Radius of curvature for the primary concentrator convex membrane	0.125 [m]
Concentration ratio for primary concentrator	1/0.23 [-]
Primary concentrator focal length	0.01 [m]
Concentration ratio for secondary concentrator	1
Secondary concentrator focal length	0.01 [m]
Thickness of primary concentrator along lens axis	0.005 [m]
Cavity maximum radius	0.0125 [m]
Cavity length	0.0501 [m]
Chamber radius	0.0015 [m]
Chamber pressure	2 [bar]
Throat radius	0.00029 [m]
Length of divergent section	0.001 [m]
Expansion ratio	1.375 [-]
Number of lines for the linear propellant tubing	8 [-]
Diameter of the propellant tubing	6.77E-4 [m]
Type of RAC	Conical
RAC material	Copper
RAC wall thickness	2.5 [mm]
Type of tubing	Linear
Type of divergent nozzle	Conical
Type of propellant	Nitrogen
Propellant flow initialization cavity temperature	650 [K]
Solar flux	2350 $[W/m^2]$
Conducting interface (between RAC and tubing) width	4.84E-5 [m]

Table 3.3: Comparison of model and test performance

Performance variable	Model	Test results (Leenders & Zandbergen 2008)
Thrust [mN]	100.6	28.9
Specific impulse [s]	71.3	38.2
Mass flow [mg/s]	104	77

neglected whereas this will not be the case during real-life tests. Finally, one should expect a higher mass flow to produce a higher specific impulse and thrust which is indeed the case for the model. The thruster model is therefore qualitatively validated.

3.4.2 Temperature validation

The concept by Leenders & Zandbergen (2008) is used once more for the validation of model temperatures. Specifically, the final cavity and propellant temperatures are checked. The Shimizu et al. (2001) concept literature is deemed unsuitable to provide enough design variables. In this case the concept can therefore not be used to conduct a reliable validation.

Although the STP system as described by the model is different than the system design

of the DUT reference concept, care is taken to approximate the design as best as possible. First, a propellant flow initialization cavity temperature of 650 K is assumed. One seventh of the outer propellant tubing radius is assumed to be the width of the conducting interface between the tubing and the RAC.
Constant mass flow is assumed. Furthermore a power input into the system of 2350 W/m^2 is applied as specified.
In terms of materials the cavity lid is made of MLI material to simulate surrounding insulation; the cavity and the propellant tubing are made of copper.
Furthermore a certain heat dissipation from the RAC to the external environment has been assumed. This heat flux has been modelled as a conductive heat flux to a MLI blanket surrounding the areas of the cavity which do not have adjacent tubing. This layer has twice the thickness of the RAC and a thermal conductivity of 0.24 W/mK. The MLI-layer is kept at a room-temperature of 293.15 K. The input variables are given in Table 3.2.

Finally, an instantaneous propellant flow initialization is assumed. This causes an initial spike in the propellant temperature which is unrepresentative of real-life conditions where the propellant flow increases over a short period to a steady flow.
In Figure 3.13 one can take a closer look at the resulting instability in the propellant temperature plot during a model validation run. In the 14th minute into the simulation a spike can be seen which drops down almost instantly after which the curve continues in a normal manner.

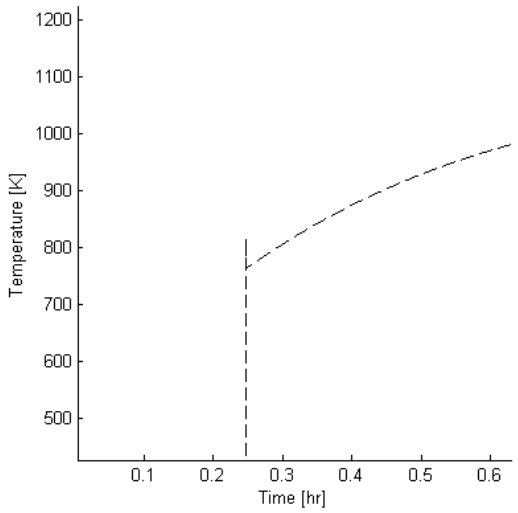

Figure 3.13: Instability of the initial propellant temperature values

To remove the instability from the results, the propellant flow temperatures during the first 11 to 30 seconds after flow initialization have been removed from subsequent plots. The simulated temperatures of the thermal nodes can be seen in Figure 3.14.

Comparing Figure 3.12 and Figure 3.14, the time till the cavity reaches 650 K is also

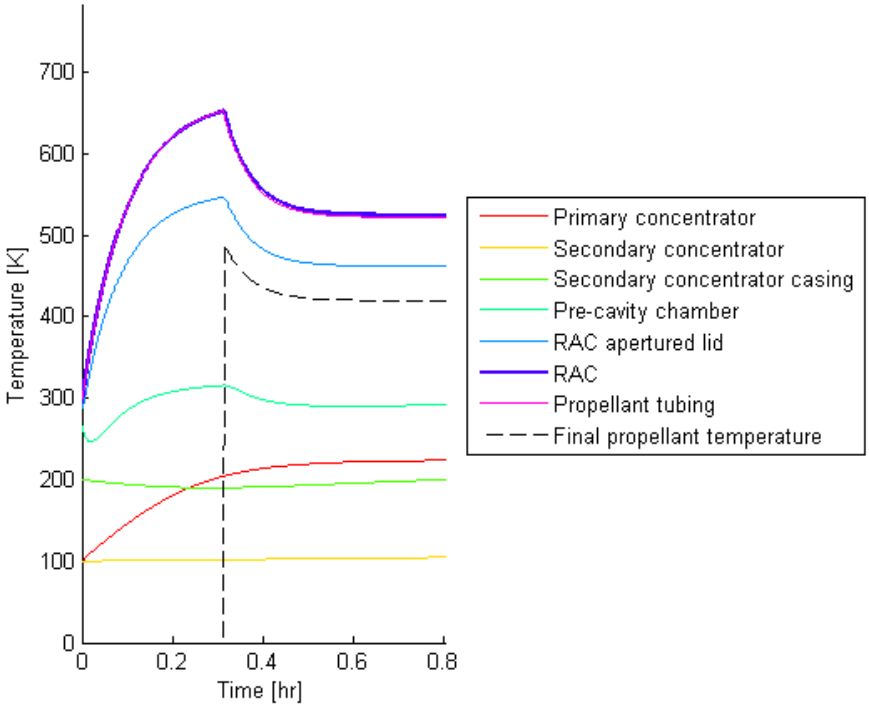

Figure 3.14: Temperatures for the DUT concept as modelled by the DAO tool

Table 3.4: Comparison of model and test temperatures

Temperature	**Model**	**Test results (Leenders & Zandbergen 2008)**
Maximum cavity temperature	652	650
Final cavity temperature	522	525
Maximum propellant temperature	489	525
Final steady propellant temperature	420	477

approximately 20 minutes for the model. The discrepancies in Table 3.4 stem from the assumed thermal uniformity of the thermal nodes, the limited number of thermal nodes, differences in mass flow in the feed lines and the non-constant propellant flow during actual testing. Furthermore, in the model the propellant tubing is not incorporated into the cavity whereas this is the case in the DUT design. One would therefore expect a larger convective area, a larger heat flux into the propellant and hence a larger propellant temperature. Adding more heat flux exchange processes between the different nodes and increasing the number of nodes will produce a more equivalent result, but will lead to an increase in the runtime of the simulation.

Furthermore, when varying the inlet pressure of the thruster the same relative ratios of mass flow are achieved. During the DUT thruster tests the mass flow increases from 77 to 128 mg/s when increasing the pressure from 2 to 3 bar. In the model the same simulated mass flow increases from 104 to 163 mg/s. This represents respectively a ratio of 0.60 and 0.64.
All these observations considered, the thermal model is qualitatively validated.

3.5 Observations

After running the model and changing different design variables, some observations can be made concerning the effect of design changes on the system's performance. The following design variables remain unchanged. The secondary concentrator casing is made of molybdenum with a white paint coating. All the other nodes are made of non-coated molybdenum, except for the cavity which has a black coating for a high solar absorptance. The propellant flow initialization cavity temperature is 1600 K.
Note that the figures in this section depict temperature profiles for a conical RAC. These results can however be extrapolated to other configurations.

3.5.1 Increasing convection area

Increasing the number of spiral turns increases the final propellant temperature. This makes sense as an increased number of turns leads to an increased length of the propellant tubing and consequently a larger convective area. One can indeed see that if in Equation 3.48 $A_{inner-tubing_{cs}}$ increases the final propellant temperature will increase. Looking at Figure 3.15 also shows an increase when the number of turns is increased from 5 to 10.
The same follows for increasing the number of feed lines in the linear tubing configuration.

If the propellant feed lines increase in diameter the $A_{inner-tubing_{cs}}$ increases as the radius of the tubing increases. The RAC temperature however decreases due to the larger heat flux going to the propellant. There is therefore a certain equilibrium when choosing the RAC and tubing design variables.
This can be seen in Figure 3.16 where with a larger tubing diameter the propellant temperature starts out at a higher initial value, but increases less compared to the smaller tubing diameter case. Eventually however the propellant temperature ends up slightly higher as the decrease in temperature during eclipse is smaller.

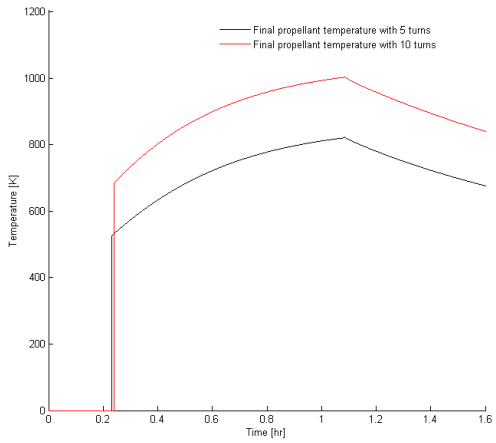

Figure 3.15: Final propellant temperature for different number of spiral tubing turns

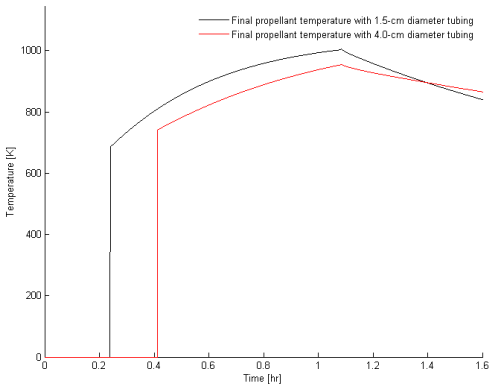

Figure 3.16: Final propellant temperature for different tubing diameters

3.5.2 Increasing cavity dimensions

Increasing the cavity diameter increases the absorber area and yields a larger tubing length. It does however increase the mass which needs to be heated. The slope of the RAC temperature curve is therefore less steep and the accompanying propellant temperature decreases (Figure 3.17).

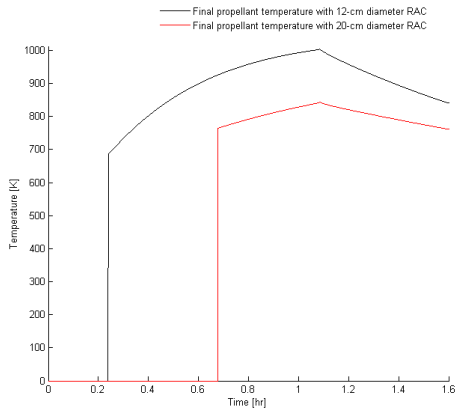

Figure 3.17: Final propellant temperature for different RAC diameters

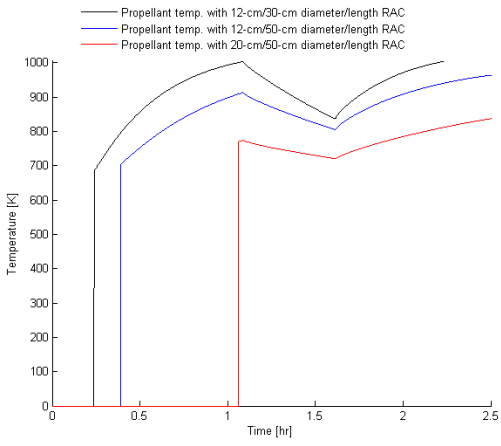

Figure 3.18: Final propellant temperature for different RAC configurations

Increasing the length of the cavity also decreases the propellant temperature. This happens because more mass needs to be heated which lowers the overall temperature of the cavity.
When one draws two plots, one with an RAC diameter of 12 cm and a length of 30 cm

and one with the same diameter and a length of 50 cm, this results in Figure 3.18. A third plot has also been added to the figure showing the combined result of increasing both the length and radius of the RAC which leads to a further decrease of the propellant temperature.

Increasing the cavity size, whilst also increasing the primary concentrator size, will however increase the propellant final temperature and cavity temperature. This occurs as the amount of absorbed solar heat and the propellant tubing convection area will increase. In Figure 3.19 the RAC is increased from 12 cm in diameter to 20 cm in diameter. The primary concentrator diameter is increased from 90 cm to 130 cm. One can indeed clearly see the resulting increase in propellant temperature.

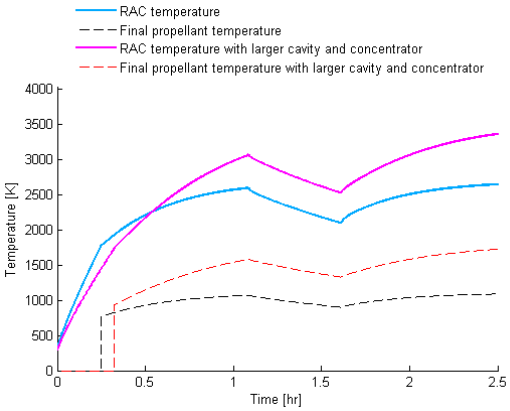

Figure 3.19: RAC and final propellant temperatures for different primary concentrator and cavity sizes

3.5.3 Too large primary concentrator

If the primary concentrator is too large and the propellant flow initialization temperature too high, the secondary concentrator temperature will easily exceed its maximum operating temperature.
A change in materials and dimensions will have to limit this temperature. In addition thermal control devices, such as thermal straps, will have to be applied. Note that the thermal straps interface with space to maximize the potential of the heat sink. Furthermore, the primary concentrator has a diameter of 1.6 m and the initialization temperature is 1800 K.
In Figure 3.20 the temperature for the secondary concentrator with and without thermal straps is shows. Here, the temperature plot for the concentrator is substantially lower when straps have been attached.

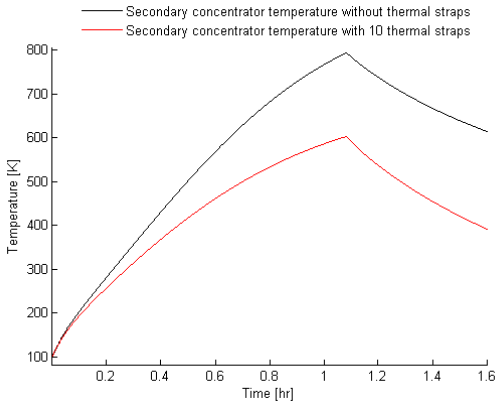

Figure 3.20: Secondary concentrator temperature with and without thermal straps

3.5.4 Increasing power output

Increasing the power output of the power subsystem decreases the cavity temperature and the final propellant temperature. In addition the ORC working fluid temperature is increased.
To complete the ORC the temperature of Node 8 and Node 9 might have to be increased. This can be achieved by increasing the number of heat conduction channels and/or increasing the radius of the evaporator heating fluid/gas channel.

In Figure 3.21 the power is increased from 100 W to 150 W with all other design variables remaining constant. The working fluid temperature indeed increases a little and the RAC and propellant temperatures decrease. The changes will be more substantial if the power output is increased further. This however will require design changes for the ORC.

3.5.5 Decreasing propellant mass flow

Decreasing the propellant mass flow and therefore flow velocity allows more time for convection and increases the final propellant temperature. This requires a smaller nozzle throat radius, assuming conditions of non-choked flow are maintained in the rest of the nozzle. This in turn will increase the specific impulse and decrease the thrust. Alternatively, the thruster chamber pressure can be decreased.
Figure 3.22 shows the results when the throat radius is decreased from 2 mm to 1 mm.

3.5.6 Applying insulation around RAC

Insulating the cavity with MLI increases the RAC and final propellant temperature. In Figure 3.23 the RAC and final propellant temperatures have been given for the design cases with and without insulation.
In the case without insulation one assumes radiative and conductive heat dissipation out of the RAC. For radiative heat exchange the emittance of the RAC is set at the level of untreated molybdenum, that is 0.18. The surrounding environment's temperature is

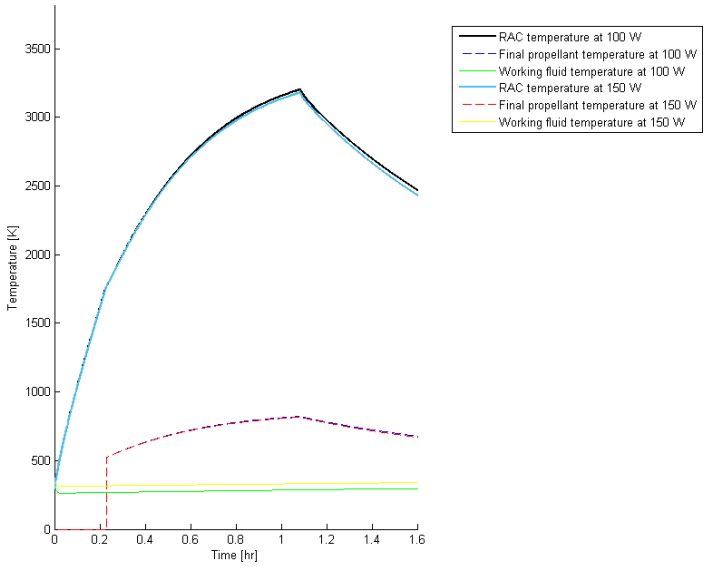

Figure 3.21: Cavity, final propellant and ORC working fluid temperatures at 100 W and 150 W power output

kept constant at 293.15 K. Conductive heat exchange is assumed through a layer with a thermal conductivity of 0.1 W/mK to simulate the non-insulation environment.

Indeed, the application of MLI is advantageous for the thermal performance of the system.

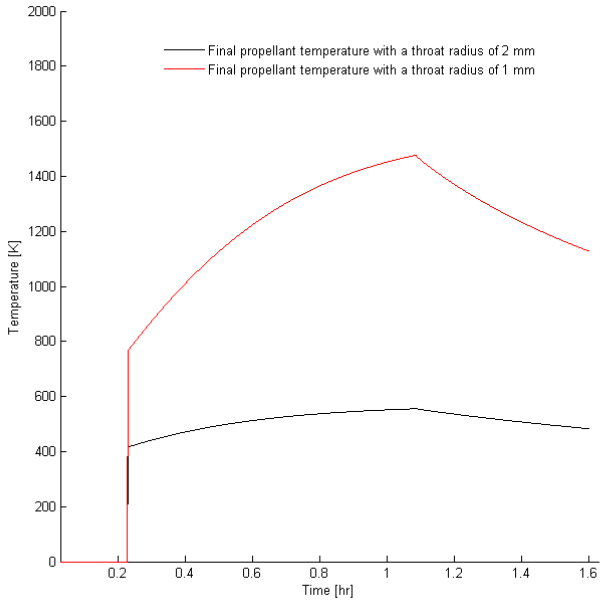

Figure 3.22: Final propellant temperatures with different throat radii

3.5.7 Conclusions concerning observations

Concluding from these observations, one can state that an optimal trade-off exists between RAC and final propellant temperature. By fine-tuning the variables of specifically Node 1 and Node 6 to Node 9 this optimal state can be achieved. Care must also be taken to ensure that during the first orbit the RAC and therefore the propellant are heated fast enough. This will result in timely power and thrust generation.
In Chapter 5 a number of conceptual designs will be synthesized based on this DAO tool.

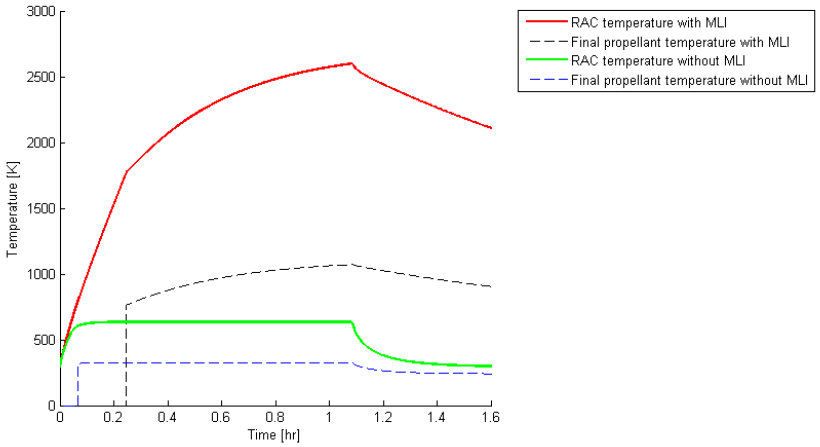

Figure 3.23: RAC and final propellant temperatures with and without RAC insulation

Chapter 4

Organic Rankine Cycles

An ORC is a means of generating power by the heating of a working fluid and using the resulting increased entropy of the fluid to convert the thermal energy to electrical energy.

Working fluids such as ammonia, hydrocarbons and refrigerants have been applied in the research of ORC systems (Hung et al. 1997). Saleh et al. (2007) has shown that the selection of a working fluid can severely affect the system maximum pressure, fluid maximum temperature, fluid mass flow and most importantly the thermal efficiency (Mago et al. 2008). Choosing a fluid is therefore critical to the ORC system design.
In Angelino & Invernizzi (1993) cyclic methylsiloxanes have been proposed as a propellant since they have good thermal stability and can operate till a temperature of 400 ° Celsius. In Rugescu (2012) toluene has been selected as the working fluid because of its good stability at high temperatures. Furthermore, Rayegan & Tao (2011) has compared a large number of candidate working fluids for ORCs and has found that toluene achieves one of the highest cycle efficiencies. This fluid is therefore chosen for the upcoming conceptual designs.

4.1 Working principles

Each ORC system has the following components. The temperature-entropy plot for a typical simple ORC is given in Figure 4.1. Below each ORC component is matched to the numbers in the figure.

- **Evaporator (2-3)** *Heat is added to the fluid up to the saturation temperature after which it evaporates and the entropy increases at constant temperature; the evaporation takes place at constant pressure*
- **Turbine (3-4)** *The working gas expands in the turbine which produces work which in turn is converted into electrical energy; as a result the entropy increases while the temperature decreases*
- **Condenser (4-1)** *Thermal energy is removed from the working gas at constant pressure until it is once more a fluid in a saturated state*
- **Pump (1-2)** *The pump forces the working fluid from the condenser to the evaporator whilst increases the pressure of the fluid to evaporator system pressure*

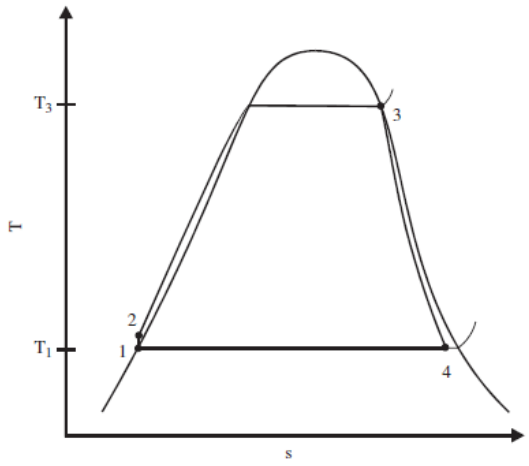

Figure 4.1: Temperature versus entropy plot for simple ORC (Saleh et al. 2007)

If thermal energy storage is required between the thermal energy generator and the evaporator, a thermal exchange cycle can be fitted to the system which releases energy to the evaporator when necessary. In Figure 4.2 one can see a set-up of such a system where a solar collector generates the thermal energy.

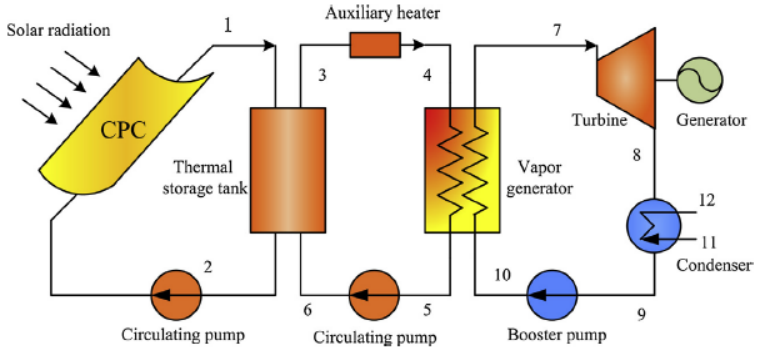

Figure 4.2: Schematic for a solar powered ORC system (Wang et al. 2014)

The net power yield of the ORC is the sum of the power output from the turbine and the required power for the pump. Sign convention dictates that power put into the system is negative. The power generated by the turbine and the required pump power can be calculated in a simplified way through Equation 4.1 (Kapooria et al. 2008).

$$P = m_{wf}(h_{inlet} - h_{outlet}) \tag{4.1}$$

Here, m_{wf} is the working fluid mass flow. The h-terms are the enthalpy of respectively the flow in front of the device and the flow behind it.
The net power generated by the power subsystem can then be calculated in Equation 4.2 (Kapooria et al. 2008). The related system schematic in Figure 4.3 shows the points in the cycle where the enthalpies are measured.

$$P_{net} = m_{fluid}\left((h_1 - h_2) - (h_4 - h_3)\right) \tag{4.2}$$

$$h = U + pV \tag{4.3}$$
$$\delta h = T\delta S + V\delta p \tag{4.4}$$

In Equation 4.3 one sees that enthalpy itself is the sum of the internal energy (U) and the achievable work of the fluid. The work is a multiplication of the fluid pressure and velocity. As such the temperature and pressure of the vaporized working fluid will have to be traded-off when designing the thermodynamic cycle.

A low inlet pressure at the turbine inlet will mean a high required temperature for the vapor. A high inlet pressure on the other hand allows the vapor to have a lower temperature without sacrificing thermal efficiency. A higher inlet pressure requires thicker tubing and therefore a larger system mass however.
The change in enthalpy in Equation 4.4 is dependent on the temperature, the change in entropy δS and the change in pressure δp. The first term in the equation is the change in internal energy and the second term the change in performed work.

The ORC thermal efficiency η_{ORC} is calculated by taking the total-cycle difference in enthalpy and dividing this by the enthalpy change associated with the input of external energy (Equation 4.5). It can also be expressed by the net difference in work divided by the incoming heat flow (Kapooria et al. 2008). Rayegan & Tao (2011) shows typical non-regenerative cycle efficiencies of 12% to 17% at an evaporator temperature of 400 K. Toluene yields an efficiency of 16%. If a higher evaporator temperature is selected, the thermal efficiency will increase.

$$\eta_{ORC} = \frac{h_1 - h_2 + h_3 - h_4}{h_1 - h_4} = \frac{W_t - W_p}{Q_{in}} \tag{4.5}$$

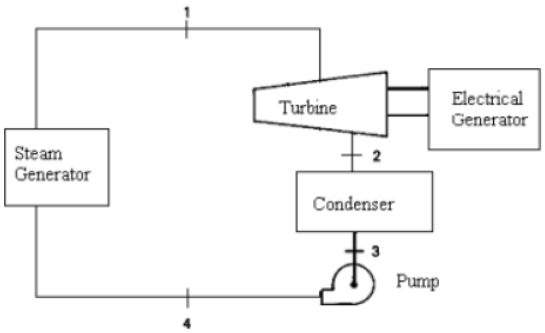

Figure 4.3: Schematic showing measurement points of enthalpy states (Kapooria et al. 2008)

Most standard ORC systems operate at relatively low temperatures where the temperatures of the working fluid reach a maximum of around 250° Celsius depending on the type of fluid, as shown by Saleh et al. (2007) and Vaja & Gambarotta (2010). Toffolo et al. (2014)

gives a maximum pressure in the turbine ranging from 14 to 67 bar using two different working fluids. Mago et al. (2008) and Li et al. (2013) show that the system thermal efficiency increases with increasing turbine inlet pressure. More is elaborated on this in Section 5.2.5.

Another way of increasing the thermal efficiency is the introduction of the process of 'regeneration'. It works as follows.
The working fluid is still heated up to a gas state in the evaporator. The working gas is forced through the high-pressure turbine stage which lowers the temperature of the gas.
At the turbine outlet a small portion of this gas is reintroduced into the evaporator where it aids the device by pre-heating the relatively colder working fluid. Since not only heat is added from an external source, the amount of input heat in the evaporator can be reduced.
The remainder of the working gas from the turbine outlet is passed to the condenser or to a second low-pressure turbine stage for additional power.
At the condenser outlet the gaseous flow will have been converted once more to a saturated liquid state.
As long as the lost work output of the bled working gas does not exceed the decrease in the amount of required external heat in the evaporator, the thermal efficiency will be increased. Mago et al. (2008) shows this for the working fluids isobutane and R113 where after applying regeneration the efficiency is respectively increased from 14% to 15% and from 20% to 24%.

Applicable heat exchangers for the evaporator found in literature are a spiral evaporator, a tubular evaporator, a circular nned-tube evaporator, a flat-plate evaporator and a space-cooled condenser. The evaporators will have to be made of high-conductance materials and the evaporator chamber itself will have to be highly insulated to prevent severe heat losses. The heat removed at the condenser will have to be fed back into the spacecraft for thermal control purposes or be radiated into space.

While designing the hybrid system, the ORC heat cycle is modelled using an adaptation of the *ORCHID-VPE* model being developed by the Flight Performance and Propulsion department at DUT's Faculty of Aerospace Engineering. This model features all the necessary devices as well as a regenerator. The evaporator and condenser use respectively a heating and cooling fluid.
Geometrical and operational constraints of a small satellite do not allow for a regenerator and an active-cooling condenser.
Therefore the regenerator is deactivated within *ORCHID-VPE*. Furthermore, the net active-cooling condenser heat flux is mimicked by a heat flux through a preliminarily designed passive space-cooled condenser.

4.2 Condenser performance

In the event that the passive condenser dissipates less heat to space than required the working fluid temperature in front of the pump will be higher than usual. This case is

analyzed by comparing two ORC settings at the same turbine inlet pressure and turbine efficiency:

1. The first setting has a turbine inlet temperature and pump inlet temperature of respectively 533.15 K and 313.15 K.
2. The second setting on the other hand has a turbine inlet temperature and pump inlet temperature of respectively 563.15 K and 343.15 K.

Looking at equation 4.2 and 4.4 this means larger enhalpies in front and behind the turbine and pump. The relative difference between the enthalpy at the inlet and outlet of the turbine is different for the second setting however since isentropic expansion is taken into account in the turbine as seen in Equation 4.6.

$$h_2 = h_1 - \eta_{turbine}(h_1 - h_{2_{is}}) \tag{4.6}$$

Here, $\eta_{turbine}$ and $h_{2_{is}}$ are respectively the turbine efficiency and the turbine outlet enthalpy under isentropic conditions.
Compared to the first setting, a higher temperature produces a larger entropy across the turbine as can be seen in Figure 4.1. As shown earlier a larger entropy generates a larger internal energy U and therefore a larger $h_{2_{is}}$ for the second setting. This in turn limits the decrease of the enthalpy over the turbine in Equation 4.6 and increases h_2. Equation 4.2 shows that this will decrease the net power.

This is verified since the generated power in the first and second setting is respectively 115 W and 105 W.

Chapter 5

Conceptual design

In this chapter a number of design concepts with different configurations have been detailed. Before concepts can be synthesized however an inventory has to be made of the system requirements and assumptions.

5.1 Conceptual system requirements and assumptions

5.1.1 Requirements

A total number of six concepts have been designed. All the different RAC configurations, namely conical, cylindrical and spherical, will be featured in these concepts. In addition all these systems will feature two different propellants, liquid ammonia and liquid hydrogen.

In Section 2.4 the system requirements were put forward. For each concept the propulsion module shall deliver at least 1 N in thrust and 100 s in specific impulse. The power budget shall be a minimum of 100 W. A required ΔV budget of 210 m/s has been previously stipulated for estimating each concept's total system mass. Finally, the system shall fit in a 1x1x1m satellite bus.

At this point in the thesis research it is unclear how large the ORC components will be. The power requirement for the ORC's small turbine are small compared to conventional turbines which have power outputs in the order of several kW. Therefore a reference micro-turbine is selected from literature for scaling of the power subsystem.
Last, each node must not surpass its maximum operating temperature. In Table 5.1 one can see the maximum temperatures for the relevant materials. The metals in the table have been previously taken into consideration in Section 3.2.2.3 due to their high thermal conductivity and commercial availability.
As component temperatures are expected to increase beyond 1400-1500 K, copper is discarded as the main constituent material of the concepts. Rather, molybdenum and tungsten are more suitable. In Section 5.2.2 molybdenum and tungsten systems are compared in terms of their performance.

Table 5.1: Maximum operating temperatures for thermal nodes

Material	Maximum Temperature [K]
CP-1 and CP-2 Polyimide film (DuPont 2014)	673
Copper (Engineering Toolbox 2000)	1357
Tungsten (Engineering Toolbox 2000)	3673
Molybdenum (Engineering Toolbox 2000)	2893
Sapphire Single-Crystal (Kyocera 2013)	1373

5.1.2 Assumptions

A number of assumptions have been made regarding the preliminary designs as obviously the lack of an entire system architecture leads to many unknowns.

5.1.2.1 Mass estimates

The mass estimate for the entire hybrid subsystem is difficult to synthesize due to design unknowns and the lack of reference systems in literature. Therefore an estimate is necessary. In Table 5.2 the mass budget is given for multiple small satellite missions. The propulsion subsystem includes the thruster, feed lines, propellant tank and the propellant itself. The power subsystem includes the electric power system (EPS) and the solar array.

Table 5.2: Reference mass budgets for small satellites

Mass [kg]	Constellation for Disaster Monitoring (Ward et al. 1999)	Proba 3 (Borde et al. 2004)	SIMONE (Wells et al. 2006)	Hummer Sat-1 (Zhang et al. 2007)	SMART-1 (Racca et al. 2002)
Power	19.6	21.6	23.3	15.7	96.3
Propulsion	15	13.4	46.2	22.1	111.2
Total	65.5	110.5	120	159.5	366.9

From the table the mean value for a conventional propulsion and the power subsystem is respectively 21% and 24% of the total spacecraft mass. As stated previously the margin for the propulsion subsystem takes into account the propellant. Assuming that half the propulsion subsystem's wet mass is propellant yields an estimate of 10.5% of the total spacecraft mass for the dry propulsion subsystem.

The total spacecraft mass is a sum of the 200-kg dry mass and the propellant mass. The propellant mass itself has a 20% margin for residual propellant. The tank volume to store this propellant has a 20% ullage margin of its own.
The dry propulsion subsystem mass is a sum of the mass of the system components, the estimated thruster mass and the 10.5% estimate for the dry propulsion subsystem.

A 10% safety margin is added on top of the 10.5% and 24% estimates.

$$M_{prop_{dry}} = M_{components} + M_{thruster} + 1.1 \cdot 0.105 M_{total} \tag{5.1}$$

$$M_{power} = 1.1 \cdot 0.24 M_{total} \tag{5.2}$$

$$f_{system} = \frac{M_{prop_{dry}} + M_{power}}{M_{total}} \tag{5.3}$$

The summed up total system mass is divided by the total spacecraft mass which yields a system mass fraction (Equation 5.3).

5.1.2.2 RAC and interfaces

It is assumed that the central part of the cavity has an interface with the evaporator and that the entire cavity is insulated with MLI. The insulation has a thickness of 43 mm, a thermal conductivity of $0.1{\cdot}10^{-3}$ W/mK and an effective emittance of 0.002 (Larson & Wertz 2005). The interior of the spacecraft and therefore also the MLI environment is assumed to be at room temperature (293.15 K). Both the radiative and the conductive heat flux from the RAC through the MLI are taken into account.
It is also assumed that there is no radiative heat exchange between a spherical RAC and the RAC lid and that the conductive heat exchange between this RAC and the lid takes place at the edge of the lid aperture.

Another assumption is that the conductive interface area between the RAC and the propellant tubing is a multiplication of the length of the propellant tubing with the tubing-cavity interface width. Although this width was previously established in Section 3.4.2, this interface width has been widened to half the propellant tubing radius to take into account additional radiative heat transfer as the tubing is relatively small compared to the adjacent high-temperature RAC.

5.1.2.3 Thermal nodes and tubing conditions

All the nodes are considered isothermal. The temperature profiles for the concepts show the mean thermal node temperatures; that is, the mean value taken over all the sub-node temperatures.

To see the order of magnitude of the thickness of each thermal node, Table 5.5 is provided. Judging from multiple molybdenum tube manufacturers such as Goodfellow (2014) the diameter to minimum wall thickness ratio ranges from 13 to 15. Therefore a ratio of 13 will be applied for the cylindrical components such as the pre-cavity chamber and the cavity itself. The propellant tubing gets a smaller factor of 8 (Rembar 2014).
The secondary concentrator casing thickness however is defined based on the width of the secondary concentrator. The cavity lid thickness is one fifth of the cavity radius to ensure that the MLI which encapsulates the lid can be adequately fastened. The surrounding MLI around the lid has a thickness of 43 mm (Johnson & Fesmire 2011) and a thermal conductivity of $0.1{\cdot}10^{-3}$ W/mK.

For the evaporator and the propellant tubing the minimum thickness is checked whether it can cope with the internal pressures, using Equation 3.19. The worst-case gas pressure in the evaporator is assumed to be 10 MPa. For the propellant tubing a maximum pressure is assumed of 20 MPa. Due to the increased tubing temperature the yield strength of molybdenum is reduced to around 150 MPa according to test results in Briggs & Campbell (1972). This results in a respective minimum thickness of 0.52 mm and 0.33 mm. This is well below the actual tube thicknesses (Table 5.5).

Concerning the propellant flow in the tubing adjacent the cavity, turbulent flow as well as a steady mass flow is assumed. This allows one to use the Sieder-Tate correlation for calculating the flow's Nusselt number (Equation 3.40). This number is used to compute the convective heat transfer coefficient between tubing inner wall and the propellant flow. As stated in Chapter 3 the propellant will change phase in the first one-third section of the RAC tubing. Therefore in this section latent heat and two-phase flow are taken into account.
Furthermore, the initial propellant temperature into the tubing is assumed to be the propellant storage temperature.
The evaporator heating fluid or gas initial temperature is assumed to be 293.15 K before convection.
The convection area between RAC and heating gas is assumed to be the area of the heating gas channel which follows the circumference of the RAC; the straight sections to and from the ORC evaporator are only for transporting the gas (Figure 5.1). No radiative heat exchange is assumed between the heating gas channel and the RAC due to the presence of MLI unless specified otherwise.

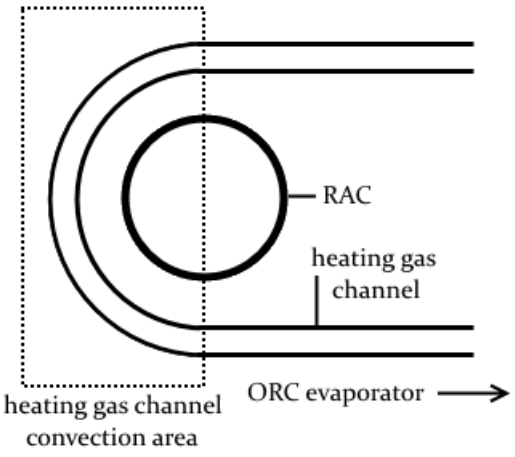

Figure 5.1: Schematic of the heating gas channel and RAC interface

5.1.2.4 External fluxes and temperatures

The assumption is made that one starts at the beginning of the daylight part of the orbit. The primary concentrator, secondary concentrator and RAC receive solar radiation, albeit

each at a reduced level due to lens throughput efficiencies. The primary concentrator, secondary concentrator and its casing receive additional Earth albedo and IR radiation. The casing does not receive solar radiation as it is assumed that the primary concentrator captures the sunlight before it can hit the casing.

The reference orbit has a 600 km altitude, a 80 degree inclination and a 50 degree initial RAAN (Table 3.1). This produces the time of eclipse at 61.78 minutes from the start of a new orbit. The eclipse itself lasts almost 32 minutes.
Once the eclipse period in the orbit has been reached, no solar flux, Earth albedo and IR radiation will hit the spacecraft for the duration of that period. During this time the propellant flow is interrupted to curb the decrease of the RAC and propellant tubing temperatures. This is verified when comparing Figure 5.2 and Figure 5.11. One sees that the propellant flow does not reach pre-eclipse temperatures and in fact drops in temperature.

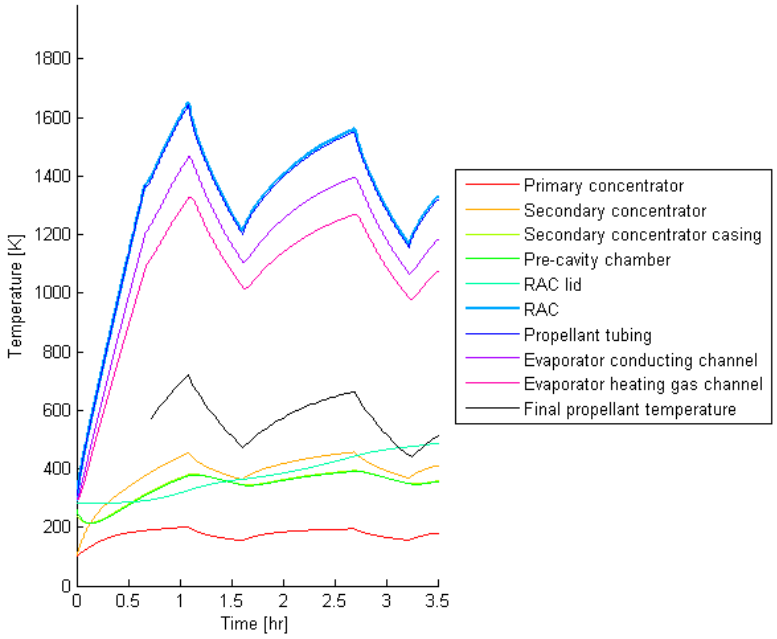

Figure 5.2: Thermal node temperatures for Concept 1 with continuous propellant flow after flow initialisation

The solar flux itself is assumed to be the mean solar flux value over the entire year of 1371 W. The on-axis primary concentrator is assumed to be pointed towards the Sun during the entire daylight-part of the first orbit. Therefore it receives the full flux during that time. During the next orbit a different pointing scheme might be used to keep the maximum RAC and propellant temperatures relatively constant to satisfy Requirement 8. After iterating the model the following conditions therefore hold. Note that these values have been tailored to the respective conceptual designs.

- For the concepts which use liquid ammonia and have a conical RAC, 68% of the available solar flux is required for subsequent orbits.
- For the concepts which use liquid ammonia and have a cylindrical RAC, 79% of the available solar flux is required for subsequent orbits.
- For the concept which uses liquid ammonia and has a spherical RAC concepts a solar flux of 96% is required.
- For the concepts which use liquid hydrogen and have a conical RAC, 98% of the solar flux needs to be received for subsequent orbits.
- For the concepts which use liquid hydrogen and have a cylindrical RAC, 99% of the entire available solar flux is required for subsequent orbits.
- For the remaining spherical concepts which use liquid hydrogen, the full solar flux is required.

As a consequence of these measures a long-term temperature increase of the RAC and propellant is prevented.
The model also assumes a worst-case scenario where thrust is constantly generated in the daylight parts of the evaluated period. Therefore, if only a small amount or no thrust is generated during that time, the pointing scheme again must be different compared to what is described above.

To increase the speed of the simulations some mean temperature values have been calculated as described below and indicated in Figure 3.8:

- The final propellant temperature upon which the propellant thruster chamber temperature during each orbit is based, is equal to the mean propellant temperature during the daylight part of each orbit.
- The final evaporator heating medium temperature for each orbit is assumed to be the mean heating medium temperature which is achieved over the entirety of each orbit. As the mean heating medium temperature changes each orbit, the turbine inlet temperature and power output change each orbit as well. This is taken into account in Section 5.2.5. This means that the system can generate power during eclipse as long as the heating medium temperature is high enough.

Finally, some assumptions govern the power subsystem in general:

- The mass flow of the ORC's working fluid is constant.
- A turbine efficiency of 75% is assumed which is in the range as defined in PowerMEMS (2014) and Schubert (2012).
- The pump efficiency is assumed 50% which is in the order of magnitude found in literature for small pumps such as Kim et al. (2014) and Laser & Santiago (2004).
- A typical pressure loss in the turbine of 2% is assumed.

5.2 General design considerations

In the previous section the requirements and assumptions were put forward. These are followed in this section by general design considerations for all the concepts.
This includes the definition of the system efficiency, which materials and gases are used, which thruster nozzle shape is adopted and which tubing configuration is selected. Finally some design parameters for the power subsystem are determined.

5.2.1 System efficiency

The system efficiency of a solar thermal power-propulsion hybrid system defines how efficient the system can convert the inserted solar heat into both power for the other spacecraft subsystems and thrust for the entire spacecraft. However, no efficiency variable has so far been defined. In this section an equation will be proposed to define this efficiency variable in order to evaluate the efficiency of the different system designs.

First of all the efficiency should include the input solar heat as this is the system's energy source.
Second, the thrust and generated net power should feature in the efficiency equation as these are the output products of the system.

To convert the thrust to power in Watts, the principle of thrust is summarized.
The application of thrust increases the spacecraft's velocity vector in a certain direction and thereby the kinetic energy of the spacecraft. This in turn alters its orbit, depending on the direction of the velocity increment. One can therefore use the expression for kinetic energy (Equation 5.4) to derive a power equation as a function of the thrust (Equation 5.5).

$$E_k = \frac{1}{2} m U^2 \tag{5.4}$$

$$P = \frac{1}{2} T \cdot U \tag{5.5}$$

Here, E_k is the kinetic energy, m is the mass and U is velocity. The P and T terms indicate the output power and output thrust respectively.
All the values except the velocity are straightforward. The velocity-term could concern the thruster exhaust velocity, the velocity increment ΔV or the orbital velocity.
As the orbital velocity is not characteristic for the system but for the spacecraft mission, it is discarded.
The thruster exhaust velocity is already used to calculate the thrust as shown in Equation 3.92. Therefore, including this velocity would make the influence of the thrust in the efficiency equation far too dominant.
Finally, ΔV indicates the amount of total velocity change which can be generated by the hybrid system. As such it provides a measure of how long thrust can be delivered. When discussing the efficiency of the system, this time-dependency of the thrust cannot be neglected, as power can be generated constantly.

Concluding, the U in Equation 5.5 becomes ΔV.

Adding the net power to the equation and dividing by the input heat, yields an expression for the total system efficiency η_{system}, Equation 5.6.

$$\eta_{system} = \frac{\frac{1}{2}T \cdot \Delta V + P_{net}}{S \cdot A_{prim_{cs}}} \tag{5.6}$$

Here, T is the thrust in Newtons, ΔV is the velocity increment as defined in Requirement 6 and P_{net} is the net power generated by the power subsystem. The denominator is the solar flux hitting the solar concentrator, which may be less than the full solar flux due to the concentrator pointing direction, multiplied by the cross-sectional area of the primary concentrator. One should see Section 5.1.2.4 for how much solar flux hits the primary concentrator.

This efficiency value shall be used in this chapter and in Chapter 6 to compare the different designs in terms of energy efficiency.

5.2.2 Materials and constituent fluids and gases

As stated previously molybdenum is a suitable material as it has high thermal conductivity and can cope with high temperatures. The material will therefore feature extensively in each concept.
All the designs have a molybdenum secondary concentrator casing with a white coating. The pre-cavity chamber is also made of molybdenum with a white coating. The molybdenum cavity lid is covered with MLI to limit the temperature of this component and to isolate the cavity and pre-cavity chamber from each other. The cavity is made of molybdenum with an interior black paint coating. The propellant tubing is made of molybdenum as well.

The evaporator heating fluid or gas channel can harbor a fluid or gas. Since phase changes of a heating fluid might induce unpredictable flow behavior, a heating gas is inserted in the channel. After a short review air is selected as it is cheap and has a relatively large thermal conductivity compared to other gases (Weast 1969).
As mentioned in Chapter 4 the ORC's working fluid will be toluene.
To facilitate a large heat flux into the evaporator heating gas, the conduction channels and heating gas channel are made of molybdenum as well. Although copper provides a larger thermal conductivity, it was found that on most occasions the temperatures of the two nodes exceeded copper's melting point.

In some concepts thermal straps have been implemented so that the temperatures of nodes do not exceed the maximum operating temperatures during the evaluated time period. One should note that for some concepts the temperature plot for the RAC lid will still show an increase during daylight hours and a little decrease in eclipse. This means that over a long period the maximum operating temperature will be reached. Hence, additional thermal control measures should be looked at during the detailed design.

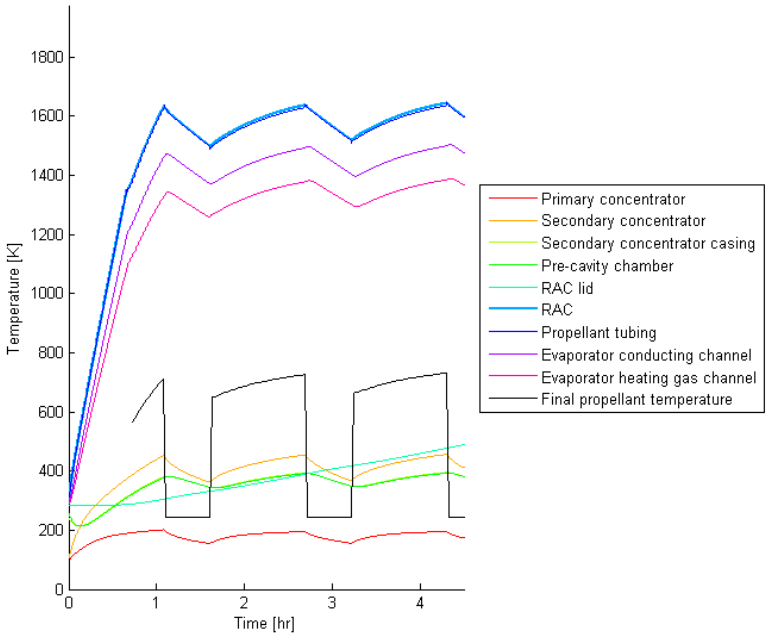

Figure 5.3: Thermal node temperatures for Concept 1 with tungsten components

The molybdenum parts can alternatively be replaced with tungsten components. Figure 5.3 and Figure 5.11 show respectively the mean temperatures of the thermal nodes for a tungsten and a molybdenum design of Concept 1.
The performance of the two metals is quite similar except for the higher melting point of tungsten. The figures show virtually no change in the temperature profile. The specific impulse and thrust remain unchanged when tungsten parts are introduced. The wet system mass fraction however increases from 0.61 to 0.69 as molybdenum is a lighter material. Therefore molybdenum is preferable; if mass concerns are less important tungsten can be used as well. In the case of very large primary concentrators and associated heat fluxes tungsten might be the only option to avoid the melting of components. In the conceptual design phase only molybdenum components will be used as the tungsten design's system mass fraction violates Requirement 2.

5.2.3 Nozzle shape

All concepts can have a conical or bell-shaped nozzle. In either case the chamber radius and pressure are respectively 1 cm and 1 bar. In addition, the throat radius is 1.5 mm. The nozzle expansion ratio is set at 100. For the conical nozzle the nozzle throat convergence and the nozzle throat divergence half angle are respectively 25 degrees and 17 degrees.
For the bell-shaped nozzle, the nozzle throat convergence half angle is also 25 degrees. The nozzle throat divergence half angle is increased to 35 degrees. The exhaust divergence angle becomes 11 degrees.
The two designs are shown in Figure 5.4 and Figure 5.5. Both nozzles have a length of 6.3 cm.

The conditions in the nozzles are such that the Mach number in the throat is 1 and that therefore the flow velocity also increases in the divergent section.

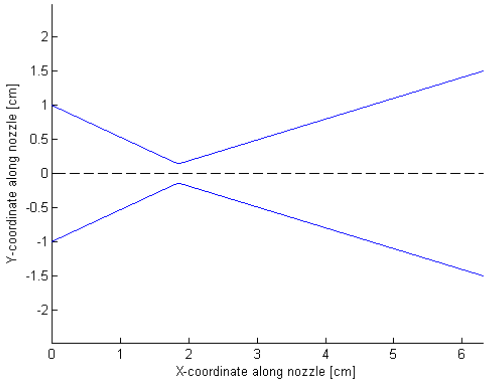

Figure 5.4: Conical nozzle design

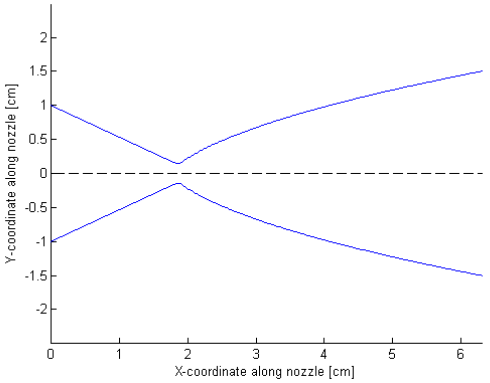

Figure 5.5: Bell-shaped nozzle design

In Table 5.3 the nozzle shapes are compared in terms of the maximum values of the specific impulse, total impulse, thrust and system efficiency. Both nozzles have been applied to Concept 1.

Table 5.3: Performance comparison between a conical and bell-shape nozzle for the same hybrid system

Nozzle	**Specific impulse[s]**	**Total impulse [kNs]**	**Thrust [N]**	**System efficiency [-]**
Conical	162	53	1.267	0.42
Bell-shape	169	51	1.273	0.42

One sees that the bell-shape nozzle generates more specific impulse and slightly less total impulse. The thrust is larger than the thrust of the conical nozzle and it has the same efficiency. Sutton & Biblarz (2001) also considers bell-shaped nozzles preferable above conical nozzles. The main downside of these nozzles however is that they are more difficult to manufacture.

In Figure 5.6 and Figure 5.7 the propellant flow velocity is shown at the end of the second orbit for respectively the conical and bell-shaped nozzle.

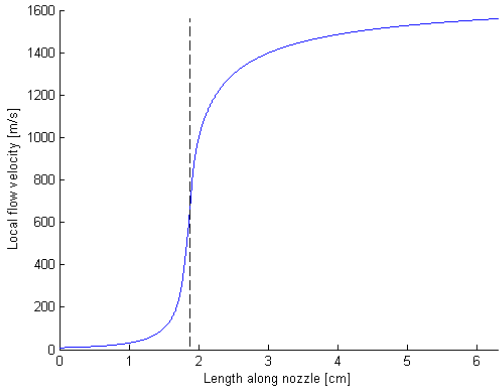

Figure 5.6: Propellant flow velocity in the conical nozzle for Concept 1

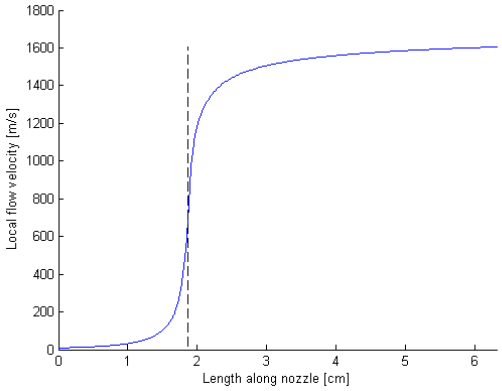

Figure 5.7: Propellant flow velocity in the bell-shaped nozzle for Concept 1

Although the bell-shaped nozzle achieves a better performance, a conical shape is chosen for the conceptual designs to keep the number of concepts limited, as there are a lot of different bell shapes possible. The bell-shaped nozzle will however be considered again when discussing the detailed design as it is more advantageous. For comparative purposes however the type of nozzle is less significant.

5.2.4 Tubing configuration

All concepts feature a spiral tubing configuration with 20 turns. Note that the stated number of turns does not take into account the assumed 8% losses in tubing length due to geometrical constraints (Section 3.2.3.1). The spiral set-up allows for a higher or equivalent propellant temperature compared to the linear tubing, since the spiral pattern produces a relatively large tubing length and conductive area with the cavity. The use of this configuration has also been recommended by Leenders & Zandbergen (2008).

One can compare the performance of the same concept with different tubing configurations to show this.
Concept 1 is fed with ammonia propellant and the tubing configuration is changed from respectively 'spiral' to 'linear' and the number of feed lines is set at 10. This results in a slight decrease of the final propellant temperature at the end of the daylight part of the third orbit from 734 to 680 K and a small decrease of the specific impulse from 162 to 156 s.

For hydrogen concepts the same holds. A comparison of Figure 5.28 and Figure 5.8 shows the changed temperature profile for Concept 3. When linear tubing with 20 feed lines is applied the final RAC temperature before eclipse is higher and the temperature increases every orbit. This indicates that there is less heat being transferred to the propellant tubing than when spiral tubing is used.
Indeed when the design switches to a linear tubing configuration the propellant temperature decreases from 908 K to 856 K with a specific impulse decrease from 181 to 175 s at the

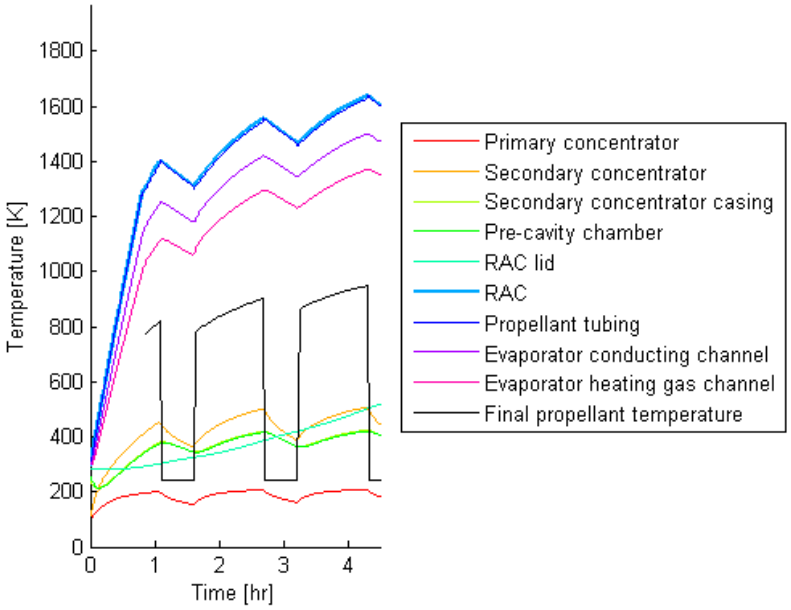

Figure 5.8: Temperature of thermal nodes for Concept 3 with a linear configuration with 20 propellant tubes

start of eclipse in the third orbit.
Only by setting the number of linear tubes to 30 and hence increasing the mass of the tubing can the same propellant temperature and specific impulse be achieved as with the spiral tubing.

Finally, a linear tubing configuration requires an additional flow divider which feeds the initial propellant flow from the propellant tank to the different tubes alongside the cavity. This increases the complexity of the system and increases the chance of flow disturbances which are both undesirable.
Therefore, one can conclude that overall a spiral tubing configuration is more advantageous.

5.2.5 Power subsystem

In the power subsystem a number of design parameters stay constant throughout the conceptual design phase.
First of all, the evaporating pressure of the ORC is set at 13.67 bar. In addition, the heating gas flow enters the evaporator at a pressure of 1 bar. This yields a thermal efficiency of 16.8% which falls in the range defined in Chapter 4. Beyond this pressure the thermal efficiency no longer increases substantially as can be seen in Figure 5.9. Second, the initial turbine inlet temperature is set at 533.15 K for the first orbit. The turbine inlet temperature will be increased with a scaled term based on the difference in mean heating gas temperature between the first and current orbit, as shown in Equation 5.7. The maximum increase in temperature of 90 K has been taken as the turbine inlet

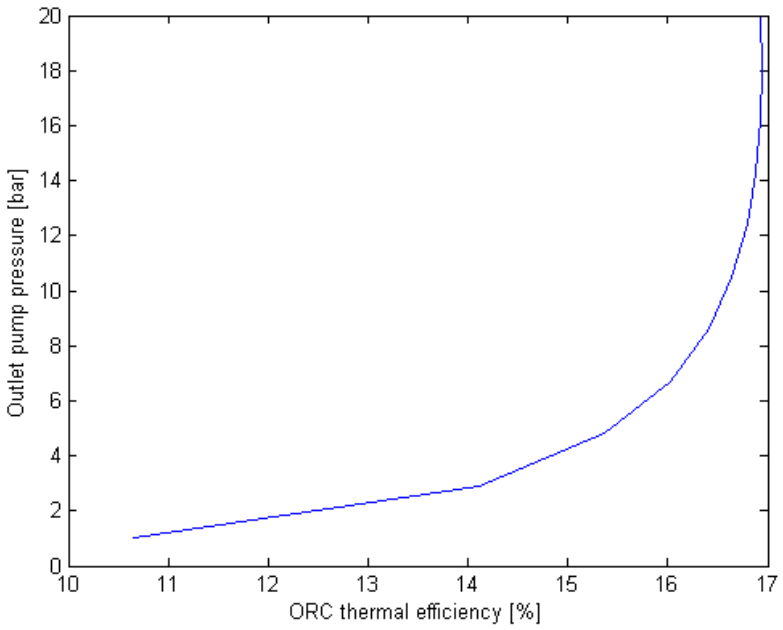

Figure 5.9: ORC thermal efficiency versus evaporating pressure for Concept 1

temperature in ORCs for toluene has an operating maximum of 350 ° Celsius (Lai et al. 2011).

$$T_{turbine-inlet} = 533.15 + 90 \cdot \frac{|T_{heating-gas}(n_{orbit}) - T_{heating-gas}(1)|}{T_{heating-gas}(1)} \tag{5.7}$$

The equation gives an indication of the increased turbine power output when the heating gas temperature is increased in the system. As the detailed design of and heat exchange process within the evaporator is unknown, the exact increased power output cannot be calculated at this point.

The *ORCHID-VPE* model assumes active fluid cooling in the condenser. Passive condenser cooling is however more advantageous in this hybrid system as has already been indicated in Chapter 4.
Passive condenser convection processes are used to transfer heat from the hot working fluid to the cooler working fluid tubing inner wall. Through conduction this heat is transferred to the tubing outer wall. Afterwards a conducting or radiating channel will conduct or radiate the heat away. The heat will be dissipated into space via some sort of radiator on the spacecraft's exterior. Alternatively, the heat is fed back into the spacecraft for thermal control. One assumes that the heat between the condenser and radiator is exchanged in the in-plane direction. This must result in a temperature of around 313 K for the working fluid behind the condenser.
To achieve a power output of at least 100 W a working fluid mass flow of 59 mL/min is necessary. This value stays constant throughout the evaluated time period.
For the conceptual design, only the required dissipated heat flux will be taken into account.

The detailed design of the condenser will be detailed in Chapter 6.

5.3 Concepts

This section will detail the different concepts. The design parameters can be found in Appendix B.
The thermal nodes and the concepts are first summarized, followed by the detailing of the concepts themselves.

5.3.1 Thermal nodes and summary of the concepts

Figure 5.10 illustrates the overall concept. One can distinguish the primary concentrator, secondary concentrator, RAC, propellant tank and tubing, the thruster and the ORC power subsystem components. Note that the concepts include a conductive interface between the RAC and evaporator heating gas channel; in the detailed design this interface might be replaced by a radiative interface.

The identifiers represent the following components or phenomena:

1: Primary concentrator
2: Secondary concentrator
3: Secondary concentrator casing
4: Pre-cavity chamber
5: Cavity lid
6: RAC
7: Propellant tubing
8: Evaporator heat conducting channel
9: Evaporator (heating gas channel)
10: Condenser (working fluid channel)
11: Condenser heat conducting/radiating channel
12: Turbine
13: Pump
14: Propellant tank
15: Propellant feed lines
16: Thruster chamber
17: Thruster nozzle
P: Power [W]
S: Solar flux [W]
T: Thrust [N]
Q: Heat flux [W]

A summary of the conceptual designs is given in Table 5.4.
In Section 5.3.2 to Section 5.3.7 these designs will be elaborated upon, including their performance.

Note that the power generation and dissipated heat from the ORC have been displayed based on their mean value over an entire orbit to limit the model's computational time.

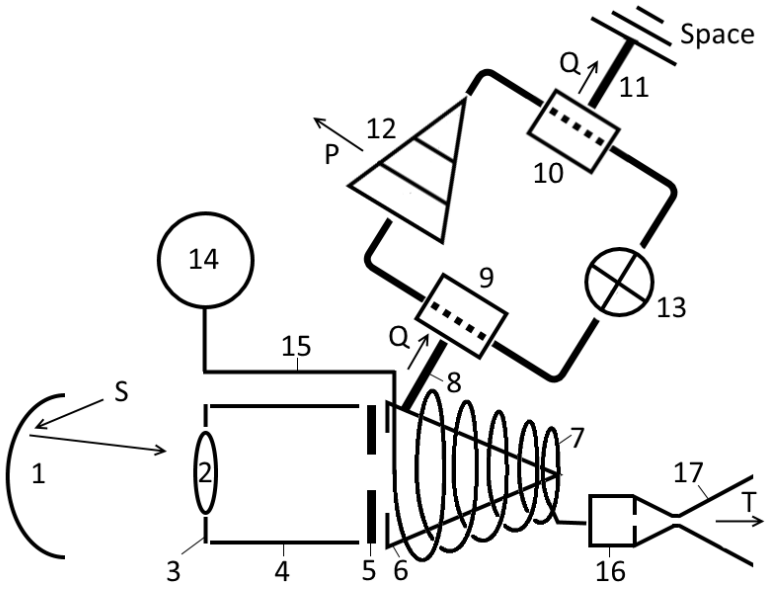

Figure 5.10: Concept schematic with conical RAC configuration

Table 5.4: Summary of the conceptual designs

Concept	RAC shape	Tubing configuration	Propellant
1	Conical	Spiral	Liquid ammonia
2	Conical	Spiral	Liquid hydrogen
3	Cylindrical	Spiral	Liquid ammonia
4	Cylindrical	Spiral	Liquid hydrogen
5	Spherical	Spiral	Liquid ammonia
6	Spherical	Spiral	Liquid hydrogen

5.3.2 Concept 1

The first concept utilizes a conical RAC. The propellant liquid ammonia is cryogenically stored at 243 K. The thickness of some nodes are given in Table 5.5 to give one a sense of the order of magnitude of the dimensions involved.

In Figure 5.11 the temperature profile is shown for all the thermal nodes in the propulsion subsystem. Figure 5.12 and 5.13 show a geometrical mesh of the front and rear of the subsystem excluding the primary concentrator and the thruster. The temperatures of the thermal nodes after one hour of flight time are incorporated. The coordinates in the figure are with respect to the center of the outer extremity of the primary concentrator. The black components represent the other side of the system whose temperatures exceed the temperature scale.

Table 5.5: Component thickness

Component	Thickness [mm]
Secondary concentrator casing	4.3
Pre-cavity chamber	10.8
RAC lid	14.0
RAC	10.8
Propellant tubing	0.625
Heating gas channel	1.2

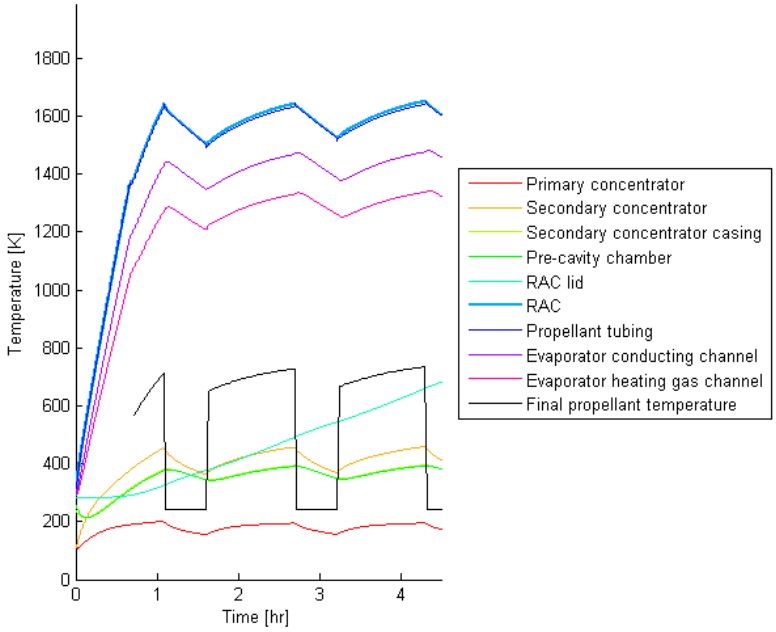

Figure 5.11: Temperature of thermal nodes for Concept 1

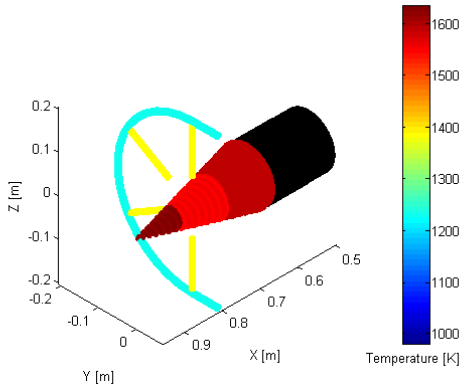

Figure 5.12: Thermal mesh rear view at 60 minutes after model initialisation for Concept 1

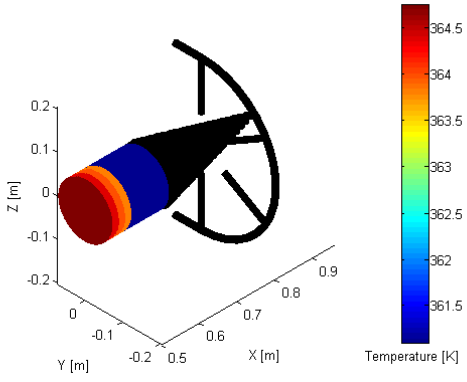

Figure 5.13: Thermal mesh front view at 60 minutes after model initialisation for Concept 1

The figures below represent the thrust, power, specific impulse for the concept. The total impulse is 53 kNs evaluated over the period required to propel all the propellant. The thrust plot shows constant values since the final propellant temperature stays fairly constant throughout each orbit, meaning that the chamber temperature stays fairly constant as well. The mass flow in the nozzle is 820 mg/s.

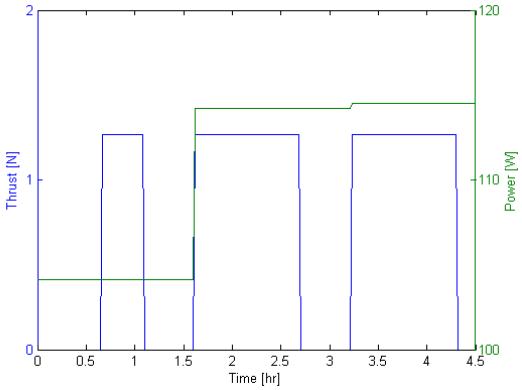

Figure 5.14: Thrust and power generation for Concept 1

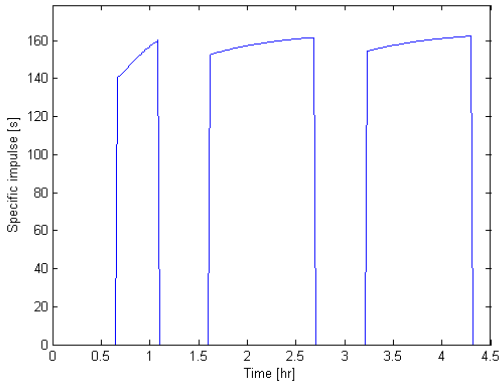

Figure 5.15: Specific impulse for Concept 1

One can see in Figure 5.14 that after the first orbit, where the system has to adjust to the increased temperatures, a more or less constant mean power generation of 115 W is achieved. The thrust stays constant at 1.267 N. In Figure 5.15 the initial maximum specific impulse of 160 s increases to 162 s in the third orbit.
The system efficiency is given in Figure 5.16. The maximum efficiency varies between 0.19 in eclipse to 0.42 in daylight.

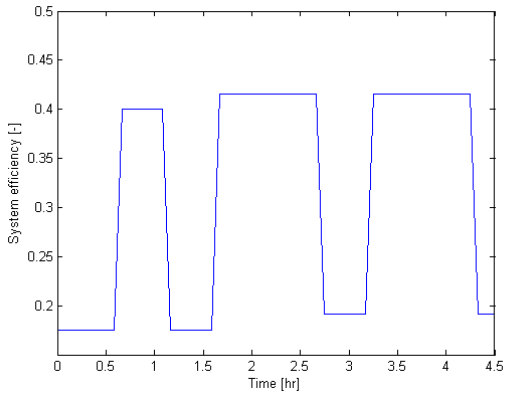

Figure 5.16: System efficiency for Concept 1

The mean dissipated heat out of the ORC condenser is plotted in Figure 5.17. The dissipated heat flux moves to a stable value of 566 W.

Finally, the required propellant storage volume, the dry system mass and the wet system mass fraction are respectively 0.06 m^3, 109 kg and 0.61.

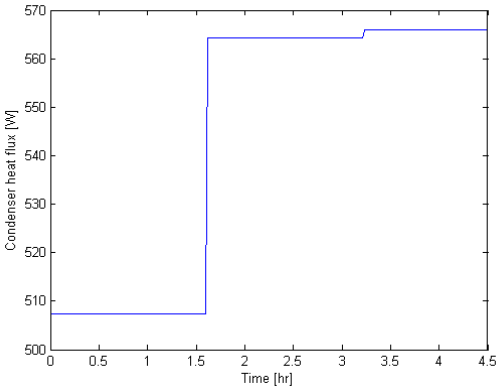

Figure 5.17: Mean dissipated heat out of ORC condenser for Concept 1

In the conceptual designs hydrogen and ammonia are used as propellants for their advantageous performance. Both propellants have to be cryogenically stored which puts more structural requirements on the spacecraft. Therefore, for a complete analysis water and hydrogen are applied to Concept 1 to see which system requirements can still be met with these non-cryogenic propellants.

5.3.2.1 Performance with water as non-cryogenic propellant

Water has a latent heat of vaporization of 2257 kJ/kg. Therefore the tubing convection area has to increase substantially for Concept 1 in order to overcome the vaporization of the liquid water and increase the temperature of the resulting water vapor to achieve sufficient thrust.
Water in a liquid state has a high thermal conductivity. As the temperature difference between the propellant and the propellant tubing will be in the order of several hundreds of Kelvin, a large heat flux between the tubing and water is expected. The propellant will therefore evaporate quickly in the spiral tubing. The assumption is therefore made that within the RAC-adjacent tubing water is in a gaseous state and that therefore the gaseous properties are used outside of the propellant tank.

First, the radius of the evaporator heating gas channel and its conducting channels are set at respectively 7.8 mm and 7.0 mm. The solar flux from the second orbit onwards is 58% of the full amount.
In Figure 5.18 the temperature profile is shown for the Concept 1 thermal nodes when water is selected as propellant. Note that the applicable water vapor properties apply for a vapor temperature of around 1000 K.

The power and thrust generated in the third orbit are respectively 114 W and 1.272 N. The specific impulse settles to a value of 148 s. As expected the specific impulse is lower than for ammonia. The system-specific impulse is 64 s which is slightly lower than for the original Concept 1.
The system efficiencies are higher than the efficiencies of the original Concept 1. In

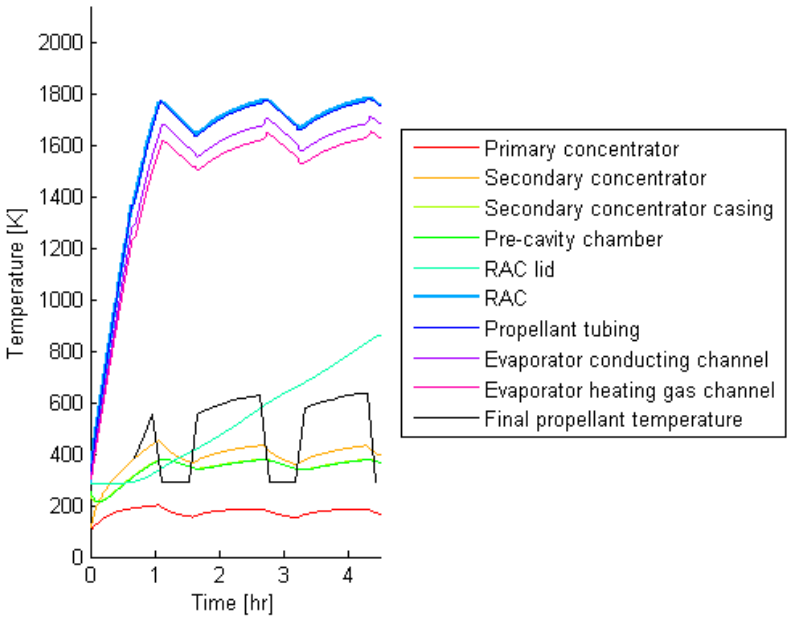

Figure 5.18: Thermal node temperatures for Concept 1 with water as propellant

daylight and eclipse they are respectively 0.49 and 0.23. The propellant tank volume is smaller than for ammonia at 0.045 m^3.
The wet system mass is 62% of the total mass, satisfying Requirement 2.

Unfortunately this performance has been achieved with a spiral tubing configuration with 80 turns which is very difficult to accurately manufacture. The large number of turns is caused by the fact that the system must overcome water's high latent heat and must therefore insert more heat into the propellant. A larger heat input requires a larger convective area and hence longer tubing. One should also note that water will freeze to a solid state below 273.15 K. If this were to occur propellant flow would be severely impeded, compromising thrust ability.
Therefore, there will have to be sufficient insulation and heating devices applied to the propellant tank to keep the water in the appropriate temperature range. The initial advantage of not having to apply cryogenic storage solutions is therefore replaced by other thermal control difficulties.
Water is therefore not an ideal propellant for this system.

5.3.2.2 Performance with nitrogen as non-cryogenic propellant

In this iteration nitrogen is uses as propellant. As a consequence the radius of the evaporator heating gas channel and its conducting conduits are set at respectively 11.7 mm and 5.8 mm. In the second and third orbit only 71% of the total solar flux is used. The power and thrust in the third orbit are 116 W and 1.213 N. The concept's maximum specific impulse settles to a value of 160 s. The system-specific impulse is 65 s which is

smaller than for water.
The efficiency in daylight and eclipse are respectively 0.39 and 0.19. The wet system mass fraction is 0.62. Figure 5.19 gives the associated temperature plots.

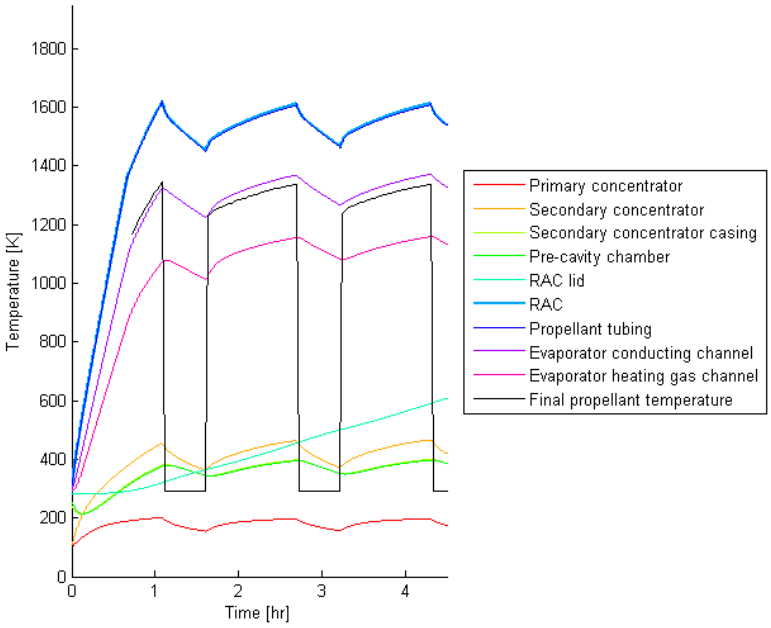

Figure 5.19: Thermal node temperatures for Concept 1 with nitrogen as propellant

Unfortunately nitrogen has a very low density. Therefore the required propellant storage volume is 35 m^3 at 1-bar storage pressure which is off-course too large for the spacecraft bus and violates Requirement 1. Using the ideal gas law yields a pressure of 35 MPa for an acceptable storage volume of 0.10 m^3. This pressure will increase the propellant tank thickness substantially and as a consequence increase the mass of the system. This makes this propellant option undesirable, even though it satisfies the other system requirements.

The next section continues the performance evaluation of the conceptual designs.

5.3.3 Concept 2

Just as Concept 1, Concept 2 utilizes a conical RAC. The propellant here is liquid hydrogen and it is cryogenically stored at 17 K. In Figure 5.21 the temperature profile for all the thermal nodes in the propulsion subsystem have been given.
Figure 5.22 and Figure 5.23 show again a geometrical mesh of the front and rear of the subsystem including temperatures. To limit the increase of the secondary concentrator temperature ten thermal straps have been attached to the concentrator circumference. The length of the thermal straps is 13 cm, their cross-section is 3.6x5 mm and their thermal conductivity is 400 W/mK as a copper-like material is assumed. Its sink temperature is

set at 293.15 K, the assumed local temperature within the spacecraft.

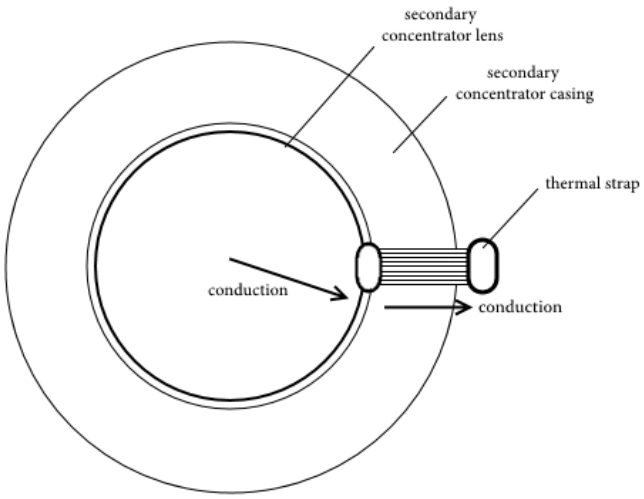

Figure 5.20: Illustration of thermal straps interfaced with the secondary concentrator

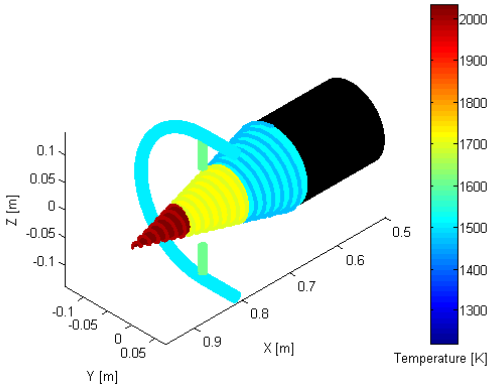

Figure 5.22: Thermal mesh rear view at 60 minutes after model initialisation for Concept 2

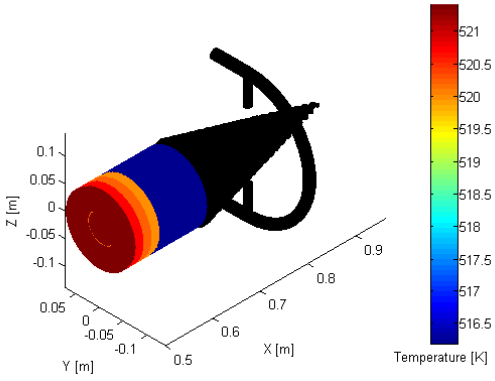

Figure 5.23: Thermal mesh front view at 60 minutes after model initialisation for Concept 2

Below the thrust, power and specific impulse performance for the concept have been shown. The total impulse becomes 50 kNs. The nozzle mass flow is substantially lower at 190 mg/s compared to the 820 mg/s for Concept 1.

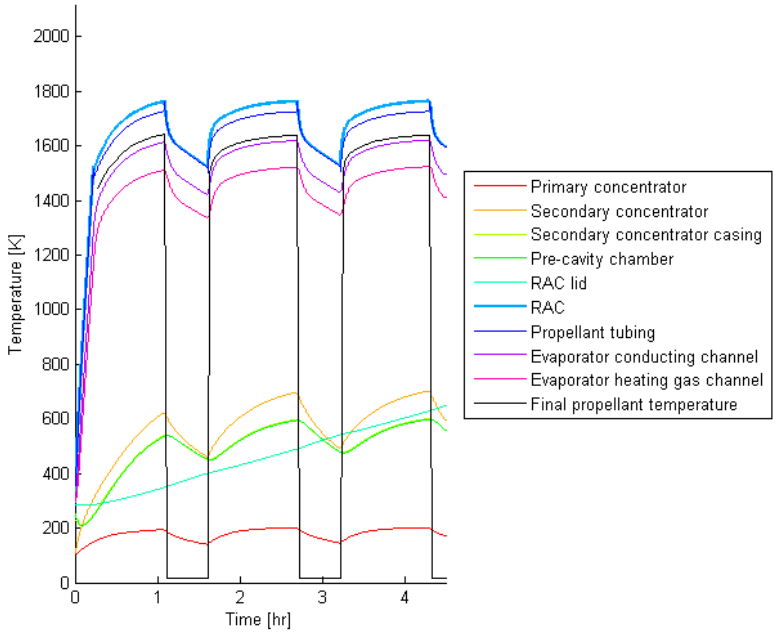

Figure 5.21: Temperature of thermal nodes for Concept 2

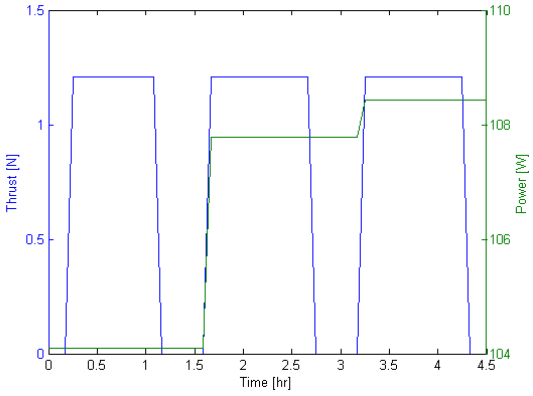

Figure 5.24: Thrust and power generation for Concept 2

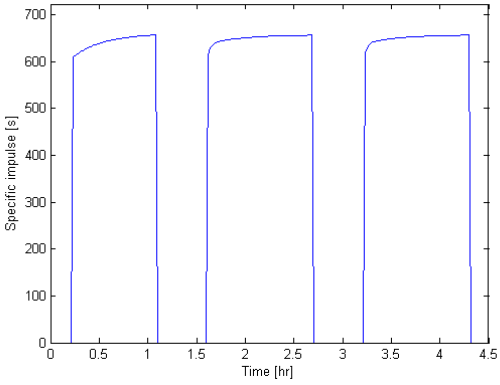

Figure 5.25: Specific impulse for Concept 2

One can see in Figure 5.24 that after the first orbit, in which the system has to adjust to the increased temperatures, a more or less constant mean power generation of 108 W is achieved. The thrust stays constant at 1.209 N. The specific impulse is shown in Figure 5.25. The initial maximum specific impulse of 657 s stays constant over the evaluated period.

The system efficiency is given in Figure 5.26. The efficiency varies between 0.04 in eclipse to 0.09 in daylight which is substantially lower than for Concept 1.

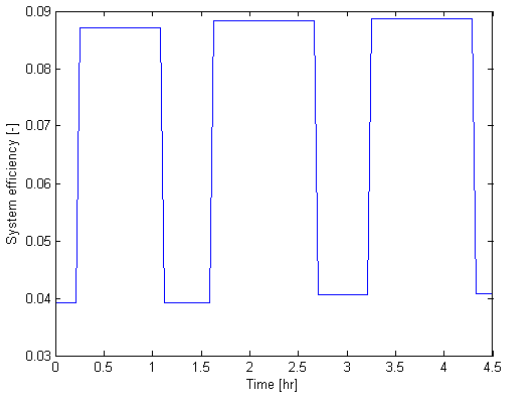

Figure 5.26: System efficiency for Concept 2

The mean dissipated heat out of the ORC condenser is plotted in Figure 5.27. The dissipated heat flux starts at 507 W and increases to a value of 531 W in the third orbit.

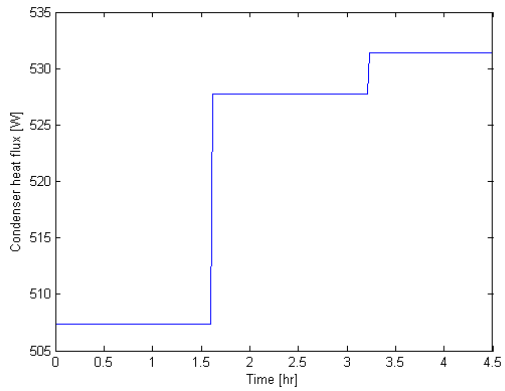

Figure 5.27: Mean dissipated heat out of ORC condenser for Concept 2

Concluding this concept, the required propellant storage volume, the system mass and the system mass fraction are respectively 0.13 m^3, 101 kg and 0.53.

5.3.4 Concept 3

Concept 3 has a cylindrical RAC. The used propellant is liquid ammonia. In Figure 5.28 the temperature profile for all the thermal nodes in the propulsion subsystem have been given. The first orbit has a maximum RAC temperature of 1365 K which stays relatively constant over the subsequent orbits.
Figure 5.29 and 5.30 show the geometrical mesh of the subsystem excluding the primary concentrator and the thruster and with the thermal node temperatures incorporated.

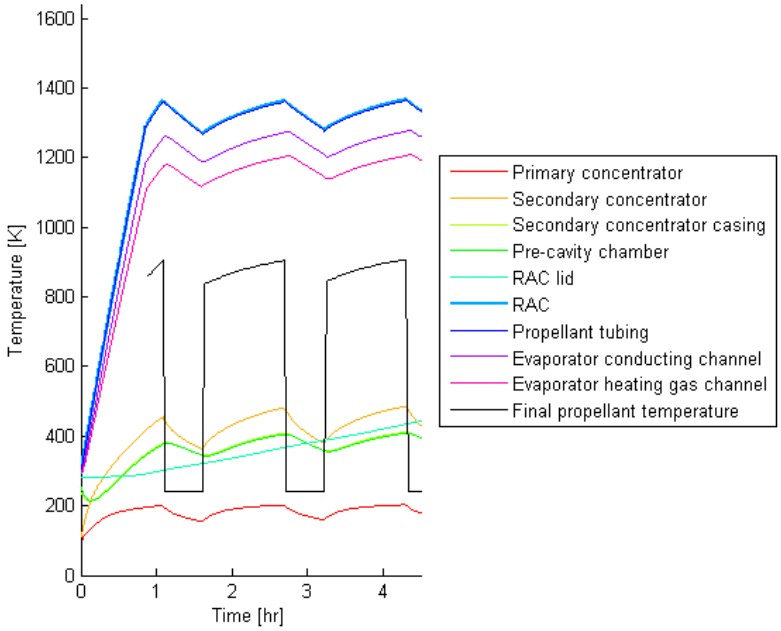

Figure 5.28: Temperature of thermal nodes for Concept 3

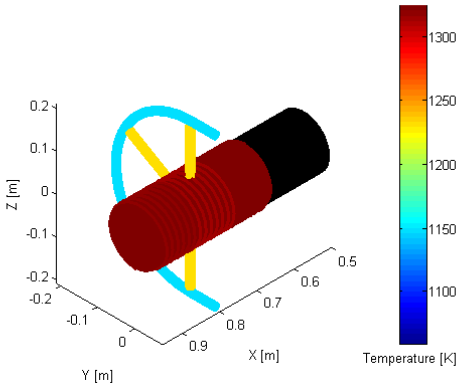

Figure 5.29: Thermal mesh rear view at 60 minutes after model initialisation for Concept 3

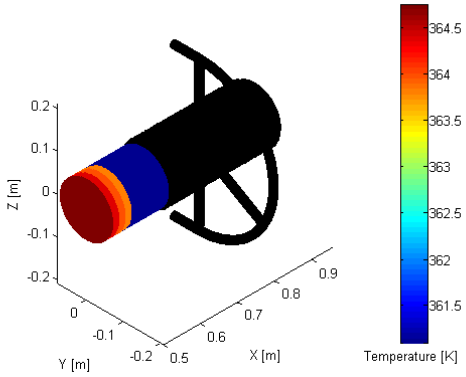

Figure 5.30: Thermal mesh front view at 60 minutes after model initialisation for Concept 3

The figures below show the performance for this design. Calculations yield a maximum total impulse of 52 kNs. The propellant mass flow is calculated to be 730 mg/s.

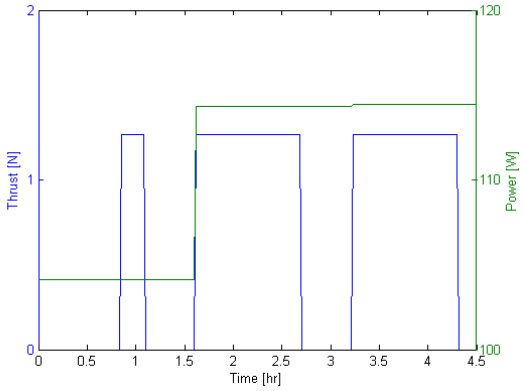

Figure 5.31: Thrust and power generation for Concept 3

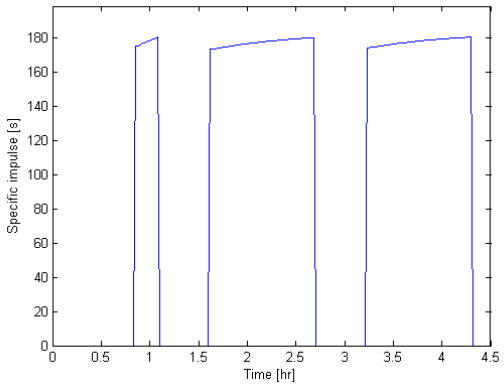

Figure 5.32: Specific impulse for Concept 3

One can see in Figure 5.31 that after the first orbit a more or less constant mean power generation of 114 W is achieved. The thrust stays constant at 1.267 N. The specific impulse plot in Figure 5.32 shows a maximum specific impulse of 181 s over the evaluated period.

The system efficiency is given in Figure 5.33. The efficiency in eclipse is 0.16. The daylight efficiency settles to a value of 0.36 in the third orbit. The mean dissipated heat out of

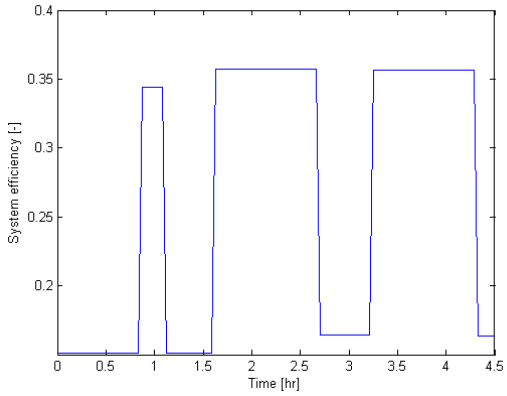

Figure 5.33: System efficiency for Concept 3

the ORC condenser is plotted in Figure 5.34. The dissipated heat flux starts at 507 W and increases to a constant value of 566 W in the third orbit.

Finally, the required propellant storage volume, the system mass and the system mass fraction are respectively 0.05 m^3, 114 kg and 0.62.

5.3.5 Concept 4

Concept 4 has a cylindrical RAC as well. The used propellant is liquid hydrogen. In Figure 5.35 the temperature profile for all the thermal nodes in the propulsion subsystem

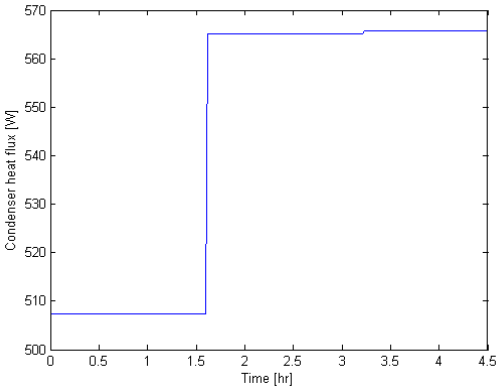

Figure 5.34: Mean dissipated heat out of ORC condenser for Concept 3

has been shown.
Figure 5.36 and 5.37 show the geometrical mesh of the subsystem, excluding the primary concentrator and the thruster and including thermal node temperatures.
As in Concept 2 ten thermal straps have been added to decrease the secondary concentrator temperature so that it does not violate its maximum temperature.

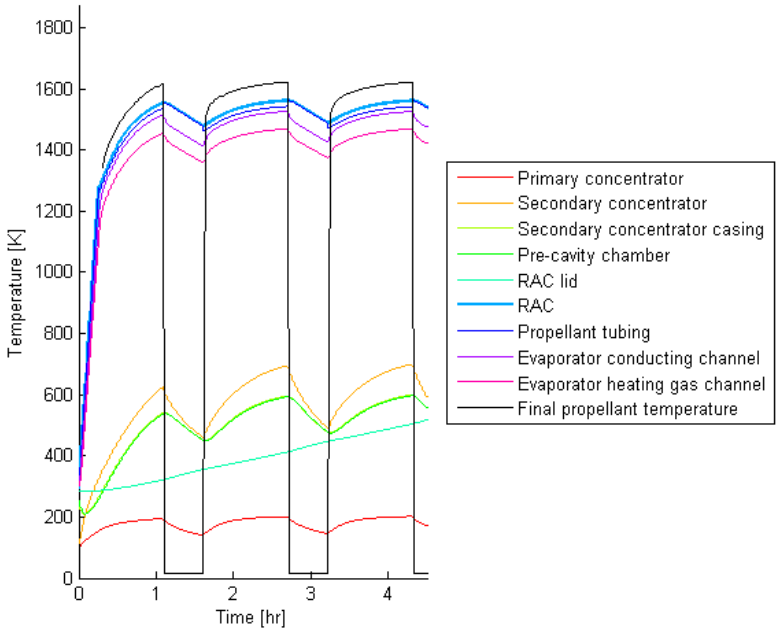

Figure 5.35: Temperature of thermal nodes for Concept 4

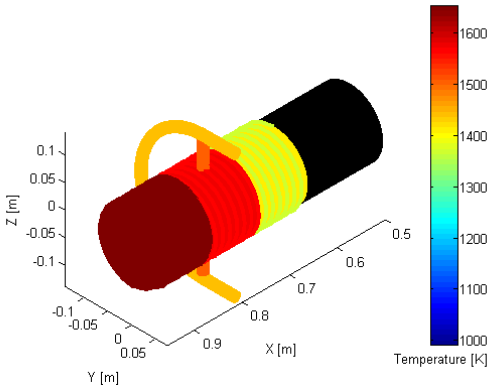

Figure 5.36: Thermal mesh rear view at 60 minutes after model initialisation for Concept 4

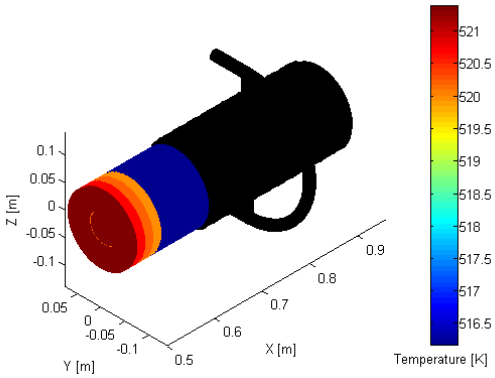

Figure 5.37: Thermal mesh front view at 60 minutes after model initialisation for Concept 4

The figures below represent performances for the concept. The total impulse is 50 kNs. The accompanying propellant flow rate during thrust is 190 mg/s.

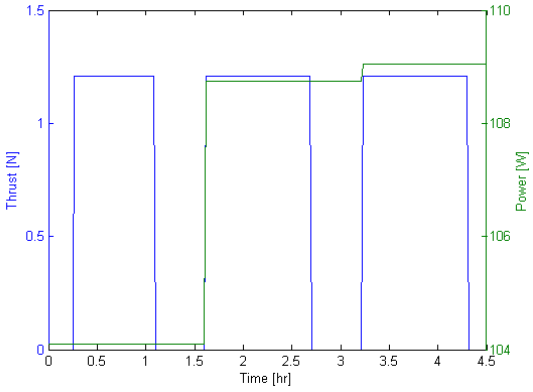

Figure 5.38: Thrust and power generation for Concept 4

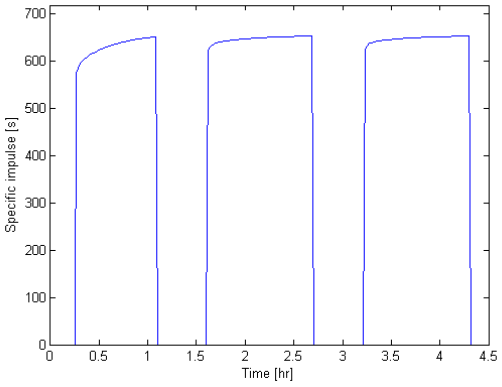

Figure 5.39: Specific impulse for Concept 4

In Figure 5.38 a power output of 109 W is generated after the first orbit. The thrust stays constant at 1.209 N, just as in Concept 2. In Figure 5.39 the maximum specific impulse in the first orbit of 651 s increases to a specific impulse of 652 s in the third orbit.

The system efficiency is shown in Figure 5.40. The efficiency in eclipse is only 0.04. The maximum daylight efficiency stays constant at 0.09 during the 4.5 hours period. These values are the same for Concept 2 and less than for Concept 3.

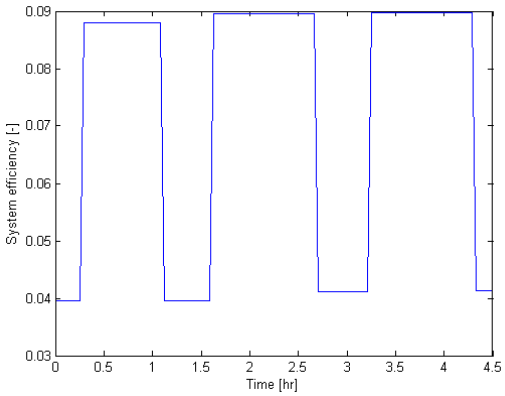

Figure 5.40: System efficiency and effective exhaust velocity for Concept 4

The mean dissipated heat out of the ORC condenser is plotted in Figure 5.41. The dissipated heat flux increases from 507 W to a constant 535 W.

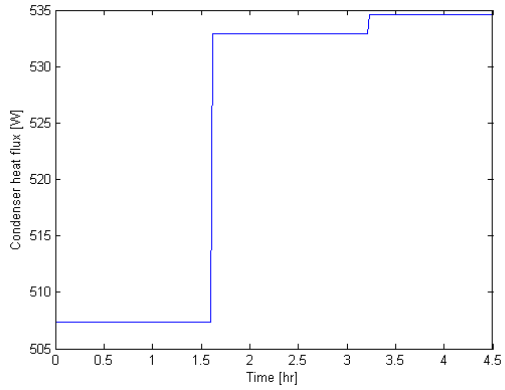

Figure 5.41: Mean dissipated heat out of ORC condenser for Concept 4

Concluding, the required propellant storage volume, the system mass and the system mass fraction are respectively 0.14 m^3, 106 kg and 0.55.

5.3.6 Concept 5

Concept 5 has a spherical RAC. The propellant is liquid ammonia. In Figure 5.42 the temperature profile for all the thermal nodes is given.
Figure 5.43 and 5.44 show the geometrical mesh for Concept 5, including thermal node temperatures.

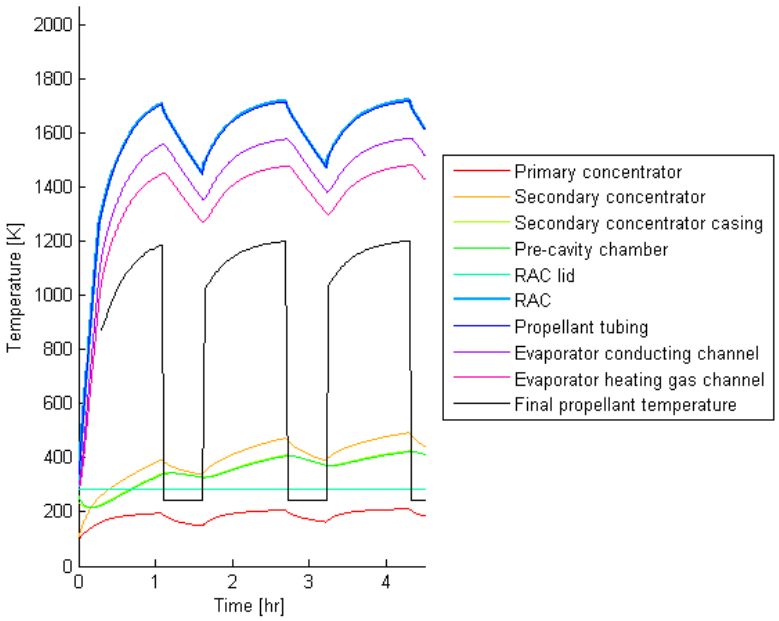

Figure 5.42: Temperature of thermal nodes for Concept 5

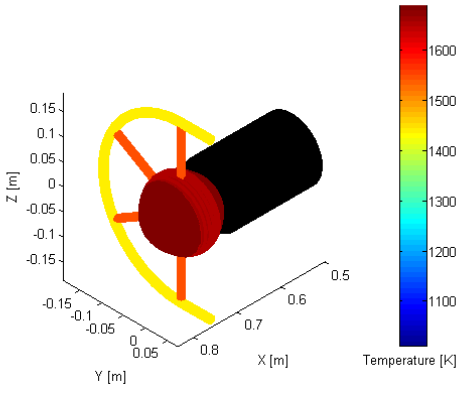

Figure 5.43: Thermal mesh rear view at 60 minutes after model initialisation for Concept 5

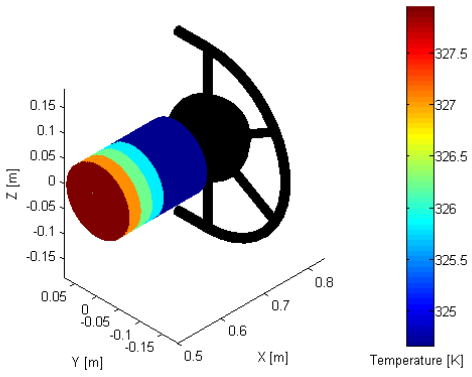

Figure 5.44: Thermal mesh front view at 60 minutes after model initialisation for Concept 5

The figures below represent performances for the concept. Calculations yield a total impulse of 52 kNs. Here, the propellant mass flow decreases even further to 630 mg/s compared with 820 mg/s for Concept 1.

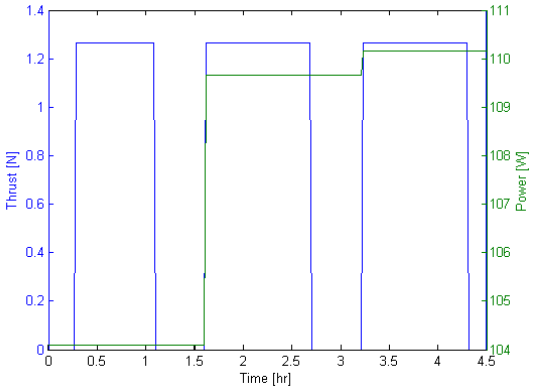

Figure 5.45: Thrust and power generation for Concept 5

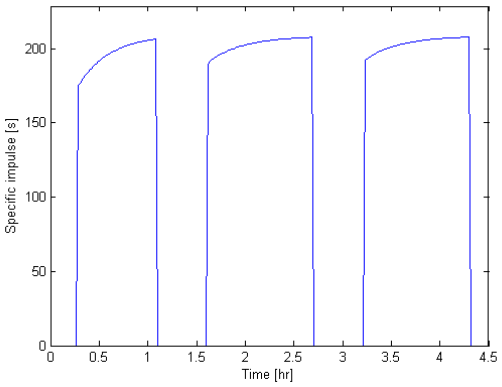

Figure 5.46: Specific impulse for Concept 5

A power output of 104 W is generated in the first orbit. In the orbits thereafter the turbine generates around 110 W. As expected, the thrust stays constant at 1.267 N. The specific impulse plot shows a constant maximum specific impulse of 208 s just before every eclipse.

The system efficiency is given in Figure 5.47. The efficiency in eclipse is only 0.13. The maximum daylight efficiency stays constant after each orbit at 0.29.

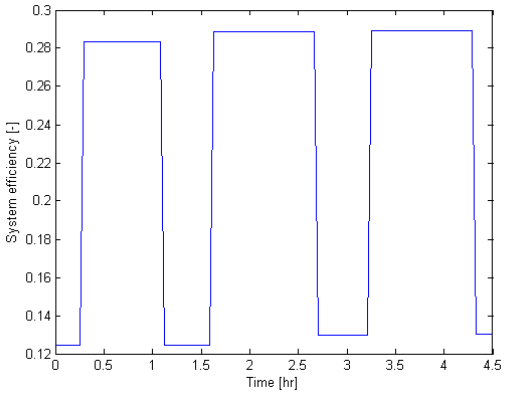

Figure 5.47: System efficiency for Concept 5

The mean dissipated heat out of the ORC condenser is plotted in Figure 5.48. The dissipated heat flux increases from 507 W in the first orbit to 541 W in the third orbit respectively.

Finally, the required propellant storage volume, the system mass and the system mass fraction are respectively 0.05 m^3, 99 kg and 0.55.

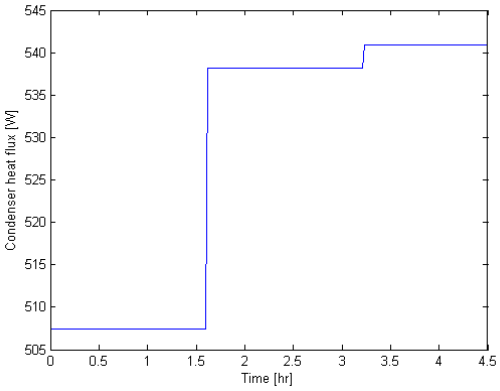

Figure 5.48: Mean dissipated heat out of ORC condenser for Concept 5

5.3.7 Concept 6

Concept 6 also has a spherical RAC. The propellant is liquid hydrogen. In Figure 5.49 the temperature profile is given for all the thermal nodes in the propulsion subsystem. A maximum propellant temperature of 1661 K is achieved.
Figure 5.50 and 5.51 show the geometrical mesh of the subsystem, including thermal node temperatures.
As in the other hydrogen concepts ten thermal straps have been added to decrease the secondary concentrator temperature. Since this has limited effect, more thermal straps will have to be added in the detailed design if this concept is selected.

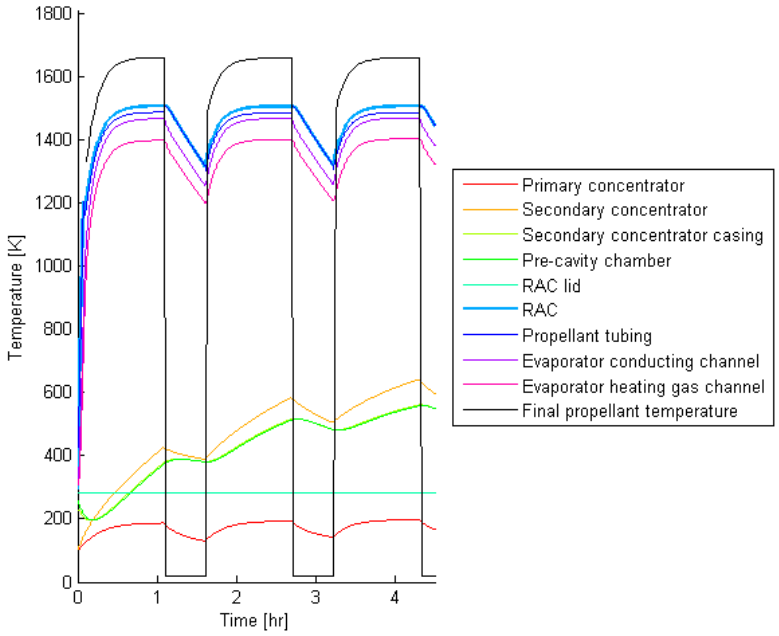

Figure 5.49: Temperature of thermal nodes for Concept 6

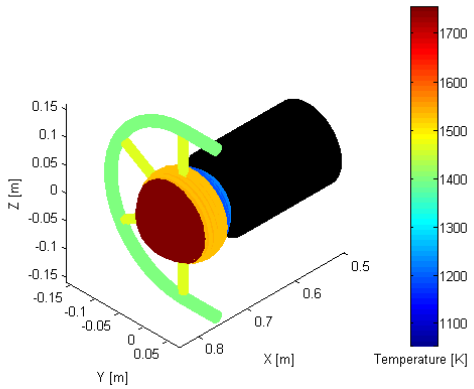

Figure 5.50: Thermal mesh rear view at 60 minutes after model initialisation for Concept 6

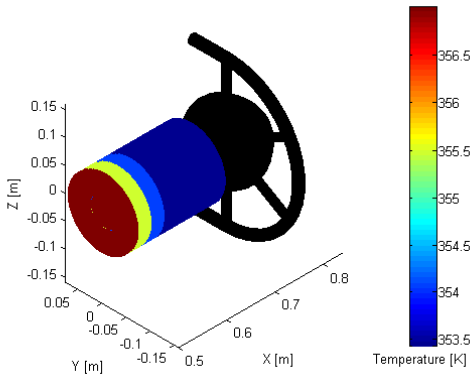

Figure 5.51: Thermal mesh front view at 60 minutes after model initialisation for Concept 6

The figures below represent performances for the concept. The total impulse for this concept is 50 kNs. During thrust the propellant mass flow in the nozzle is 190 mg/s.

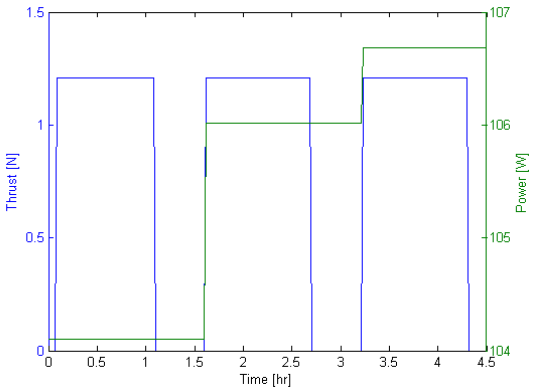

Figure 5.52: Thrust and power generation for Concept 6

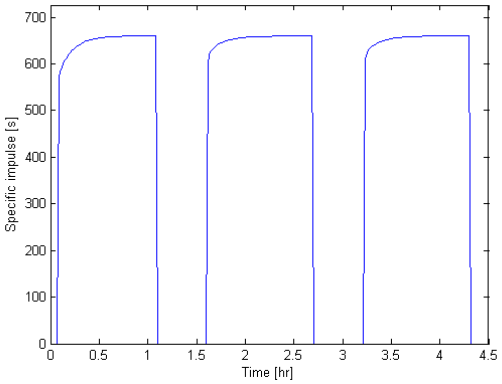

Figure 5.53: Specific impulse for Concept 6

In Figure 5.52 a power output of 107 W is generated after the 4.5-hour period. The thrust stays constant during this time at 1.209 N as one has seen with the other hydrogen concepts. The specific impulse plot in Figure 5.53 shows a stable maximum specific impulse of 660 s before eclipse.

The system efficiency is given in Figure 5.54. The eclipse efficiency is 0.04 and the daylight efficiency is 0.09 which is the same as for Concept 2 and Concept 4.

The mean dissipated heat out of the ORC condenser is plotted in Figure 5.55. The dissipated heat flux starts at 507 W. It then increases to 522 W in the third orbit.

Finally, the required propellant storage volume, the system mass and the system mass fraction are respectively 0.13 m^3, 94 kg and 0.49.

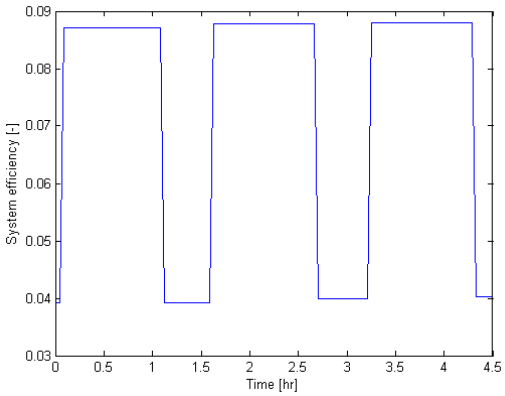

Figure 5.54: System efficiency for Concept 6

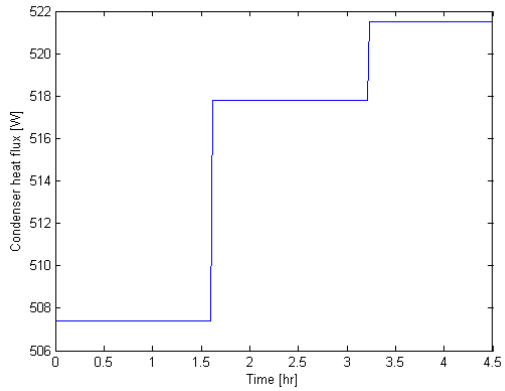

Figure 5.55: Mean dissipated heat out of ORC condenser for Concept 6

5.4 Mass and size comparison of concepts

Although the mass and size between the concepts vary relatively little, the two properties need to be taken into account at this phase in the design process. First the mass will be discussed; afterwards a section will detail the size of each concept.

5.4.1 Mass of the concepts

The mass of the concepts is currently evaluated based on three indicators:

1. Total mass *The total mass of the spacecraft, including propellant*
2. Wet system mass *The mass of the hybrid propulsion and power system, including propellant*
3. Wet system mass fraction *Mass fraction of the hybrid propulsion and power system, including the propellant, with respect to the total spacecraft mass*

Table 5.6 details the different mass indicators for each concept.
All concepts satisfy Requirement 2. Given that the current mass estimates are mostly derived from the propellant mass, the concepts with liquid hydrogen propellant are preferable in terms of absolute mass over the concepts with liquid ammonia. The liquid ammonia concepts also have a higher wet mass fraction.
In terms of absolute total mass Concept 2, 4 and Concept 6 are the lightest. The lightest wet system mass is achieved with Concept 5 and Concept 6. The smallest mass fractions are achieved with Concept 2 and Concept 6.

Table 5.6: Mass comparison of the concepts

Concept	Total Mass [kg]	Propellant mass [kg]	Dry system mass [kg]	Wet system mass fraction[-]
1	234	34	109	0.61
2	208	8	101	0.53
3	230	30	114	0.62
4	208	8	106	0.55
5	226	26	99	0.55
6	208	8	94	0.49

5.4.2 Size of the concepts

First, size can be evaluated by determining the footprint of the system in the spacecraft. The footprint is defined as the top-view area of an imaginary box around the system beyond which the system does not interfere with other spacecraft subsystems. Figure 5.56 illustrates this.

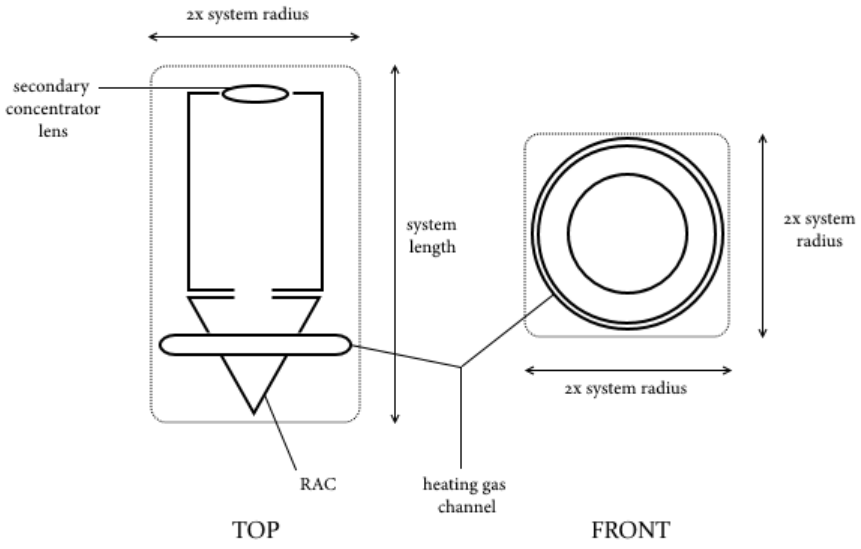

Figure 5.56: Illustration of the system's footprint

By multiplying the length and two times the system radius with each other, a very rough estimate of the footprint of each system can be obtained.
The system radius is the maximum extent of the heating gas channel because it defines the maximum extent where other parts of the spacecraft can interfere geometrically.
The length of the system is the length from the front of the secondary concentrator lens to the rear of the RAC. Table 5.7 gives the results.

Table 5.7: Estimate of the footprint of the concepts

Concept	Footprint [cm^2]
1	1888
2	1293
3	1911
4	1282
5	1219
6	1049

If one looks at this size aspect of each concept, Concept 1 fares the worst. Concept 2,4 and 5 have almost equal footprints. The concepts with the spherical RACs have the smallest footprints due to the short spherical cavity. Clearly the long shapes in the first four concepts make for a larger system.
The differences in footprint between the conical and cylindrical concepts are larger compared to the differences between the spherical concepts as the decrease in size of the evaporator interface is less pronounced for the latter category when moving from ammonia to hydrogen. A possible explanation could be that the spherical RAC geometry allows for a more evenly distributed heat within the cavity. The resulting higher RAC temperature at the front of the cavity decreases the influence of propellant choice and convective heat transfer on the RAC temperature in that region. When propellants are changed, this requires a smaller design change in the evaporator heat transfer interface in order to guarantee the same heat transfer to the power subsystem. Thus, the change in footprint would be smaller than when other RAC configurations are applied.

Second, the propellant tank volume will dominate the total volume of the system and therefore deserves a closer look.
Concept 2, 4 and 6 use liquid hydrogen and as a consequence feature the largest propellant tanks, as seen in Table 5.8. Concept 5 has the smallest propellant tank, whereas Concept 4 has the largest.

The primary concentrator for all concepts which use hydrogen are around a factor of 1.75 as large as the concentrators for the concepts which use ammonia.
This has to do with the fact that the liquid hydrogen propellant flow has a larger thermal conductivity. This causes a larger convective heat flux from the propellant tubing inner wall to the propellant. In turn, the cavity will decrease in temperature faster which will limit the temperature of the evaporator heating fluid, thus moving the ORC heat cycle out of equilibrium.
Only by increasing the solar radiation flux into the system can the heat cycle equilibrium be restored, unless large amounts of heat can be diverted from elsewhere in the spacecraft.

Table 5.8: Size comparison of the concepts

#	System length in X [cm]	Width in Y or Z [cm]	Primary concentrator diameter [m]	Diameter of turbine [mm]	Propellant tank volume [m^3]
1	45.91	20.56	0.90	19	0.06
2	46.19	14.00	1.57	19	0.13
3	45.51	21.00	0.90	19	0.05
4	45.79	14.00	1.57	19	0.14
5	32.51	18.75	0.90	19	0.05
6	32.79	16.00	1.57	19	0.13

5.5 Performance comparison of concepts

Not only the mass and size of the system are important. One also needs to look at whether the concepts exceed Requirement 3 to 6 and to what degree they exceed them. This will also give an idea about scalability of each design.
In Table 5.9 the performance of each concept in terms of the three parameters is stated. The condenser dissipated flux in Watts has been included as has been the daylight system efficiency.
The system-specific impulse is shown in Table 5.10.

Table 5.9: Performance comparison of the concepts

#	Thrust [N]	Specific impulse [s]	Power [W]	Condenser dissipated flux [W]	Efficiency [%]
1	1.267	162	115	566	42
2	1.209	657	108	531	9
3	1.267	181	114	566	36
4	1.209	652	109	535	9
5	1.267	208	110	541	29
6	1.209	660	107	522	9

As can be seen in the table all concepts satisfy Requirement 3 to 5. Concept 5 and 6 have the highest specific impulse in their respective class of concepts with the same propellant. The mean power output after three orbits is slightly higher for the ammonia concepts. The liquid hydrogen concepts generate more specific impulse and slightly less thrust. This is as expected as hydrogen has a higher specific heats ratio and thermal conductivity than ammonia.
The system efficiency is the highest for Concept 1 and decreases for the other ammonia concepts. The efficiencies for all the hydrogen concepts are the lowest at 9%. One can therefore conclude that the hydrogen concepts convert the inserted solar energy the least efficiently to power and thrust.

In Table 5.10 the total impulse and system-specific impulse are given for each concept to compare the concepts from a system-perspective. The total impulse also takes into

account the total thrust time. One sees that the hydrogen concepts generate a smaller total impulse but produce a larger system-specific impulse. This means that these concepts generate more impulse per kg of propulsion subsystem. A larger value is therefore advantageous for the total mass budget of the spacecraft. Concept 6 in this regard produces the largest system-specific impulse.

Table 5.10: System-specific impulse and related variables for the concepts

#	**Wet propulsion system mass [kg]**	**Total impulse [kN·s]**	**System-specific impulse [s]**
1	81	53	66
2	54	50	94
3	83	52	65
4	59	50	87
5	66	52	80
6	47	50	108

In terms of the recovery of cavity and propellant temperatures after eclipse all concepts have been tailored to a fast temperature recovery with close-to-equal maximum propellant temperatures just before each orbit's eclipse.
The concepts with thermal straps limit the increase of the secondary concentrator and pre-cavity chamber somewhat. Concepts without thermal control devices see an increase of these components over time. As Concept 5 and Concept 6 have no heat transfer between the lid and the RAC, the lid's temperature stays constant. In the other concepts the cavity lid increases almost linearly over time. Further thermal control must hence be exercised in the detailed design.

Not only thermal control of the propulsion subsystem must be performed. Thermal control of other parts of the spacecraft is also necessary. Batteries for example only work in temperatures from about -5 to +15 degrees Celsius. Thermal control of other subsystems can include diverting the dissipated heat from the passive condenser in the power subsystem to other regions of the spacecraft interior. Looking at Table 5.9, Concept 1 and Concept 3 can dissipate the most heat in this regard.

5.6 Scalability

This section deals with the scalability of the system. Since power, thrust and specific impulse are the KPPs in terms of system performance, scalability will be discussed in terms of these parameters.
Concept 1 will be used as a reference to scale the system. The focus in each subsection is solely on whether the increase of the specific performance parameter is feasible; other performance parameters or component constraints have not been looked into.
Table 5.11 and 5.12 give a summary of the results, excluding in terms of the specific impulse.

5.6.1 Power

First, the required power output of the turbine will be increased from 100 W to 200 W. Second, it will be further increased from 200 W to 400 W to see whether a scaling relationship exists.
When the power is increased to 200 W, the primary concentrator diameter needs to increase from 0.9 m to 1.0 m. The cavity radius stays constant at 7 cm. The heating gas channel radius increases from 7.8 mm to 14 mm. The evaporator conducting channels' radius is increased from 7 mm to 11.7 mm.
The power subsystem's working fluid mass flow needs to increase from 59 mL/min to 118 mL/min. The turbine diameter increases from 19 mm to 27 mm. The dissipated power increases from 566 W to 1083 W.

Second, the power is increased further to 400 W. The cavity radius stays constant at 7 cm. The primary concentrator diameter increases from 1.0 m to 1.1 m. The evaporator heating gas channel's radius is increased from 14 mm to 23.3 mm and the evaporator conducting channels' radius is increased from 11.7 mm to 14.0 mm.
The micro-turbine diameter becomes 38 mm. This is twice the diameter for a power output 1/4 the current one. Furthermore the working fluid mass flow increases further to 236 mL/min. Calculations yield a required dissipated heat flux out of the working fluid of 2104 W.

The 1083 W and 2104 W are very large fluxes for a radiator mounted to a 1x1x1 m bus to cope with. Therefore, radiator fins or deployable radiators will be necessary to dissipate the heat. This will add to the satellite mass. Thus, scalability is limited for a small satellite beyond power levels of around 100 W.

Increasing the primary concentrator diameter, increasing the size of the evaporator conducting channel and enlarging the condenser allows theoretically for an even larger power output. One should however note that a larger system will decrease the available spacecraft volume for instruments and increase the complexity of deploying a larger primary concentrator. Furthermore, the external radiators will increase in number and/or size.

Table 5.11: Scalability results in terms of power

Power [W]	**Dissipation heat flux [W]**	**Primary concentrator diameter [m]**	**Turbine diameter [mm]**	**Working fluid mass flow [mL/min]**
100	566	0.9	19	59
200	1083	1.0	27	118
400	2104	1.1	38	236

5.6.2 Thrust

In this subsection one will aim to increase the thrust from 1.26 N to 2.52 N. In the second iteration the thrust will be increased to 5.04 N. This means that the thruster chamber

pressure needs to be increased from 1 bar to 2 bar and subsequently from 2 bar to 4 bar.

After the first iteration the primary concentrator diameter stays constant at 0.9 m. As a result the specific impulse decreases from 162 s to 125 s. This is still within requirements so no other design variables need to change.

When the pressure is increased to 4 bar, the primary concentrator diameter is increased from 0.9 to 1.0 m. The evaporator conducting channels' radius decreases from 7 mm to 4.4 mm. The evaporator heating gas channel decreases in radius from 7.8 mm to 7 mm. As a result the specific impulse drops further to 112 s. This again still satisfies the requirements. One can therefore state that scalability up to 5 N is possible.

Table 5.12: Scalability results in terms of thrust

Thrust [N]	**Thruster chamber pressure [bar]**	**Primary concentrator diameter [m]**	**Specific impulse [s]**
1.26	1	0.9	162
2.52	2	0.9	125
5.04	4	1.0	112

5.6.3 Specific impulse

The specific impulse can only be increased by increasing the propellant temperature. This can be done by:

- changing to a propellant with a higher thermal conductivity;
- increasing the propellant flow initialization cavity temperature;
- increasing the external heat flux into the RAC;
- and reducing the mass flow of the propellant in the tubing.

The first two options are easiest to implement and do not influence the size of the system. The external flux is increased by increasing the primary concentrator size.
The last option necessitates decreasing the thruster chamber pressure. This will however decrease the thrust severely and is therefore undesirable. A combination of these measures is also possible.

An example is put forward.
First, the primary concentrator diameter is increased from 0.9 to 1.0 m.
Second, the evaporator heating gas channel becomes 11.6 mm in outer diameter and the heat conducting channel becomes 14 mm in diameter.
Third, the initialization temperature is increased from 1300 K to 1600 K.
As a result the specific impulse increases from 162 s to 183 s. Increasing the specific

impulse further necessitates a more elaborate redesign for Concept 1. In particular the interface between the RAC and evaporator will have to be altered; in the current design the high initialization temperature will lead to a very high evaporator heating gas temperature.
This is illustrated for Concept 2. The 'normal' heating gas temperature for the concept is around 980 K. Increasing the primary concentrator diameter to 1.8 m and increasing the initialization temperature to 2000 K increases the heating gas temperature to 1280 K. This in turn violates thresholds within the ORC.
Scalability in terms of specific impulse is therefore limited.

5.7 Thermal stresses

Due to the large temperature increases of some of the thermal nodes and temperature differences between adjacent nodes, significant thermal stresses could be generated within the system. Therefore one needs to know whether the system can cope with these stresses.

Assuming the nodes' material is linearly elastic and isotropic, the thermal stress in normal direction can be computed by equation 5.8 (Barron & Barron 2011).

$$\sigma_{normal} = \frac{\alpha_{te} \cdot \Delta T \cdot E}{1 - 2\nu} \tag{5.8}$$

Here E is the Young's modulus and ΔT is the temperature difference between the initial temperature (assumed room temperature) and the temperature at a particular time instance. The variable α_{te} is the material's thermal expansion coefficient and ν is the material's Poisson's ratio.

In Table 5.13 the maximum thermal stresses for Node 3 to Node 9 are displayed. The concepts have been indicated by their RAC configuration and propellant for ease of use.

Table 5.13: Maximum thermal stresses for each concept's thermal nodes in GPa

Node	Con.[1]- Ammonia	Con. - Hydrogen	Cyl.[2]- Ammonia	Cyl. - Hydrogen	Spher.[3]- Ammonia	Spher. - Hydrogen
3	8	17	9	17	10	15
4	5	14	6	14	7	12
5	5E-1	5E-1	2E-1	3E-1	6E-4	1E-3
6	59	74	47	59	63	62
7	59	74	47	59	63	62
8	51	58	42	53	55	50
9	45	54	39	50	51	47

[1] Con. = Conical RAC
[2] Cyl. = Cylindrical RAC
[3] Spher. = Spherical RAC

The largest thermal stresses in all concept occur in Node 6 and Node 7. This is to be expected as these nodes reach the largest temperatures in the system. The yield stress for molybdenum is 329 GPa. The largest stresses in the two nodes do not exceed this

value and therefore the thermal stresses do not endanger the structural integrity of the molybdenum parts.
Node 5 is made of a core material of molybdenum and is encapsulated in MLI material. This material's yield stress is 2 GPa. The thermal stress in the node is lower than that, so there are no structural problems for the lid either.

When Concept 1's molybdenum components are replaced with tungsten the thermal stress decreases by 8.5% in Node 6 and Node 7. In Node 8 and Node 9 the thermal stress decreases by respectively 7.8% and 4.4%. The other nodes see virtually no change.

The thermal expansion decreases as well, for example by as much as 18% for the propellant tubing's axial expansion. Therefore, one can conclude that tungsten can better cope with large temperatures than molybdenum. Equation 5.9 is used to calculate the expansion values (Barron & Barron 2011).

$$\Delta L = \alpha_{te} \cdot \Delta T \cdot L \tag{5.9}$$

In Table 5.14 the maximum displacements are shown in axial and radial direction to see whether the system will be structurally compromised. One should note that no constraints have been assumed so that the components can expand or contract freely.

Table 5.14: Maximum thermal expansion in axial and radial direction for each concept's thermal nodes in mm

Node	Direction	Con.[1]-Amm.[2]	Con. - Hyd.[3]	Cyl.[4]-Amm.	Cyl. - Hyd.	Spher.[5]-Amm.	Spher. - Hyd.
3	Axial	0.04E-1	0.01	0.05E-1	0.01	0.01	0.01
	Radial	0.02	0.14	0.07	0.14	0.08	0.13
4	Axial	0.01	0.03	0.01	0.03	0.02	0.04
	Radial	0.04	0.11	0.05	0.11	0.05	0.10
5	Axial	0.11	0.10	0.04	0.07	0.13E-3	0.23E-3
	Radial	0.56	0.51	0.22	0.33	0.64E-3	0.12E-2
6	Axial	0.69	0.87	0.55	0.69	0.17	0.17
	Radial	0.48	0.46	0.39	0.48	0.49	0.44
7	Axial	17.60	16.94	17.07	19.98	22.59	19.15
	Radial	0.02	0.02	0.01	0.02	0.02	0.02
8	Axial	0.71	0.34	0.59	0.31	0.65	0.41
	Radial	0.04	0.06	0.05	0.06	0.05	0.05
9	Axial	3.26	2.60	2.88	2.40	3.34	2.61
	Radial	0.04	0.06	0.05	0.06	0.05	0.06

[1] Con. = Conical RAC
[2] Amm. = Ammonia propellant
[3] Hyd. = Hydrogen propellant
[4] Cyl. = Cylindrical RAC
[5] Spher. = Spherical RAC

The concepts show very little axial expansion in Node 3 to 5. In the other nodes one can see a varying profile for the linear deformation. Linear expansions and circumferential

expansions of more than 1 mm have to be specifically addressed. The latter is equal to a radial expansion of 0.16 mm.

All concepts feature a significant axial expansion of the propellant tubing. This requires allowances when attaching this section of tubing to the rest of the propellant feed system. No other measures have to be taken as all expansions are 0.3-0.4% of the total tubing length.

The axial expansion of the evaporator heating gas channel is less of a concern as these are isolated from the rest of the system by the evaporator heat conducting channels. The channels themselves show less than 0.16 mm radial expansion which is acceptable. The cavity radial expansion can be dealt with by employing a small allowance between the cavity insulation and the cavity itself or attaching constraints at the mounting points of the RAC. The same applies for the cavity lid.

5.8 Overall comparison of concepts

5.8.1 Performance

One can state that using liquid hydrogen produces a lighter system with the downside of having a more voluminous system.
In addition liquid hydrogen generates a substantially higher average specific impulse around 650 s versus about 200 s for liquid ammonia. The resulting thrust however is slightly lower.
Liquid hydrogen concepts also generate more system-specific impulse. Concept 1, 3 and 5 on the other hand provide the highest total impulse in comparison with the other concepts.
No clear winners can be discerned with respect to the size criterion as each concept varies in performance in terms of footprint and propellant tank volume. All concepts are capable of generating 100 W in power.

Judging by the inquiries concerning scalability and extrapolating from Concept 1 to the other concepts, the concepts can generate around 100 W without a significant enlarging of the system. A higher power output will require large passive condensers for the power subsystem and a larger system as a whole.
Along the same line of thought, thrust levels up to 5 N can be achieved for all concepts without violating Requirement 4.
Scalability in terms of specific impulse is limited as large increases will require a significant redesign of each concept.

5.8.2 Thermal stresses and expansions

All the calculated thermal stresses are below the yield strengths of the components' materials.
For Concept 1 to 4 thermal expansion measures are required for the cavity and cavity lid

as these nodes feature radial expansion of 0.2 to 0.6 mm.
All concepts have to deal with the axial expansion of the propellant tubing with values up to 2 cm. This can be done through larger design allowances and constraints.

In Section 5.9 a trade-off will be made based on the discussed performance parameters to select the concept which will be designed in more detail.

5.9 Conceptual trade-off

This thesis aims to synthesize a detailed design of a solar thermal hybrid system. Therefore a conceptual design must be selected which will be pursued further in the design process. This requires a trade-off of the six conceptual designs. This trade-off uses a classical scheme. Before this trade-off can be made, some trade-off criteria need to be identified.

5.9.1 Trade-off criteria

The trade-off criteria are:

1. Specific impulse
2. System-specific impulse
3. Thrust
4. Wet system mass fraction
5. System volume
6. System complexity

One notes that power is absent even though it is a system requirement and KPP. It has been omitted since all concepts have shown to satisfy the 100 W requirement and are capable of scaling up the power output through a small change of design variables. As such there will not be a difference in the performance of the concepts in this regard.
With the criteria defined, their relative importance needs to be addressed in the form of weighting factors.

5.9.1.1 Weighting factors

To determine the weighting factors of each criterion the theory of Analytical Hierarchy Process (AHP) is applied (Saaty 1990). This theory states that the criteria must be compared with each other in terms of relative importance.
Table 5.15 gives the resulting comparison matrix as defined in Equation 5.10 which

represents this relative importance. The set of weighting factors is the associated eigenvector v of the nxn comparison matrix as calculated in the Equation 5.11.

$$W = \begin{bmatrix} \frac{w_1}{w_1} & \cdots & \frac{w_1}{w_n} \\ \vdots & \ddots & \vdots \\ \frac{w_n}{w_1} & \cdots & \frac{w_n}{w_n} \end{bmatrix} \tag{5.10}$$

$$(W - \lambda I)v = 0 \tag{5.11}$$

Table 5.15: Trade-off criteria comparison matrix

Criteria	1	2	3	4	5	6	Weighting factors
1	1	1/3	1	1/4	1/3	1/5	0.101
2	3	1	2	1/2	1/3	1/4	0.193
3	1	1/2	1	1/3	1/2	1/4	0.125
4	4	2	3	1	2	1/4	0.359
5	3	3	2	1/2	1	1/5	0.276
6	5	4	4	4	5	1	0.855

Here, there are six criteria so n is 6. In addition the maximum and only non-zero eigenvalue λ is 6.37.
Equations 5.12 and 5.13 are used to calculate respectively the consistency index CI and the consistency ratio CR.
Tummala & Ling (1998) gives a comparison of different calculations of the random consistency index (RCI) and states that an RCI of 1.24 is accurate for an n of 6.

$$CI = \frac{\lambda_{max} - n}{n - 1} \tag{5.12}$$

$$CR = \frac{CI}{RCI} \cdot 100\% \tag{5.13}$$

A consistency index and ratio of respectively 0.074 and 6% are determined. A matrix with a ratio below 10% is considered consistent, so the calculated weighting factors are confirmed to be acceptable.

5.9.1.2 System volume criterion

The performance of the concepts in all but the fifth criterion has already been determined in Chapter 5. The preliminarily estimated system volume is considered a sum of the propulsion subsystem length times its maximum diameter squared and the propellant tank volume as shown in Equation 5.14. The power subsystem is not taken into account as its characteristics are as of yet unknown. Furthermore, its volume will stay constant no matter which concept is selected since each concept generates about the same amount of power.

$$V_{system} = V_{tank} + L_{propulsion} \cdot d^2_{propulsion} \tag{5.14}$$

Table 5.16 for the system volume for each conceptual design.

Table 5.16: System volume estimate of concepts

Concept	System volume $[m^3]$
1	0.137
2	0.171
3	0.133
4	0.171
5	0.092
6	0.167

Since the propellant tank volume is dominant, it is no surprise that the concepts which use liquid ammonia have a substantially smaller system volume. Concept 5 has the smallest volume whereas Concept 2 and 4 have the largest volume.

5.9.1.3 System complexity criterion

System complexity is a measure of how difficult it will be to manufacture, assemble and operate the system. The geometry of the system naturally influences integration and manufacturing. Sections which are symmetric and straight along the longitudinal axis are more advantageous in this regard.
For example, a cylindrical cylinder and spiral tubing with the same spiral radius are easier to manufacture than spherical chambers and spiral tubing with variable radii. Furthermore, fastening tubing to a cylindrical RAC is less intricate than fastening it to a spherical RAC. Therefore, in order of increased complexity the cylindrical, conical and spherical are placed after each other.

In addition, the cryogenic propellant storage increases the complexity of the propellant storage and feed subsystem considerably. The cryogenic storage temperature for hydrogen and ammonia are respectively 17 K and 243 K. Clearly ammonia can be kept at that temperature more easily with less thermal control measures than hydrogen at its own temperature.
This is illustrated in Figure 5.57 which shows a simulated temperature profile for a Al-6061 propellant tank for Concept 2. The MLI insulation around the tank is 4 cm thick. Here, only radiation and conduction to the spacecraft interior is taken into account. The interior is assumed to be a favorable 100.15 K.

One can see that even with such a low environment temperature the temperature of the tank increases from 17 K to 19 K after only 4.5 hours. Even within this short period of time the increase in propellant tank temperature is large. Keeping temperatures low, let alone at 17 K, will require additional devices and additional system mass.
Active coolers however increase the mass of the system substantially according to ter Brake & Wiegerinck (2002). Passive cooling is therefore favorable as it usually entails integration of radiators in the existing spacecraft structure.

A test case for passive cooling of the propellant tank of Concept 2 is evaluated to check for feasibility. One assumes again an interior temperature of 100.15 K. Four copper

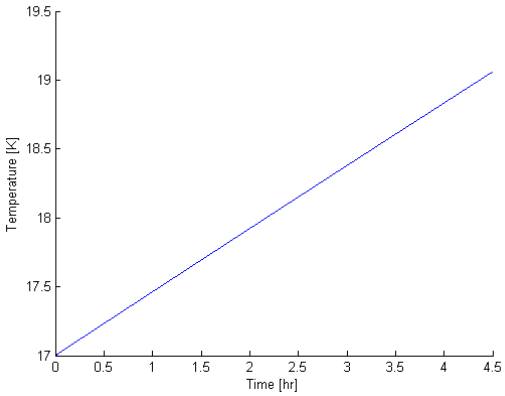

Figure 5.57: Propellant tank temperature for Concept 2

conductors conduct heat to a carbon-carbon honeycomb radiator. It has an area of 2 m^2, a thickness of 1 cm, a density of 1884 kg/m^3, a thermal conductivity of 233.5 W/mK, a specific heat capacity of 687 J/kgK (Ohlhorst et al. 1997) and finally an emittance of 0.91 due to the application of a silicone black paint coating (AZ Technology 2008).
This yields Figure 5.58. The tank temperature increases from 17 K to 20.1 K in a 4.5 hour

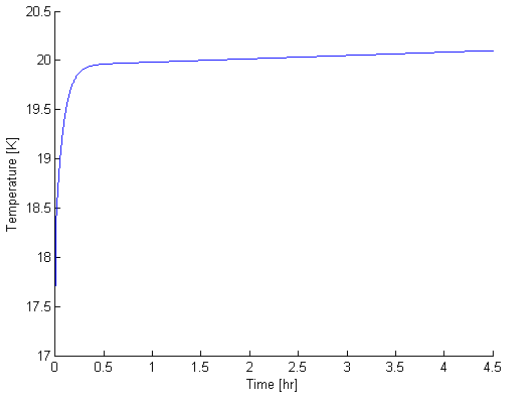

Figure 5.58: Propellant tank temperature with passive radiator cooling

time frame with a slightly increasing temperature gradient at the end of the evaluated period. Not only does the propellant tank temperature still exceed the 17-K requirement, the temperature increase has in fact worsened.
Note that in this test case the single radiator is very large; if more than one propellant tank is required the design becomes even more challenging.
Taking all the observations in this section into consideration, the concepts which use liquid hydrogen get a severe complexity penalty.

5.9.2 Trade-off and selection of final concept

Finally, before the concepts can be compared and traded-off, the score range must be determined to compare the concepts. To make differences between the concepts the most

clear, scores from 1-5 can be given for each criterion, '5' being the best in performance and '1' being the worst. The weighting factors are taken from Section 5.9.1.1.
In Table 5.17 the total score for each concept is given as well as the scores for each criterion.

Table 5.17: Concepts trade-off

Concept	**Specific impulse**	**System specific impulse**	**Thrust**	**Wet system mass fraction**	**System volume**	**System complexity**	**Total**
Weight	0.101	0.193	0.125	0.359	0.276	0.855	
1	1 (0.101)	1 (0.193)	5 (0.625)	2 (0.718)	4 (1.104)	4 (3.44)	**6.181**
2	4 (0.404)	4 (0.772)	4 (0.500)	4 (1.436)	2 (0.552)	1 (0.855)	4.519
3	2 (0.202)	1 (0.193)	5 (0.625)	2 (0.718)	4 (1.104)	5 (4.275)	**7.117**
4	4 (0.404)	3 (0.579)	4 (0.500)	3 (1.077)	2 (0.552)	1 (0.855)	3.967
5	3 (0.303)	3 (0.579)	5 (0.625)	3 (1.077)	5 (1.380)	2 (1.710)	5.674
6	5 (0.505)	5 (0.965)	4 (0.500)	5 (1.795)	3 (0.828)	1 (0.855)	5.448

The final sum of scores yields two concepts with a high score, namely Concept 1 and 3. Looking at Section 5.9.1.3 the system complexity and difficulties of integrating the spherical RACs and, in the case of Concept 6, cryogenic systems in the small spacecraft bus, make Concept 5 and 6 less desirable.
Concept 1 differs slightly with Concept 3 as it has a more complex geometry and less specific impulse, having respectively an impact on system assembly and performance scalability. Concept 3 is therefore the preferred concept.
It has a relatively low system complexity, a high thrust and a low system volume estimate. Its main disadvantage is the low system-specific impulse meaning more system mass will be required to generate a certain amount of impulse.

Chapter 6 will discuss Concept 3 and its detailed design further.

Chapter 6

Detailed design

In Chapter 5.9 Concept 3 was selected to be designed in more detail.
First, the chapter will discuss the secondary concentrator and its casing. Subsequently the pre-cavity chamber will be shortly described. Afterwards the mounting and design of the cylindrical RAC and its lid will be detailed. The propellant tubing and propellant feed system are thereafter discussed, followed by the interface with the evaporator.
Additionally, the thruster design is detailed.
Finally, the chapter concludes with the subsystem integration.

6.1 System architecture and design options

This section will detail the overall system architecture and the design options for each of the system components.
In Figure 6.1 the hybrid system architecture can be seen. For the components within the power and propulsion subsystems different design options have been given. The red options have been discarded whereas the green options have been selected in the conceptual design phase.

The primary concentrator can be on-axis or off-axis with respective to the RAC. Since an on-axis concentrator requires a less complex deployment and pointing mechanism the on-axis option is selected for this design. According to Nakamura et al. (2004) the off-axis concentrator however has been previously estimated to be lighter.

In Wong & Macosko (1999) the refractive secondary concentrator's advantages over a reflective one have been presented. In terms of throughput efficiency and concentration ratio the reflective concentrator has worse performance than the refractive concentrator. The refractive secondary concentrator is therefore selected and the concentrator in question is made of a single-crystal sapphire material.

In Chapter 5 conical, cylindrical and spherical RACs were analyzed and compared. The selected cylindrical RAC for Concept 3 is further developed.

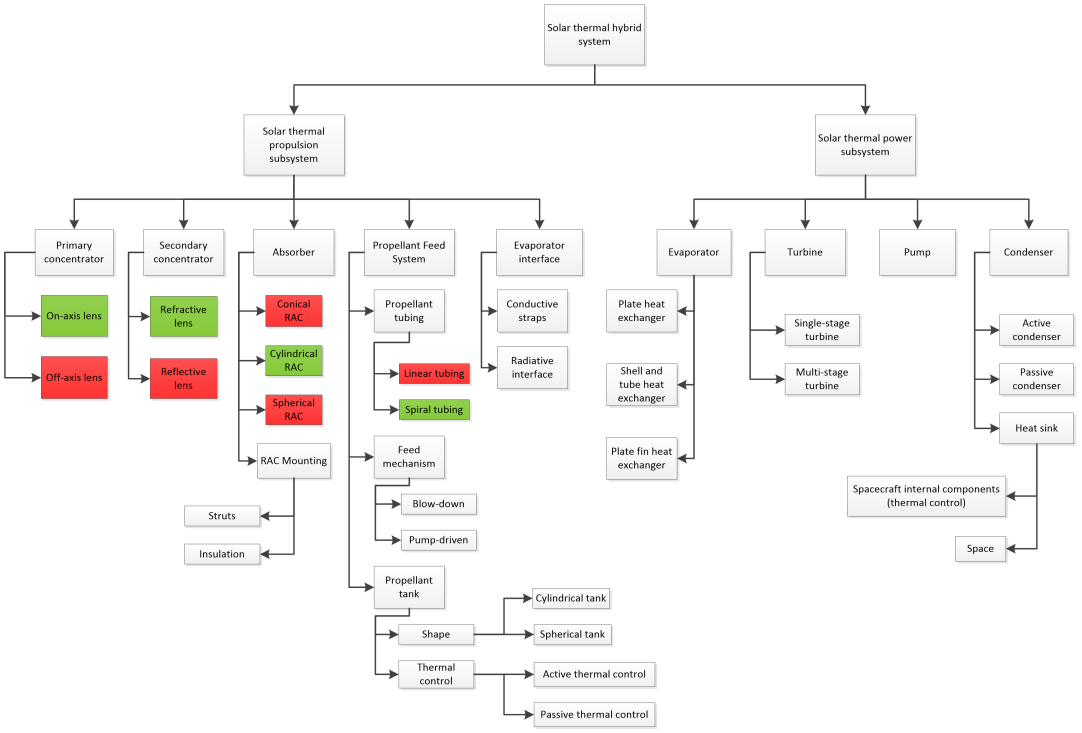

Figure 6.1: System architecture and design options

The propellant feed system features a number of design choices. Only the tubing configuration has been predetermined in Section 5.2.4, namely spiral propellant tubing.

6.2 Propulsion subsystem

6.2.1 Functional and physical architecture

Looking at Figure 2.1 one can get an idea of the functionalities of the propulsion subsystem. The functionalities can be visualized by a socalled Hatley-Pirbhai diagram which shows the system inputs and outputs with the intermediate processes.
In this diagram the propellant flow has been engaged as the sun sensor has verified that the spacecraft is in the daylight phase of its orbit.
In case enough thrust has been provided and the RAC and propellant tubing temperatures exceed the operational constraints, respectively the propellant flow is deactivated and the primary concentrator pointing mechanism is directed to reposition the concentrator.

By matching this diagram with the physical architecture in Figure 6.3, the latter can be verified so as not to omit any components.
The sun sensor will not be included in the detailed design as this device will also be part of the ADCS and small micro-electro-mechanical systems (MEMS) sun sensors are easily available, therefore not compromising feasibility.

The propellant tank will have MLI, but may also include additional thermal control measures. See Section 6.2.5.4 for further discussion on this topic.

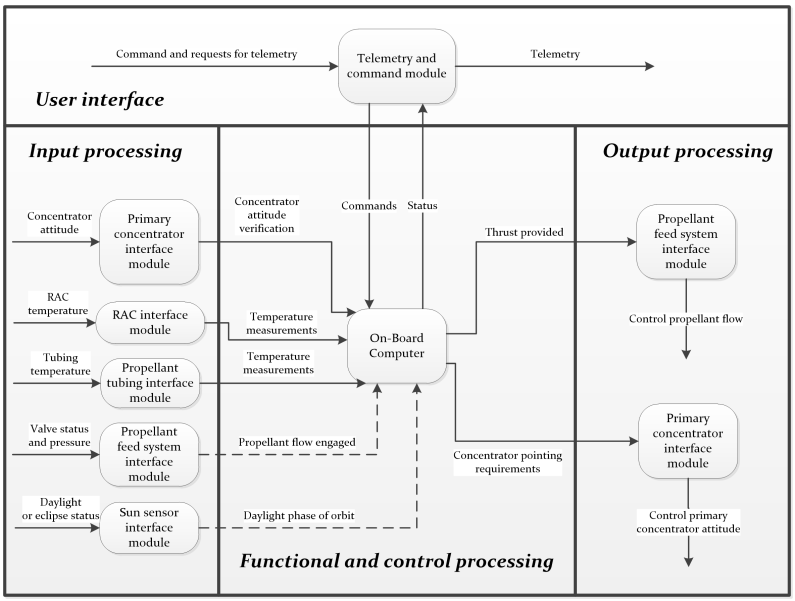

Figure 6.2: Hatley-Pirbhai diagram for propulsion subsystem

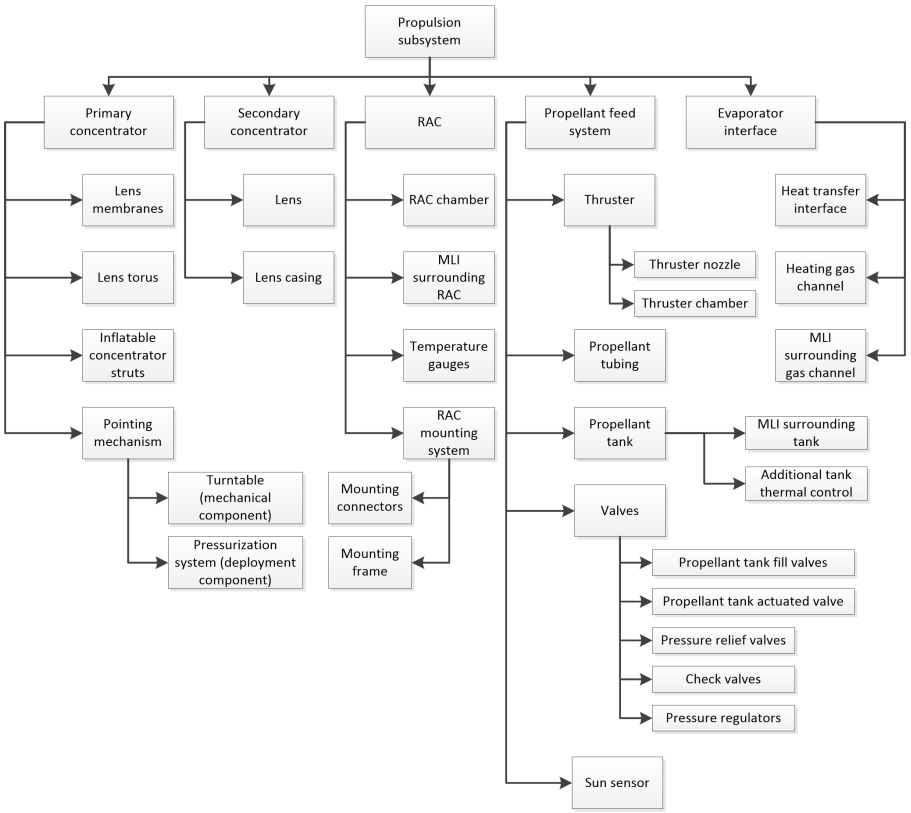

Figure 6.3: Propulsion subsystem physical architecture

6.2.2 Secondary concentrator

The refractive secondary concentrator serves to decrease the pointing requirements for the primary concentrator as the solar image from the primary concentrator is further decreased in size. Its lens is made of a single-crystal sapphire material. A 2.5-cm-diameter single-crystal sapphire lens with a focal length of 5 cm was found to be easily procurable (Edmund Optics 2014).

6.2.2.1 Concentrator lens

The bond between the lens and concentrator casing needs to be sufficiently rigid and capable of handling large temperature differences so that the focusing ability of the lens is not compromised during its service life. To fasten the lens to the casing a high-temperature adhesive is applied to the side of the lens. The casing is made of two half-cylinders and made to close around the circumference of the sapphire lens after which the adhesive strengthens the permanent bond.
In the event that there has to be some reversibility in the system integration process, the adhesive has to be omitted. In order to achieve the same level of fastening and circumvent lens jitter a high-temperature silicone rubber O-ring can be placed between the casing and the lens. The fastening of the two half-cylinders in that case is done by bolts through integrated flanges. This also requires a small allowance between the casing and lens for the O-ring and for the thermal expansion of the lens.
The thermal expansion in the plane of the lens according to Kyocera (2013) is $7.5{\cdot}10^{-6}$ K^{-1} at the maximum temperature of 486 K (see Figure 5.28).

This results in a radial expansion of 0.03 mm according to Equation 5.9. This is an increase of 0.2%. The decrease of the focal length due to thermal expansion will also be small, in the order of several microns (O'Shea et al. 2004). Wong et al. (2000) and Wong (2000) do not mention significant concentration ratio differences during high-temperature tests.
Concluding the allowance for thermal expansion can be very small. An allowance of 1 mm should therefore be sufficient to assemble the parts and leave room for thermal expansion.

To limit the temperature of the lens during multiple heating cycles, 15 thermal straps are attached to the outer extremities of the lens.
The thermal straps feed-through holes in the concentrator casing and interface with heat sinks within the interior of the spacecraft, assumed to be at a temperature of 293.15 K. A length of 15 cm is assumed behind the feed-through holes per thermal strap. These thermal straps have a mass of 77 g, a thickness of 3.6 mm and a conductance of 0.82 W/K (Thermacore 2014). They have a custom width of 5 mm.
This yields a thermal conductivity of 9247 W/mK according to Equation 6.1 which is derived from Pouillet's law. This law expresses electrical resistance as a function of electrical resistivity which are respectively reciprocal to thermal conductance and thermal conductivity.

$$\kappa = \frac{G \cdot L}{A} \tag{6.1}$$

Here, κ is the thermal conductivity and G is the thermal conductance.

The total thermal strap mass estimate is 1.155 kg. The secondary concentrator and its casing are respectively 0.008 kg and 0.638 kg.
In Figure 6.4 the resulting temperature plot can be seen. Comparing this plot to Figure 5.28 shows that the lens maximum temperature in the third orbit has decreased from 486 K to 362 K.

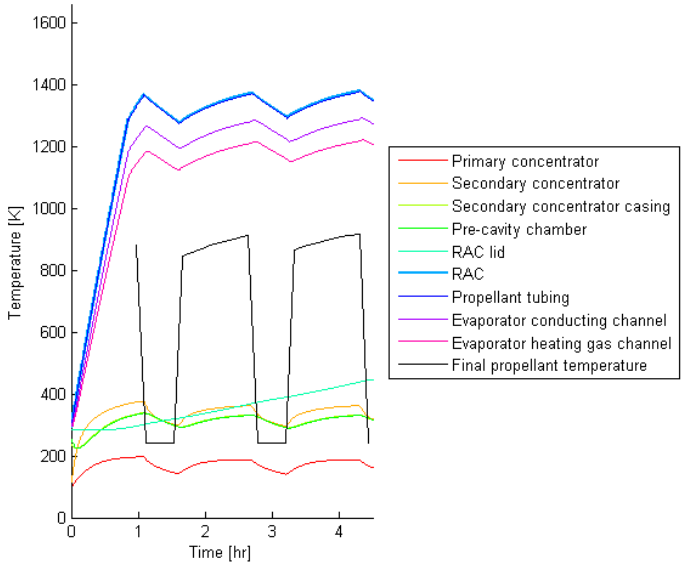

Figure 6.4: Temperature profile for Concept 3 with 15 thermal straps attached to the secondary concentrator lens

6.2.2.2 Concentrator casing

The casing is made of two molybdenum half-cylinders with a length of 4.3 mm, an inner radius of 18 mm and a width of 53 mm.
The inner radius has been determined taking into account the spacing of 1 mm between the edge of the concentrator lens and the casing as detailed in the previous section.
The two parts can be fastened together by including a small baffle on one side of each part along its entire length. The application of some bolts and nuts will facilitate the fastening. Note that these mechanical fasteners need to withstand mechanical and acoustic loads during launch. The casing is surrounded by MLI.
The front of the casing faces space and is therefore coated with a white-paint coating to limit its temperature. The casing frontal surface itself is bolted to the exterior of the spacecraft as well as to some attachment points inside the spacecraft bus.
In Figure 6.5 a schematic is given for the concentrator and its casing.

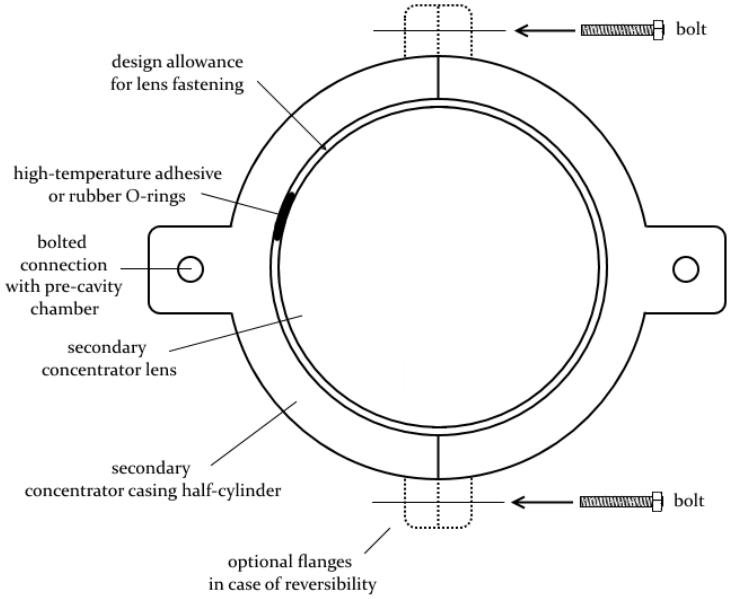

Figure 6.5: Schematic for secondary concentrator assembly

6.2.3 Pre-cavity chamber

The pre-cavity chamber connects the secondary concentrator and its casing with the RAC lid and prevents radiation from spreading to the rest of the spacecraft interior.
It is a molybdenum cylinder with a 10.8 mm wall thickness with about the length of the secondary concentrator focal length and an interior coating of white paint. The coating is applied to limit solar absorptance in the event misalignment of the primary concentrator leads to solar radiation falling on the chamber interior surface. Its exterior is covered with MLI to prevent heat from leaking into the interior of the spacecraft.
The cylinder attaches to the RAC lid and secondary concentrator casing through mechanical fastening of their flanges (Figure 6.6).

Conductive tape with a grounding strap can be used to ground the MLI. Hook-and-pile fasteners can fasten the insulation to the metal substrate by tightening the insulation material around the chamber. The fasteners themselves can be attached by adhesives or riveting (Finckenor & Dooling 1999). The chamber itself has a mass of 2.022 kg.

6.2.4 RAC and RAC lid

One of the most important components in the hybrid system is the RAC.
The RAC lid has a 10.5-cm wide aperture to allow the incoming solar flux to heat the cavity. The surroundings of the cylindrical RAC and its lid are insulated with MLI, except for some cut-outs for attached components. The insulation is applied as a shell surrounding the cavity and propellant tubing.

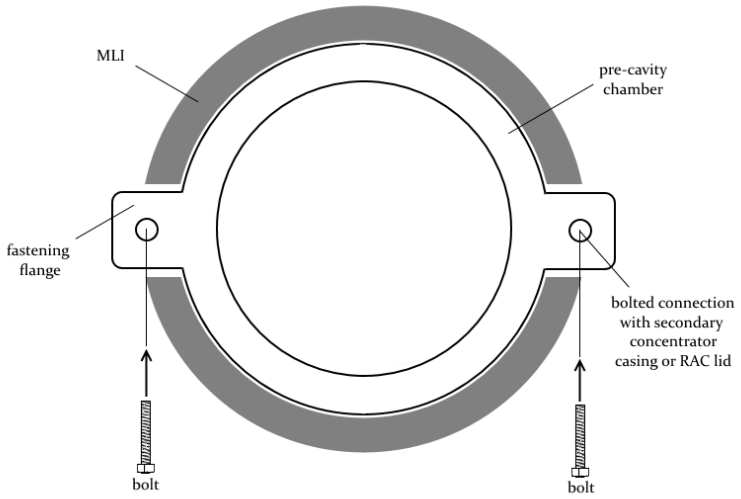

Figure 6.6: Schematic for pre-cavity chamber assembly

The lid is considered a separate component as it is mounted separately from the cavity. Its core structure is made of molybdenum which is encompassed by MLI to achieve sufficient insulating performance. The molybdenum serves to limit the thermal expansion of the lid. The thickness of the molybdenum core is 14 mm. On both sides a 43-mm thick MLI blanket has been attached to the core.
There is a 1 mm small spacing between the RAC and lid to allow for some thermal expansion of the RAC.
Summing up the insulation and the core material, the lid has a mass of 0.987 kg.

The RAC is a cylinder as has already been determined. In the model a wall thickness of 10.8 mm is calculated as explained in Section 5.1.2. On the inside it has a black paint coating for the best absorptive properties. It is open-ended on one side whereas the rear of the cavity is closed. The cavity itself is mounted to a surrounding frame with mounting points to the rest of the spacecraft and attachment points for insulation.
There are different options for mounting the RAC to the frame. Two distinctive mounting categories have been given in Figure 6.1. Three specific options are evaluated:

1. PODS attached to both the frame and the RAC
2. Aluminium struts attached to both the frame and the RAC
3. Clamping of the RAC within the frame by using a large amount of MLI and hook-and-pile fasteners

During the evaluation of the different options a spacing between the frame and the top of the propellant tubing of 10 cm is assumed. The sink temperature has been set at 293.15 K. The options are detailed in Section 6.2.4.1 to Section 6.2.4.3.

6.2.4.1 PODS

First of all, the PODS option is analyzed. (Plachta et al. 2006) gives more information concerning these devices. In this case their core is made of a graphite epoxy composite. Their function is to limit heat transfer by limiting the cross-sectional area through which heat can be transferred and by having a low thermal conductivity. This in turn limits the decrease of temperature of the RAC. In Figure 6.7 a schematic is provided for these devices.

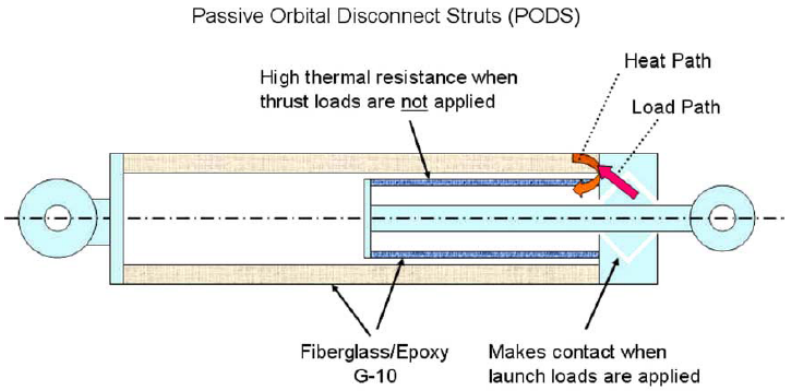

Figure 6.7: Schematic for PODS (Plachta et al. 2006)

The size of the PODS is determined by the mass of the RAC. Since it is only 18.7 kg without support structures, no large struts are required. Using Hopkins & Payne (1987) one can calculate a preliminary calculation of PODS dimensions. In this calculation the paper states a limit load of 10g in any direction and a maximum safety factor of 1.8. Equation 6.2 is a rudimentary calculation of the critical loads for these PODS. It yields a load of 3302 N. The outer tube wall thickness for the struts is calculated with Equation 6.3 and results in a thickness of 0.181 mm.

$$F_{critical} = M_{RAC} \cdot 10 \cdot 9.81 \cdot f_{safety} \tag{6.2}$$

$$t_{PODS} = \sqrt{\frac{F_{critical}}{0.942E}} \tag{6.3}$$

$$R_{PODS} = \left(\frac{F_{critical} L^2}{\pi^3 E \cdot t_{PODS}} \right)^{1/3} \tag{6.4}$$

Here, $F_{critical}$ is the critical load, R_{PODS} is the PODS minimum tube radius and t_{PODS} is the PODS outer tube wall thickness. The variable f_{safety} is the safety factor and E is the modulus of elasticity for the graphite epoxy which is 106869 MPa according to Hopkins & Payne (1987). In addition, a thermal conductivity of 3.5 W/mK for graphite epoxy composites has been stated.

Assuming a length of 10 cm for each PODS, the outer tube diameter becomes 7.6 mm. To estimate the mass of each PODS, it is considered a solid rod made of only graphite fibers. The density is assumed to be 1772 kg/m^3 (Armanios 1997, p. 71). This yields a

mass of 8 g per rod.

Figure 6.8 shows a schematic for the proposed RAC assembly. Note that only half the RAC is given as the design is assumed to be symmetric around the axis of symmetry.

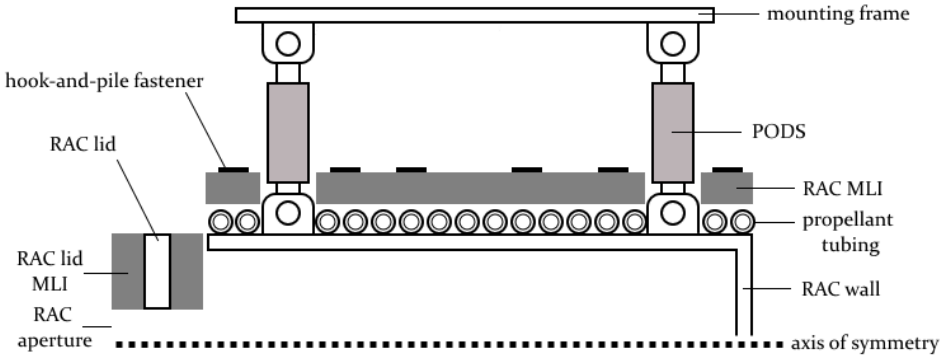

Figure 6.8: Cross-sectional schematic for RAC assembly

Since the RAC is a relatively small component compared to the rest of the spacecraft, a total of 8 PODS are attached, each at a different point along the cavity circumference. This gives a total mass for this solution of 64 g. Figure 6.9 gives a rear view to better illustrate this configuration.

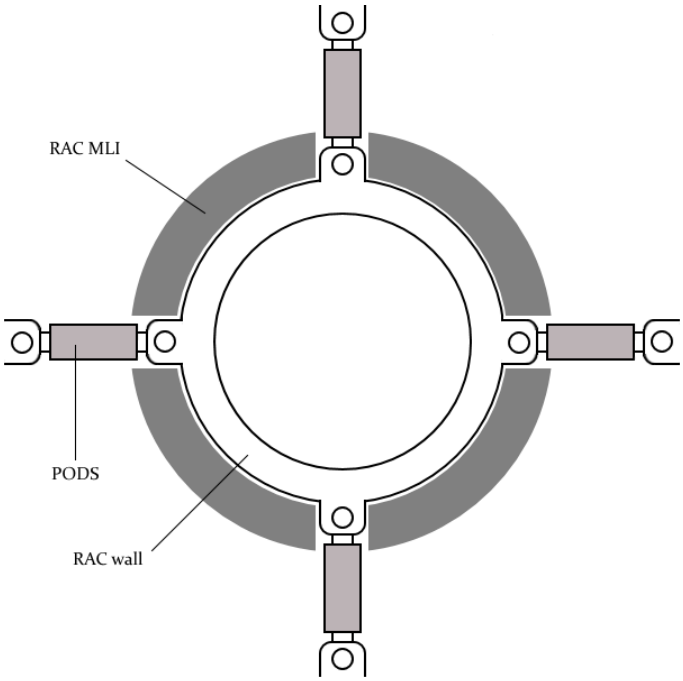

Figure 6.9: Rear-view schematic for RAC assembly

The model is run with 4 PODS at the front and 4 at the rear of the cavity. The RAC maximum temperature in the last evaluated orbit is calculated to be 12 K lower at 1368 K than in the case without PODS as can be seen in Figure 6.10. This is a decrease of 0.9% which is acceptable. The specific impulse as a consequence decreases by only one second to 180 s.

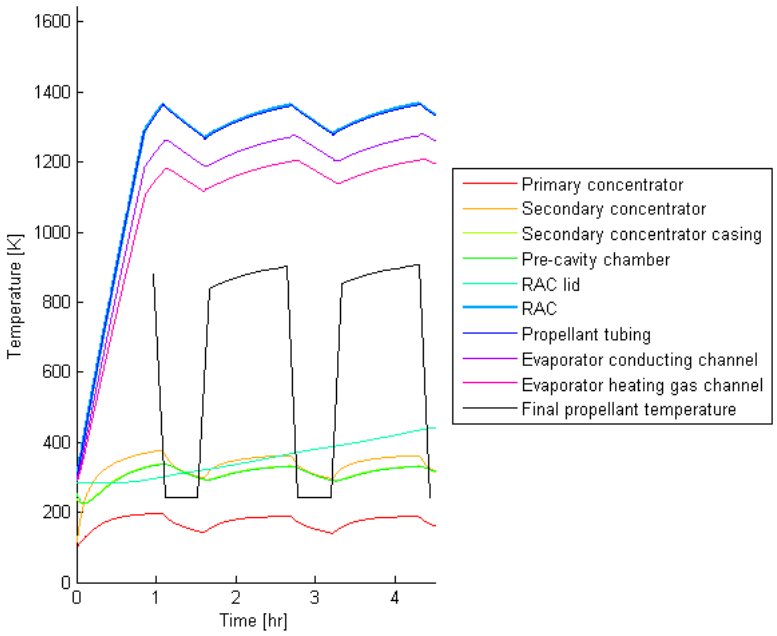

Figure 6.10: Temperature profile for Concept 3 with PODS

6.2.4.2 Aluminium struts

Aluminium struts are solid rods which have attachment points at the frame and at the cavity. To compare them with the PODS they too must cope with a launch load of 3302 N.
The Al 6061-T6 material in question has a density of 2700 kg/m^3, a thermal conductivity of 167 W/mK and a tensile yield strength of 276 MPa (ASM Aerospace Specification Metals Inc. 2014).
A solid rod with a diameter of 7.6 mm which needs to cope with 3302 N suffers a normal stress of 73 MPa which does not exceed the previously defined yield strength. The mass of such a rod is 12.2 g. Eight of these aluminium rods give a total mass of 98 g.

In Figure 6.11 one can see the effect of having the RAC transferring heat through the aluminium rods. Comparing the figure to Figure 5.28 gives one a sense of the thermal disturbances caused by the struts. The third orbit maximum cavity temperature decreases from 1380 K to 1025 K. As a consequence the specific impulse at the end of the evaluated period decreases from 181 s to 148 s.

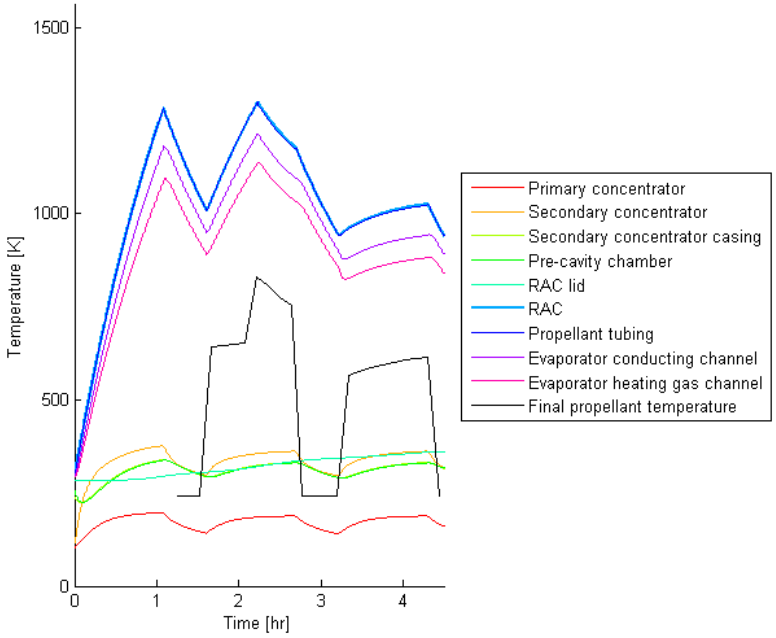

Figure 6.11: Temperature profile for Concept 3 with Al 6061-rods between mounting frame and RAC

6.2.4.3 MLI and fasteners

Johnson & Fesmire (2011) gives a thermal conductivity of 0.1 mW/mK and a density of 45 kg/m^3 for the MLI material. If the 10-cm spacing needs to be completely filled with MLI one comes to a maximum of 0.0143 m^3 insulation. This gives a mass of 0.645 kg. The fastener mass cannot be defined without detailed knowledge of the number of fasteners and is therefore not taken into account. Even without this value however it becomes clear that this option represents a larger mass increase than the other two options.

A 10-cm MLI blanket can have 100 aluminized Mylar layers if one extrapolates from (Johnson & Fesmire 2011). According to (Larson & Wertz 2005, p. 438) the effective emittance then drops to merely 0.00025. In Figure 6.12 one can see the resulting temperature profile for the propulsion subsystem.
The MLI surrounding the RAC increases in thickness from 4.3 cm to 10 cm so it does not come as a surprise that the maximum RAC temperature increases as less heat is allowed to dissipate from the cavity. In the third orbit this temperature increases from 1380 K to 1381 K. The specific impulse increases by one second to 182 s.

6.2.4.4 Comparison of mounting options

Comparing the three options it becomes clear that the last option is the heaviest, but also preserves the RAC temperature the best. The PODS option has the least mass and achieves virtually no temperature change with respect to the initial conceptual design.

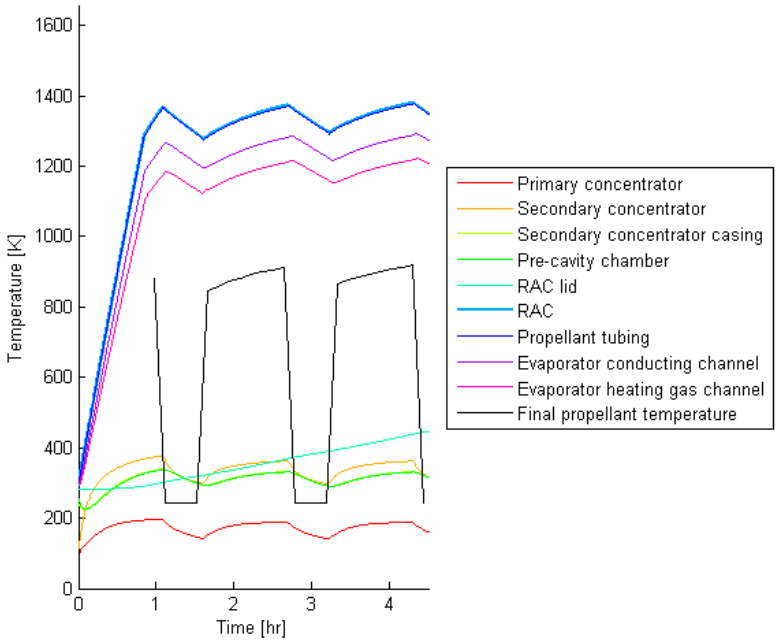

Figure 6.12: Temperature profile for Concept 3 with 10-cm thick MLI around RAC

Furthermore, additional insulation can be applied at other locations around the cavity to further decrease heat dissipation, thereby mimicking the thermal control ability of the last option.
Concluding, in order to save mass, the first option is selected.

6.2.4.5 Mass budget

In Table 6.1 the mass budget for this part of the system is given.
An MLI blanket of 43-mm thickness is still wrapped around the RAC and is taken into account in the mass budget. This yields a mass for the RAC of almost 19 kg. Summing up all the different components a total mass of 24.8 kg is computed for the RAC system.

Table 6.1: Mass budget for RAC system

Component	Mass [kg]
Primary concentrator	0.94
Secondary concentrator	0.01
Secondary concentrator casing	0.64
Thermal straps	1.16
Pre-cavity chamber	2.02
RAC lid incl. MLI	0.99
RAC incl. MLI	18.96
PODS	0.06
Total	24.78

6.2.5 Propellant feed system

The propellant feed system performs the physical transportation of the propellant from the propellant tank along the RAC to the thruster chamber. Figure 6.1 gives two different regimes for achieving propellant flow, namely pump-driven and blow-down schemes:

- Pump-driven *An electric (micro)pump forces the flow down-line. This requires input power, but there is accurate active control of the propellant flow.*
- Blow-down *The propellant is pressurized with a pressurant gas within the propellant tank and a valve down-line of the tank controls the propellant flow. Regulation by the valve will guarantee that the correct tank outlet pressure is maintained independent of how much propellant is expelled out of the tank. The pressurant gas and propellant can be optionally separated by a membrane. There is less control of the flow but virtually no power is required.*

The propellant tank itself is small as well as the amount of required propellant. Therefore a blow-down system should not be difficult to achieve.
A major disadvantage of blow-down systems is that they typically increase the mass of the propellant tank as its thickness must increase to accommodate the larger internal pressure.
In addition the ullage volume must be filled up with pressurant gas. A separate pressurant gas tank can also be considered although the small spacecraft bus volume imposes some constraints for integration.
A pump-fed system requires relatively heavy and large pumps with a large number of moving parts, therefore increasing the mass of the spacecraft and reducing system reliability. This makes the system unsuitable for small low-thrust propulsion systems.
Taking all these advantages and disadvantages together, it becomes clear that for a small system the blow-down option is the most advantageous.

One is reminded that liquid ammonia is used as propellant. The pressurant gas for the liquid ammonia will be helium as ammonia has a higher boiling point than helium, meaning that at the cryogenic storage temperature helium is in a gaseous state.

In order to design the propellant feed system one needs to work from the back to the front of the feed system. Hence, the thruster is the first component to be discussed. Afterwards the propellant tubing and the propellant tank are detailed.

6.2.5.1 Thruster

The thruster encompasses the thruster chamber and the nozzle. It is made of molybdenum to cope with the high-temperature exhaust gases. The thruster in question falls within the small thruster category with a chamber radius of 1 cm, a chamber length of 4 cm and a throat radius of 1.5 mm. The chamber pressure is set at 1.0 bar.
To elaborate on the discussion in Section 5.2.3 twelve different bell-shaped nozzles are compared. The length of each set of three nozzles is set at respectively 6, 7, 8 and 9 cm. The expansion ratio for each set of nozzles is set at 150, 225 and 300 which yields a nozzle exhaust diameter of respectively 3.67 cm, 4.50 cm and 5.20 cm.
Table 6.2 gives the accompanying angles. The nozzle throat convergence half angle is 25 degrees for all nozzles.

Table 6.2: Final comparison of nozzle shapes

Nozzle length [cm]/ Exhaust diameter [cm]	**Nozzle throat divergence half angle [deg]**	**Nozzle exhaust divergence half angle [deg]**	**Specific impulse [s]**	**Thrust [N]**
6/3.67	45	14.5	184	1.242
7/3.67	40	11.5	184	1.254
8/3.67	35	9.7	184	1.271
9/3.67	30	8.5	184	1.289
6/4.50	45	19.0	185	1.271
7/4.50	40	15.2	185	1.277
8/4.50	35	12.8	185	1.289
9/4.50	30	11.2	185	1.303
6/5.20	45	22.5	185	1.29
7/5.20	40	18.5	185	1.294
8/5.20	35	15.8	185	1.304
9/5.20	30	13.8	185	1.315

In Figure 6.13 the nozzle length-exhaust diameter ratio has been plotted against the generated thrust. One can see that for every expansion ratio there is a separate curve. The thrust increases with a larger expansion ratio as well as with a larger nozzle length-exhaust diameter ratio. There is virtually no change in the specific impulse.
As can be seen in the figure, an expansion ratio of 300 and a nozzle length of 9 cm are selected to maximize thrust. The nozzle's divergent section is situated just outside the exterior of the spacecraft on the opposite side of the side which features the primary concentrator. The thruster chamber itself is mechanically fastened to the exterior of the spacecraft.

As molybdenum has a high maximum operating temperature no thruster cooling is required. The flow effective exhaust velocity is 1.85 km/s. The mass flow at that point is 732 mg/s.

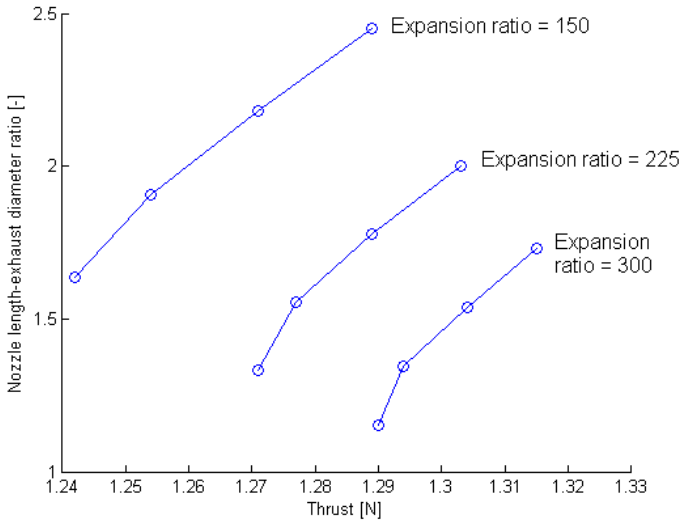

Figure 6.13: Nozzle length-exhaust diameter ratio versus thrust

The mass of the chamber and nozzle itself is estimated by assuming that the chamber is an open-ended cylinder and the nozzle is formed by two hollow cones. The thruster thickness is assumed 1 mm. This yields a thruster mass of 0.064 kg. The final required propellant mass becomes 29.3 kg.

6.2.5.2 Propellant tubing

The molybdenum spiral propellant tubing has a thickness of 0.625 mm and an inner diameter of 3.75 cm.
This thickness has been calculated by assuming a certain diameter-thickness ratio based on parts procurement data (Section 5.1.2).
To calculate the pressure within the propellant tank in Section 6.2.5.3 the total pressure loss has to be determined. Looking at equation 3.62 the total tubing length and the flow conditions in the tubing need to be known to calculate the pressure loss.
Below the three distinguishable feed lines are identified. The spiral tubing includes the 8% reduction as described in Section 3.2.3.1.
There are three feed lines:

- One from the cavity to the thruster chamber;
- One section of RAC-adjacent spiral tubing;
- One from the cavity to the propellant tank

$$L_{tubing_{RAC-thruster}} = 1 - L_{system} - L_{nozzle} - L_{chamber} \tag{6.5}$$

$$L_{tubing_{tank-RAC_1}} = 0.5 - R_{tank} - L_{tank}/2 - x_{front-RAC} \tag{6.6}$$

$$L_{tubing_{tank-RAC_2}} = 0.5 - R_{RAC} - R_{tank} - t_{ins} - t_{tank} \tag{6.7}$$

$$L_{tubing_{tank-RAC_{total}}} = \left(L_{tubing_{tank-RAC_1}} + L_{tubing_{tank-RAC_2}}\right) \cdot 1.1 \tag{6.8}$$

The length of the RAC-adjacent tubing has already been calculated based on the number of turns and the RAC size. This yields a length of 8.471 m.

The feed line from the RAC to the thruster is calculated by taking the entire width of the spacecraft bus of 1 m and subtracting the length of the system, the nozzle and the thruster chamber as seen in Equation 6.5. These are respectively 45.5 cm, 9 cm and 4 cm. The assumption is made that the system is coaxial with one of the axes of symmetry of the spacecraft. This yields a length for this feed line of 41.5 cm.

The third feed line length depends on the position of the propellant tank within the spacecraft bus. The propellant tank is placed above the RAC to limit the complexity of the feed line. Furthermore by concentrating the propellant mass as much at the center of the spacecraft as possible the spacecraft's stability will be increased. This in turn will cause less attitude disturbances due to propellant sloshing. A 10% margin is included in this feed line for bends.
In equations 6.6 to 6.8 the length of this feed line is calculated. The length for this feed line then becomes 14 cm. Here, $x_{front-RAC}$ is the location of the front of the RAC with respect to the bus side wall. The variables t_{ins} and t_{tank} are the thicknesses of the RAC insulation and the RAC wall.
Figure 6.14 gives an illustration of the geometry involved. Summing the three tubing

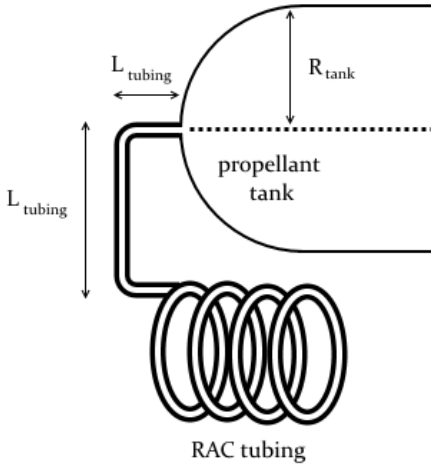

Figure 6.14: Schematic for propellant tubing from propellant tank to RAC

lengths up yields a total tubing length of 9.14 m. This results in a tubing mass of 0.914 kg.

The pressure losses in the tubing can be compartmentalized in four different parts.

- Friction pressure losses when the propellant is in a liquid state
- Friction pressure losses when the propellant is in a gaseous state
- Friction pressure losses when the propellant is in a two-phase state

- Acceleration pressure losses due to the vaporization of the propellant

6.2.5.2.1 Pressure loss for liquid propellant

The liquid ammonia propellant is present from the tank to the RAC as it is stored as a liquid.
The assumption is that the propellant will change phase in the first third section of the RAC propellant tubing. This assumption also means that only in the first sub-node of node 7 will the propellant temperature be decreased due to the latent heat. This heat is required to vaporize the propellant.
Equation 3.49 shows that indeed the temperature decreases, since less convective heat is put into heating the propellant.

The pressure loss in bends is taken into account here as bends will be present within the tubing from the propellant tank to the RAC where the propellant is still in a liquid state. Figure 6.14 shows two bends. An additional third bend can be defined at the start of the spiral tubing. The radii of the 90° bends are assumed to be two times the tubing diameter.
Idel'chik (1986) gives equations to calculate the pressure loss in bends δp_{bend} which is defined in Equation 6.11. The pressure loss coefficient ξ which is required, is determined according to Equation 6.10. The liquid flow Reynolds number is 538 and therefore Equation 6.9 applies to calculate the loss scaling factor λ.

$$\lambda = \frac{20}{Re^{0.65}} \left(\frac{D_{inner-tubing}}{2R_{bend}} \right)^{0.175} \tag{6.9}$$

$$\xi = 0.0175\lambda \left(\frac{R_{bend}}{D_{inner-tubing}} \right) \delta_{bend} \tag{6.10}$$

$$\delta p_{bend} = \frac{\xi \rho_{prop} U_{prop}^2}{2} \tag{6.11}$$

Here, R_{bend} is the bend radius and δ_{bend} is the bend angle in degrees.
A loss coefficient of 0.83 is calculated. The pressure loss per bend is calculated to be 0.93 Pa. This yields a total pressure loss in the bends of 2.8 Pa.
Equation 3.62 is used to calculate the friction loss in the straight tubing sections which yields 4.6 Pa.
Therefore a total pressure loss of 7.4 Pa in the liquid state has to be taken into account.

6.2.5.2.2 Pressure loss for gaseous propellant

The gaseous ammonia is present in two-thirds of the RAC tubing and in the tubing from the RAC to the thruster.
The spiral tubing can be represented by twenty 360° bends. As two-thirds of the spiral tubing features the gaseous flow only fourteen bends will be used to calculate the total loss in the bends.
The inner radius of the tubing is 2.35 mm and the bend radius is 71 mm. The mean flow properties are applied to calculate the pressure loss (Equation 6.11).
With a mean Reynolds number of $2.07 \cdot 10^4$ λ becomes approximately 0.045 (Idel'chik 1986,

p. 210).

This yields a pressure loss in each bend of 1.25 kPa and therefore a total bend loss in the RAC of 17.5 kPa.
Equation 3.62 calculates the friction pressure loss along the two-thirds length of the spiral tubing. This results in a pressure loss of 85.6 kPa.
Finally, the pressure loss in the tubing from RAC to the thruster chamber is calculated. The density of the propellant when it runs from RAC to the thruster is based on the ideal gas law and the mean propellant temperature during propellant flow. Equation 3.62 is applied here as well. The resulting friction pressure loss is only 9.3 kPa.
This yields a total pressure loss in the gaseous state of 112.4 kPa.

6.2.5.2.3 Two-phase propellant and acceleration pressure losses

When calculating the two-phase friction loss in one third of the spiral tubing, the assumption is made that half the propellant flow is in the liquid phase and half in the vapor phase. The surface tension for liquid ammonia at 240 K is $33.9 \cdot 10^{-3}$ N/m. The Baker parameters B_x and B_y are respectively 0.93 and $2.81 \cdot 10^4$. From Figure 3.9 this yields an annular two-phase flow in the tubing and the following correlation for the unit loss ϕ.

McKetta Jr. (1992) gives Equation 6.12 for the unit loss in an annular flow.
D is the inner diameter of the pipe in inches. L is the tubing length in feet.
Equation 6.13 calculates the actual pressure loss based on the friction loss when the entire flow in the section is evaporated. The friction loss δp_{vapor} has been calculated using mean gaseous flow conditions. Finally, a two-phase pressure loss of 12.6 kPa is calculated.

$$\phi = aX^b \tag{6.12}$$
$$a = 4.8 - 0.3125D$$
$$b = 0.343 - 0.021D$$
$$X = \sqrt{(W_l/W_v)^{1.8} \cdot (\rho_v/\rho_l) \cdot (\mu_l/\mu_v)^{0.2}}$$
$$\delta p = \delta p_{vapor} \phi^2 \cdot L/100 \tag{6.13}$$

Equation 3.67 computes the pressure losses due to the expansion of the propellant as a result of evaporation. As the volume of the propellant increases, a pressure loss in the propellant occurs which needs to be compensated. This acceleration pressure loss has a value of 3 kPa.

6.2.5.2.4 Total pressure loss

In Table 6.3 the pressure losses are summed up according to Equation 3.68.

Clearly, the gas-phase friction pressure losses are most severe, mainly due to the large feed line length and the high flow velocity of the gaseous propellant. The total pressure loss amounts to 1.28 bar. With a chamber pressure of 1 bar, the tank pressure at the total evacuation of the tank must therefore be 2.28 bar.

Table 6.3: Pressure losses

Pressure loss	Value [kPa]
Friction pressure loss - liquid-phase	7.4E-3
Friction pressure loss - gas-phase	112.4
Friction pressure loss - two-phase	12.6
Acceleration pressure loss	3.0
Total pressure loss	128.0

The spiral propellant tubing is fastened on the outside of the cavity. This fastening has to be performed adequately as during launch high-frequency vibrations could cause large excitations in this part of the system.
At the beginning and end of the tubing, two 2 cm wide titanium-alloy rings are clamped around the tubing as seen in Figure 6.15. The clamping locations are also fastened to the frame. A titanium-alloy has been chosen to prevent large heat dissipation as the material can have a thermal conductivity as low as 4.8 W/mK (AZO Materials 2014).

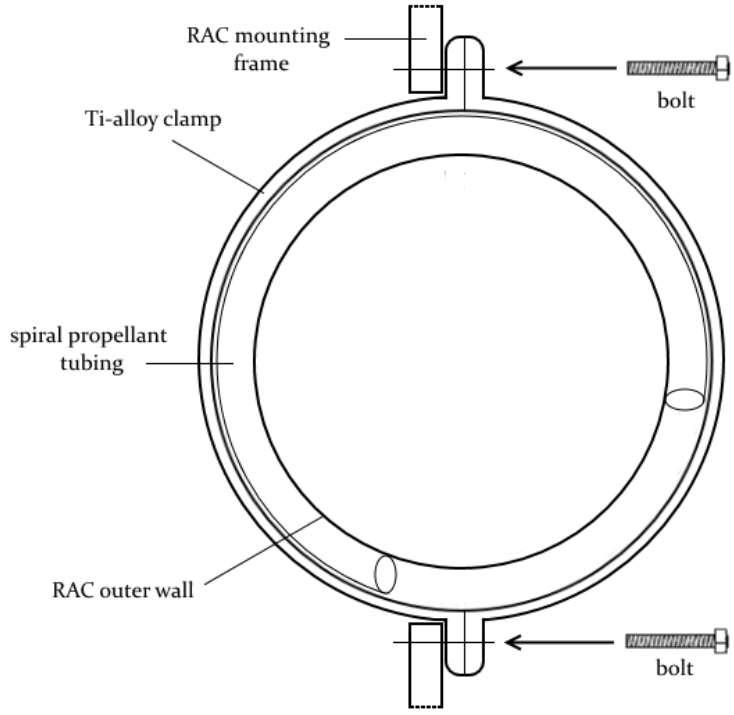

Figure 6.15: Schematic for propellant tubing fasteners

The end points of the RAC tubing are threaded so that feed lines from the propellant tank and to the thruster can be independently mounted.

6.2.5.3 Propellant tank

The system volume estimate is a sum of the volume estimate for the RAC and for the propellant tank as these are the two major components contributing to the system volume. The propellant tank takes up more than half of the system volume estimate, namely 0.052 m^3 out of a total volume of 0.08 m^3.
If a spherical tank is adopted, it must have an inner diameter of 46 cm. This leads to a limited remaining volume within the spacecraft bus. Therefore to conserve practical space within the bus, a cylindrical tank with hemispherical end-caps will be adopted instead of a spherical tank.
After a number of iterations one single tank was deemed feasible with an inner radius of 17.6 cm and a length of 30 cm excluding the end-caps. The total (inner) length of the tank becomes 65.2 cm which fits easily inside the spacecraft bus and leaves room for a feed line and insulation.
Passive and/or active thermal control can be used to keep the propellant tank and its contents at a cryogenic temperature of 240 K. See the subsequent paragraphs for more details.

As seen in Section 6.2.5.2 the pressure at the flow control valve behind the tank needs to be 2.28 bar. Recall that 80% of the tank volume is propellant and 20% is ullage which is filled with helium pressurant gas.

$$\frac{PV}{T} = c \tag{6.14}$$

Taking the combined gas law in Equation 6.14 and assuming a constant temperature within the propellant tank, the product of pressure and volume stays constant. This yields the following equation:

$$p_{tank_{max}} = \frac{p_{tank_{nominal}} V_{tank}}{0.2 V_{tank}} \tag{6.15}$$

A maximum pressure of 11.4 bar is calculated for the helium pressurant so that the 2.28 bar propellant pressure is still achieved at total evacuation of the propellant tank.
With a pressure loss of 1.28 bar the chamber pressure of 1 bar is then maintained.
Since a higher pressure will result in a higher boiling point temperature (Equation 6.14) no changes to the propellant storage temperature are necessary. Using the ideal gas law for computing the density of the helium yields a pressurant gas mass of 23.2 g.

The maximum pressure requires a certain thickness of the propellant tank shell. The selected propellant tank material is Al 6061-T6, an aluminium alloy, which has a low density of 2700 kg/m(3), a thermal conductivity of 167 W/mK and a yield strength of 276 MPa (ASM Aerospace Specification Metals Inc. 2014).
From Swearengen (1972) one knows that the aluminium alloy yield strength in the temperature range 200 K to 350 K is independent of material temperature. No temperature-dependent corrections in the tank thickness therefore need to take place.
Liquid ammonia is non-corrosive and therefore no corrosion allowance is applied when calculating the minimum design thickness for the tank shell.

The maximum of the results from solving Equation 6.17 and 6.16 is considered the minimum thickness. The longitudinal yield strength and the circumferential yield strength are considered equal as the material is considered isotropic. These equations have been derived from ASME (2013).

$$\sigma_{yield_{circ}} = \frac{p_{max} \cdot (R_{tank} + 0.6t_{tank})}{t_{tank}} \tag{6.16}$$

$$\sigma_{yield_{long}} = \frac{p_{max} \cdot (R_{tank} - 0.4t_{tank})}{2t_{tank}} \tag{6.17}$$

Here, R_{tank} is the tank internal radius and t_{tank} is the tank shell thickness.
A minimum tank wall thickness of 1.1 mm is calculated with a safety factor of 1.5.

$$\sigma_{normal} = F_{axial}/A_{cs} \tag{6.18}$$

Equating Equation 6.18 to the yield strength of the tank material, yields a minimum wall thickness. The axial loading F_{axial} of 5.4 kN is calculated according to Equation 6.2; instead however the mass considered is the sum of the masses of the tank, the propellant and the pressurant gas. The safety factor stays 1.8. This yields a minimum thickness of 0.02 mm. As one can see the minimum tank wall thickness causes no problems for axial loading.
As the surface area of the propellant tank is 0.72 m^2 this yields an estimate of the total tank mass of 2.10 kg. Together with the propellant and pressurant gas a total propellant tank mass of 31.4 kg is determined.

6.2.5.4 Propellant tank thermal control

In Figure 6.1 passive and active thermal control options are discerned. Passive control has the advantage that it does not require power. The thermal control ability is constrained however. Active control requires heavy and relatively complex components, but achieves larger cryogenic cooling. The following solutions are available:

- Passive thermal control:
  - MLI
  - Surface coatings
  - Radiators
  - Optical Solar Reflectors (OSR)
- Active thermal control:
  - Heat pipes
  - Thermal control louvers
  - Electric heaters
  - Thermoelectric coolers

Since the spacecraft bus is small and there is already a significant amount of tubing within the spacecraft, a heat pipe system is considered too troublesome to integrate.
Thermoelectric coolers are heavy and require large amounts of power. For example in Zhang et al. (2007) a pulse-tube cooler achieves 10 W of cooling power by supplying 190 W of electrical power. According to the review by (ter Brake & Wiegerinck 2002) this cooler would be in the mass range of 8-9 kg. Therefore these coolers will not be used here.
Electric path heaters however are small Kapton-film heaters which can be attached in large numbers to heat certain surfaces. They also use relatively little power.
Thermal control louvers consist of blades which can open and close and can therefore prevent or encourage a heat flux being transferred across it. They are actuated through thermally sensitive springs and can reject six times as much heat in an open state than in a closed state (Larson & Wertz 2005, p. 442).

In terms of the passive thermal control options, OSRs are used on the surface of space-facing structures and components. Since they have a high emittance and low absorptance, they are very good at keeping surfaces cool, even when the surfaces are illuminated by Earth albedo and direct sunlight.
Radiator panels are also used as a thermal control interface with the external environment. They usually are mounted as part of the bus or in the form of a (deployable) external fin. The radiator panel is coated to achieve high emittance and low absorptance properties for maximum heat rejection to space. If a radiator is integrated into the bus, the additional mass can be very small.
Not only externally, but also internally can coatings serve to create a favorable thermal environment.
As shown previously MLI is very effective in insulating parts of the spacecraft against large heat fluxes.

To see which (combined) measures are the most effective in terms of heat transfer and mass, three different solutions will be analyzed:

- Propellant tank covered in MLI
- Propellant tank covered in MLI and interfacing with a radiator-panel
- Propellant tank covered in MLI, partly interfacing with space and covered in OSRs

6.2.5.4.1 Propellant tank covered in MLI

When computing the MLI insulation mass surrounding the tank, first one needs to determine the thickness of the insulation.
One assumes that only radiative and conductive heat fluxes occur between the tank and its environment as MLI only interacts through radiation and conductance.

Previously in Section 5.1.2 an effective emittance of $2{\cdot}10^{-3}$ was provided for a 43-mm thick MLI blanket. Section 6.2.4.3 gives an even lower effective emittance for a 100-mm thick MLI blanket of $2.5{\cdot}10^{-4}$ as determined in Section 6.2.4.3. These effective emittances are

needed to calculate the radiative heat transfer through the different insulation blankets. The calculations for the conductive heat transfer through the MLI use a MLI thermal conductivity of $0.1{\cdot}10^{-3}$ W/mK.
Furthermore, heat transfer through natural convection is assumed between the propellant and the inner tank wall. The propellant mass is modelled as one thermal node.

In Equations 6.24 and 6.25 the changes in temperature of the propellant and associated heat fluxes are computed based on the calculated convective heat transfer coefficient as seen in Equation 6.23. This coefficient uses the Nusselt number for natural convection in a horizontal cylinder as calculated in Equation 6.22 and derived from Churchill & Chu (1975). The associated Pr, Gr and Ra are respectively the Prandtl, Grashof and Rayleigh number Bergman et al. (2011).

$$Pr = \frac{\mu_l \rho_l c_{specific,l}}{k_l} \tag{6.19}$$

$$Gr = (9.81 \cdot \beta \cdot (T_{tank} - T_{prop}) \cdot \frac{2R_{tank}^3}{\mu_l^2} \tag{6.20}$$

$$Ra = Gr \cdot Pr \tag{6.21}$$

$$Nu = (0.6 + \frac{0.387 Ra^{1/6}}{(1 + (0.559/Pr)^{9/16})^{8/27}})^2 \tag{6.22}$$

$$h_{c_{prop}} = \frac{Nu \cdot k_l}{2R_{tank}} \tag{6.23}$$

$$T_{prop}(t) = T_{prop}(t-1) + \frac{h_{c_{prop}}(T_{tank}(t) - T_{prop}(t-1))A_{tank}}{M_{prop} c_{specific,l}} t \tag{6.24}$$

$$Q_{prop} = h_{c_{prop}}(T_{tank}(t) - T_{prop}(t-1))A_{tank} \tag{6.25}$$

$$\tag{6.26}$$

Here, $h_{c_{prop}}$ is the convective heat transfer associated with the natural convection between the propellant and the tank. The variables T_{tank} and A_{tank} represent respectively the propellant tank temperature and the propellant tank internal area.

The temperature at the insulation outer wall is kept constant at 273.15 K. The initial inner wall tank temperature is set close to the propellant storage temperature at 244 K. Natural convection processes in the tank are only taken into account for the propellant as convection to the helium gas will be limited due to the small thermal conductivity of the gas.
Comparing the different cases for the MLI the 43-mm thickness blankets are selected as the additional thermal control of thicker insulation is off-set by the increased insulation mass.

6.2.5.4.2 Propellant tank covered in MLI and interfacing with radiator panel

This design option is an adaptation of the previous option, but includes a circular dissipation conduit leading to a radiator panel. This panel dissipates the heat flow from the tank into space. A black-paint-coated radiative heat conduit runs from the tank on one side to the

Table 6.4: MLI performance

MLI blanket thickness [mm]	**Mass [kg]**	**Propellant tank temp. after 10 hrs [K]**
43	1.40	243.2
100	3.26	243.1

carbon-carbon honeycomb radiator panel on the other side. The tank radiative surface facing the radiator as well as the radiator interior and exterior have a silicone black paint coating and an emittance of 0.91 (AZ Technology 2008).
The conduit has a square cross-sectional area of $3{\cdot}10^{-3}$ m^2 and a length of 0.05 m. The panel has a frontal area of 0.01 m(2). Note that since the propellant tank is modelled as a single node and the surrounding unknown internal heat fluxes cannot be modelled, the conduit and radiator will most likely increase somewhat in size in real-life.

In Figure 6.16 a schematic is given for this thermal control system.
The assumption is made that the radiator sits constantly in the shadow-side of the spacecraft thereby not having to cope with external heat fluxes from the Sun or Earth.
In addition one assumes that the tank outer wall and inner wall have the same temperature.
After 30 hours the radiator panel temperature increases from the initial 100 K temperature to 139 K. The tank and propellant temperature stay constant at 243 K during the same period.
The radiator mass is 0.188 kg. The MLI mass is decreased by 6 g since a cut-out must be made for the conduit. As stated earlier, this panel can be integrated into the spacecraft bus, thereby not increasing the overall mass of the spacecraft. The radiator mass will however be included when comparing all the options.

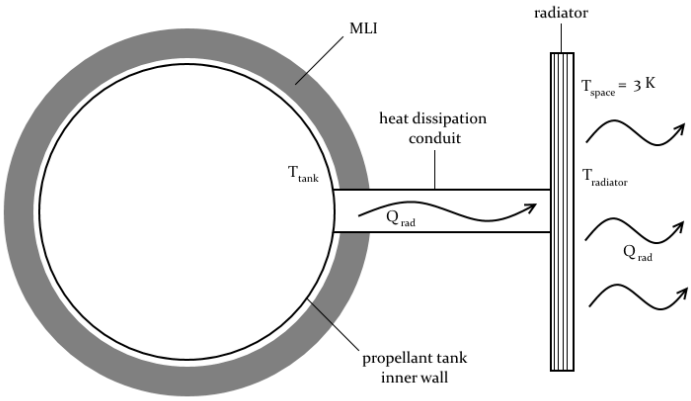

Figure 6.16: Schematic for radiator-propellant tank interface

The following heat flux equations apply to calculate the radiator and propellant tank temperature. Equation 6.25 and 6.27 are inserted into Equation 6.29. The term H is the width of the square radiator channel divided by the distance between the tank outer wall and the radiator interior.

$$F_{tank} = sqrt(1 + H^2) - H \tag{6.27}$$

$$C_{internal} = \frac{A_{tank}}{(t_{tank}/k_{tank}) + (t_{ins}/k_{ins}))} \tag{6.28}$$

$$\begin{aligned}\Delta Q_{tank} = &-Q_{prop} - \epsilon_{tank} A_{diss_{cs}} F_{tank} \epsilon_{rad_{int}} \sigma \left(T_{tank}^4 - T_{radiator}^4\right) \\ &+ \epsilon^* A_{tank} \sigma (T_{env}^4 - T_{tank}^4) + C_{internal}(T_{env} - T_{tank})\end{aligned} \tag{6.29}$$

$$T_{tank}(t) = T_{tank}(t-1) + \Delta Q_{tank} / \left(M_{tank} c_{tank}\right) \cdot t \tag{6.30}$$

$$\begin{aligned}\Delta Q_{rad} = &\epsilon_{tank} A_{diss_{cs}} F_{tank} \epsilon_{rad_{int}} \sigma \left(T_{tank}^4 - T_{radiator}^4\right) \\ &- \epsilon_{rad_{ext}} A_{radiator} \sigma T_{radiator}^4\end{aligned} \tag{6.31}$$

$$T_{rad}(t) = T_{radiator}(t-1) + \Delta Q_{rad} / \left(M_{radiator} c_{rad}\right) \cdot t \tag{6.32}$$

Here, $A_{diss_{cs}}$ is the heat conduit cross-sectional area. The mass of the propellant tank is M_{tank}. F_{tank} is the view factor from the tank to the radiator. Finally, T_{env} is the local environment temperature.

6.2.5.4.3 Propellant tank covered in MLI and covered with OSRs

The final thermal control option which is analyzed is the propellant tank which interfaces directly with space and uses OSRs to cope with the external heat fluxes which are dominant in a LEO environment.
Ten percent of the tank inner surface area is adopted as the area outside of the spacecraft bus. It is covered with OSRs. The remaining surface is covered with 43-mm thick MLI. The OSRs have an emittance and absorptance of respectively 0.83 and 0.085 (Qioptiq 2014). They have a density of 2.5 g/cm^3 and an assumed thickness of 0.5 mm. As the OSR area is 0.072 m^2, this yields a mass of 91 g.
For this option, Equation 6.29 changes to Equation 6.33.

$$\begin{aligned}\Delta Q_{tank} = &-Q_{prop} + Q_{ext} - \epsilon_{osr} \sigma A_{osr} T_{tank}^4 \\ &+ \epsilon^* \left(A_{tank} - A_{osr}\right) \sigma (T_{env}^4 - T_{tank}^4) + C_{internal}(T_{env} - T_{tank}) \\ &- \epsilon_{tank} A_{diss} F_{tank} \epsilon_{rad_{interior}} \sigma \left(T_{tank}^4 - T_{rad}^4\right) \\ Q_{ext} = &\epsilon_{osr} A_{osr} S_{Earth_{ir}} + \alpha_{osr} A_{osr} S_{Earth} + abs_{osr} A_{osr} S\end{aligned} \tag{6.33}$$

Here ϵ_{osr} is the OSR emittance, α_{osr} is the OSR absorptance, ϵ^* is the effective emittance of the propellant tank, ϵ_{tank} is the emittance of the coated tank wall, A_{osr} is the OSR area, A_{tank} is the total tank outer area and A_{diss} is the area of the dissipation conduit. Finally, $S_{Earth_{IR}}$ is the IR radiation emitted by the Earth, S_{Earth} is the Earth albedo and S is the incoming solar flux.

Analysis yields that the tank temperature after 10 hours increases to 245.9 K with an increasing temperature gradient.

6.2.5.4.4 Comparison of propellant tank thermal control options

In Table 6.5 the thermal control options for the propellant tank are compared.

Table 6.5: Comparison of thermal control options

Thermal control option	MLI mass [kg]	Propellant tank temp. after 10 hrs [K]
43-mm thick MLI	1.40	243.2
43-mm thick MLI and radiator	1.58	243.0
43-mm thick MLI and OSRs	1.49	245.9

Applying only MLI is the best option in terms of mass. Over the entire one-year mission the propellant tank will however increase in temperature. Applying an additional radiator keeps the temperature constant and adds a relatively large amount of mass.
The OSR option causes a substantial increase of the propellant tank temperature as the external heat fluxes cannot be overcome by the system.
Given that the radiator can be integrated into the bus, the MLI-radiator option is therefore selected.

6.2.5.5 Valves

A number of valves are used to control the propellant flow in the propulsion subsystem as dictated by Requirement 7. The following sections give examples of the commercial valves which have been found after a small procurement study. In case the relief and check valves cannot cope with the high propellant temperatures, molybdenum or tungsten coatings and materials could be used. During the procurement study however, no small valves with such materials were found, so in that case custom options should be pursued.

6.2.5.5.1 Solenoid valves

A solenoid valve is used to activate the propellant flow at the propellant tank once the OBC decides the temperature in the cavity is high enough. Here, the propellant flow initialization cavity temperature is 1300 K.
Upon eclipse, when the sun sensor gives no more output, or when thrust is no longer necessary, the OBC commands the solenoid valve to deactivate the flow.
A Gems B-Cryo Series solenoid valve can handle cryogenic temperatures down to 77.15 K. It has a length of 5.8 cm, a maximum width of 5 cm at the lead connectors and 1 cm diameter for the tube ports. It uses 9 W of power (Gems 2014) and has a mass of 0.154 kg.

6.2.5.5.2 Pressure regulator valve

Behind the solenoid valve one pressure regulator valve limits the propellant flow pressure to the appropriate level.
Temperature gauges around the RAC and behind it monitor the temperature of the RAC and the propellant flow. The readings are sent to the OBC which directs the pressure regulator to open or close its valve.
The pressure regulator needs to cope with cryogenic temperatures and must decrease the feed pressure from 11.4 bar to 2.28 bar at the maximum. A Samson 2357-1 Pressure Reducing Valve is used. It operates from 1 to 25 bar and can handle temperatures as low

as 77 K. Hence, this valve satisfies the requirements. It has a length of 20 cm, a width of 15 cm and a rather large mass of 2 kg. Its inlet and outlet diameters are 1.5 cm (Samson 2014).

6.2.5.5.3 Pressure relief valves

The pressure relief valves have to handle high-temperature inlet gases when a certain pressure is exceeded downstream of the RAC tubing. These valves will not be actuated frequently, but only in emergency situations to prevent over-pressurization in the thruster and subsequent damage to the nozzle.
A Flowsafe F84 Micro Safety Valve can be used which has an 3.5 mm inlet diameter, a length of 17 cm and a width of 6.6 cm. It operates from 1.03 bar to 280.75 bar and temperatures from 20.4 K to 547 K (Flowsafe 2014). Its mass is 0.454 kg due to the heavy metal body.
In the case of large excess pressure in front of the thruster, the flow is diverted to two relief valves which expel the flow into space. Each relief valve leads to the opposite side of the spacecraft with respect to the other to prevent spacecraft attitude disturbances upon flow venting. The combined mass therefore is 0.908 kg.

6.2.5.5.4 Check valves

A check valve is positioned right in front of the thruster chamber to prevent a propellant flow with sub-chamber pressure to propagate into the thruster.
Two check valves are also used to fill the propellant tank with propellant and pressurant gas. These valves are known as fill check valves.
A Spirax Sarco DCV41 disc check valve is used. Its maximum operating temperature is 673.15 K and maximum operating pressure is 30 bar. It is 50 mm in length and 34 mm in width. Its mass is 0.2 kg (Spirax Sarco 2014).

Summing up all valve masses yields a total valve mass of 3.66 kg.

A schematic of the feed system architecture is provided in figure 6.17.
Note that a solar sensor is included and is connected with the OBC to check whether the spacecraft is in daylight or eclipse as to not activate the propellant flow while in eclipse. This would lead to low RAC temperatures, as seen in Section 5.1.2.4.

6.2.6 Mass budget

In Table 6.6 the mass budget for the propellant feed system is given.
The total mass is calculated by summing the budget up and including a 10% design margin.
The tank radiator is not included as it can be integrated into the spacecraft bus. This yields a total propulsion subsystem mass of 36.2 kg.

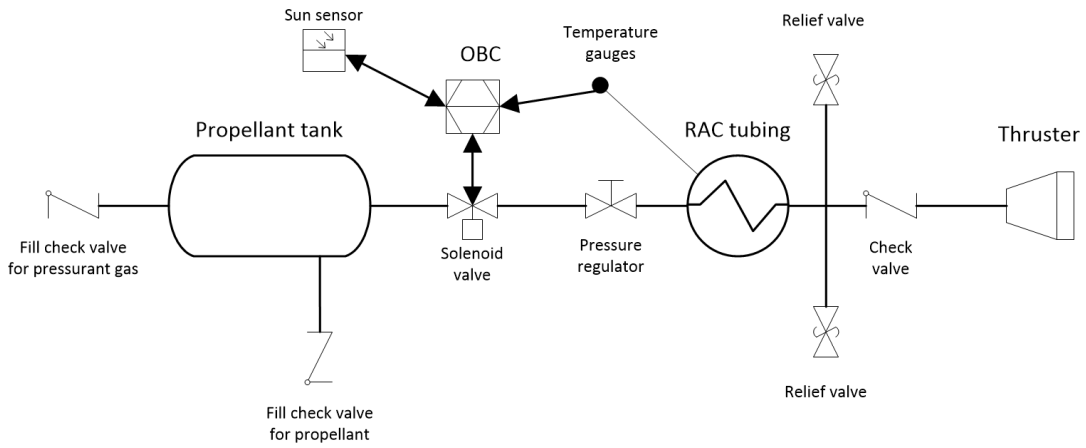

Figure 6.17: System architecture of the propellant feed system

Table 6.6: Mass budget for propulsion subsystem

Component	Mass [kg]
RAC system	24.78
Propellant tank	2.10
Propellant tubing	0.91
Valves	3.66
Tank insulation	1.40
Thruster	0.06
Design margin	3.29
Total	36.2

6.3 Power subsystem

6.3.1 Functional and physical architecture

As in Section 6.2.1 a functional and physical architecture are synthesized for the power subsystem.
Figure 6.18 shows the functional architecture. The output power and condenser radiator temperature define the system behavior as values outside of the operational range can cause sudden loss of power and damage to the subsystem components, in turn lowering reliability.
In case the radiator temperature increases too much due to exposure to external fluxes, the radiator must be pointed away from these fluxes by the ADCS. Also when the power output is too high a part of the electrical energy needs to be dissipated to space or redistributed to other parts of the spacecraft by the thermal control subsystem.

This diagram is compared with the physical architecture in Figure 6.19 to ensure completeness. One notes that a lot of pressure and temperature gauges are present. This is to have a sufficient amount of measurement points as the ORC maintains a delicate energy balance in order to function with enough efficiency. More measurement data means that the OBC

can detect changes in the working fluid conditions more easily and faster. This allows it to faster mitigate any disturbances caused by external factors or power subsystem errors.

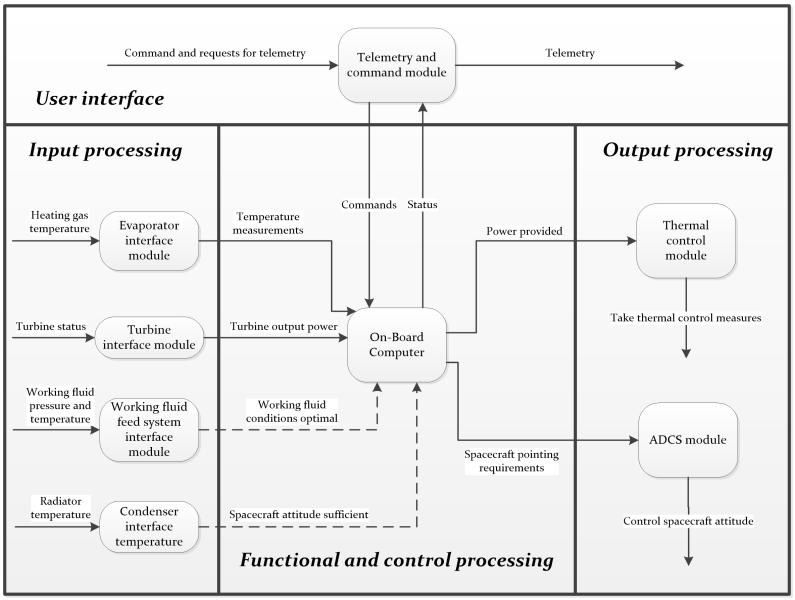

Figure 6.18: Hatley-Pirbhai diagram for power subsystem

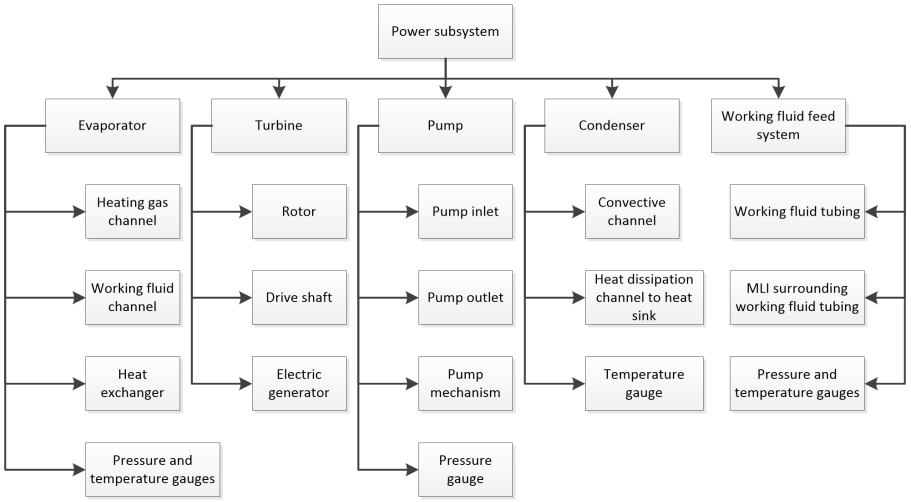

Figure 6.19: Propulsion subsystem physical architecture

6.3.2 Evaporator

Previously, the evaporator received heat from the RAC through a number of heat conducting channels since these were easy to model.
There is however also the possibility of using radiation to transfer heat from the RAC to the evaporator heating gas channel inner wall as shown in Figure 6.1.

The former and latter options will be compared with one another. Recall that the heating gas in the channel is air.

6.3.2.1 Heat transfer through conduction

The conducting channels were modelled by four solid molybdenum rods.
In order to facilitate an equal distribution of heat from the RAC to the evaporator in real-life, the rods will have to be replaced by a larger number of molybdenum straps. A thickness of 5 mm, a width of 18 mm and a length of 120 mm for each rectangular thermal strap is determined. The system then requires 14 straps.
The thermal straps are attached to the cavity outside wall and to the evaporator heating gas channel outer wall with bolted connections. These connections protrude from the RAC and evaporator circumferences. Their combined mass is 1.54 kg.
The saved mass due to MLI cut-outs is 3 g.

6.3.2.2 Heat transfer through radiation

Radiative heat transfer is achieved by removing the MLI between the heating channel and the RAC and optimizing the emittance of both outer surfaces.
This creates a radiative heat transfer channel through which heat can be transmitted. The sides of the channel are bounded by insulation to make sure no residual heat is transferred to other parts of the spacecraft interior.
When calculating the view factor in Equation 6.34, the propellant tubing is not taken into account. The exposed RAC area is modelled as a flat plane. The heating gas channel is modelled as a symmetrically placed cylinder since it runs along the circumference of the RAC.

$$F_{RAC-channel} = \frac{1}{\pi} \arctan \frac{b}{a} \frac{A_{channel}}{A_{RAC}} \tag{6.34}$$

Here, b represents the width of the plane opposite the cylinder and a is the distance from the plane to the center of the cylinder.
The heat flux from the RAC to the heating gas channel is then estimated as follows:

$$Q_{RAC-channel} = \epsilon_{RAC} A_{interface} \epsilon_{channel} \sigma \left(T_{RAC}^4 - T_{channel}^4 \right) \tag{6.35}$$

In Figure 6.20 the two options are illustrated,

After iterating it becomes clear that the radiative heat transfer necessitates a redesign of the heating gas channel.
Its inner diameter increases from 1.69 cm to 2.96 cm, its wall thickness from 1.5 mm to 2.7 mm and the minimum length between channel outer wall and RAC outer wall decreases from 12 cm to 2 cm. As a result the mass of the heating gas channel which is adjacent the RAC increases from 0.571 kg to 0.940 kg. An RAC section with a width of 10.5 cm needs to be left uninsulated on the side of the heating gas channel. This saves an MLI mass of 45 g.
In addition the generated specific impulse decreases and the thrust increases slightly.

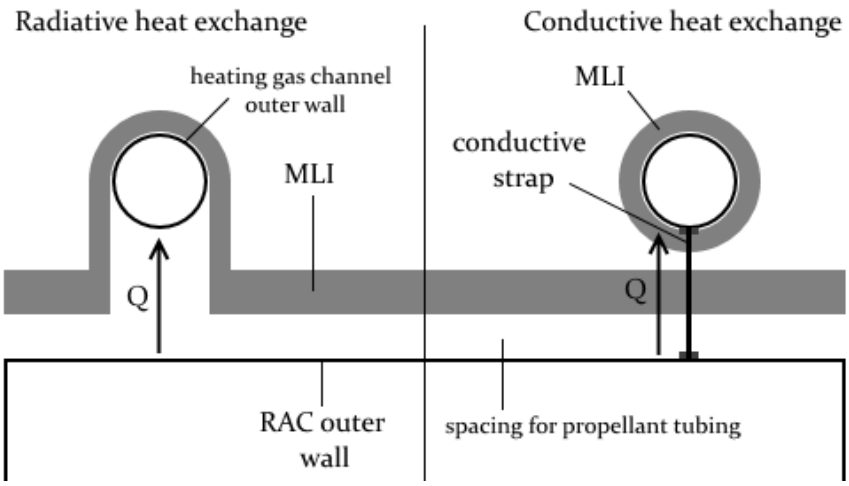

Figure 6.20: Schematic for heat exchange options between RAC and heating gas channel

6.3.2.3 Comparison of heat transfer options

The two options can be compared in terms of resulting system volume, mass increase with respect to the initial system and complexity. In terms of complexity the insulation integration around the RAC becomes more challenging for the second option. On the other hand for the first option fitting the conductors and making sure the heat is spread evenly around the heating channel is daunting as well. Therefore, no significant simplicity advantages are to be gained from either option. Table 6.7 gives the comparison for the other two criteria.

Table 6.7: Mass budget for propulsion subsystem

Option	Mass increase [kg]	System Volume [m^3]
Radiative heat exchange	0.324	0.079
Conductive heat exchange	1.537	0.132

Not only does the adoption of the radiative exchange option decrease the system volume, it also decreases the system mass. Concluding, the radiative heat transfer channel is applied as interface between the RAC and the evaporator heating gas channel.

6.3.2.4 Evaporator heating gas channel properties

The evaporator heating gas channel is a thin-walled molybdenum tube which enters and exits the evaporator heat exchanger at one end and wraps around the RAC on the other end. The air in the heating gas channel is fed into the heat exchanger at a pressure of 5 kPa.
Between the cavity and the heating gas channel outer wall a spacing of 2 cm exists. The heating gas channel itself is also insulated with MLI to prevent heat dissipation to the interior of the spacecraft.
A part of the heating gas channel is fastened mechanically to the previously mentioned cavity frame.

The channel has an outer diameter of 3.5 cm and a tube thickness of 2.7 mm. The heating gas channel around the RAC has a mass of 0.940 kg.

6.3.2.5 Evaporator heat exchanger

The heat exchanger is one of the most important components, next to the turbine, as it puts energy into the system. In Figure 6.1 three different heat exchanger options are specified:

- a plate heat exchanger;
- a shell and tube heat exchanger;
- and a pate fin heat exchanger.

The scope of this thesis is such that a full examination of the performance of the different options will not be performed. It does however merit further analysis in future research efforts.
For the sake of the design, a representative plate fin heat exchanger is selected with 18 plates GEA-PHE Systems (2014). This heat exchanger uses plates with fins in between to transfer heat from a gas to a liquid. The heat exchanger is designed for a gas input temperature of 905 K and a liquid input temperature of 355 K which is in the range of the temperatures for the system. Furthermore the maximum gas pressure is 13.8 kPa which is more than the required 5 kPa.
The heat exchanger has a volume of of $9.21 \cdot 10^{-3}$ m^3 and a mass of 14 kg. In addition, the fluid tubing connector diameter is a minimum of 1.27 cm which is less than the evaporator tubing diameter of 1.75 cm, making integration possible.

6.3.3 Turbine

As seen in 6.19 the turbine consists basically of a rotor or fan, a drive shaft and an electric generator which converts the turbine mechanical power into usable electrical power.
Due to the small required power output, the turbine will be small and fall in the micro-turbine category. Even in this category power outputs can still reach 1-100 kW depending on the mass-flow.
The turbine in this system must deal with a turbine inlet temperature of the toluene of 565 K, an inlet pressure of 13.67 bar and a working fluid flow rate of 0.85 g/s. According to the *ORCHID-VPE*-model it will deliver a power of 115 W after the third orbit in space.
In Invernizzi et al. (2007) the mass flow rate versus the power output for a number of commercial micro-turbines is given. The minimum two data points are given at 300 g/s and 400 g/s which respectively yield 30 and 40 kW power. Linearly scaling this down results in 100 W power at a mass flow rate of 1 g/s which is close to the actual working fluid mass flow.

Although such a low power turbine seems infeasibly small, MEMS technologies allow turbines to function through a large number of cycles. Different micro-turbine designs have been found in literature:

- Epstein (2003) provides a turbine. This turbine delivers 198 W with a volume of only 66 mm^3 at a mass flow rate of 0.18 g/s and a flow inlet temperature of 500 K. The cross-sectional area for this device is 60 mm^2 which represents a turbine rotor diameter of around 8 mm. The turbine in this ORC is assumed axisymmetric and circular.
- PowerMEMS (2014) details a larger gas turbine with a rotor diameter of 20 mm. The turbine efficiency for this device has been determined to be 78%. This gas turbine can generate 100 W of power at 280,000 rpm and a turbine inlet gas temperature of 700 K. The turbine is designed for a nominal working gas mass flow of 20 g/s.
- Yamamoto et al. (2001) provides test results for an aluminium micro-turbine with 18 blades and a diameter of 3 cm. Tests show that when the working fluid is water and the evaporator heat input is 18.2 kW, the turbine generates 150 W at a rotational rate of 20,000 rpm.
- Schubert (2012) details the design of a 66-g micro-turbine which generates a power output of 16 W. It has been tested up to a speed of 160,000 rpm.

Looking at the devices above, the rotor radius for the turbine in this design will most likely be in the range of 1-3 cm.
Figure 6.1 mentions a choice between single-stage and multi-stage turbines. Multi-stage turbines only offer a small efficiency increase with respect to single-stage turbines. Furthermore the additional mass and decreased reliability is undesirable. In addition, most micro-turbines are single-stage devices (Soares 2015, p. 836-837). Therefore a single-stage configuration is selected.
To estimate the mass of the turbine the mass given in Schubert (2012) is scaled linearly to the appropriate power output as stipulated by Epstein et al. (1997). This yields a turbine mass of 0.413 kg for the turbine.

Concluding from this group of turbines, the micro-turbine necessary for this hybrid system will have to be designed specifically for the system.
The literature cited in this section however gives the author confidence that such a turbine is feasible for manufacturing and laboratory testing thereby achieving at least a TRL of 4. In particular the turbine's performance over long periods and for a very large number of cycles should be tested to ensure that power generation can occur during the entire mission.

6.3.4 Condenser

In Figure 6.1 an active and passive condenser are considered for dissipating the ORC excess heat.
An active condenser would make the system design more complex as more (cooling) fluid tubing must be integrated. Furthermore, the additional tubing and heat exchangers would make the condenser subsystem unnecessarily heavy.
Therefore, a passive condenser is chosen where heat is either dissipated to space or redistributed into the spacecraft. A combination of the two is also possible with the

application of louvers.

The active condenser in the *ORCHID-VPE*-model needs to dissipate 573 W to ensure a working fluid temperature of 313 K. The same amount of heat needs to be dissipated by the passive condenser.
In Baturkin (2005) thermal control for small satellites is discussed alongside temperature ranges for typical spacecraft components. Batteries and OBCs operate between -5 and +15 degrees Celsius. Other electrical and ADCS equipment requires a range of -5 to +40 degrees Celsius. A number of assumptions are made in order to make a rough estimate of the amount of heat which is required to keep some of these components within acceptable temperatures:

- A representative box with a total external area of 1 m^2 with an emissivity of 0.80 must be kept at a temperature of 15 degrees Celcius or 288.15 K.
- The volume is not insulated and interfaces with an interior spacecraft environment at a constant temperature of 173.15 K.
- The area has a view factor of 0.9 to its surroundings.

Using Equation 3.54 this requires 223 W of heat.

The radiator must therefore dissipate 350 W to space. The heat can be transferred through radiation or conduction between the condenser and the radiator. Radiative heat transfer would however necessitate a condenser radiating surface to the radiator panel, assuming a radiation path length of 1 cm, of 3-4 m^2 which is too large for the system.
Hence, conducting conduits are mounted between the condenser and the radiator. The condenser working fluid channel and the conduits are made of copper because it has a high conductivity and can withstand the involved temperatures. It also has a lower density than the tungsten and molybdenum alloys under consideration.

After a number of iterations a condenser conducting conduit with a length of 10 cm and a diameter of 16 mm is calculated to transfer the heat. The condenser outer radius is 8.5 mm and the length over which the working fluid is cooled is 5 cm. The wall thickness of the section is 1.3 mm, taking the same ratio as used for the tubing in the propulsion subsystem (Section 6.2.5.2). The mass for the condenser channel and the condenser conducting conduit are respectively 0.029 kg and 0.180 kg which yields a total mass of 0.209 kg.
The black-paint-coated radiator panel has a total cross-sectional area of 0.4 m^2. The aim is to incorporate this radiator into the spacecraft bus or otherwise provide a body-mounted radiator.
Deployable radiators are also an option but increase the mass and system complexity of the satellite (Lashley et al. 1998).
Alternatively, more of the heat flux can be diverted for additional spacecraft thermal control which will decrease the size of the radiator and condenser. Internal louvers, thermal straps and coatings can propagate the right amount of heat into the spacecraft.

6.3.5 Pump

The micro-pump which will be used will use miniaturized and/or MEMS technology. A reference micro-pump is selected to estimate a mass for the component. Recall that the mass flow of the working fluid in the ORC is 59 mL/min and that the pressure in front of the turbine is 13.67 bar. Micropump (2014) provides the GA Series pump. This device is a magnetic drive pump with a maximum speed of 8000 rpm. It operates for a minimum and maximum mass flow of respectively 8.5 and 552 mL/min and a maximum pressure of 21 bar. The device uses 100 mW and has only a mass of 0.34 kg.

6.3.6 Working fluid feed system

Finally, an estimate of the working fluid tubing length and mass need to be given. This necessitates an estimate of the tubing path within the spacecraft bus.
Due to the relatively low temperature of the working fluid, an Al-6061 aluminium alloy is used for the working fluid tubing.
The tubing's maximum extent runs adjacent the RAC to the 10 cm separating the condenser from the radiator. This is a distance of 33 cm as the RAC sits in the center of the spacecraft.
The assumption is made that the tubing runs in a more or less rectangular cycle with the evaporator, condenser, pump and turbine being placed on each side. Two sides have a length of 33 cm. The other sides have an arbitrary length of 15 cm. This yields a total tubing length of 1.06 m, including a 10% margin for bends.
The outer tubing radius and wall thickness are assumed to be 8.5 mm and 1.3 mm, the same properties as the condenser channel.
Multiplying the cross-sectional area with the total length and the alloy density yields a working fluid tubing mass of 0.184 kg.

Note that since the system can deliver power continuously, no batteries are required. In case less power than 100 W is used or more power is generated, power will have to be dissipated or fed back to the RAC. The design of such a system is beyond the scope of this thesis, but will have to be performed for a flight-ready system.

6.3.7 Mass budget

In Table 6.8 the mass budget is given for the power subsystem. The total mass amounts to 19.3 kg. A 20% design margin is applied on top of the other mass components to account for unknowns, such as the toluene and air mass in the power subsystem.

Table 6.8: Mass budget for power subsystem

Component	Mass [kg]
Evaporator & interfaces	14.94
Turbine	0.41
Condenser	0.21
Pump	0.34
Working fluid tubing	0.18
Design margin	3.22
Total	19.30

6.4 System integration

Before all the components can be assembled, functional test need to validate that the components are functioning as planned.
If these tests are successful, first the spacecraft bus needs to be fitted with the mechanical support structures for the components of the propulsion and power subsystems, such as the frame surrounding the RAC.
After aligning the secondary concentrator, its casing and all other components leading up to the RAC, these components are mechanically fastened. Thereafter the insulation is placed around the components. At this point the cavity is fitted next to the cavity lid and the thermal straps are attached. The propellant tubing is fitted with the molybdenum fasteners. Now, the insulation can be applied around the cavity with the necessary cut-out for the interface with the evaporator heating gas channel and the PODS. The heating gas channel is mounted to the RAC frame.
The tubing can now be mechanically fastened at the threaded ends to the up-stream propellant feed system and the down-stream tubing leading to the thruster chamber. In the mean time the thruster has already been mounted on the other side of the spacecraft and the remainder of the tubing is connected to the chamber.

Once the power subsystem and the propellant tank and valve have been mounted, the hybrid system is integrated and can be tested Integration tests yield whether the integrated system functions and acts as expected. This is not only in terms of the actual hardware but also in terms of the software. Fault detection and mitigation is part of the latter for example. Environmental tests will validate whether the integrated system can cope with the harsh radiation and temperature environment in LEO.

In Table 6.9 the mass budget for the entire hybrid system is given. The final propellant mass is also included for comparison. A total mass of 85 kg has been determined which is almost 60% the original 144 kg estimate. Note that the previously mentioned MLI surrounding the entire propulsion subsystem is not included as its geometry is dependent on the total spacecraft interior architecture.
After calculations, roughly 0.83 m^3 remains of the total 1 m^3 spacecraft bus volume for instruments and other subsystems. This estimate takes into account the square envelope of the propellant tank rather than just the storage volume as in Section 6.2.5.3. This hybrid solution can therefore be considered a high-density system.

Table 6.9: Mass budget for total hybrid system

Subsystem	Mass [kg]
Propulsion	36.2
Power	19.3
Propellant	29.3
Total	84.8

After running the model for a final time, Figure 6.22 and Figure 6.23 yield a thrust, specific impulse and power of respectively 1.31 N, 185 s and 115 W. Figure 6.21 shows the temperature profile for the design. Figure 6.24 yields a maximum efficiency in the third orbit of 0.37 and a minimum efficiency in eclipse of 0.17. The system-specific impulse is 65 s.

This detailed design is compared to a conventional system in the next section.

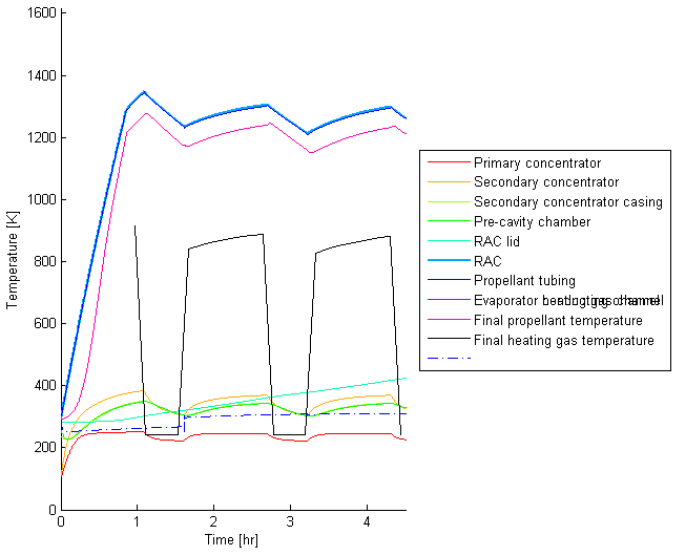

Figure 6.21: Temperature profile for detailed design

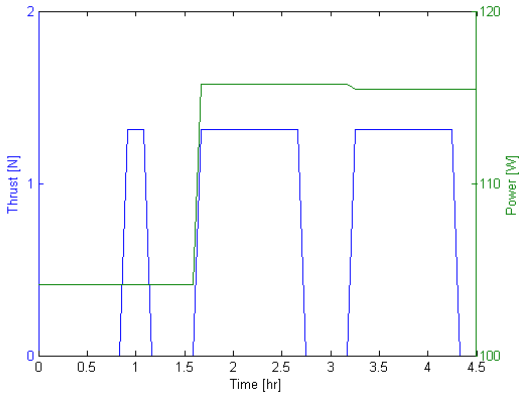

Figure 6.22: Thrust and power for detailed design

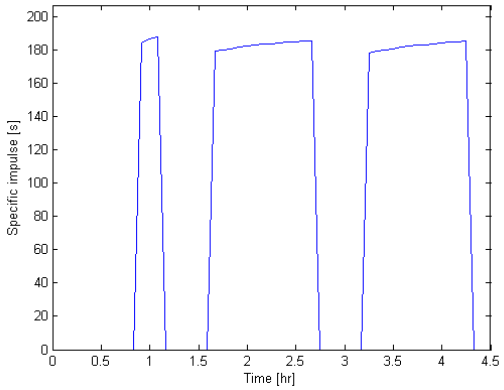

Figure 6.23: Specific impulse for detailed design

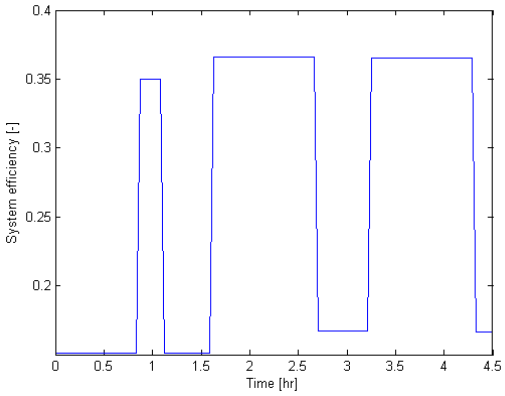

Figure 6.24: System efficiency for detailed design

6.5 Comparison with conventional system

In this section the detailed design which was synthesized in Chapter 6 is compared with a conventional power and propulsion system. The comparison criteria are the following:

- System mass
- System volume
- Power generating capability
- Specific impulse
- Thrust

These criteria represent the power and propulsion performance of the two systems as well as their impact on spacecraft mass and integration.

The two systems must provide at least 100 W power during both daylight and eclipse. In eclipse 10% dissipation is assumed in the power storage subsystem which yields a required power of 110 W for the conventional system. The hybrid system can dispense with batteries and therefore has to generate 100 W in eclipse.

6.5.1 Conventional power and propulsion system

A conventional small satellite uses solar cells and a mono-propellant thruster to generate power and thrust. In eclipse a number of batteries must be fitted so that the spacecraft can keep functioning whilst orbiting in the shadow of the Earth. Larson & Wertz (2005) gives overall design data and equations for the conventional system.

6.5.1.1 Power subsystem

The solar array efficiency in eclipse and daylight, $\eta_{eclipse}$ and $\eta_{daylight}$, are respectively 0.60 and 0.80. The inherent degradation I_d factor for Gallium Arsenide solar cells is 0.77. The lifetime degradation rate per year L_d is 2.75%. The multi-junction cells have an efficiency of 27% as reported by Andreev (2011) and confirmed by procurement data in Emcore (2014).

The following equations can be applied to calculate the necessary solar cell area.

$$P_{required} = \frac{\frac{P_{nominal}T_{eclipse}}{\eta_{eclipse}} + \frac{P_{nominal}T_{daylight}}{\eta_{daylight}}}{T_{daylight}} \tag{6.36}$$

$$P_{EOL} = S\eta_{cell}I_dL_d\cos(\theta) \tag{6.37}$$

$$A_{solar-array} = \frac{P_{required}}{P_{EOL}} \tag{6.38}$$

The T-terms stand for the periods of eclipse and daylight during each orbit. The S is the received mean solar flux in the specific orbit (1371 W/m^2) and θ is the solar incidence angle. In this analysis the worst-case scenario of 23.5 degrees is assumed. Finally, η_{cell} is the previously discussed solar cell efficiency.

The mass of the solar cells are calculated by summing up the mass of the solar cells with the mass of the underlying honeycomb substrate panel. The density of the solar cells is 84 kg/m^2 (Emcore 2014). An Al-5052 aluminium alloy honeycomb material is selected for the substrate panel. According to Hexcel Composites (2014) the density of a 16-mm thick panel is 64 kg/m^2. Multiplying the two density values with the solar array area of 0.842 m^2 and summing them up, yields a total solar array mass of 1.56 kg. This solar array can easily be fitted on a 1-m wide spacecraft bus.

Batteries need to supply at least 110 W during eclipse as the power supply will be maintained during the daylight part of the orbit. Maximum eclipse time is 0.53 hours. The batteries therefore need to supply 59 Wh.
Two GomSpace NanoPower BP4 lithium ion battery packs are therefore fitted to the

spacecraft. Each can store 38.5 Wh of power. Their combined mass is 0.48 kg (GomSpace 2014).
Assuming a 43 mm-thick MLI layer surrounding the two batteries, a worst-case environment temperature of 100.15 K and an internal dissipation of 10 W, 10 W needs to be dissipated away to keep the batteries within their 0-20° Celsius temperature range.
In case of no insulation, no conductance with the environment and a low emissivity for the batteries of 0.1, 8.5 W needs to be dissipated for thermal control.
The sum of the battery and solar array mass is 2.04 kg.

6.5.1.2 Propulsion subsystem

Astrium (2012) provides a small hydrazine mono-propellant thruster which satisfies the system requirements. It generates 1.1 N in thrust and has a specific impulse of 220 s. It has a mass of 290 g and the thruster outer envelope volume is $2.16 \cdot 10^{-4}$ m^3.

The required propellant mass is calculated according to Equation 3.93. The equivalent exhaust velocity U_{eq} is calculated by multiplying the thruster's given specific impulse with the standard gravitational acceleration g_0.

The Al-6061 aluminium alloy propellant tank has a thickness of 1 mm, a mass of 1.81 kg and a volume of 0.037 m^3. As in the hybrid system an extra 20% residual propellant is fed into the tank. In addition a 20% ullage volume is added. The feed system is assumed to have half the mass of the propellant tank. The hydrazine propellant mass is 24.53 kg. A 43-mm thick MLI blanket is applied around the propellant tank and has a mass of 1.3 kg. The combined mass for the wet propulsion subsystem then becomes 28.84 kg.
The total impulse and system-specific impulse are respectively 35 kN·s and 123 s. Note that pressurant gas is not taken into account, but that its mass is assumed negligible.
The total mass then becomes 30.9 kg. The system encompasses an estimated total volume of 0.07 m^3.

6.5.2 Performance comparison

In Table 6.10 the hybrid and conventional power and propulsion systems are compared. They are compared in terms of mass, volume, thrust, specific impulse, system-specific impulse and operational constraints.

Table 6.10: Hybrid and conventional systems comparison

System	**Mass [kg]**	**System volume estimate** [m^2]	**Thrust [N]**	**Specific impulse [s]**	**System-specific impulse [s]**	**Power [W]**
Conventional	30.9	0.07	1.10	220	123	110
Hybrid	84.8	0.08	1.31	185	65	115

One can see that in terms of the performance parameters the conventional system performs better than the hybrid system.

The hybrid system under-performs especially in terms of mass and system-specific impulse. Looking at operational constraints, the following statements can be made:

1. The hybrid system can generate power during the entire orbit, whereas the conventional system has to store significant amounts of power during orbit eclipse.
2. The hybrid system's primary concentrator will have to be positioned differently depending on the RAC's temperature and the Sun incidence angle. An on-axis concentrator configuration will hence limit the maneuverability of the spacecraft. The conventional system does not have this problem.
3. Hydrazine features in many conventional thrusters, is highly toxic and therefore needs to be handled carefully when filling the propellant tank. There is however a lot of experience with hydrazine systems.
4. When the solar array is integrated into the spacecraft bus, this leaves less room for cut-outs, instruments and thermal control devices.

Concluding, the hybrid system has the clear advantage of not needing batteries and being able to deliver power the entire orbit. This allows the spacecraft to perform at peak-power at any moment in the orbit without using batteries. The hybrid system is however inferior to the conventional system in terms of size, mass and system-specific impulse.

Chapter 7

Answering research questions

In Chapter 2 the research questions were introduced. This chapter will answer these questions based on the thesis study as reported in previous chapters.

What is the difference in thrust and specific impulse when the propellant is changed?
If one looks at the difference in thrust and specific impulse when the propellant is changed from ammonia to hydrogen, the thrust decreases only marginally by 5%. The specific impulse however is increased by a factor of 3.2 to 4.0, depending on the RAC configuration. Nitrogen lowers the thrust by 4% and the specific impulse drops only two seconds with respect to ammonia. Water will barely increase the thrust and increases the specific impulse by 9%.

What is the difference in system mass and volume when the propellant is changed?
On average the tank volume increases by a factor of 2.2-2.6 if ammonia is replaced by hydrogen. The wet propulsion system mass decreases by a factor of 1.4-1.5 with respect to ammonia, even though the dry mass decreases by only 5-7%. This is caused by the fact that hydrogen has a higher energy-density than ammonia and therefore those systems require less propellant. The total system mass therefore also decreases.
The hydrogen concepts have a 1.7 times larger primary concentrator diameter than the ammonia concepts.
The difference in footprint area within the spacecraft varies between individual concepts, although ammonia concepts have a larger footprint than the hydrogen concepts.
One can therefore conclude that using liquid hydrogen creates a lighter system with a larger volume with respect to the use of liquid ammonia.

Judging from the answer to this research question and the previous one, liquid hydrogen is the best propellant in terms of performance. Cryogenic storage issues as detailed in Section 5.9.1.3 make the use of liquid hydrogen very difficult however.

How representative is the performance of an STP thruster with gaseous nitrogen with respect to a thruster which uses a liquid propellant?
Concept 1 is used as a reference. Since the room-temperature density of gaseous nitrogen is lower than that of liquid propellants, the storage volume is infeasible at 35 m^3.
Alternatively, a small storage volume of 0.10 m^3 needs a very large pressurization of 35 MPa which significantly increases the propellant tank mass. This research question however only applies for testing purposes which require less ΔV. Therefore, the storage volume is of less a concern.

Model results yield that by replacing liquid ammonia in Concept 1 with gaseous nitrogen a specific impulse is achieved of 160 s which is 2 s less than the original concept. The thrust only decreases from 1.267 N to 1.213 N which is a 4% decrease. One can therefore state that the 'nitrogen' results approach the performance of the liquid ammonia systems.
If one looks at the performance of Concept 2 however, replacing the liquid hydrogen propellant with the gas provides one with an unrepresentative result as the specific impulse of liquid hydrogen systems exceeds 600 s. This is a level of performance which a simple replacement of the propellant cannot achieve. A complete system redesign could make it possible, but that would defeat the purpose of a representative terrestrial thrust test with nitrogen.

Concluding, nitrogen can be used in tests to validate a liquid ammonia solar thermal hybrid system with a margin in terms of accuracy. Hence, these tests should only be used to initially validate the system if funds are limited; to fine-tune the design a test with gaseous nitrogen is not suitable.

Which design keeps the primary concentrator size to a minimum?
As stated in Chapter 5 the concepts which use ammonia, namely Concept 1, 3 and 5, limit the primary concentrator size the most.

Which combined propellant tubing and RAC configuration provides the fastest and largest heat exchange between the RAC and the propellant?
This question is a measure of the specific impulse and the time at which the propellant flow is initialized in the first orbit. First of all, Concept 2 and 6 have the highest specific impulse.
Second, Table 7.1 gives the results for the second criterion. Clearly Concept 2 and Concept 6 again have the best scores. Overall, the spherical RACs achieve the 1300 K initialization temperature the fastest.
In terms of system efficiency the conical RAC is the most efficient, both in eclipse and daylight periods, followed from higher to lower efficiency by the cylindrical and spherical RACs.

Table 7.1: Flow initialization times for concepts

Concepts	Time [hr]
1	0.72
2	0.28
3	0.89
4	0.31
5	0.31
6	0.11

Which interface design with the power subsystem offers the required heat transfer whilst keeping its size and volume limited?
In Section 6 both a conductive and radiative interface were modelled and compared. A conductive interface is smaller in size and volume, since a radiative interface needs a large radiating area between the heat exchanging surfaces. The radiative interface has a smaller mass however as it requires no physical connection between the RAC and the evaporator heating gas channel.
Therefore a radiative interface is more advantageous here since mass is a KPP for the design.

What is the degree of scalability of each system design?
This has been discussed in Section 5.6.
In terms of thrust the systems are quite scalable since doubling the thrust requirements twice is possible within the same design with only minor design changes.
The power cannot be scaled easily as the large dissipative heat flux out of the condenser cannot be easily achieved with higher power outputs.
Scaling the specific impulse requires not only the selection of other propellants, but also the redesign of the interface between the RAC and the evaporator heating gas channel.
Therefore appreciable scalability within the same system can only be achieved for thrust.

How can one define the efficiency of the total hybrid system?
The efficiency equation itself is stated in Section 5.2.1.
In Chapter 5 it was determined that liquid ammonia concepts attain higher daylight efficiencies compared to liquid hydrogen concepts. The absolute difference ranges from 20 to 30 percentage points. In eclipse the hydrogen concepts all have an efficiency of 4% compared to a value of 13-19% for the ammonia concepts.
The detailed design has a daylight efficiency of 37%.

To increase the efficiency for the same power output, one should increase the thrust by increasing the propellant temperature and/or changing the nozzle shape to limit thrust loss. This can be verified if one recalls that Concept 3 with the conical nozzle achieves with respect to the detailed design a smaller maximum efficiency of 36% with a lower thrust of 1.27 N.
One can also increase the efficiency by increasing the required ΔV for the spacecraft. According to Equation 3.93 this will increase the propellant mass and therefore the wet propulsion subsystem mass. Looking at Equation 3.94 to 3.96 the total impulse will also

increase, assuming the same propellant mass flow. From running the DAO tool it seems that the total impulse increases relatively more than the wet propulsion system mass. As a result the system-specific impulse will increase.
For example, increasing the ΔV from 210 m/s to 310 m/s leads to a system-specific impulse increase from 65 s to 81 s. System mass, total impulse and system efficiency will therefore have to be traded-off if this last course of action is taken.

Chapter 8

Conclusions and recommendations

8.1 Conclusions

In this thesis research report the feasibility of a solar thermal power and propulsion system has been confirmed for a small satellite. The integration of this system gives the satellite constant power generation capability. This comes at the cost of mass, size and system-specific impulse.

For larger satellites with a larger bus and mass this system will be more appropriate as it will need a relatively smaller fraction of the bus volume and mass due to non-linear scaling of the system. When comparing conventional and hybrid systems for these spacecraft, the differences in mass, size and system-specific impulse will then have decreased.
For micro-satellites the system unfortunately has too much mass to be feasible.

Caveats to feasibility have to be mentioned.
First of all, the design and operation of the primary concentrator pointing mechanism is crucial for the generation of sufficient power and ADCS operations in general. The spacecraft must still be able to point antennae and instruments without compromising the power supply.
Second, the RAC and the fluid and gas tubing will have to be sufficiently insulated to guarantee a stable thermal environment and therefore stable propulsion and power generation. Alongside the original system volume, additional MLI will limit the usable volume in the bus.
Third, the amount of ΔV for which the system is feasible in a small bus is limited to around 200 m/s as otherwise the propellant tank volume will become too large. Also, the propellant mass will become very large for such a small spacecraft.
Finally, the modelled conditions in the DAO tool have been based on simplifications and assumptions which may not be entirely representative of a real-life system. Extensive quantitative model validation and laboratory testing therefore still need to be performed before feasibility can unequivocally be asserted.

Concerning the question of economy, a conventional system is still preferable over this hybrid system for small satellite missions in LEO. The main disadvantage for the hybrid system concerns the lower system-specific impulse.

For larger satellites beyond Earth orbit however, the system might be more suitable as no eclipse will be present in that environment. Despite the lower solar flux, this could increase or at least equate the power and propulsion capabilities of the system with respect to the LEO case. Furthermore, as indicated previously the system would scale non-linearly, therefore taking up relatively less mass and volume. The additional lack of batteries would open up more mass and space for propellant or instrumentation, increasing spacecraft functionality. As missions beyond Earth tend to involve a lot of funds and long development time, this would not be an insignificant improvement over conventional spacecraft.

8.2 Recommendations

8.2.1 Test recommendations

As stated in the previous section and in Section 3.4 quantitative model validation has to be performed. This requires the development of a representative structural thermal model for the hybrid system. This will have to include at least the cylindrical RAC, the spiral tubing and the thruster as well as the radiative interface to the heating gas channel and the gas channel itself.
Temperature measurements will have to be taken at the edge of the secondary concentrator and in the pre-cavity chamber. In addition, three temperature gauges will have to be mounted in three different locations on the RAC, the propellant tubing and at three different locations along the heating gas channel. These gauges' measurements will validate the thermal model. Especially the cooling down and heating of the RAC and tubing during and after eclipse will have to be tested. This can be done by temporarily shutting down the test light source.

The thruster model will be validated by measuring the propellant mass flow, the thrust and the chamber inlet pressure. The final measurement is to check whether the pressure losses have been accurately estimated. Combined they should give a thruster characterization which agrees with the modelled results.
If costs and time permit, the power subsystem should be included in the hardware to characterize the entire system. This includes evaporator heat exchanger, condenser, micro-turbine and micro-pump. For the heat exchanger different types of heat exchangers can be integrated to analyze their respective performances. This comparison should yield the best heat exchanger option for the power subsystem.

Different design variables should be employed during testing.
Three different tank pressures should be used to achieve three different chamber pressures. This ensures accurate thruster model validation. It also allows validation of thrust scalability for the same system. Furthermore, each test should run for at least three orbits or a time span of 4.5 hours.
During the time when there is no eclipse the light source should be varied according to Section 5.1.2.4 and in two alternative tests should be kept at full capacity.
Furthermore, at least two different RAC shapes should be tested. Since conical and

cylindrical shapes are the easiest to manufacture these RAC shapes are most likely to be selected.
This yields a set of eight different tests, each lasting 4.5 hours:

1. Test at 1 bar thruster chamber pressure for the conical RAC
2. Test at 2 bar thruster chamber pressure for the conical RAC
3. Test at 4 bar thruster chamber pressure for the conical RAC
4. Test at 1 bar thruster chamber pressure for the cylindrical RAC
5. Test at 2 bar thruster chamber pressure for the cylindrical RAC
6. Test at 4 bar thruster chamber pressure for the cylindrical RAC
7. Test at 1 bar thruster chamber pressure for the conical RAC with full solar flux during every orbit's daylight period
8. Test at 1 bar thruster chamber pressure for the cylindrical RAC with full solar flux during every orbit's daylight period

8.2.2 Research recommendations

The design and analysis of the primary concentrator deployment and pointing mechanisms were unfortunately beyond the scope of this study. These mechanisms are however crucial to the functioning of the system. Further research into this topic should therefore be pursued. Especially the advantages of on-axis and off-axis concentrators are as of yet unclear since a precise pointing algorithm and system have yet to be devised. The same applies for the deployment system for a small-diameter concentrator, although test literature such as Holmes (2000) and Freeland et al. (1997) offer a good starting point.

Loss of pressurization and outgassing of residual gases are dangers which should be taken into account for the deployment mechanism design. Damage to the polyimide-film concentrator from orbital debris and other space particles will require additional pressurization after deployment.
For the pointing mechanism the relative positioning of the condenser radiator panel with respect to the concentrator is crucial. In the event that the radiator receives external fluxes its heat dissipation capacity will be compromised causing a higher evaporator inlet working fluid temperature. This will throw the ORC off-balance decreasing the amount of power that is generated, as shown in Section 4.2.
In the event that less power is used or more power is generated by the power subsystem, mechanisms have to be designed to dissipate the extra power or feed it back into the ORC.
In addition, redundancy measures and emergency modes for the ADCS will have to be incorporated to decrease the chances of system faults thereby increasing the reliability of the solar thermal power-propulsion system.
Finally, the long-term performance of micro-turbines should be analyzed, tested and

validated due to the lack of enough test data. In case that long-term performance is not feasible, batteries should still be fitted to the spacecraft to allow the turbine to be deactivated in eclipse and thereby extend its life.

References

ASME (2013), ASME Boiler and Pressure Vessel Code, Technical report, ASME.

ESA (1989), Spacecraft Thermal Control Design Handbook: View factors, Technical report, NASA/JPL.

Anderson, J. (2010), *Fundamentals of Aerodynamics*, 5th edn, McGraw-Hill.

Andreev, V. (2011), GaAs and High-Efficiency Space Cells, *in* 'Practical Handbook of Photovoltaics', 2nd edn, Academic Press.

Angelino, G. & Invernizzi, C. (1993), 'Cyclic Methylsiloxanes as Working Fluids for Space Power Cycles', *Journal of Solar Energy Engineering* **115**, 130–137.

Armanios, E. A. (1997), *Composite Materials: Fatigue and Fracture*, 6th edn, ASTM International.

ASM Aerospace Specification Metals Inc. (2014), 'Aluminum 6061-T6; 6061-T651', ASM Material Data Sheet. [Accessed on 09/23/2014].
URL: *http://asm.matweb.com/search/SpecificMaterial.asp?bassnum=MA6061t6*

Astrium (2012), '1-N Mono-propellant thruster', Product Data Sheet. [Accessed on 12/12/2014].
URL: *http://cs.astrium.eads.net/sp/brochures/thrusters/1N%20Thruster.pdf*

AZ Technology (2008), 'Spacecraft Thermal Control and Conductive Paints/Coatings and Services Catalog', AZ Techology Company Website. [Accessed on 05/21/2014].
URL: *http://www.aztechnology.com/PDFs/materials-catalog.pdf*

AZO Materials (2014), 'Titanium Alloys - Physical Properties', AZO Materials Company Website. [Accessed on 11/12/2014].
URL: *http://www.azom.com*

Barron, R. & Barron, B. (2011), *Design for Thermal Stresses*, 1st edn, John Wiley and Sons.

Baturkin, V. (2005), 'Micro-satellites thermal controlconcepts andcomponents', *Acta Astronautica* **56**, 161 170.

Bergman, T., Lavine, A., Incropera, F. & Dewitt, D. (2011), *Fundamentals of Heat and Mass Transfer*, 7th edn, John Wiley and Sons Inc.

Berton, J. (1991), Divergence Thrust Loss Calculations for Convergent-Divergent Nozzles: Extensions to the Classical Case, Technical report, NASA.

Borde, J., Teston, F., Santandrea, S. & Boulade, S. (2004), Feasibility of the Proba 3 formation flying demonstration mission as a pair of microsats in GTO, *in* 'Proceedings of The 4S Symposium: Small Satellites, Systems and Services (ESA SP-571)'.

Briggs, T. & Campbell, J. (1972), 'The effect of strain rate and temperature on the yield and flow of polycrystalline niobium and molybdenum', *Acta Metallurgica* **20**, 711–724.

Calabro, M. (2003), Solar thermal upper stages, *in* 'Proceedings of the International Conference on Recent Advances in Space Technologies (RAST)', pp. 287–295.

Çengel, Y. & Boles, M. (2011), *Thermodynamics: An Engineering Approach*, 7th edn, McGraw-Hill, p. 912.

Churchill, S. & Chu, H. (1975), 'Correlating Equations for Laminar and Turbulent Free Convection from a Vertical Plate', *International Journal of Heat and Mass Transfer* **18**, 1323–1329.

Cornelisse, J., Schöyer, H. & Wakker, K. (1979), *Rocket Propulsion and Spaceflight Dynamics*, 1st edn, Pitman.

DuPont (2014), 'Kapton summary of properties', DuPont Company Website. [Accessed on 09/19/2014].
URL: *http://www.dupont.com/content/dam/assets/products-and-services/membranes-films/assets/DEC-Kapton-summary-of-properties.pdf*

Edmund Optics (2014), 'Sapphire Plano-Convex (PCX) Lenses', Edmund Optics Company Website. [Accessed on 09/22/2014].
URL: *http://www.edmundoptics.com/optics/optical-lenses/ir-lenses/sapphire-plano-convex-pcx-lenses/3078*

Ekpo, S. C. & George, D. (2013), 'A System Engineering Analysis of Highly Adaptive Small Satellites', *IEEE Systems Journal* **7**, 642 – 648.

Emcore (2014), 'ATJM Photovoltaic Cell', Emcore Data Sheet. [Accessed on 11/26/2014].
URL: *http://www.emcore.com/wp-content/themes/emcore/pdf/ATJM_Web.pdf*

Engineering Toolbox (2000), 'Metals - Melting Temperature', The Engineering Toolbox website. [Accessed on 09/19/2014].
URL: *http://www.engineeringtoolbox.com/melting-temperature-metals-d_860.html*

Epstein, A. (2003), Millimeter-scale, mems gas turbine engines, *in* 'Proceedings of the ASME Turbo Expo 2003'.

Epstein, A., Senturia, S., Al-Midani, O., Anathasuresh, G., Ayon, A., Breuer, K., Chen, K.-S., Ehrich, F., Esteve, E., Frechette, L., Gauba, G., Ghodssi, R., Groshenry, C., Jacobson, S., Kerrebrock, J., Lang, J., Lin, C.-C., London, A., Lopata, J., Mehra, A., Miranda, J. M., Nagle, S., Orr, D., Piekos, E., Schmidt, M., Shirley, G., Spearing, S., Tan, C., Tzeng, Y.-S. & Waitz, I. (1997), Micro-heat engines, gas turbines, and rocket engines, *in* 'Proceedings of the 28th AIAA Fluid Dynamics Conference'.

Fang, X., Xu, Y., Su, X. & Shi, R. (2012), 'Pressure drop and friction factor correlations of supercritical flow', *Nuclear Engineering and Design* **242**, 323 – 330.

Finckenor, M. & Dooling, D. (1999), Multilayer Insulation Material Guidelines, Technical report, NASA/Marschall Space Flight Center.

Flowsafe (2014), 'F80 Series Product Catalog', Flowsafe Company Website. [Accessed on 09/30/2014].
URL: *http://www.flowsafe.com/usr/Documents/catalogs/F80-Catalog.pdf*

Freeland, R., Veal, G., Bilyeu, G., Steiner, M. & Carson, D. (1996), Large inflatable deployable antenna flight experiment results, Technical report, NASA/JPL.

Freeland, R., Veal, G., Bilyeu, G., Steiner, M. & Carson, D. (1997), Large inflatable deployable antenna flight experiment results, *in* 'Proceedings of the 48th Congress of the International Astronautical Federation'.

GEA-PHE Systems (2014), 'GP Series Brazed Plate Heat Exchangers', GEA-PHE Systems Product Data Sheet. [Accessed on 11/25/2014].
URL: *http://www.gea-phe.com/fileadmin/user_upload/documents/product_datasheets/NA_GP_Series_usa.pdf*

Gems (2014), 'B-Cryo Series', Gems Sensors and Controls Company Website. [Accessed on 09/30/2014].
URL: *http://www.gemssensors.com/Products/Solenoid-Valves/Cryogenic/B-Cryo-Solenoid-Valve*

Gilmore, D. (2002), *Spacecraft Thermal Control Handbook - Volume I: Fundamental Technologies*, 2nd edn, The Aerospace Press.

GomSpace (2014), 'NanoPower BP series datasheet', GomSpace Company Website. [Accessed on 10/03/2014].
URL: *http://gomspace.com/documents/gs-ds-bp4.pdf*

Goodfellow (2014), 'Molybdenum (Mo) Tube Material Information', Goodfellow Company Website. [Accessed on 10/17/2014].
URL: *http://www.goodfellow.com/E/Molybdenum-Tube.html*

Hexcel Composites (2014), 'HexWeb™Honeycomb Attributes and Properties', Hexcel Company Website. [Accessed on 10/07/2014].
URL: *http://www.hexcel.com/Resources/DataSheets/Brochure-Data-Sheets/Honeycomb_Attributes_and_Properties.pdf*

Holmes, M. (2000), 'Solar Rocket Propulsion Ground and Space Technology Demonstration', Powerpoint presentation. [Accessed on 03/25/2014].
URL: *http://pointfocus.com/images/pdfs/sun_rocket4d_holm.pdf*

Hopkins, R. & Payne, D. (1987), 'Optimized support systems for spaceborne dewars', *Cryogenics* **27**, 209 – 216.

Howell, J. (2010), 'A catalog of radiation heat transfer configuration factors', Online resource for Thermal Radiation Heat Transfer, 5th edition. [Accessed on 09/19/2014].
URL: *http://www.thermalradiation.net/tablecon.html*

Hung, T., Shai, T. & Wang, S. (1997), 'A review of organic Rankine cycles (ORC's) for the recovery of low-grade waste heat', *Energy* **22**, 661–667.

Idel'chik, I. (1986), *Handbook of Hydraulic Resistance*, 1st edn, Israel Program for Scientific Translations.

Invernizzi, C., Iora, P. & Silva, P. (2007), 'Bottoming micro-rankine cycles for micro-gas turbines', *Applied Thermal Engineering* **27**, 100–110.

Jenkins, F. & White, H. (1957), *Fundamentals of Optics*, 3rd edn, McGraw-Hill.

Johnson, W. & Fesmire, J. (2011), Thermal performance of low layer density multilayer insulation using liquid nitrogen, Technical report, National Aeronautics and Space Administration (NASA).

Kapooria, R., Kumar, S. & Kasana, K. (2008), 'An analysis of a thermal power plant working on a Rankine cycle: A theoretical investigation', *Journal of Energy in Southern Africa* **19**, 77–83.

Kim, C. T., Lee, J. & Kwon, S. (2014), 'Design, fabrication, and testing of a dc mhd micropump fabricated on photosensitive glass', *Chemical Engineering Science* **117**, 210 – 216.

Kyocera (2013), 'Single crystal sapphire', Kyocera Company Website. [Accessed on 05/21/2014].
URL: *http://americas.kyocera.com/kicc/pdf/Kyocera%20Sapphire.pdf*

Lai, N. A., Wendland, M. & Fischer, J. (2011), 'Working fluids for high-temperature organic Rankine cycles', *Energy* **36**, 199 – 211.

Larson, W. & Wertz, J. (2005), *Space Mission Analysis and Design*, 3rd edn, Microcosm Inc.

Laser, D. & Santiago, J. (2004), 'A review of micropumps', *Micromechanics and Microengineering* **14**, 35 – 64.

Lashley, C., Krein, S. & Barcomb, P. (1998), Deployable Radiators - A Multi-Discipline Approach, *in* 'Proceedings of the International Conference on Environmental Systems'.

Leenders, H. & Zandbergen, B. (2008), Development of a solar thermal thruster system, *in* 'Proceedings of the 59th IAC Congress'.

Li, C., Kosmadakis, G., Manolakos, D., Stefanakos, E., Papadakis, G. & Goswami, D. (2013), 'Performance investigation of concentrating solar collectors coupled with a transcritical organic Rankine cycle for power and seawater desalination co-generation', *Desalination* **318**, 107–117.

Mago, P., Chamra, L., Srinivasan, K. & Somayaji, C. (2008), 'An examination of regenerative organic Rankine cycles using dry fluids', *Applied Thermal Engineering* **28**, 998–1007.

McKetta Jr., J. (1992), *Rocket Propulsion Elements*, 1st edn, CRC Press.

Micropump (2014), 'GA Series', Micropump Company Website. [Accessed on 10/03/2014].
URL: *http://www.micropump.com/support_documents/Series_GA-GAH_Technical_Specs.pdf*

Nakamura, T., Sullivan, D., McClanahan, J., Shoji, J., Partch, R. & Quinn, S. (2004), Solar thermal propulsion for small spacecraft, *in* 'Proceedings of the 40th AIAA/ASME/SAE/ASEE Joint Propulsion Conference and Exhibit'.

Ohlhorst, C., Vaughn, W., Ransone, P. & Tsou, H.-T. (1997), Thermal Conductivity Database of Various Structural Carbon-Carbon Composite Materials, Technical report, NASA.

O'Shea, D. C., Suleski, T. J., Kathman, A. D. & Prather, D. W. (2004), *Diffractive Optics: Design, Fabrication, and Test*, 1st edn, SPIE Press.

Plachta, D., Christie, R., Jurns, J. & Kittel, P. (2006), 'Passive ZBO storage of liquid hydrogen and liquid oxygen applied to space science mission concepts', *Cryogenics* **46**, 89 – 97.

PowerMEMS (2014), 'Ultra micro gas turbine generator', PowerMEMS Project Website. [Accessed on 10/23/2014].
URL: *http://www.powermems.be/gasturbine.html*

Qioptiq (2014), 'Optical Solar Reflectors', Qioptiq Product Data Sheet. [Accessed on 11/22/2014].
URL: *www.qioptiq.com/download/Qioptiq_Optical-Solar-Reflectors_Dec10.pdf*

Racca, G., Marini, A., Stagnaro, L., van Dooren, J., di Napoli, L., Foing, B., Lumb, R., Volp, J., Brinkmann, J., Grünagel, R. ., andE. Tremolizzo, D. E., McKay, M., Camino, O., Schoemaekers, J., Hechler, M., Khan, M., Rathsman, P., Andersson, G., K. Anflo, S. B., Bodin, P., Edfors, A., Hussain, A., Kugelberg, J., Larsson, N., Ljung, B., Meijer, L., Mortsell, A. M., Nordebäck, T., Persson, S. & Sjöberg, F. (2002), 'SMART-1 mission description and development status', *Planetary and Space Science* **50**, 1323 1337.

Rayegan, R. & Tao, Y. (2011), 'A procedure to select working fluids for Solar Organic Rankine Cycles (ORCs)', *Renewable Energy* **36**, 659 670.

Rembar (2014), 'Refractory Metal Supplies - Molybdenum Tubing', Rembar Company Website. [Accessed on 10/30/2014].
URL: *http://www.rembar.com/materials.html*

Rugescu, R. (2012), *Solar Power*, 1st edn, InTech, p. 199.

Saaty, T. (1990), 'How to make a decision: The Analytic Hierarchy Process', *European Journal of Operational Research* **48**, 9 26.

Sahara, H. & Shimizu, M. (2003), Solar thermal propulsion system for a japanese 50kg-class microsatellite, *in* 'Proceedings of the 39th AIAA/ASME/SAE/ASEE Joint Propulsion Conference and Exhibit'.

Sahara, H., Shimizu, M., Fujii, T., K.Okamoto, Takaoka, S. & Nakamura, Y. (2000), Single and opposed-cavity solar thermal thrusters made of single crystal tungsten, *in* 'Proceedings of the 3rd International Conference on Spacecraft Propulsion'.

Saleh, B., Koglbauer, G., Wendland, M. & Fischer, J. (2007), 'Working fluids for low-temperature organic Rankine cycles', *Energy* **32**, 1210–1221.

Samson (2014), 'Type 2357-1 and Type 2357-6 Pressure Regulators', Samson Company Website. [Accessed on 09/30/2014].
URL: *http://www.samson.de/pdf_en/t25570en.pdf*

Schlichting, H. & Gersten, K. (2000), *Boundary-Layer Theory*, 1st edn, Springer.

Schubert, D. (2012), Mems-Concept Using Micro Turbines for Satellite Power Supply, Technical report.

Shimizu, M., Naito, H., Sahara, H., Fujii, T., Yugami, H. & Okamoto, K. (2001), 50mm Cavity Diameter Solar Thermal Thruster Made of Single Crystal Molybdenum, *in* 'Proceedings of the 37th AIAA/ASME/SAE/ASEE Joint Propulsion Conference and Exhibit'.

Sieder, E. N. & Tate, G. E. (1936), 'Heat Transfer and Pressure Drop of Liquids in Tubes', *Ind. Eng. Chem.* **28 (12)**, 1429 1435.

Soares, C. (2015), *Gas Turbines*, 2nd edn, Elsevier.

Spirax Sarco (2014), 'DCV41 Austenitic Stainless Steel Disc Check Valve', Spirax Sarco Company Website. [Accessed on 09/30/2014].
URL: *http://www.spiraxsarco.com/pdfs/TI/p601_18.pdf*

Stewart, J. & Martin, J. (1995), Dual fuel solar thermal propulsion for LEO to GEO transfer: Ideal rocket analysis, *in* 'Proceedings of the 31st AIAA/ASME/SAE/ASEE Joint Propulsion Conference and Exhibit'.

Sutherland, W. (1893), 'The Viscosity of Gases and Molecular Force', *Philosophical Magazine* **36**, 507 531.

Sutton, G. P. & Biblarz, O. (2001), *Rocket Propulsion Elements*, 7th edn, John Wiley and Sons.

Swearengen, J. (1972), 'The Thermo-Mechanical Behavior of 6061 Aluminum-Magnesium-Silicon Alloy', *Materials Science and Engineering* **10**, 103–117.

Tennekes, H. & Lumley, J. L. (1972), *A First Course in Turbulence*, 1st edn, MIT Press.

ter Brake, H. & Wiegerinck, G. (2002), 'Low-power cryocooler survey', *Cryogenics* **42**, 705 – 718.

Thermacore (2014), 'Thermal Straps: Efficient Cooling without Structural Loading', Thermacore Company Website. [Accessed on 09/22/2014].
URL: *http://www.thermacore.com/products/thermal-straps.aspx*

Toffolo, A., Lazzaretto, A., Manente, G. & Paci, M. (2014), 'A multi-criteria approach for the optimal selection of working fluid and design parameters in Organic Rankine Cycle systems', *Applied Energy* **121**, 219–232.

Tummala, V. & Ling, H. (1998), 'A note on the computation of the mean random consistency index of the analytic hierarchy process (AHP)', *Theory and Decision* **44**, 221 230.

Vaja, I. & Gambarotta, A. (2010), 'Internal Combustion Engine (ICE) bottoming with Organic Rankine Cycles (ORCs)', *Energy* **35**, 1084–1093.

Wang, J., Yan, Z., Zhao, P. & Dai, Y. (2014), 'Off-design performance analysis of a solar-powered organic Rankine cycle', *Energy Conversion and Management* **80**, 150–157.

Ward, J., Jason, S. & Sweeting, M. (1999), Microsatellite Constellation for Disaster Monitoring, Technical report, University of Surrey.

Weast, R. (1969), *CRC Handbook of Chemistry and Physics*, 50th edn, The Chemical Rubber Co.

Wells, N., Walker, R., Green, S. & Ball, A. (2006), 'SIMONE: Interplanetary microsatellites for NEO rendezvous missions', *Acta Astronautica* **59**, 700–709.

Wong, W. (2000), High-Efficiency Solar Thermal Vacuum Demonstration Completed for Refractive Secondary Concentrator, Technical report, NASA.

Wong, W., Geng, S., Castle, C. & Macosko, R. (2000), Design, Fabrication and Test of a High Efficiency Refractive Secondary Concentrator for Solar Applications, *in* 'Proceedings of the 35th Intersociety Energy Conversion Engineering Conference'.

Wong, W. & Macosko, R. (1999), Refractive Secondary Concentrators for Solar Thermal Applications, *in* 'Proceedings of the 34th Intersociety Energy Conversion Engineering Conference'.

Yamamoto, T., Furuhata, T., Arai, N. & Mori, K. (2001), 'Design and testing of the Organic Rankine Cycle', *Energy* **26**, 239–251.

Zhang, X., Xie, B., Dai, S., Zhang, W., Hu, G. & Lan, D. (2007), 'First micro-satellite and new enhanced small satellite series in DFH Satellite Co. Ltd.', *Acta Astronautica* **61**, 234 242.

Appendix A

View factors

This appendix contains the equations to calculate the different view factors between the thermal nodes of the DAO tool. ESA (1989) and Howell (2010) have been used to find the appropriate view factor equations for the particular geometries.
Recall that all view factors from one node's surface have to add up to 1. Furthermore there is a reciprocal relation for view factors as discussed in Section 3.2.5.

A.1 Node 1 to Node 5

The view factor between Node 1 and Node 2 is calculated as a view factor from one spherical cap to another.
First, the view factor from a sphere to a spherical cap is calculated. Afterwards the sphere is converted to a spherical cap by multiplying the original view factor with a correction factor $1/c$.

$$
\begin{aligned}
R &= \frac{R_{curvature_{sec}}}{R_{curvature_{prim}}} \\
S &= \frac{d_{concentrators}}{R_{curvature_{prim}}} \\
d_{angular} &= 2\sin\left(\frac{R_{prim}}{R_{curvature_{prim}}}\right) \\
c &= \frac{d_{angular}}{\pi} \\
F_{1-2} &= \frac{1}{c}\cdot\frac{1}{2}\left(1-\frac{1}{\sqrt{1+\left(\frac{R\sin(\theta)}{1+S+(1-\cos(\theta)R}\right)^2}}\right)
\end{aligned}
\tag{A.1}
$$

Here, R_{prim} and R_{sec} are respectively the cross-sectional radius of the primary and secondary concentrators. The $R_{curvature}$ terms are the radii of the rear membrane of the primary concentrator and the front membrane of the secondary concentrator, $d_{concentrators}$ is the minimum distance between the concentrators and $d_{angular}$ is the spherical cap angular diameter, in this case for the rear of the primary concentrator.

The view factors between Node 1 and Node 3, Node 2 and Node 4 and Node 2 and Node 5 are calculated as view factors from one spherical cap to a disk. An example for the first set is given in Equation A.2.

$$\begin{aligned} R &= R_3/d_{1-3} \\ F_{1-3} &= \frac{1}{2}\frac{1}{c}\left(1 - \frac{1}{\sqrt{1+R^2}}\right) \end{aligned} \tag{A.2}$$

Here, R_3 is the outer radius of Node 3 and d_{1-3} is the distance between the center of the spherical cap of Node 1 and Node 3. The correction factor $1/c$ is the same as for equation A.1.

The view factors between Node 3 and Node 5 are calculated as view factors between opposite disks (Equation A.3.

$$\begin{aligned} R_a &= R_3/d_{3-5} \\ R_b &= R_5/d_{3-5} \\ x_{ab} &= 1 + \frac{1+R_b^2}{R_a^2} \\ F_{disk-disk} = F_{3-5} &= 1/2\left(x_{ab} - \sqrt{x_{ab}^2 - 4(R_b/R_a)^2}\right) \end{aligned} \tag{A.3}$$

Here, R_3 and R_5 are the radii of Node 3 and 5. d_{3-5} is the distance between the two nodes.

The apertures in both disks of Node 3 and 5 are taken into account by subtracting certain view factors. In Equation A.4 an example is given of the outer sub-nodes of Node 3 and 5, $3A$ and $5A$.

$$F_{3A5A} = (F_{3-5} - F_{3_i-5}) - (F_{3-5_i} - F_{3_i-5_i}) \tag{A.4}$$

Here, F_{3-5} is the view factor of a disk with the outer radius of Node 3 to a disk with outer radius of Node 5. F_{3_i-5} is the view factor from the cancelled out parts of the full disk of Node 3 to the full disk of Node 5. F_{3-5_i} is the view factor from the full disk of Node 3 to the cancelled out parts of the full disk of Node 5. Finally, $F_{3_i-5_i}$ is the view factor from the cancelled out parts of Node 3 to the cancelled out parts of Node 5. The same equation applies to the inner sub-nodes of Node 3 and 5, $3B$ and $5B$.

The view factors between Node 3 and Node 4 and Node 5 and Node 4 are calculated with view factors from a disk to a disk and using the unity sum of all view factors from one surface: $1 - F_{disk-disk}$. In this case the view factor from the disk to each cylindrical sub-node and beyond is 1. By subtracting the view factor to the outer base of the cylinder, which is a disk, the radiation which is passed on to the next sub-node is cancelled out.

The view factors from Node 4's sub-nodes to themselves and to each other are respectively calculated as view factors from a cylinder to itself (Equation A.5) and from a cylinder to another cylinder (Equation A.6). Sub-nodes $4A$, $4B$ and $4C$ represent respectively the

front, middle and rear of the pre-cavity chamber with respect to the primary concentrator.

$$
\begin{aligned}
H &= \frac{H_{4A}}{2R_4} \\
F_{4A4A} &= (1+H) - \sqrt{1+H^2} \qquad \text{(A.5)} \\
H_1 &= \frac{H_{4A}}{R_4} \\
H_2 &= \frac{H_{4B}}{R_4} \\
F_{4A4B} &= \frac{H_2}{2} + \frac{1}{4}\left(\sqrt{4+H_1^2} + \left(\frac{H_2}{H_1}\sqrt{4+H_2^2}\right) - \left(1+\frac{H_2}{H_1}\right)\sqrt{4+(H_1+H_2)^2}\right) \qquad \text{(A.6)}
\end{aligned}
$$

Here, H_{4A} and H_{4B} are the length of the first and second cylindrical sub-node and R_4 is the radius of the cylinder.

A.2 Node 6

A.2.1 Conical RAC

The view factor from Node 6's front sub-node to itself (F_{6A6A}) and center sub-node to itself (F_{6B6B}) is calculated as a view factor of a frustum of a cone to itself. Here, H_i is the distance of the frustum top to the base of the entire cone, H_{total} is the total cone length and θ_{cone} is the half cone angle in radians. Equation A.7 and A.8 calculate respectively the local slant length and the total slant length.

$$
\begin{aligned}
\theta_{cone} &= \arctan(R_6/H_6) \\
\xi &= H_i/\cos(\theta_{cone}/2) \qquad \text{(A.7)} \\
x &= H_{total}/\cos(\theta_{cone}/2) \qquad \text{(A.8)} \\
X &= \xi/x \\
F_{6A6A} &= 1 + \frac{\left((1-X)\cos(\theta_{cone}/2)^2 - \sqrt{(X+1)^2 - 4X\cos(\theta_{cone}/2)^2}\right)}{(1+X)\sin(\theta_{cone})} \qquad \text{(A.9)}
\end{aligned}
$$

The rear sub-node $F-6C6C$ is the unity view factor minus the view factor of the interior of the cone to its base as seen in Equation A.11.

$$
\begin{aligned}
F_{cone_{6C}-base} &= \frac{1}{\sqrt{1+\left(\frac{H_{6C}}{R_{6C}-t_6}\right)^2}} \qquad \text{(A.10)} \\
F_{6C6C} &= 1 - F_{cone_{6C}-base} \qquad \text{(A.11)} \\
F_{6C6A} &= F_{cone_{6C}-base} F_{disk_{6C}-disk_{6B}} \left(1 - F_{disk_{6B}-disk_{6A}}\right) \qquad \text{(A.12)} \\
F_{6C6B} &= F_{cone_{6C}-base} \left(1 - F_{disk_{6C}-disk_{6B}}\right) \qquad \text{(A.13)}
\end{aligned}
$$

View factors F_{6B6A} and F_{6A5} are calculated with the view factor from a frustum of a cone to its base as in Equation A.14.

$$\begin{aligned} H &= (H_6/3)/R_{6B} \\ R &= R_6/R_{6B} \\ X &= (1 + R^2 + H^2) \\ F_{6A5} &= \frac{2R^2 - X + \sqrt{X^2 - 4R^2}}{2\sqrt{X - 2R}(1 + R)} \end{aligned} \tag{A.14}$$

$$F_{6B6A} = F_{6B6A'}(1 - F_{6A5}) \tag{A.15}$$

Here, $F_{6B6A'}$ is only the view factor of sub-node 6B to its base, whereas F_{6B6A} takes into account that the receiving sub-node also can radiate to its base. To correct for this the last term is added in Equation A.15.

A.2.2 Cylindrical RAC

The view factors F_{6A6A} and F_{6B6B} are a view factor from a cylinder to itself which is calculated through Equation A.5. The view factor F_{6C6C} is the sum of view factor F_{6B6B} and the view factor from the cylinder to a disk (Equation A.16).

$$\begin{aligned} R &= r_1/r_2 \\ H_1 &= h_1/r_2 \\ H_2 &= h_2/r_2 \\ X_1 &= H_1^2 + R^2 + 1 \\ X_2 &= H_2^2 + R^2 + 1 \\ F &= \frac{1}{4R(H_2 - H_1)} \left((X_1 - X_2) - \sqrt{X_1^2 - 4R^2} + \sqrt{X_2^2 - 4R^2} \right) \end{aligned} \tag{A.16}$$

Here, r_1 and r_2 are respectively the radii of the cylinder and the disk. h_1 and h_2 are respectively the minimum distance of the cylinder to the disk and the maximum distance of the cylinder to the disk, therefore taking into account the length of the cylinder.

The view factor from sub-node $6A$ to sub-node $6B$ is calculated as a view factor from a cylinder to another cylinder (Equation A.5). The view factor from sub-node $6A$ to sub-node $6C$ is as follows:

$$F_{6A6C} = F_{6A-6B6C} - F_{6A6B} + F_{cylinder_{6A}-disk_{6C}} \tag{A.17}$$

The view factor F_{6B6C} is calculated as a view factor from a cylinder to an adjacent cylinder (Equation A.5) summed up with a view factor from a cylinder to a disk separated by one third the RAC length (Equation A.16).
The view factor F_6A5 is calculated as a view factor from a cylinder to a disk at a small distance.

A.2.3 Spherical RAC

The view factor from node $6A$ to itself, F_{6A6A}, is calculated as the view factor from a spherical cap to itself through Equation A.18.

$$H = h_{cap}/r_{cap}$$
$$R = r_{sphere}/r_{cap}$$
$$F_{cap-itself} = \frac{H}{2R} \tag{A.18}$$
$$F_{cap-base} = \frac{1}{H^2 + 1} \tag{A.19}$$

Here, h_{cap} is the spherical cap height, r_{cap} is the radius of the spherical cap at its base and r_{sphere} is the radius of the sphere from which the spherical cap is derived.
Equation A.20 holds due to symmetry of the spherical RAC.

$$F_{6A6A} = F_{6C6C} \tag{A.20}$$

The view factor from the front sub-node to the center sub-node uses both Equation A.19 and A.3. The last equation employs the base of the spherical cap of sub-node $6A$ as a disk to the disk of sub-node $6B$ which are equal in size due to symmetry.

$$F_{6A6B} = F_{cap-base}\,(1 - F_{disk_{6A}-disk_{6B}}) \tag{A.21}$$

The view factor F_{6B6B} is two times the view factor of the RAC hemisphere to itself minus the view factor F_{6A6A}. Thus Equation A.18 is used. This yields the following:

$$F_{6B6B} = 2\,(F_{hemisphere-itself} - F_{6A6A}) \tag{A.22}$$

The view factors from Node 6 to Node 5 are zero for the spherical RAC as no heat transfer is assumed between the two nodes.

Table A.1 shows the different view factors as estimated by the DAO tool for the detailed design which features a cylindrical RAC. As can be seen not all the view factors for each thermal node sum up to unity. After long and careful deliberation this issue remains unresolved; consulting thermal analysis software is therefore recommended to accurately calculate the view factors in future research. For the purposes of this feasibility study however these estimates are considered acceptable.

Table A.1: View factors for detailed design

NODE	1	2	3A	3B	4A	4B	4C	5A	5B	6A	6B	6C
1	0	2E-3	0.02	0.01	0	0	0	0	0	0	0	0
2	0.51	0	0	0	0.38	0.01	0	0	0.03	0	0	0
3A	0.33	0	0	0	0.11	0	0	0	0.02	0	0	0
3B	0.17	0	0	0	0.03	0.01	0	0	0.03	0	0	0
4A	0	0.12	0.17	0.03	0.13	0.11	0.08	4E-3	0	0	0	0
4B	0	3E-3	0	0.01	0.11	0.13	0.13	0.01	0	0	0	0
4C	0	0	0	0	0.08	0.11	0.13	0	0.02	0	0	0
5A	0	0	0	0	0.01	0.01	0	0	0	0.01	2E-3	1E-3
5B	0	0.01	0.07	0.04	0	0	0.04	0	0	0.53	0.10	0.05
6A	0	0	0	0	0	0	0	1E-3	0.05	0.54	0.19	0.04
6B	0	0	0	0	0	0	0	0	0.01	0.19	0.54	0.23
6C	0	0	0	0	0	0	0	0	3E-3	0.03	0.19	0.76

A.3 View factors to space

The view factors of Node 1 to Node 3 to space are as follows:

$$F_{1S} = 1 - F_{12} - F_{13} \tag{A.23}$$

$$F_{2S} = \frac{A_{2_{front}}}{A_{2_{front}} + A_{2_{rear}}} - F_{21} \tag{A.24}$$

$$F_{3AS} = 1/2 - F_{3A1} \tag{A.25}$$

$$F_{3BS} = 1/2 - F_{3B1} \tag{A.26}$$

$$\tag{A.27}$$

The $A_{2_{front}}$ and $A_{2_{rear}}$ indicate the front and rear surface areas of the secondary concentrator as seen from the primary concentrator.

The view factors to space are respectively 0.97, 0, 0.17 and 0.33. Clearly the primary concentrator is so large that the space-facing side of the secondary concentrator only sees the primary concentrator. The primary concentrator emits almost all its thermal radiation to space.

Appendix B

Design parameters for conceptual designs

Table B.1: Design parameters for Concept 1

Parameter	**Value**	**Unit**
Primary concentrator radius	0.45	$[m]$
Primary concentrator concentration ratio	700	$[-]$
Primary concentrator focal length	0.5	$[m]$
Secondary concentrator radius	0.017	$[m]$
Secondary concentrator focal length	0.05	$[m]$
Cavity type	Conical	$[-]$
Cavity radius	0.07	$[m]$
Cavity length	0.30	$[m]$
Cavity lid aperture radius	0.0525	$[m]$
Number of turns in the spiral propellant tubing	20	$[-]$
Inner diameter of propellant tubing	0.0047	$[m]$
Number of conduction conduits	4	$[-]$
Conduction conduit radius	0.0070	$[m]$
Conduction conduit length	0.12	$[m]$
Inner diameter of evaporator heating gas channel	0.0132	$[m]$
Thruster chamber radius	0.01	$[m]$
Thruster chamber pressure	1	$[bar]$
Thruster throat radius	0.0015	$[m]$
Thruster divergent section length	0.05	$[m]$
Thruster expansion ratio	100	$[-]$
Propellant flow initialization cavity temperature	1300	$[K]$
Propellant type	Ammonia	$[-]$

Table B.2: Design parameters for Concept 2

Parameter	**Value**	**Unit**
Primary concentrator radius	0.7850	$[m]$
Primary concentrator concentration ratio	700	$[-]$
Primary concentrator focal length	0.5	$[m]$
Secondary concentrator radius	0.0297	$[m]$
Secondary concentrator focal length	0.05	$[m]$
Cavity type	Conical	$[-]$
Cavity radius	0.07	$[m]$
Cavity length	0.30	$[m]$
Cavity lid aperture radius	0.0525	$[m]$
Number of turns in the spiral propellant tubing	20	$[-]$
Inner diameter of propellant tubing	0.0047	$[m]$
Number of conduction conduits	2	$[-]$
Conduction conduit radius	0.0088	$[m]$
Conduction conduit length	0.05	$[m]$
Inner diameter of evaporator heating gas channel	0.017	$[m]$
Thruster chamber radius	0.01	$[m]$
Thruster chamber pressure	1	$[bar]$
Thruster throat radius	0.0015	$[m]$
Thruster divergent section length	0.05	$[m]$
Thruster expansion ratio	100	$[-]$
Propellant flow initialization cavity temperature	1300	$[K]$
Propellant type	Hydrogen	$[-]$

Table B.3: Design parameters for Concept 3

Parameter	**Value**	**Unit**
Primary concentrator radius	0.45	$[m]$
Primary concentrator concentration ratio	700	$[-]$
Primary concentrator focal length	0.5	$[m]$
Secondary concentrator radius	0.017	$[m]$
Secondary concentrator focal length	0.05	$[m]$
Cavity type	Cylindrical	$[-]$
Cavity radius	0.07	$[m]$
Cavity length	0.30	$[m]$
Cavity lid aperture radius	0.0525	$[m]$
Number of turns in the spiral propellant tubing	20	$[-]$
Inner diameter of propellant tubing	0.048	$[m]$
Number of conduction conduits	4	$[-]$
Conduction conduit radius	0.010	$[m]$
Conduction conduit length	0.12	$[m]$
Inner diameter of evaporator heating gas channel	0.017	$[m]$
Thruster chamber radius	0.01	$[m]$
Thruster chamber pressure	1	$[bar]$
Thruster throat radius	0.0015	$[m]$
Thruster divergent section length	0.05	$[m]$
Thruster expansion ratio	100	$[-]$
Propellant flow initialization cavity temperature	1300	$[K]$
Propellant type	Ammonia	$[-]$

Table B.4: Design parameters for Concept 4

Parameter	**Value**	**Unit**
Primary concentrator radius	0.785	$[m]$
Primary concentrator concentration ratio	700	$[-]$
Primary concentrator focal length	0.5	$[m]$
Secondary concentrator radius	0.0297	$[m]$
Secondary concentrator focal length	0.05	$[m]$
Cavity type	Cylindrical	$[-]$
Cavity radius	0.070	$[m]$
Cavity length	0.30	$[m]$
Cavity lid aperture radius	0.0525	$[m]$
Number of turns in the spiral propellant tubing	20	$[-]$
Inner diameter of propellant tubing	0.0037	$[m]$
Number of conduction conduits	2	$[-]$
Conduction conduit radius	0.01	$[m]$
Conduction conduit length	0.05	$[m]$
Inner diameter of evaporator heating gas channel	0.017	$[m]$
Thruster chamber radius	0.01	$[m]$
Thruster chamber pressure	1	$[bar]$
Thruster throat radius	0.0015	$[m]$
Thruster divergent section length	0.05	$[m]$
Thruster expansion ratio	100	$[-]$
Propellant flow initialization cavity temperature	1300	$[K]$
Propellant type	Hydrogen	$[-]$

Table B.5: Design parameters for Concept 5

Parameter	**Value**	**Unit**
Primary concentrator radius	0.45	$[m]$
Primary concentrator concentration ratio	700	$[-]$
Primary concentrator focal length	0.5	$[m]$
Secondary concentrator radius	0.017	$[m]$
Secondary concentrator focal length	0.08	$[m]$
Cavity type	Spherical	$[-]$
Cavity radius	0.070	$[m]$
Cavity length	0.070	$[m]$
Cavity lid aperture radius	0.0525	$[m]$
Number of turns in the spiral propellant tubing	20	$[-]$
Inner diameter of propellant tubing	0.0047	$[m]$
Number of conduction conduits	4	$[-]$
Conduction conduit radius	0.0078	$[m]$
Conduction conduit length	0.10	$[m]$
Inner diameter of evaporator heating gas channel	0.0149	$[m]$
Thruster chamber radius	0.01	$[m]$
Thruster chamber pressure	1	$[bar]$
Thruster throat radius	0.0015	$[m]$
Thruster divergent section length	0.05	$[m]$
Thruster expansion ratio	100	$[-]$
Propellant flow initialization cavity temperature	1300	$[K]$
Propellant type	Ammonia	$[-]$

Table B.6: Design parameters for Concept 6

Parameter	**Value**	**Unit**
Primary concentrator radius	0.785	$[m]$
Primary concentrator concentration ratio	700	$[-]$
Primary concentrator focal length	0.5	$[m]$
Secondary concentrator radius	0.0297	$[m]$
Secondary concentrator focal length	0.08	$[m]$
Cavity type	Spherical	$[-]$
Cavity radius	0.070	$[m]$
Cavity length	0.07	$[m]$
Cavity lid aperture radius	0.0525	$[m]$
Number of turns in the spiral propellant tubing	20	$[-]$
Inner diameter of propellant tubing	0.0047	$[m]$
Number of conduction conduits	4	$[-]$
Conduction conduit radius	0.0078	$[m]$
Conduction conduit length	0.070	$[m]$
Inner diameter of evaporator heating gas channel	0.0174	$[m]$
Thruster chamber radius	0.01	$[m]$
Thruster chamber pressure	1	$[bar]$
Thruster throat radius	0.0015	$[m]$
Thruster divergent section length	0.05	$[m]$
Thruster expansion ratio	100	$[-]$
Propellant flow initialization cavity temperature	1300	$[K]$
Propellant type	Hydrogen	$[-]$